FACULTY
OF MATHEMATICS
AND PHYSICS
Charles University

DOCTORAL THESIS

Lenka Kubíčková

Study of properties of iron-containing nanoparticles stressing their application potential

Department of Low-Temperature Physics

Supervisor of the doctoral thesis: doc. Mgr. Jaroslav Kohout, Dr.
Study programme: Physics
Study branch: Physics of Condensed Matter and Materials Research

Prague 2021

I declare that I carried out this doctoral thesis independently, and only with the cited sources, literature, and other professional sources. It has not been used to obtain another or the same degree.
I understand that my work relates to the rights and obligations under the Act No. 121/2000 Coll., the Copyright Act, as amended, in particular the fact that Charles University has the right to conclude a license agreement on the use of this work as a school work pursuant to Section 60 subsection 1 of the Copyright Act.

In Prague, date July 22, 2021

Lenka Kubíčková

Acknowledgment

First and foremost, I would like to thank my supervisor, Dr. Jaroslav Kohout, for his patient guidance, optimism, and support during my Ph.D. studies. I am deeply indebted to my co-supervisor Dr. Ondřej Kaman for his help and a healthy pressure which did not allow me to rest on my laurels. I heartily thank both for their willingness to devote their time to me, and finally for reading and commenting on this text.

I would also like to express my gratitude to all colleagues that participated in the presented studies. I wish to thank my coworkers from the Institute of Physics of CAS, namely Dr. Pavel Veverka, Jarmila Kuličková, Dr. Tereza Kořínková, and Dr. Petr Brázda among other things for synthesis and coating of the studied nanoparticles, to Dr. Jakub Koktan for experiments on magnetic separation, Dr. Mariia Pashchenko for her help with magnetic measurements, Dr. Zdeněk Jirák for his helpful insights during preparation of the manuscripts, Dr. Karel Knížek for his help and consultation on XRD, Dr. Jiří Hejtmánek and Dr. Petr Levinský for thermoelectric measurements, and Dr. Mariana Klementová for HRTEM and electron diffraction. Further, I would also like to thank Dr. Karel Bernášek for his help with ultra-high-field MRI and Petr Dvořák for introducing me to operating the NMR spectrometer, Dr. Vít Herynek for his help with relaxivity measurements, evaluation of cytotoxicity and an *in vivo* MRI experiment, Dr. Karel Královec and Dr. Radim Havelek for biology-related studies, Dr. Magda Vosmanská for the ICP-MS analysis, Dr. Miroslav Veverka and Dr. Janja Stergar for some of the syntheses and coatings, Dr. Florence Porcher for neutron diffraction data, and Prof. Peter Baláž and his colleagues for the mechanochemical synthesis of chalcopyrites and some of the related characterizations.

Further, I wish to thank my colleagues from the Laboratory of Mössbauer spectroscopy, especially to Dr. Tomáš Kmječ and Denisa Kubániová for their friendly reception, their support during my studies at the faculty, and their invaluable help with measurements. Special thanks belong to our esteemed Dr. Karel Závěta, who, with his typical kindness and gentle humor, provided every one of us with countless pieces of precious advice and insights, and who also contributed with his comments on this text. I would also like to thank Prof. Angela Möller and Dr. Vadim Ksenofontov for their warm acceptance at JGU Mainz.

Last but not least, I am extremely grateful to my boyfriend for his loving support, all his help during my studies, and for pushing me to become a better version of myself. Following my path, though highly inspiring and provoking curiosity, to the final destination would not have been possible without the support and nurturing of my beloved family, who deserve undying gratitude and who have been there for me, in any weather, always…

Title: Study of properties of iron-containing nanoparticles stressing their application potential

Author: Lenka Kubíčková

Department: Department of Low-Temperature Physics

Supervisor: doc. Mgr. Jaroslav Kohout, Dr., Department of Low-Temperature Physics

Abstract: Magnetic nanoparticles offer a plethora of application possibilities in various fields of human endeavors. The fundamental understanding of their physical properties, related to the constituent magnetic phase, surface termination, and possible coating, synthesis method, size, shape, or even clustering, is crucial for their effective use and optimization for the intended applications. This thesis aims to contextualize original results, concerning especially the structure and magnetic properties, obtained during fundamental research on nanoparticles of selected iron-containing systems and employ these findings in testing the nanoparticles in chosen applications.

Iron presents an ideal constituting element due to its low cost, high abundance in the Earth's crust, exploitability, and low toxicity. The selected systems involved in this thesis comprise iron-containing oxides (ferrites, and various polymorphs of iron(III) oxide, including ε-Fe_2O_3 and doped counterparts), and sulfides (greigite, chalcopyrite), all of which exhibit specific properties such as magnetic or structural transitions. Among the studied applications, the largest attention is devoted to the use of magnetic nanoparticles as contrast agents in magnetic resonance imaging, and the analysis of their efficacy in contrast enhancement – their relaxivity – with respect to various factors. Since this application is directed to medicine, some of the promising systems were also subjected to cytotoxicity studies. Further, magnetic solid-phase extraction is included as a representative analytical application of magnetic nanoparticles with possible use for example in environmental protection, food analysis, and medicine. Finally, the thermoelectric applications of nanostructured phases are briefly introduced.

Keywords: nanoparticles; relaxivity; hyperfine interactions; Mössbauer spectroscopy; magnetic resonance imaging

Contents

1 Introduction

Over several last decades, nanotechnology or the "science of miniaturization" has evolved into one of the major branches in material research providing attractive solutions throughout virtually all fields of human activity. Many proposed applications have received an enthusiastic response in practice, spanning from cultural heritage conservation [1–3] to cancer treatment [4–6], though appreciably more ideas and concepts have been suggested, either waiting for broader acceptance or just demonstrating an elegant principle while being unsuitable for commercial production. However, the rapid transfer of nanomaterials from laboratories into our everyday life, often without preceding reliable studies on their safety and usually faster than any health or environmental administration could follow with their regulations, raises concerns about the impact of nanotechnology on public health, nature, and our environment [7,8].

Undoubtedly, most potential applications of nanomaterials – including a number of very ambitious suggestions – have been building on the use of nanoparticles, which can be defined as nano-objects with all three dimensions ranging between 1 and 100 nm [9]. Such reduction in dimensionality offers numerous benefits – not only a large specific surface area compared to bulk materials, but also new physical phenomena related to a relatively small number of atoms forming the nanoparticles (starting at the order of hundreds or thousands in contrast to ~10^{10}–10^{16} atoms in grains of microcrystalline bulk), for example, a quasi-discrete band structure or superparamagnetism.

This work aims to acquaint the reader with several interesting topics in the vast field of nanoparticle research, illustrating them by the attached publications, in the preparation of which the author has participated both at the Department of Low-Temperature Physics at the Faculty of Mathematics and Physics, Charles University, and at the Department of Magnetics and Superconductors at the Institute of Physics of the Czech Academy of Sciences (FZU CAS). The pivot around which the research presented here revolves is magnetic nanoparticles which contain iron, a cheap and abundant element with low toxicity and thereby promising their high application potential. Moreover, the presence of iron enabled us to employ the ^{57}Fe Mössbauer spectroscopy as one of the key methods in our research. In Chapter 2, we discuss magnetic effects emerging at the nanoscale. In Chapter 3, we sketch selected synthesis methods and, as most applications require at least some surface modification or encapsulation of the particles, we complement this chapter with the description of coating procedures employed in our studies.

Chapter 4 takes a closer look at the studied materials – iron oxides, spinel ferrites, or sulfides – and uses examples thereof to introduce selected phenomena. Applications of magnetic nanoparticles considered in our studies and their specifics are reviewed in Chapters 5 and 6, where – consistently with our experimental efforts – contrast enhancement in magnetic resonance imaging receives the highest attention.

The references to articles authored or co-authored by L. Kubíčková that are directly included in the doctoral thesis as relevant for the given topic are numbered independently as [D…] in chronological order, whereas references to other articles not included in the thesis are marked as [O…]. The author of this thesis largely engaged in the experimental work and the analysis of the data, such as in the measurement and analysis of Mössbauer spectra, magnetic properties, relaxivity, dynamic light scattering, or the analysis of size distribution from transmission electron microscopy (TEM), the author also actively participated in the preparation of the manuscripts. Nevertheless, as solid-state science is grounded in cooperation, it is important to emphasize that many other colleagues participated in achieving the presented results, including participation in the tasks mentioned above as well, and they are acknowledged with profound gratitude in the acknowledgment section.

2 Magnetic nanoparticles – magnetism at nanoscale

Although the nanoparticles of magnetically ordered phases have come into focus of rapid development, naturally, they are not a human invention. Magnetic nanoparticles are common and occur widely across the Earth's ecosphere. In rocks and soils, they are abundant and can under certain circumstances provide paleomagnetic records of the direction of the Earth's magnetic field at the time of their formation [10]. It has been speculated that they might enable orientation with the help of the geomagnetic field to many animal species [11–14] – among others ants and bees [15], migratory birds [13], fish [16–18], or mammals [19,20], although in several groups this hypothesis remains controversial and other mechanisms of magnetic perception have been proposed as well (e.g., the radical-pair mechanism has found supportive data in some night-migratory songbirds, such as European robin (*Erithacus rubecula*) [21]). Actually, iron oxide nanoparticles have already been discovered in many animals and may be mostly associated with iron metabolism – the relation of the particles to magnetoreception must be well supported by their location and consistent presence in other individuals of the same species [11]. Interestingly, magnetic particles have been found also in human tissues like the brain [22] or spleen [23], where they are rather a minor metabolic product that may, however, indicate a pathophysiological situation [24,25]. As a means of orientation in space, certain bacteria produce nanoparticles of magnetite or greigite (in anoxic conditions) in organelles – magnetosomes – covered by a membrane [26–29], for examples see Figure 2-1. These so-called magnetotactic bacteria are a suspected source of some nanoparticles found in deposits [30,31] and have been even speculated to be the mediators of magnetoreception in certain animals [32]. Nanoparticles of metal Fe were shown to result as a product of "space weathering", the effects of processes acting on surfaces in space, of regoliths on the Moon, asteroids, or stone planets like Mercury or Mars, and influence their optical properties [33]. Magnetic nanoparticles have been found also in Fe-Ni metal-bearing meteorites [34] or interstellar dust [35,36]. The discovery of carbonate globules containing single-domain nanoparticles of iron oxides and sulfides, which could be of biogenic origin, in the Martian meteorite ALH84001 collected in Antarctica [37] boosted the search for signs of life on Mars.

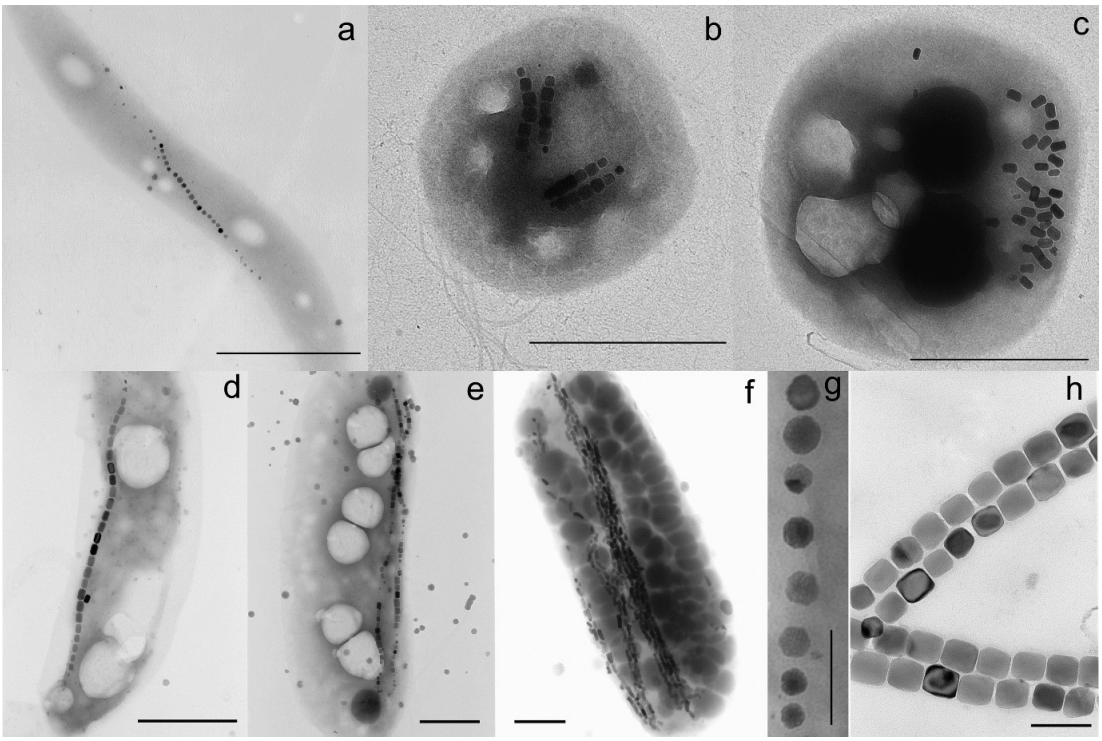

Figure 2-1. Various magnetotactic bacteria with magnetosomes of different shapes that form various arrangements: a – *Magnetospirillum* sp. with cubooctahedral particles (detail of a similar one in g), b – *Magnetococcus* sp. with double chains of prismatic particles (detail of a similar one in h), c – *Magnetococcus* sp. with clustered elongated particles, d and e – *Magnetovibrio* sp. with a single and a double chain of particles, f – *Magnetobacterium* sp. with bullet-shaped particles arranged in multichains; scale bars in a–f mark 1 μm, in g–h denote 100 nm. Reproduced from [38].

The research of new nanomaterials sometimes draws inspiration from nature (an eccentric example is the proposed term "earthicles" [39], particles resembling in their structure the Earth) and targets both fundamental effects and enhancement of suitable properties through modification of relevant parameters. With the reduction of size, two types of effects increase in importance: finite-size effects resulting from quantum confinement of electrons [40], and surface effects related to translational symmetry breaking at the boundary of the particle, which are significantly manifested due to the large surface-to-volume ratio. The shape, as well as the size, can influence the particle's interaction with its environment, as in the case of cellular uptake [41,42], or efficiency in certain applications. Inevitably, the synthesis method impacts both the innermost structure of the particles – such as their crystallinity, stoichiometry, cation distribution, and presence of chemical gradients in substituted compounds – and the character of their surface, for example through the presence of surfactant remnants or specific terminal groups (e.g., a saturation of surfaces with oxygen might increase the overall valence of

transition metal ions [43]). In an ensemble of nanoparticles, be it a powder, particle suspension, or nanogranular solid, interactions between particles may modify considerably the extrinsic properties of the whole system. Whereas the synthesis methods and issues related to the particle structure will be discussed in the following chapters, the rest of this chapter is devoted to magnetism confined to nanoscale dimensions.

2.1 Intrinsic magnetic properties

The intrinsic magnetic properties of nanoparticles such as spontaneous magnetization or magnetocrystalline anisotropy are determined by exchange interactions between magnetic atoms on an atomic scale or several interatomic distances, usually at the characteristic length of less than 1 nm [44]. Before we move up in the length scale, we will discuss briefly the various types of exchange interactions between magnetic atoms and the origins of magnetic anisotropy.

2.1.1 Exchange interactions

Magnetic moments of transition metal atoms/ions originate from unpaired electrons in their partly filled electron shells and have two contributions – the spin, and currents from the orbital motion of the electrons. Intra-atomic exchange, i.e., the balance between the Coulomb repulsion of electrons and the tendency to occupy the lowest-energy states allowed due to the Pauli exclusion principle, decides the magnitude of the magnetic moment per atom. If the magnetic atoms are not isolated, the electronic structure of the atom/ion is affected by its surroundings, which can be described in the terms of the crystal or ligand field theory, and co-determines the number of unpaired electrons. The inter-atomic magnetic interactions occur between the atoms with unpaired electrons and can lead to magnetic ordering.

The exchange interactions between magnetic atoms differ according to the particular geometry of the local arrangement, possible exchange pathways, and the orbital structure of the atoms under consideration. The exchange interaction Hamiltonian between two spins $\boldsymbol{S_i}$ and $\boldsymbol{S_j}$ takes a general form

$$\mathcal{H}_{ij} = \boldsymbol{S}_i \cdot \hat{J} \cdot \boldsymbol{S}_j = \sum_{\alpha\beta} S_{i\alpha} J_{\alpha\beta} S_{j\beta} \,, \tag{2.1}$$

where $\hat{J}$ is an exchange tensor and indices $\alpha, \beta = x, y, z$. Without the spin-orbit coupling, the exchange interaction reduces to the scalar Heisenberg exchange,

$$\mathcal{H}_{ij} = J\boldsymbol{S}_i \cdot \boldsymbol{S}_j \,. \tag{2.2}$$

If the interacting atoms have localized d-electrons and an integer number of d-electrons per site, the sign and strength of the inter-atomic spin-spin exchange follow the *Goodenough-Kanamori-Anderson* (GKA) rules [45–48]. This interaction is mediated by virtual or real electron transfers between overlapping orbitals of the interacting atoms (**direct exchange**) or the two metal atoms and a bridging ligand with no unpaired electrons such as oxygen anion (**superexchange**). When the crystal structure enables an overlap between half-filled (magnetically active) orbitals of neighboring metal atoms (Figure 2-2a) or via a p-orbital of a ligand (Figure 2-2c), mostly in the 180° configuration of the participating atoms, the virtual hopping is allowed only for electrons with antiparallel spins. Such exchange is antiferromagnetic and strong. If the half-filled orbitals of the two atoms are orthogonal and virtual hopping of the electrons can take place only from the half-filled to an empty orbital, either by direct d-d hopping (Figure 2-2b) or via the same p-orbital of the ligand (Figure 2-2d), the exchange is weak and ferromagnetic. In a geometry where the interacting metal atoms form 90° angle with the ligand (Figure 2-2e), the half-filled orbitals of metal atoms overlap each with a different p-orbital of the ligand. This interaction mediated by virtual hopping of electrons between the p-orbitals of the ligand and the respective d-orbital of the metal atom is weak and ferromagnetic as well [49]. If the geometry of participating atoms deviates from 180° or 90°, the exchange must be analyzed for each interacting system individually.

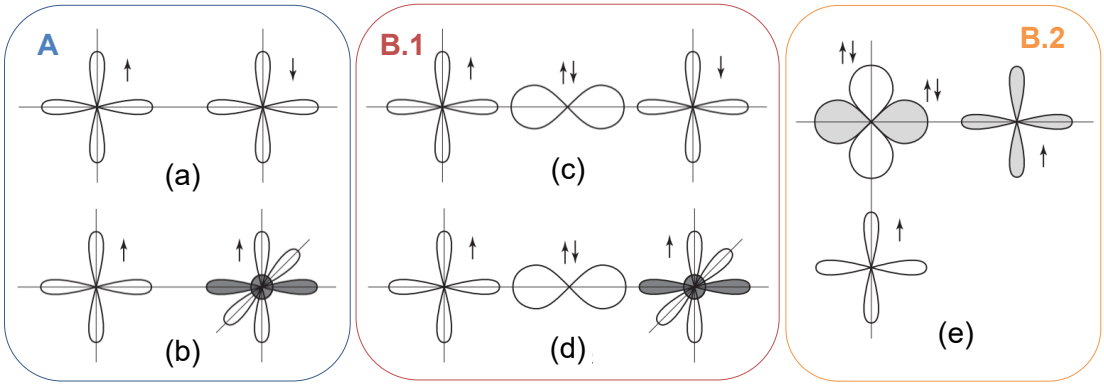

Figure 2-2. Overview of exchange interactions in different situations according to GKA rules, details are provided in the text. (A) Direct exchange due to direct d-d electron hopping, (B) superexchange via p-orbitals of the ligand. The half-filled (with one electron) d-orbitals are shown unshaded or lightly shaded, empty orbitals are darkly shaded. Adapted from [49].

If itinerant electrons are present in the system, the exchange coupling of localized electrons can be mediated by these conducting electrons. If the itinerant electrons occupy a broad conduction band filled up to the Fermi energy ε_F, the mediated interaction between the localized electrons is called the **Ruderman-Kittel-Kasuya-**

Yosida (RKKY) **interaction** [50–52]. The RKKY interaction is long-range and its sign and magnitude oscillate in space as

$$J_{\mathrm{RKKY}}(r) \sim \frac{I_{\mathrm{sd}}^2}{\varepsilon_{\mathrm{F}}} \frac{\cos(2k_{\mathrm{F}}r)}{r^3}, \tag{2.3}$$

where $I_{\mathrm{sd}} \ll \varepsilon_{\mathrm{F}}$ is the coupling constant between conduction s and localized d-electrons, k_{F} is the radius of the Fermi sphere and r is the distance between the localized electrons. The RKKY interaction dominates the exchange in many rare-earth metals and intermetallic compounds and is also responsible for example for the formation of spin-glass states in alloys of magnetic metals diluted in a nonmagnetic metallic matrix [49].

In the opposite case of narrow conduction bands and a small $\varepsilon_{\mathrm{F}} \lesssim I_{\mathrm{sd}}$, where I_{sd} may also represent the interaction between the itinerant and localized d-electrons, the coupling between the localized d-electrons is in fact ferromagnetic. The extra electron, a charge carrier, of an atom with otherwise localized d-electrons has its spin parallel to the localized d-shell due to Hund's rules. In the systems with antiferromagnetically coupled localized spins, such a mobile charge carrier would not be allowed to hop to the neighboring site. However, the gain in kinetic energy of itinerant electron hopping among sites can outweigh the loss from the ferromagnetic ordering of the localized spins that tend to antiferromagnetic interaction. This **double exchange** can manifest already at relatively little doping with charge carriers. It was first suggested by C. Zener [53] to explain the ferromagnetism in the mixed-valence manganites with perovskite structure, and since then has become famous especially for the special case of interaction between atoms of the same kind and with valences differing by one, such as Mn^{3+}/Mn^{4+} or Fe^{2+}/Fe^{3+}. In the double exchange, the real transfer of electrons takes place and the hopping electrons are practically delocalized, in contrast to the direct exchange and the superexchange, in which the electron transfer is virtual and the electrons remain practically localized at one of the interacting centers [54]. If the doping is not sufficient to induce the ferromagnetic state, a homogeneous canted state can emerge, in which both the antiferromagnetic and ferromagnetic interactions compete; alternatively, phase separation into ferromagnetic metallic inclusions in the antiferromagnetic matrix might occur [49].

The interactions discussed above do not take the spin-orbit coupling into account. Without the spin-orbit coupling $\lambda \boldsymbol{S} \cdot \boldsymbol{L}$, the spin system is practically decoupled from the lattice. Only after introducing additional terms to the Heisenberg Hamiltonian (2.2) which reflect the symmetry of the structure, the orientation of spins is anchored with respect to crystal axes. The spin-orbit coupling, therefore,

gives rise to magnetic anisotropy which will be discussed in more detail in Section 2.1.2. We will now turn our attention to exchange interactions that emerge from breaking the isotropic character of the Heisenberg exchange.

In general, the exchange interaction tensor $\hat{J}$ in the Hamiltonian (2.1) is a 3 x 3 tensor which contains also off-diagonal terms and can be divided into a symmetrical and an antisymmetrical part. The symmetrical part can be diagonalized and divided into an isotropic Heisenberg part, and an anisotropic part that can be represented by a traceless tensor (**anisotropic** or **pseudo-dipolar exchange**) [55]. For example, the exchange interaction Hamiltonian considering symmetrical part of $\hat{J}$ in a tetragonal structure can be represented as

$$\mathcal{H}_{ij}^{\text{tet}} = \sum_{ij} J_{\parallel} S_{i,z} S_{j,z} + J_{\perp}\left(S_{i,x} S_{j,x} + S_{i,y} S_{j,y}\right), \qquad J_{\parallel} \neq J_{\perp}\,. \tag{2.4}$$

Whereas for $J_{\parallel} > J_{\perp}$, the Ising-like interaction dominates, for $J_{\parallel} < J_{\perp}$ the magnetization lying in the *xy* plane is preferred [49].

The antisymmetrical part of the exchange interaction, the **Dzyaloshinskii-Moriya interaction** [56,57], comes into play if the two interacting metal centers are not related by inversion symmetry. It contributes to the exchange energy by

$$\mathcal{H}_{ij}^{\text{DM}} = \boldsymbol{D}_{ij} \cdot \left(\boldsymbol{S}_i \times \boldsymbol{S}_j\right), \tag{2.5}$$

in which $\boldsymbol{D}_{ij}$ is the Dzyaloshinskii-Moriya vector for the given pair *i–j*. This interaction leads to canting of neighboring spins to make the vector product $\boldsymbol{S}_i \times \boldsymbol{S}_j$ nonzero and parallel to $\boldsymbol{D}_{ij}$ (see Figure 2-3). The canting angle ξ is then roughly proportional to $\sim D_{\text{DM}}/J$, where D_{DM} is the magnitude of the overall vector from the summed $\boldsymbol{D}_{ij}$ of individual interacting pairs and J is the isotropic exchange from the formula (2.2). The ratio D_{DM}/J is usually of the order of $\sim 10^{-2}$. Consequently, in antiferromagnets, the canting results in total magnetization $\sim\langle S\rangle D_{\text{DM}}/J$ perpendicular to the sublattice magnetization, with $\langle S\rangle$ being the average sublattice magnetization. The Dzyaloshinskii-Moriya interaction thus can lead to weak ferromagnetism of antiferromagnets, as in the case of hematite (see Section 2.3). Nevertheless, sometimes the effect of the spin canting of different atom pairs might cancel out and no net ferromagnetic moment is manifested. In ferromagnets, the canting slightly reduces the overall magnetic moment and introduces a weak perpendicular antiferromagnetic component. However, under certain conditions, the Dzyaloshinskii-Moriya interaction can induce a large-period spiral magnetic structure with a small canting angle between neighboring atoms in otherwise collinear ordering. A well-known example is $BiFeO_3$, whose two antiferromagnetic sublattices form a spiral with a period of ~62 nm [58].

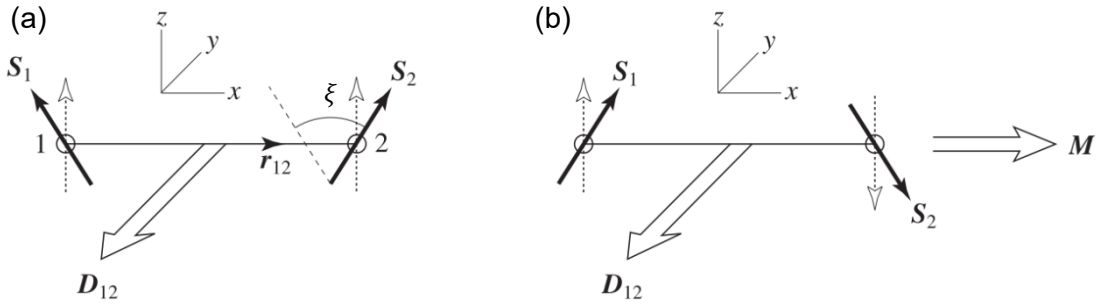

Figure 2-3. Scheme of the spin canting due to the Dzyaloshinskii-Moriya interaction in (a) a ferromagnet and (b) an antiferromagnet. Adapted from [49].

2.1.2 Magnetic anisotropy

As already mentioned above, the spin-orbit coupling determines the orientation of the spin system and thereby the resulting magnetization with respect to the crystal lattice. The phenomenological description of **magnetocrystalline anisotropy**, therefore, depends on the orientation of the magnetization with respect to crystal axes. The energy of magnetocrystalline anisotropy must be scalar and must be constant under the symmetry operations of the lattice as well as time inversion. Consequently, it must be an even function of magnetization $\boldsymbol{M}$ and its directional cosines with respect to main crystal axes, $\alpha_\beta = \frac{M_\beta}{|\boldsymbol{M}|}, \beta = x, y, z$; naturally, the cosines follow $\alpha_x^2 + \alpha_y^2 + \alpha_z^2 = 1$. The anisotropy can be then written as a series of those directional cosines that satisfy the given crystal symmetry, and the higher-order terms can be usually neglected. In the simplest case of a uniaxial anisotropy, such as in the tetragonal symmetry, the density of magnetocrystalline anisotropy energy can be written as

$$f_{\mathrm{mc}}^{\mathrm{uni}}(\theta) = K_1\left(\alpha_x^2 + \alpha_y^2\right) = K_1(1 - \alpha_z^2) = K_1 \sin^2\theta\,, \qquad (2.6)$$

in which θ denotes the angle between magnetization and the *z*-axis and K_1 is the first magnetocrystalline anisotropy constant. If $K_1 > 0$, the spins are oriented along the *z*-direction (the easy-axis anisotropy, Figure 2-4b), whereas if $K_1 < 0$, the spins lie in the *xy*-plane (the easy-plane anisotropy, Figure 2-4c). The expression (2.6) can be expanded with higher-order powers of cosines, $f_{\mathrm{mc}}^{\mathrm{uni}\prime}(\theta) = K_1 \sin^2\theta + K_2 \sin^4\theta + K_3 \sin^6\theta + \cdots$, which enables achieving of more complicated spin structures with $0 < \theta < \frac{\pi}{2}$. One such example is the easy-cone anisotropy (Figure 2-4d), which arises if $K_1 < 0$ and $K_2 > -K_1/2$ and the magnetization leans away from the *z*-axis by $\theta_{\mathrm{cone}} = \arcsin(|K_1|/2K_2)$ [59]. For a cubic crystal, the three coordinate axes are equivalent so the lowest terms in the density of anisotropy energy are of the fourth order

$$f_{\mathrm{mc}}^{\mathrm{cub}} = K_1\left(\alpha_x^2\alpha_y^2 + \alpha_y^2\alpha_z^2 + \alpha_z^2\alpha_x^2\right) + K_2\alpha_x^2\alpha_y^2\alpha_z^2 + \cdots \qquad (2.7)$$

If $K_1 > 0$, the magnetization lies along one of the cubic axes (Figure 2-4e), whereas for $K_1 < 0$, it is oriented along the cube diagonal (Figure 2-4f) [54]. The anisotropy constants generally depend on temperature and can even change the sign, then a *spin-reorientation transition* might occur at a corresponding temperature. Such a situation can be encountered for example in magnetite, in which the negative K_1 changes upon cooling to positive (see Figure 2-5 and Section 4.1.2); moreover, upon further cooling, magnetite undergoes the Verwey transition and the cubic structure transforms to a monoclinic one [60].

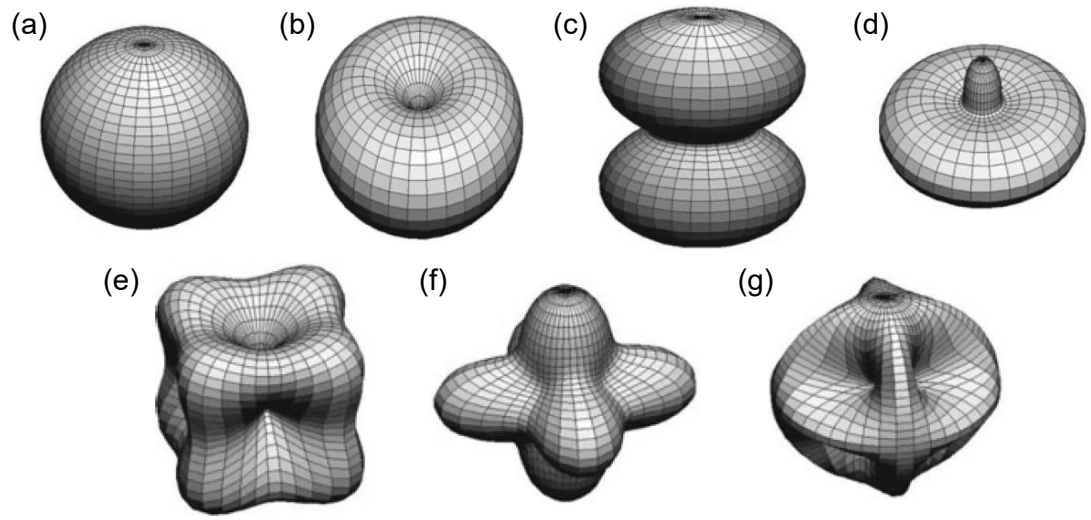

Figure 2-4. Magnetocrystalline anisotropy energy surfaces, minima show easy directions, maxima the hard directions: (a) isotropic case, (b) uniaxial easy axis, (c) uniaxial easy plane, (d) uniaxial easy cone, (e) cubic iron-type anisotropy with easy axes along the ⟨100⟩ axes, $K_1 > 0$, (f) cubic nickel-type anisotropy with easy axes along the ⟨111⟩ axes, $K_1 < 0$, (g) contribution due to $K_2 > 0$ in cubic anisotropy, with easy axes along the ⟨111⟩ axes, but different landscape than (f). Adapted from [59].

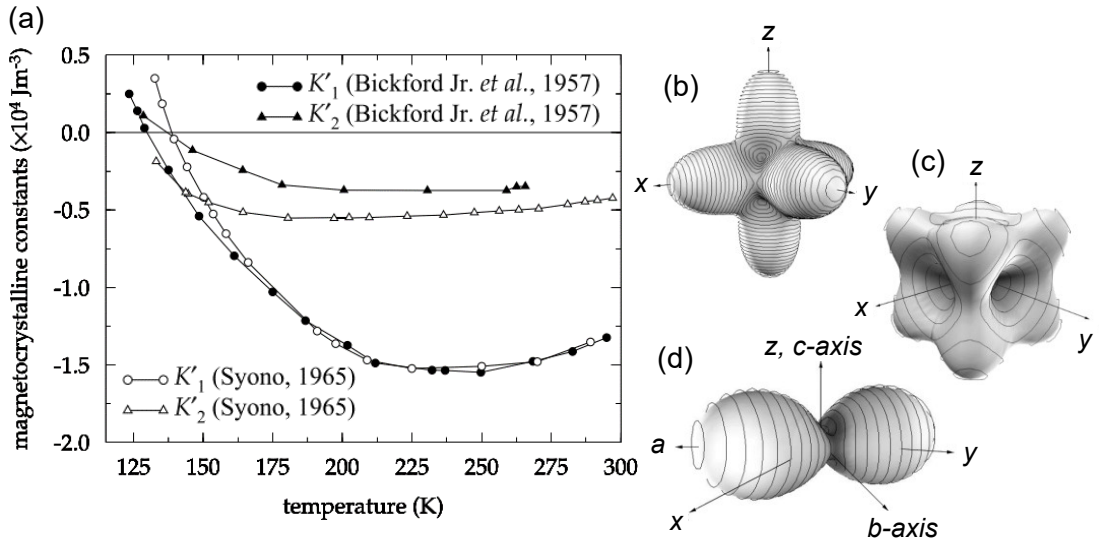

Figure 2-5. Magnetocrystalline anisotropy of magnetite: (a) the temperature dependence of the first and second anisotropy constants including the magnetostrictive contribution (therefore K'_i), from two independent datasets [61] and [62], (b) cubic anisotropy of magnetite at 290 K, easy axes along the ⟨111⟩ and hard axes along ⟨100⟩ directions, (c) cubic anisotropy at 126 K, easy axes along the ⟨100⟩ and hard axes along ⟨111⟩ directions, (d) monoclinic anisotropy at 110 K below the Verwey transition, easy axis along the *c*-axis, hard axis along the *a*-axis. Adapted from [60].

At the microscopic scale, there are two main sources of magnetic anisotropy. The first one is the **exchange anisotropy** due to the anisotropic exchange [54,63] discussed in the previous section. Nevertheless, in systems of metal atoms interconnected with ligands, the ligands – usually anions – not only mediate the exchange interactions but also create an electrostatic field at the metal site. This *crystal field* (ligand field) acts only on the orbital moment, modifies the electronic configuration of the metal atom, and brings forth the **single-site** (**single-ion**) **anisotropy**. Moreover, the splitting of energy levels of the metal ion due to the crystal field, as described in more detail in Section 4.1, favors the suppression – quenching – of the orbital moment.

Single-ion anisotropy is the main contribution to the magnetocrystalline anisotropy in most systems and combines both the crystal-field effects and the spin-orbit coupling. In solids, the electrostatic crystal field and relativistic spin-orbit coupling compete, and the outcome of this competition determines the degree of the quenching of the orbital moment. In 3d metals, the orbital moment is usually largely quenched, and the spin-orbit coupling is just a perturbation to the dominating crystal-field splitting. In the first approximation, the exchange field splits the orbital ground state to $2S + 1$ levels according to the possible orientations of the spin $\boldsymbol{S}$ in space. These levels are occupied according to the Boltzmann

statistics and if we expand the respective free energy into directional cosines, we get the single-ion contribution to phenomenological expressions of the type (2.6) or (2.7). In the case of an at least partially unquenched orbital moment, the spin-orbit coupling then modifies the position of the $2S + 1$ levels depending on the orientation with respect to crystal axes and splits the ground state if originally orbitally degenerated [54].

Finally, traditional dipole-dipole interactions can contribute to magnetocrystalline anisotropy as well, nevertheless, their effect in transition metal compounds is usually weak [49].

2.2 Mesoscopic magnetism

2.2.1 Micromagnetism

Before turning our attention to the magnetic properties of nanoparticles, we will briefly stop at the field of *micromagnetism*. This – from the point of view of the present work rather unfortunate – name refers to length scales spanning over more interatomic distances and was originally used to contrast the atomic view with the traditional long-range approach to magnetization processes via domain walls [64]. One of the topics of micromagnetism is linking the inherent properties of a given phase, such as magnetocrystalline anisotropy constants or saturation magnetization, and macroscopic properties, most importantly the hysteresis loops.

While the effects on the atomic scale determine the spontaneous magnetization M_S, the magnetic moment per volume in the zero magnetic fields, and the easy magnetization direction, it is rather easy to rotate the magnetization vector since the rotation does not change the absolute value of M_S. However, the rotation of magnetization shapes certain macroscopic properties of the magnetic sample, including its hysteresis loops. Hysteresis represents a complex nonequilibrium, nonlinear and nonlocal phenomenon, which arises as the anisotropy-related metastable energy minima separated by field-dependent energy barriers are gradually overcome with the applied field [44]. Although the magnetization rotation is influenced by parameters such as the exchange interactions or magnetic anisotropy, the hysteresis loop is obtained by averaging, and therefore it is largely determined by the real structure of the sample, its morphology, or chemical and structural homogeneity.

The magnetization curve is already treated by continuum formalism. For example, the exchange coupling constant J_{ij} is substituted with exchange stiffness $A_{\mathrm{ex}} \sim J/a$, where a is the distance between magnetic atoms [59]. The basic energy functional

(temperature-dependent micromagnetic free energy) of a uniaxial magnet then consists of the following contributions

$$E = \int \left\{ A_{\mathrm{ex}} \left[\nabla \left(\frac{\boldsymbol{M}}{M_s} \right) \right] - K_1 \frac{(\boldsymbol{n} \cdot \boldsymbol{M})^2}{M_s^2} - \mu_0 \boldsymbol{M} \cdot \boldsymbol{H} - \frac{\mu_0}{2} \boldsymbol{M} \cdot \boldsymbol{H}_{\mathrm{d}}(\boldsymbol{M}) \right\} \mathrm{d}V \,, \qquad (2.8)$$

i.e., the interatomic exchange, the uniaxial anisotropy, Zeeman interaction, and magnetostatic self-interaction, respectively. In the given expression, $\boldsymbol{n}(\boldsymbol{r})$ denotes the position-dependent unit vector of the easy axis, μ_0 the permeability of free space, $\boldsymbol{H}$ the external or Zeeman field, and $\boldsymbol{H}_{\mathrm{d}}(\boldsymbol{M})$ the magnetostatic self-interaction field

$$\boldsymbol{H}_{\mathrm{d}}(\boldsymbol{r}) = \frac{1}{4\pi} \int \frac{3(\boldsymbol{r} - \boldsymbol{r}')(\boldsymbol{r} - \boldsymbol{r}') \cdot \boldsymbol{M}(\boldsymbol{r}') - |\boldsymbol{r} - \boldsymbol{r}'|^2 \boldsymbol{M}(\boldsymbol{r}')}{|\boldsymbol{r} - \boldsymbol{r}'|^5} \mathrm{d}V'. \qquad (2.9)$$

In ellipsoids of revolution, which are homogeneously magnetized along the symmetry axis, the magnetostatic self-interaction field equals the demagnetizing field [59]. From the dimensional analysis of the expression (2.8), we obtain two fundamental length scales: (i) the *wall-width parameter* $\delta_0 = \sqrt{A_{\mathrm{ex}}/K_1}$ controlling the thickness of the domain wall, and (ii) the *exchange length* $l_{ex} = \sqrt{A_{\mathrm{ex}}/(\mu_0 M_s^2)}$, which characterizes the length scale below which interatomic exchange interactions dominate over the magnetostatic self-interaction. While the exchange length is typically 1–2 nm in most magnetic materials, the wall-width parameter can vary from ∼1 nm in magnetically hard materials to several hundred nm in soft magnetics.

Whereas bulk magnetic materials are formed by uniformly magnetized domains separated by domain walls, such structure minimizing magnetostatic energy becomes less favorable upon decreasing the size of a grain due to the high energy cost of domain-wall formation. Therefore, a **single-domain (SD) state** emerges below a certain critical size. Taking the example of Figure 2-6, if we consider a spherical particle with uniaxial anisotropy and a radius r_{p} which is divided into two hemispherical domains with opposite directions of magnetization, the domains are separated by a domain wall with the domain-wall energy $\gamma = 4\left(\pi r_{\mathrm{p}}^2\right)\sqrt{A_{\mathrm{ex}}K_1}$. To form the SD state, the gain in magnetostatic energy $\sim \mu_0 M_s^2 V/12$, roughly equal to half of the single-domain energy, must be smaller than the cost of the domain-wall formation. It follows that for a spherical particle, the critical radius is approximately [44]

$$r_{\mathrm{SD}} = \frac{36\sqrt{A_{\mathrm{ex}}K_1}}{\mu_0 M_s^2}\,. \qquad (2.10)$$

Typically, r_{SD} can vary between tens to hundreds of nm, e.g., 15 nm for Fe, 35 nm for Co, or 100 nm for NdFeB [66]. The transition to the SD state upon decreasing the particle size is accompanied by a strong increase in the coercive field.

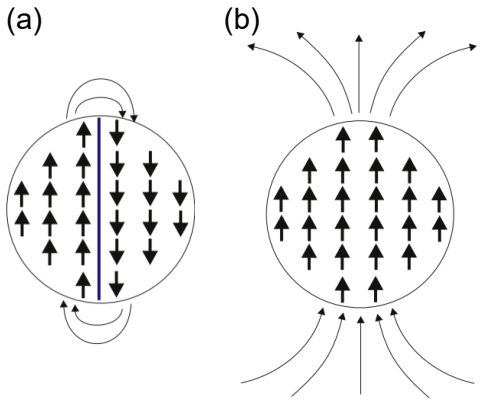

Figure 2-6. A spherical ferromagnetic particle (a) with two domains separated by a domain wall with energy $\gamma = 4\pi r_{\mathrm{p}}^2\sqrt{A_{\mathrm{ex}}K_1}$ and (b) in a single-domain state with large demagnetizing field. Adapted from [65].

Another critical radius, r_{coh}, characterizes the size below which exchange energy between spins dominates and all spins rotate coherently in an applied field [67]. In general, $r_{\mathrm{coh}} \ll r_{\mathrm{SD}}$ and typically reaches 5–10 nm [44], for example, r_{coh}~10 nm for Co nanoparticles. For larger SD particles, the magnetization reversal follows more complicated processes such as curling modes or surface pinning. The coherent rotation below r_{coh} has been shown experimentally in, e.g., Co nanoparticles [68]. Under such conditions, the magnetic moment of a particle behaves as a superspin, which overcomes a single energy barrier during the magnetization reversal.

The magnetization of a SD particle points in a direction that minimizes the total anisotropy energy of the particle. In the first approximation, the total anisotropy can be considered as uniaxial and characterized by a volume-dependent energy barrier $E_{\mathrm{B}} = KV$, where K is the effective anisotropy constant; the anisotropy energy is then, similarly to the expression (2.6),

$$E_{\mathrm{an}}^{\mathrm{uni}}(\theta) = KV\sin^2\theta\,, \qquad (2.11)$$

in which θ denotes the angle between magnetization and the anisotropy axis (so-called easy axis; $\theta = 0$ or π in zero magnetic fields). Application of an external magnetic field $\boldsymbol{H}$, which forms angle ψ with the anisotropy axis, modifies the particle energy as [66]

$$E_{\mathrm{an}}^{\mathrm{uni}}(\theta,\psi) = KV\sin^2\theta - \mu_0 HMV\cos(\theta-\psi)\,. \qquad (2.12)$$

The characteristic angles are highlighted in the coordinate system of the particle in Figure 2-7a. The field dependence of the energy barrier of the particle can be expressed by a simple analytical expression [68]

$$E_{\mathrm{B}}(H) = KV\left(1 - \frac{H}{H_{\mathrm{sw}}}\right)^{\alpha_{\mathrm{ph}}}, \qquad (2.13)$$

where $H_{\mathrm{sw}} = 2K/M$ is the switching (coercive) field at zero temperature and α_{ph} is a phenomenological exponent equal to 2 for the field applied along the anisotropy axis, while in general, it is approximately 3/2 for randomly oriented particles [40,69]. The angular dependence of the energy barrier in a particle with uniaxial anisotropy, both without an applied field and in the field, is depicted in Figure 2-7b.

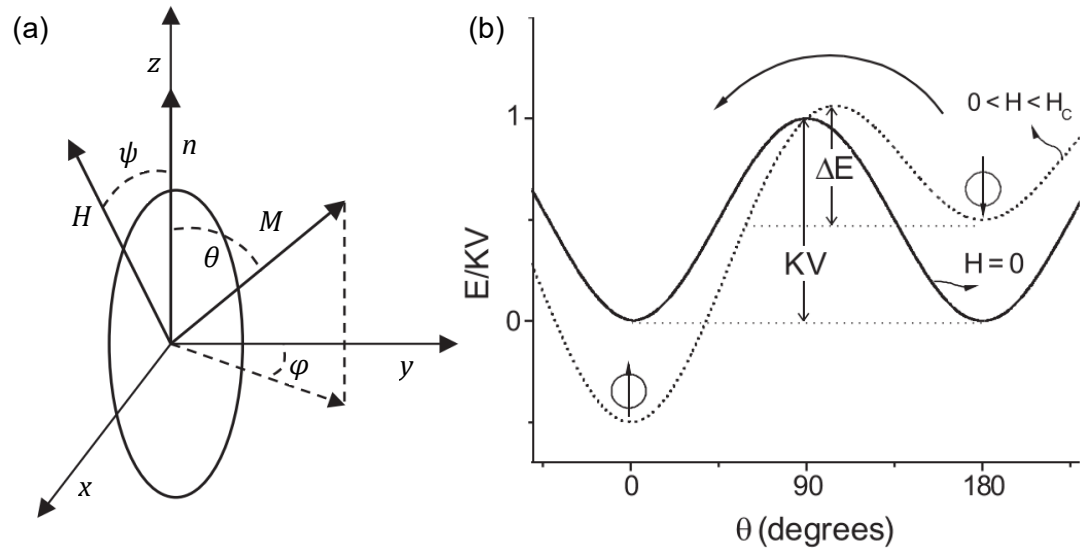

Figure 2-7. (a) Definition of the axis system of a fine particle; adapted from [70]. (b) The dependence of the energy barrier of a particle with uniaxial anisotropy on θ at zero fields (solid line) and in the external field applied along the particle easy axis, which is lower than the coercive field (dotted line; the energy barrier follows the formula (2.13) with α_{ph} = 2); adapted from [71].

The magnetization reversal in noninteracting ellipsoidal SD particles was studied by Stoner and Wohlfarth [72]. For a single SD particle, minimizing the expression (2.12) with respect to θ and ψ leads to hysteresis curves which are rectangular for $\psi = 0$ or π with the coercive field $H_{\mathrm{c}}(\|) = 2K/M_{\mathrm{sat}}$, whereas linear shape with no hysteresis is observed for $\psi = \pi/2$. For an ensemble of randomly oriented noninteracting particles, the hysteresis curve is characterized by a reduced coercive field $h_{\mathrm{c}} = H_{\mathrm{c}}/H_{\mathrm{c}}(\|) = 0.48$ and remanence $m_{\mathrm{r}} = M_{\mathrm{r}}/M_{\mathrm{r}}(\|) = M_{\mathrm{r}}/M_{\mathrm{sat}} = 0.5$, where M_{r} and M_{sat} are the remanent and saturation magnetization [72,73]. Several hysteresis curves modeled for an ensemble of particles aligned with their anisotropy axes are depicted in Figure 2-8 for selected angles between the easy axis of the particles and the applied magnetic field.

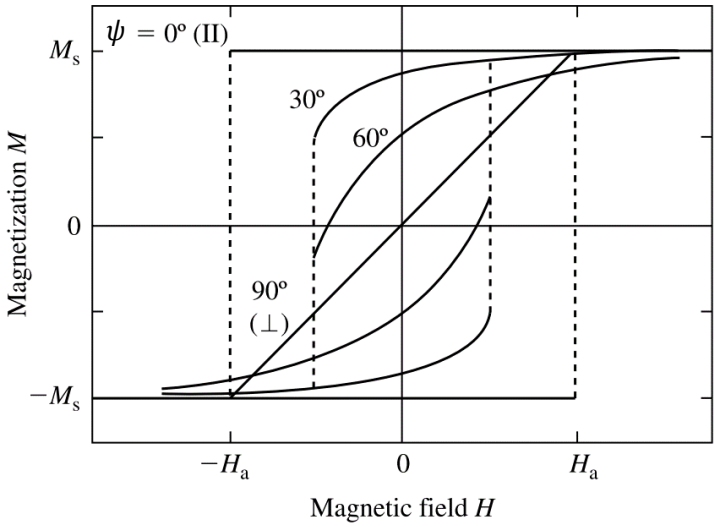

Figure 2-8. Stoner-Wohlfarth model: the dependence of hysteresis loops of aligned particles on the angle between the applied field $\boldsymbol{H}$ and the anisotropy axis (see expression (2.12)). Reproduced from [59].

2.2.2 Superparamagnetism

In the limiting case when the energy barrier is much higher than thermal excitations ($E_B \gg k_B T$, where k_B is the Boltzmann constant and T is the temperature), the particle is in a so-called **blocked state** with magnetization fixed with respect to the crystal lattice. However, in sufficiently small SD nanoparticles and at finite temperatures, thermal excitations can help to overcome E_B and induce spontaneous reversal of the particle superspin from one easy direction to the other on a given time scale. According to the simplest model, the relaxation of magnetization follows an Arrhenius-type law

$$M(t) = M_0 e^{-\frac{t}{\tau_N}}, \tag{2.14}$$

where M_0 is the initial magnetization and τ_N is a characteristic relaxation time

$$\tau_N = \tau_0 e^{\frac{E_B}{k_B T}}. \tag{2.15}$$

Here, τ_0 characterizes the time between jump attempts of the particle moment between opposite directions of the easy axis, and typically ranges 10^{-13}–10^{-9} s [66]. In general, τ_0 depends on various factors, including saturation magnetization, temperature, the direction of the applied field, or a phenomenological damping constant, which prevents the particle moment from rotating indefinitely around the applied magnetic field axis and ensures its aligning into the direction of the applied field [70,74,75]. This relaxation was first studied by Néel [76] and further developed by Brown [74,77]; the expression (2.15) together with a simplifying assumption of constant τ_0 is now known as the Néel-Brown model [70].

In the limit of $E_B \ll k_B T$, the particle superspin freely fluctuates due to thermal excitations and resembles thus a fluctuating atomic moment of a paramagnet; therefore, such behavior of a SD particle has been termed as **superparamagnetism**

(SPM). Analogically to paramagnetism, the average magnetic moment $\langle m \rangle$ of a nanoparticle pointing in the direction of the applied field can be described – when neglecting the E_B – by the Langevin function $L(x) = \coth x - 1/x$

$$\langle m \rangle = mL\left(\frac{m\mu_0 H}{k_B T}\right). \tag{2.16}$$

It follows that particles in the SPM state show no hysteresis.

The actually observed behavior of a nanoparticle strongly depends on the characteristic time τ_m of the probing method. While the particle is in the blocked state and its moment appears "frozen" for $\tau_m \ll \tau_N$, only averaged magnetic moment for a particle in the SPM state is observed for $\tau_m \gg \tau_N$. Therefore, it is useful to define a **blocking temperature** T_B as a temperature at which $\tau_m \approx \tau_N$ (see expression (2.15)):

$$T_B \approx \frac{E_B}{k_B \ln\left(\frac{\tau_m}{\tau_0}\right)}. \tag{2.17}$$

The typical τ_m ranges from 10^{-12}–10^{-10} s for inelastic and quasielastic neutron scattering [78] or 10^{-9}–10^{-7} s for Mössbauer spectroscopy (related to the lifetime of the Mössbauer excited state, which is of the order of 100 ns for ^{57}Fe [79]) up to ~1–100 s for DC magnetic measurements. As the blocking temperature depends on the particle volume via $E_B \propto KV$, its distribution obtained experimentally reflects the size distribution of particles in the studied ensemble. However, the measurements of bare samples are affected by dipole-dipole interactions, as discussed below.

The most frequently applied method of determining T_B is the zero-field-cooling/field-cooling (ZFC/FC) routine in DC magnetometry. First, the demagnetized sample is cooled in a zero magnetic field, a small magnetic field is applied (~1-100 mT) and the temperature dependence of susceptibility is measured during heating (ZFC). Second, the sample is cooled again in the applied field and its susceptibility is measured during heating (FC). If the sample achieves fully SPM behavior in the examined temperature range, ZFC and FC curves meet. Different approaches how to extract T_B of nanoparticle assemblies from the data have been proposed, for example, the inflection point of the ZFC curve when the susceptibility is rising due to unfreezing particle moments, the maximum of the ZFC curve T_{max}, or the bifurcation point of the ZFC and FC curves (temperature of irreversibility, T_{irr}). However, many of these widely used approaches yield distorted results for polydisperse real systems. Bruvera et al. [80] demonstrated that the most reliable method of determining the T_B is the so-called Micha's model [80–82], in which the T_B distribution is directly associated with the temperature

derivative of the difference in susceptibilities $-\mathrm{d}(\chi_{\mathrm{FC}}-\chi_{\mathrm{ZFC}})/\mathrm{d}T$, as shown in Figure 2-9.

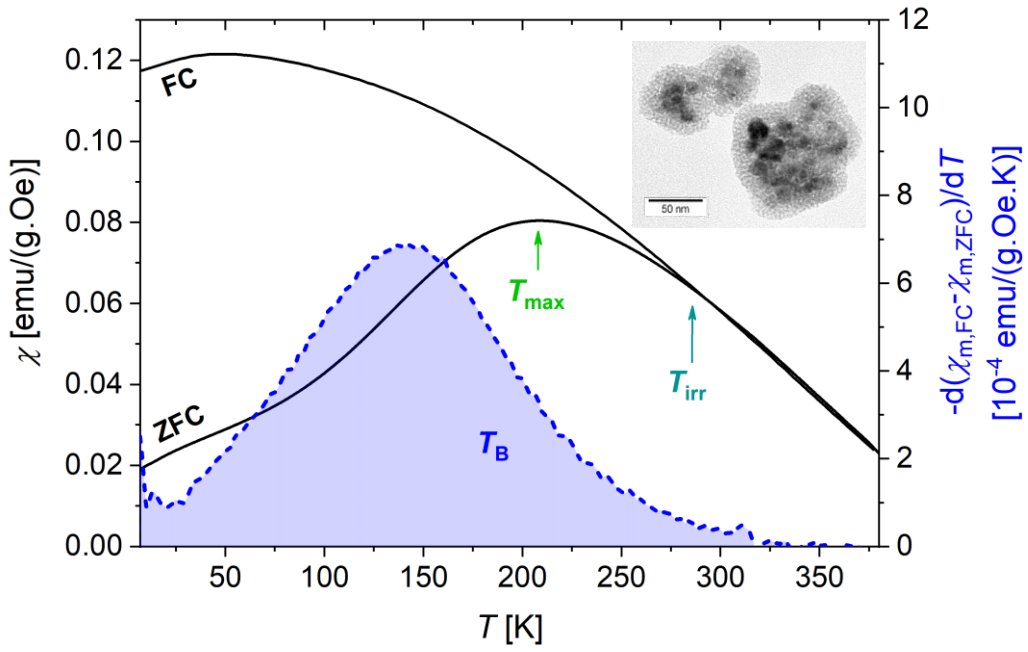

Figure 2-9. Typical ZFC/FC measurement of $Mn_{0.62}Zn_{0.41}Fe_{1.97}O_4$ nanoparticles coated with mesoporous silica in the probe field of 20 Oe ($\mu_0 H = 2$ mT); data from [D2], the mean size of crystallites ~12 nm, thickness of the coating ~22 nm, transmission electron micrograph of the particles in the inset. The distribution of blocking temperatures $-\mathrm{d}(\chi_{\mathrm{FC}}-\chi_{\mathrm{ZFC}})/\mathrm{d}T$ is shown in blue dashed curve (right axis), at the same time, the maximum of the ZFC curve T_{max} and bifurcation of ZFC/FC curves T_{irr} are marked for comparison. In this case, although the interaction between coated particles is suppressed by the silica coating, interactions between crystallites inside a coated aggregate still distort the resulting T_{B} distribution.

Superparamagnetism is restricted to a defined size range of the particles – the upper limit being the emergence of the SD state, while if the particle is too small (typically below 2 nm [66]), almost all atoms lie at the surface and different models of magnetic relaxation should be applied.

Finally, we will note that in a suspension of magnetic nanoparticles, two main relaxation mechanisms occur: the **Néel relaxation** with the characteristic time τ_{N}, as introduced in the formula (2.15), and the rotational **Brownian relaxation** due to collisions with molecules of the medium, characterized by the *Brownian relaxation time*

$$\tau_{\mathrm{B}} = \frac{3\eta V_{\mathrm{hd}}}{k_{\mathrm{B}}T}. \qquad (2.18)$$

Here, η is the dynamic viscosity of the medium and V_{hd} is the hydrodynamic volume of the particle. Whereas the Néel relaxation dominates in superparamagnetic nanoparticles, Brownian relaxation is relevant for nanoparticles with high anisotropy in the blocked state. The effective relaxation time is then

$$\frac{1}{\tau_{\mathrm{eff}}} = \frac{1}{\tau_{\mathrm{N}}} + \frac{1}{\tau_{\mathrm{B}}}. \tag{2.19}$$

2.2.3 Surface effects

With the decreasing size of particles, the surface effects gain importance. The breaking of the translation symmetry is followed by processes attempting to decrease the surface energy, and the resulting properties of the surface are co-determined [83] by the lower coordination number of atoms at the surface, saturation with oxygen and overoxidation [43], expansion or contraction of the lattice that can introduce additional strain anisotropy, increased roughness, or an unquenched orbital moment [84]. The breaking of magnetic exchange pathways leads to magnetic frustration [70].

The anisotropy increases with the decreasing particle size, which is described by the general term **surface anisotropy**. The structure relaxation of surface layers and point defects occurring at higher concentrations induce local crystal fields, whose axes are approximately perpendicular to the surface as a result of dipole moments of the nearest neighbors. Such local fields add energy term $\propto K_{\mathrm{cf}} S_{\xi}^{2}$ [85], in which S_{ξ} is the spin component normal to the surface and the anisotropy constant $K_{\mathrm{cf}} > 0$ corresponds to the easy-plane and $K_{\mathrm{cf}} < 0$ to the easy-axis anisotropies [70,86]. As a consequence of the surface anisotropy, the surface layers are magnetically harder than the particle core. Importantly, in cubic materials, the surface anisotropy easily dominates the bulk anisotropy since the second-order terms are usually two orders of magnitude larger than the fourth-order terms (see the formula (2.7)) [59].

The second effect related to the surface is the **strain anisotropy**, which is a direct consequence of the magnetostriction. The strains are effective in the direction of the magnetization, providing a magnetoelastic contribution to the total energy. This effect is usually much smaller compared to other anisotropies present in the sample and strongly depends on the peculiarities of each studied system [66].

Interestingly, both the increase and decrease in magnetization of nanoparticles due to surface effects have been described [87]. The former has been reported for nanoparticles of several ferromagnetic metals with itinerant magnetism [88]. It was suggested that the lower coordination at the surface induces expansion of nearest-

neighbor spacing, narrowing of the bands, and localization of partially delocalized d-orbitals [89], as well as charge and spin-density oscillations propagating towards the particle core [90,91]. Consequently, the magnitude of the itinerant moment can change significantly with the distance from the surface. Mössbauer spectroscopy of nanocrystalline Fe revealed that although the magnetization of the surface layer was larger than in the particle core, it decreased more rapidly with increasing temperature [92].

On the other hand, the reduced magnetization is typical for nanoparticles of magnetic compounds with localized magnetic moments, as ferrimagnetic oxides [70]. To explain the lowered magnetization when compared to the bulk value, the presence of a so-called magnetically dead layer of paramagnetic nature at the surface was originally proposed [93]. In later studies, the reduction in magnetization was ascribed to a certain spin disorder in the surface layer due to competing exchange interactions [94,95] and supported, e.g., by Mössbauer spectroscopy studies on nanoparticles with ^{57}Fe and ^{57}Co-enriched surface [96–99]. Also, isothermal magnetization loops of many ferrimagnetic and antiferromagnetic nanoparticles display high closure fields at low temperatures and do not saturate even at very high fields ~10 T, which means that some of the spins have switching fields even larger [100]. At the same time, magnetic experiments demonstrated only mild temperature dependence of high-field differential susceptibility [101], which is not consistent with paramagnetic or superparamagnetic origin but can be explained by spin canting, and a shift of hysteresis loops after cooling the sample at high fields, which vanishes above a certain temperature T_f [102,103]. The observations above were ascribed to the existence of a surface layer of canted spins which undergo a spin-glass-like transition to a frozen state at the freezing temperature T_f upon cooling [100,102,104]. One of the characteristic fingerprints of the spin-glass-like state, the dependence of T_f on the magnetic field which follows de Almeida-Thouless line $\delta T_f \propto H^{2/3}$ [105,106], where $\delta T_f(H) = T_f(0) - T_f(H)$, was demonstrated for example for surface spins of γ-Fe_2O_3 nanoparticles [102] (see Figure 2-10). Exchange coupling between the spin-glass-like surface layer and magnetically ordered core of the particle then causes shifting of magnetization loops after cooling in magnetic fields and modifies the magnetization reversal [70]. Over the years, the term “dead layer” has been extensively used and established to describe such surface layers with modified magnetism with respect to the core, not only in the paramagnetic state. Irrespective of a detailed structure of surface layers, separation of a nanoparticle into a bulk-like core with collinear spins and the surface layer with canted or disordered spins has become the essence of the **core-shell model** [94,98], which has been widely

applied in the interpretation of data on nanoparticle systems, e.g., in Mössbauer spectroscopy [98,107],[D3], [D5],[O1],[O2].

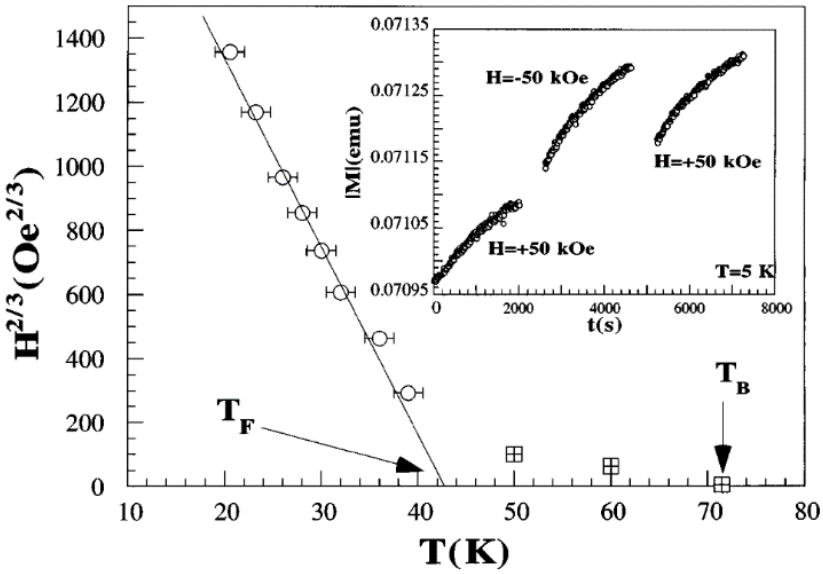

Figure 2-10. The field dependence of the freezing temperature of spins in the shell of maghemite nanoparticles, which follows the de Almeida-Thouless line $\delta T_f \propto H^{2/3}$, where $\delta T_f(H) = T_f(0) - T_f(H)$. The inset shows the time dependence of the absolute value of magnetization in the given fields after a ZFC process. Reproduced from [102].

Although the assumption of collinear "core" spins and canted or disordered "shell" spins often provides a satisfactory explanation of the experimental data on ferrimagnetic nanoparticles, it might be oversimplified in some cases [108]. For example, defects present in the core of the particle can induce the local canting of spins [109,110]. The presence of spin canting in the whole volume of the particles as a finite-size effect has been proposed as well [111]. Therefore, we should stress that the nature of a magnetically dead layer in ferrites, in which the magnetic state is governed by the superexchange, remains a rather controversial issue. In contrast, the dead layer has been widely accepted in Mn^{3+}/Mn^{4+} mixed-valence perovskite manganites, whose ferromagnetic state is driven by the double exchange mediated by itinerant e_g d-electrons. The surface layer concentrates lattice defects including the oxygen overstoichiometry (dominating Mn^{4+}), which hinders the e_g electron itinerancy, weakens the double exchange and results in an insulating magnetically disordered layer [112,113]. Alternatively, the existence of antiferromagnetically coupled ferromagnetic clusters in the shell has been proposed [114].

2.2.4 Shape effects

The shape of a nanoparticle represents another property with a significant impact both on the magnetic properties and the intended applications and is given by the

synthesis route employed, including detailed conditions such as concentration of precursors, temperature, chemical nature of species in the reaction mixture, etc. [115]. From the classical theory, it follows that only ellipsoidal bodies can be uniformly magnetized [116]. Any departure from the ellipsoidal shape produces additional anisotropy, which can lead to inhomogeneous magnetization states (see for example the iron nanocubes in Figure 2-11), shift the onset of the SD or SPM state, influence the susceptibility, or pronounce magnetic hysteresis [117]. Moreover, the shape determines the relative number of atoms at the particle surface for a given particle volume.

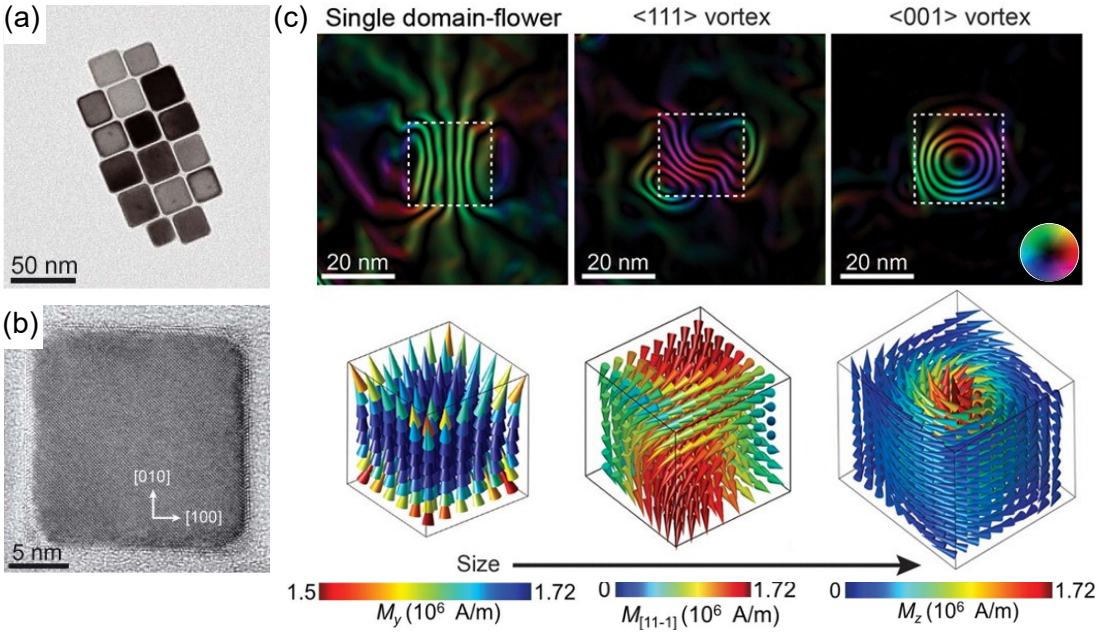

Figure 2-11. Magnetization states of isolated nanocubes of ferromagnetic iron: (a) TEM and (b) high-resolution TEM (HRTEM) images; in (c), three different states of the cubic particle (SD and two vortex states) are introduced, in the upper part, a 2D visualization of the magnetic induction flux lines by the TEM electron holography method, whereas the 3D models of the respective cubes are beneath them. The dashed lines mark the position of the cube, the inset color wheel in the right indicates the direction of the magnetic induction. The colors of arrows in the simulations denote the magnitude of local magnetization. Adapted from [118].

The **shape anisotropy** originates in the magnetostatic energy, more specifically through the anisotropy of demagnetizing fields arising from long-range dipolar interactions in the particle. Whereas a uniformly magnetized SD sphere possesses no shape anisotropy because of isotropic demagnetizing factors, it is easier to magnetize an ellipsoid along a long axis rather than the shorter one. For example, the magnetostatic energy of a uniformly magnetized ellipsoid can be expressed as [73]

$$E^{sh} = \frac{1}{2}\mu_0 V\left(N_x M_x^2 + N_y M_y^2 + N_z M_z^2\right), \tag{2.20}$$

where N_α and M_α are demagnetizing factors [119] and components of magnetization along the axes $\alpha = x, y$ and z, respectively.

However, in atom clusters that are small enough, smaller than the characteristic exchange length l_{ex} [120], the exchange coupling dominates, and such clusters are practically uniformly magnetized regardless of the shape since the gain in magnetostatic energy cannot counterbalance the expense of distorting the short-range order [40].

2.3 Nanoparticles of antiferromagnetic materials

Nanoparticles of antiferromagnetic materials (for simplicity further denoted as antiferromagnetic nanoparticles) as, for example, α-Fe_2O_3, $CuFeS_2$, or most iron oxyhydroxides require an alternative viewpoint on the magnetic phenomena discussed in previous sections. In contrast to ferromagnetic materials, the magnetization of antiferromagnets originates in defects. If the antiferromagnetic order is preserved in the core of the particles, their magnetic moment is dominated by the uncompensated surface spins and broken exchange interactions [121]. As a consequence, the magnetization of such a system far exceeds the bulk value ("superantiferromagnetism" [122]) and as the surface-to-volume ratio increases with the decreasing size of the nanoparticles, the saturation magnetization increases. The microstructure giving rise to the uncompensated moment also dictates the temperature dependence of coercivity and magnetization, including the development of superparamagnetism.

The mean uncompensated moment of an antiferromagnetic particle decreases with rising temperature [123] and follows the $-\varsigma T^2$ antiferromagnetic magnon law as was shown for example for small ferritin ($FeOOH \cdot nH_2O$) nanoparticles [123,124]. The isothermal dependence of magnetization of antiferromagnetic nanoparticles on the external magnetic field can be divided into two contributions [124]:

$$M_{\mathrm{AFM}}(T, H) = \chi_{\mathrm{AFM}}(T)H + M_{\mathrm{unc}}(T, H). \tag{2.21}$$

The antiferromagnetic susceptibility $\chi_{\mathrm{AFM}}(T)$ arises due to canting of spins of the two magnetic sublattices in the applied field and decreases with increasing temperature. The magnetization originating in the uncompensated moments $M_{\mathrm{unc}}(T, H)$ above the blocking temperature is usually assumed either in the form of a Langevin function weighted with the distribution of magnetic moments [123] or following the "random magnetic orientation" model [124,125], in which the particle moments fluctuate between two opposite directions along the easy axis of

each randomly oriented nanoparticle. The latter model provides higher magnetization at low fields, often in better correspondence with experimental data. Nevertheless, it might be difficult to separate both contributions to M_{AFM} if the magnetization is far from saturation. Similarly to the ferromagnetic and ferrimagnetic nanoparticles, the sublattice magnetization of surface atoms decreases more sharply with increasing temperature than in the antiferromagnetic core (see, e.g., [126] for comparison of ferrimagnetic γ-Fe_2O_3 and antiferromagnetic α-Fe_2O_3 nanoparticles).

Decreasing the size of particles largely impacts critical temperatures and fields of the material, for example, reduces the Néel temperature, which denotes the transition from the antiferromagnetic to the paramagnetic state. It also diminishes the critical magnetic field of the *spin-flop transition*, i.e., the field which, when applied parallel to the sublattice spins, causes the spins of the two sublattices to "flop" to the direction perpendicular to the applied field [127]. Nevertheless, the observed critical field of the spin-flop transition follows from two competing effects due to the decrease in the particle size: diminishing ascribed to weakening of exchange interactions and increasing the size of the uncompensated magnetic moment of the particle which, in contrast, leads to the enhancement of the critical field [128].

Another closely related example of a striking size dependence is represented by the Morin temperature T_{M} in hematite [129],[O3], the characteristic temperature of a spin-flop Morin transition occurring even without an applied magnetic field [130]. Hematite is the most thermodynamically stable polymorph of iron(III) oxide, crystallizes in the hexagonal structure of the corundum type with space group $R\bar{3}c$ and hexagonal close packing of anions (see Figure 2-12a). Depending on its origin, hematite can contain a certain amount of OH^- groups instead of O^{2-}, accompanied with Fe^{3+} vacancies (protohematite). Hematite has two magnetic sublattices interpenetrating in the basal plane. Below T_{M}, the spins of the two antiferromagnetically coupled sublattices are antiparallel and lie along the axis of the local electric field gradient (EFG) tensor, tilted from the hexagonal *c*-axis by about ~7°. At T_{M}, the anisotropy constant K_1 changes its sign from positive to negative because of two competing effects with different temperature dependence: (i) the Fe^{3+} single-ion anisotropy and (ii) magnetic-dipole anisotropy [131]. Above T_{M}, the spins lie in the basal plane (111) and are slightly canted from the antiferromagnetic axis by <0.1° as a result of the Dzyaloshinskii-Moriya interaction, creating thus a weak net magnetic moment in the (111) plane [132]. In bulk, the Morin transition occurs at $T_{\mathrm{M}} \approx 263$ K [133]. It follows that at room

temperature and up to the Néel temperature of 956 K, hematite behaves as a weak ferromagnet. The magnetic moments emerging from the noncollinearity of the almost antiparallel spins (see Figure 2-12b) lie along the *c*-axis.

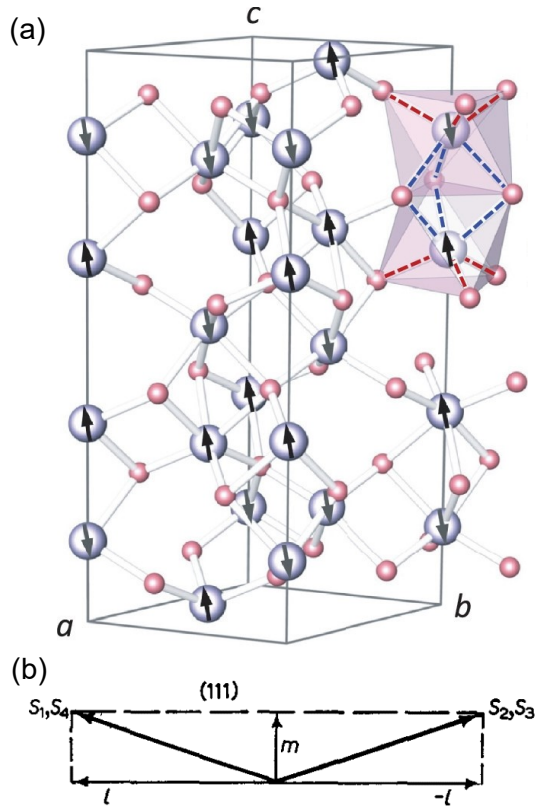

Figure 2-12. (a) Ball-and-sticks model of hematite structure with an indicated low-temperature magnetic structure (Fe atoms grey, O pink). Two face-sharing octahedra are shown to demonstrate the off-center position of Fe atoms – longer Fe–O bonds are indicated by the blue dashed lines, shorter bonds by the red lines. (b) The origin of the weak magnetic moment in the high-temperature phase is hinted in the I. Dzyaloshinskii's scheme, S_i, i = 1–4, denote spins of the four Fe atoms in the rhombohedral unit cell, each of which lies in a different {0001} plane in the hexagonal cell. Reproduced from [56,134].

A representative dependence of T_M on parameters characterizing the size of the particles is depicted in Figure 2-13, which also captures the difference between various theoretical models describing the size dependence of T_M, as summarized in our work [O3]. Apart from the size of the nanoparticles, Morin transition is very sensitive to defects, strain, incorporated H_2O or OH^- groups, cation substitutions, surface effects, and also the morphology of the particles, thereby the onset of T_M strongly depends on the synthetic route. These parameters can also deflect the spin-flop angle from 90° or even lead to a suppression of the transition. In [O3], we found that the transition was suppressed for particles smaller than ~10 nm, they remained weakly ferromagnetic down to liquid helium temperatures with a larger canting angle of the spins from the basal plane ~15–30°. In nonideal samples, the antiferromagnetic and weakly-ferromagnetic phases can coexist over a broad temperature range [135]. The application of external magnetic fields shifts the Morin transition to lower temperatures [136].

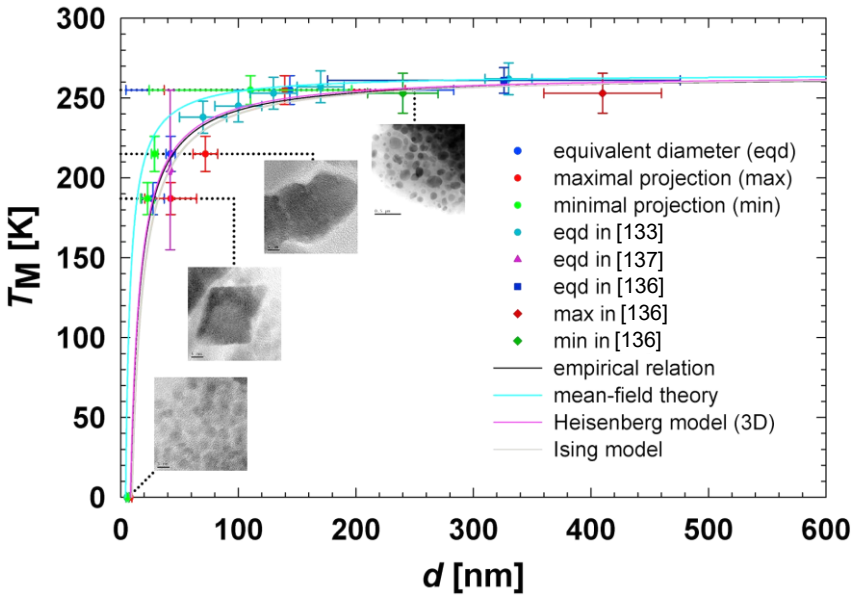

Figure 2-13. The dependence of Morin temperature on parameters characterizing the particle size; adapted from [O3].

2.4 Magnetic interactions between nanoparticles

In an idealized case, the interactions between nanoparticles are similar to those of spins in the bulk, just differing in scale. They are – especially the dipole-dipole interaction – almost always present in real systems and can significantly enhance the anisotropy energy [66]. The existence of exchange interactions has been hypothesized in the case of particles in direct contact [73]. In certain cases, when the particles are embedded in a nonmagnetic conducting matrix, RKKY interaction mediated by conduction electrons can also play a role [65,66]. RKKY interaction energy depends on the interparticle distance r as $1/r^3$, similarly to dipolar interactions. Depending on the strength of the interactions between nanoparticles, the magnetic behavior of the ensemble can be described by different models, ranging from modified superparamagnetism to superferromagnetism. Generally, the interactions increase the blocking temperature (see, for example, Figure 2-14) and broaden its distribution in the ensemble. However, it is important to note that the analysis of interparticle interactions in a real ensemble is an extremely complex problem due to many levels of disorder present in the system, including different degrees of crystallinity, volume and shape distribution, or randomness of orientations of easy axes of individual particles [40].

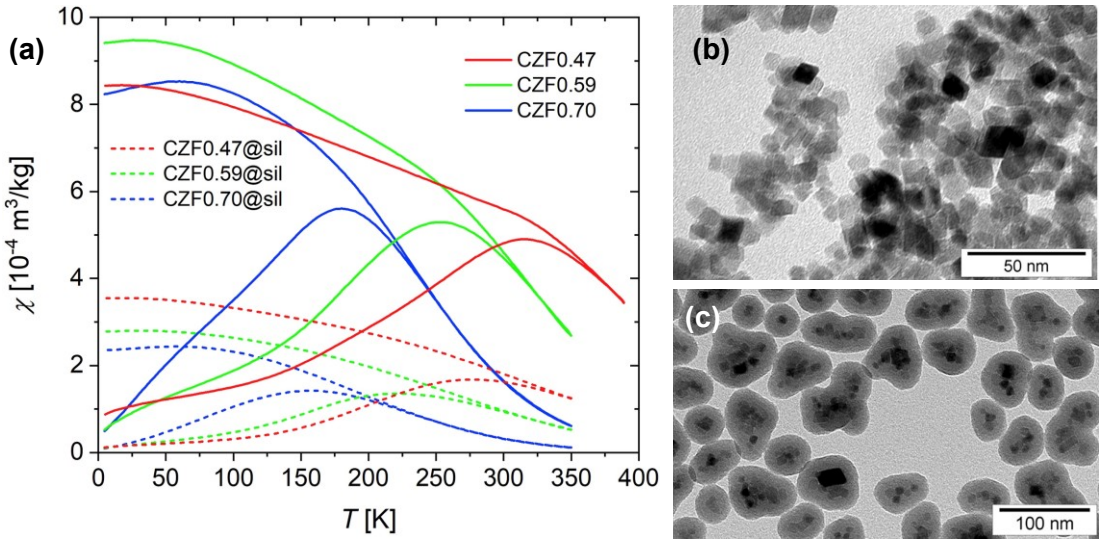

Figure 2-14. (a) ZFC and FC susceptibility at 100 Oe of bare and silica-coated ("@sil") Co-Zn ferrite nanoparticles that illustrate the effects of dipole-dipole interactions ($Co_xZn_yFe_{3-x-y}O_4$, $3-x-y = 1.86$, y is indicated by the number in sample codes); TEM micrographs of (b) CZF0.70 and (c) CZF0.59@sil. Adapted from [D10].

Whereas the dipole-dipole interactions between magnetic moments of atoms in the crystal structure are usually negligible compared to exchange interactions, the **dipole-dipole interactions** between moments of nanoparticles, which can reach 10^3-10^5 μ_B with μ_B being the Bohr magneton, strongly modify the magnetic properties of such an ensemble [73]. In general, the dipole-dipole interactions modify the energy barrier of a single particle E_B and thereby its superparamagnetic relaxation; however, a transition to a *collective state*, in which the magnetic behavior of the ensemble is no longer governed by E_B, is also possible. The energy of dipole-dipole interaction between two magnetic moments $\boldsymbol{m}_1$ and $\boldsymbol{m}_2$ separated by a position vector $\boldsymbol{r}$ (distance r) can be written as

$$E_{dd} = \frac{\mu_0}{4\pi r^3}\left[\boldsymbol{m}_1 \cdot \boldsymbol{m}_2 - \frac{3(\boldsymbol{m}_1 \cdot \boldsymbol{r})(\boldsymbol{m}_2 \cdot \boldsymbol{r})}{r^2}\right], \qquad (2.22)$$

which can, in the case of particle moments, correspond to the ordering temperature $T_o \propto E_{dd}/k_B$ of several tens of kelvins. Nevertheless, in ensembles of antiferromagnetic nanoparticles, the dipole-dipole interactions are usually of minor importance due to rather small uncompensated moments of individual particles, and the respective ordering temperature is often well below 1 K [108].

Although the dipole-dipole interaction between antiferromagnetic nanoparticles (or weakly ferromagnetic due to the Dzyaloshinskii-Moriya interaction) is not significant even for particles in direct contact, radically different magnetic dynamics have been observed in ensembles of bare and coated particles. For example, the blocking temperature of the former can exceed T_B of coated particles

of the same material by more than 100 K, or the SPM relaxation can be even suppressed [138,139]. The significant slowdown of the dynamics was well demonstrated with the Mössbauer spectroscopy, in which spectra of noninteracting particles show two distinct subspectra (a Zeeman-split sextet for particles in the blocked state and a doublet for superparamagnetic particles), whereas spectra of interacting particles in close contact consist of an asymmetrically broadened sextet (see Figure 2-15). This extreme change in the dynamics was attributed to **exchange interactions** between surface ions of neighboring particles in close contact [138].

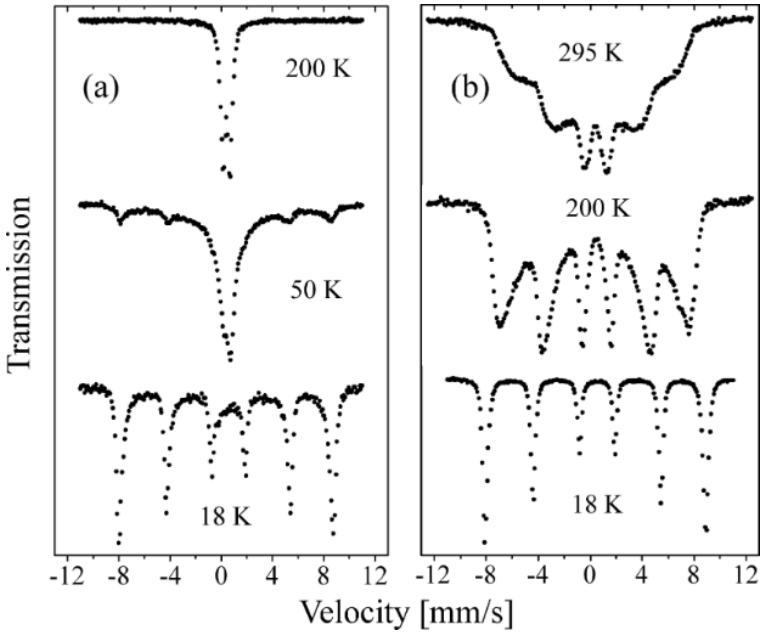

Figure 2-15. ^{57}Fe Mössbauer spectra of 8 nm hematite nanoparticles: (a) coated with phosphate ($T_B \sim 40$ K), and (b) bare particles from the same batch. Reproduced from [139].

2.4.1 From superparamagnetism to collective arrangements

If superparamagnetic nanoparticles are very distant from each other, for example in a diluted suspension or silica matrix, the dipole-dipole interactions are negligible and the relaxation behavior can be described by the Néel-Brown relaxation model (2.15).

In the limit of weak interactions, the effect of dipole-dipole interactions can be included as a perturbation that modifies the energy barrier of a particle. This effect can be introduced by correcting the real temperature with a phenomenological temperature T_0, which provides an estimate of the interaction strength:

$$\tau_{VF} = \tau_0' e^{\frac{E_B(H)}{k_B(T-T_0)}}. \qquad (2.23)$$

This expression, where $E_B(H) = V(K + H_{int}M)$ with H_{int} being the mean interaction field, applies for $T \gg T_0$ and is denoted as the Vogel-Fulcher law [140]. Importantly, this model cannot be applied close to T_0 [140].

For sufficiently strong interactions (and/or low temperatures), the relaxation processes cannot be described by any modification of the superparamagnetic regime, the one-particle approach of a single energy barrier is no longer applicable and the complex energy landscape of the ensemble with multiple energy minima comes to the fore [141]. The interactions then move the system away from single-particle blocking towards collective freezing of particle superspins.

Interactions of medium strength in a concentrated system induce **spin-glass-like freezing** by which the ensemble transits to a collective state characterized by the randomness of particle anisotropy axes and magnetic frustration. The nonequilibrium dynamics of interacting nanoparticle assemblies resemble the one of spin glasses by showing the aging and "memory" effects in different cooling/heating rates, waiting times at a given temperature, or upon cycling the temperature [70]. Nevertheless, some important differences have been established. Classic spin glasses arise from a true thermodynamic phase transition at a well-defined glass-transition temperature, which is described by a set of critical parameters determining the behavior of characteristic properties as the diverging susceptibility or slowing relaxation [40]. In contrast, in real magnetic nanoparticle assemblies in the collective state, the dynamics are determined by a large distribution of relaxation times that are temperature-dependent and smeared over a much broader range compared to noninteracting particles. As a consequence of the particle size distribution, some particles which are large enough might be frozen in the whole examined temperature range [70]. The collective state is also highly sensitive to the application of the external magnetic field, and it has been shown that it forms only during cooling in low fields, whereas it can be suppressed already by a moderate field applied during cooling [142]. Flatness or decrease in the susceptibility during cooling at an applied field at temperatures below the transition temperature is another characteristic feature of the spin-glass-like state, sometimes accompanied also by a "kink-like" shape in the vicinity of a characteristic freezing temperature of the ensemble [143,144]. The first feature is ascribed to the dominance of interaction energy of the particles with their neighbors over the Zeeman energy in sufficiently small fields, the moments of the particles can thus freeze also in the opposite orientation than the direction of the applied field. The "kink" can be explained by the gradual development of

magnetization over a nonzero waiting time during the acquisition of the data at a temperature that induces freezing of larger clusters [143].

For great interaction strengths and highly concentrated ensembles, the collective freezing can generate the **superferromagnetic state** [145], characterized by ferromagnetic-like correlations in the ordering of particle superspins. Such an ensemble can form magnetic domains with the practically collinear ordering of superspins and separated by domain walls (see Figure 2-16), which can undergo similar domain-wall motions as in bulk ferromagnets. If the particles in the ensemble are randomly arranged, a certain degree of local magnetic disorder is preserved and the disorder influences magnetization processes in the ensemble (see an example of a real system in Figure 2-17). In a special case of particles distributed in a regular cubic lattice, the antiferromagnetic (for a simple cubic arrangement of particles) or ferromagnetic (for bcc and fcc, which is the natural close-packed structure) ordering due to dipole interactions were predicted [146].

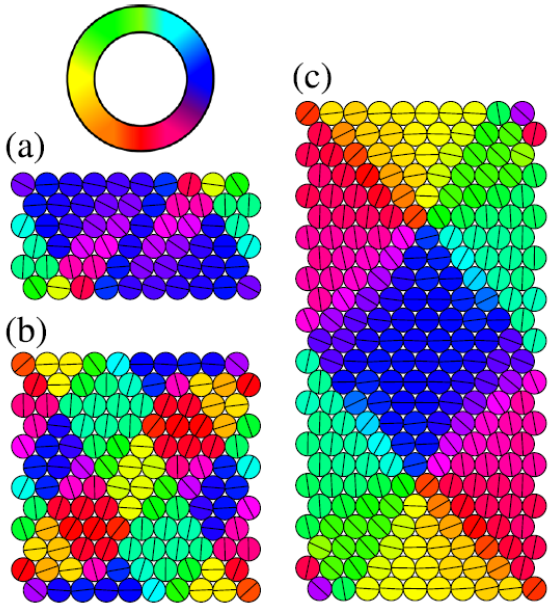

Figure 2-16. Molecular-dynamics simulation of a regular 2D array of magnetic nanoparticles for different length-to-width ratios, starting from a fully ferromagnetic order. Adapted from [147], the model examines spherical Co particles with a diameter of 15 nm and magnetic saturation $M_{\mathrm{sat}} = 1.4 \cdot 10^3$ kA m^{-1}, i.e., a magnetic moment of $m = 2.47 \cdot 10^{-18}$ A m^2; the circle provides a legend to the direction of the magnetic moment of the particles.

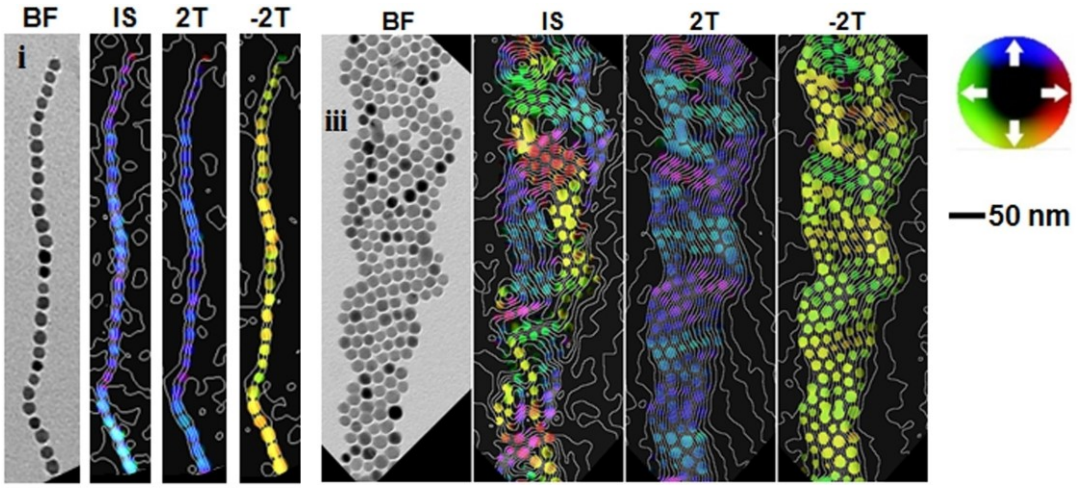

Figure 2-17. Bright-field (BF) TEM images and holographic magnetic field maps in the remanent magnetic state (IS) and applied field of 2 T in opposite directions in a chain (i) and an agglomerate of spherical ε-Co nanoparticles (iii). The direction of the magnetic field projected into the plane of nanoparticles is indicated by the color, the magnitude by white contours (each contour corresponds to a change by 1/64 of the magnetic flux quantum $\Phi_0 = 2.07 \cdot 10^{-15}$ T m^2). Adapted from [148].

3 Synthesis and functionalization of magnetic nanoparticles

3.1 Synthesis of magnetic nanoparticles

Numerous methods to produce nanoparticles have been devised and further developed into a plethora of variants. Importantly, the details of the employed method determine the properties of the prepared nanoparticles – not only their size, shape, and surface properties and termination, but also their crystallinity, composition, or cation distribution, which modify the macroscopic properties of the sample. At the same time, the targeted characteristics of the product differ according to the intended applications, making the diversification of the synthesis methods highly desirable.

The synthesis of nanoparticles follows two main approaches. In the **bottom-up methods**, the nanoparticles are built "piece by piece" from precursors, and for example co-precipitation, hydrothermal, sol-gel, or thermal decomposition syntheses fall into this category. The bottom-up methods usually allow a more effective control over the resulting properties of the particles, as the size distribution and shape. In contrast, **top-down methods** like high-energy milling rely on the fragmentation of bulk and larger particles. In the following text, we will describe the methods employed in our studies.

3.1.1 Thermal decomposition

The thermal decomposition method, which we used in our study on Zn-substituted magnetite nanoparticles for magnetic solid-state extraction [D8], allows the production of small and highly monodisperse nanoparticles with high crystallinity and bulk-like magnetization [149]. Typically, the size of the particles ranges 4–15 nm but can reach down to ~1.5 nm [150] or above 15 nm [151] in seed-mediated growth procedures. It is based on the thermal decomposition of suitable precursors containing metal atoms (e.g., metal acetylacetonates, cupferronates, or carbonyls, see Figure 3-1) in high-boiling organic solvents in the presence of stabilizing surfactants [152]. The high boiling point of the solvents, e.g., octadecane, dioctyl ether, dibenzyl ether, etc., enables the reaction mixture to reach the decomposition temperature of the precursors, which often exceeds 200 °C. In general, the process of particle formation can be described by the LaMer mechanism [153], which assumes three phases. At the prenucleation stage, the thermolysis of the precursors gradually increases the concentration of reacting metal species up to a critical value. Then, a short burst of nucleation from the supersaturated solution is initiated and continues until the forming seeds decrease the concentration of the reacting species below the critical value. Finally, the seeds

keep growing slowly and uniformly by binding the available metal species diffusing to their surface [154],[D8]. The surfactants like oleic acid or other fatty acids and oleylamine bind to the growing particles, decrease the rate of crystal growth, which enables obtaining nanosized particles, and stabilize the resulting particles in the hydrophobic solvent.

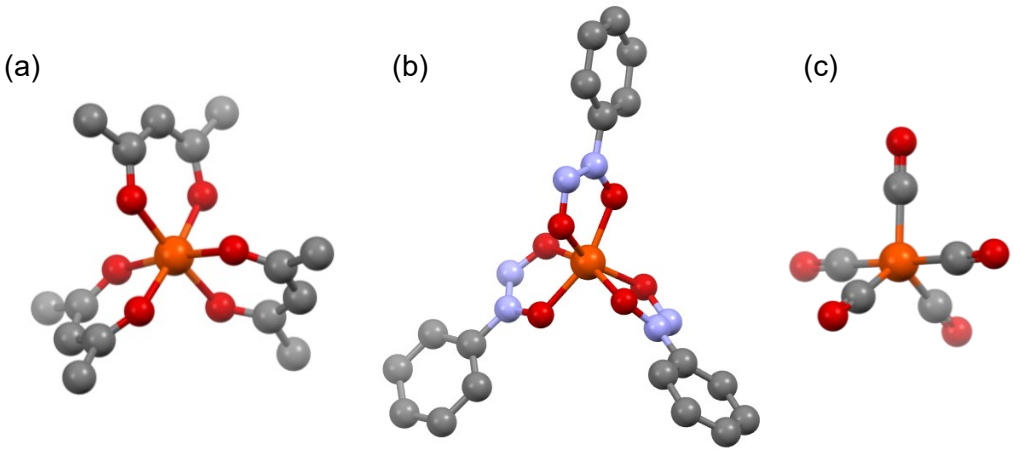

Figure 3-1. Molecular structure of (a) iron(III) acetylacetonate, $Fe(acac)_3$; (b) iron(III) cupferronate, $Fe(Cup)_3$ (Cup = *N*-nitrosophenylhydroxylamine); (c) iron pentacarbonyl, $Fe(CO)_5$, based on single-crystal structure data. Colors of atoms: Fe – orange, O – red, N – blue, C – grey; hydrogen atoms are omitted. Structures obtained from the Cambridge Structural Database [155].

The key to the synthesis of monodisperse nanoparticles is the successful separation of burst nucleation and growth processes; otherwise, new nuclei would be formed concurrently with the growth of the existing ones. The size and shape of the resulting particles are strongly affected by the concentration of precursors and surfactants, temperature program, and aging effects [154] (see Figure 3-2 left for an example of shape evolution of cobalt ferrite nanoparticles during thermal decomposition). The synthesis produces nanoparticles capped with surfactants (see Figure 3-2 right), which are dispersible in nonpolar organic solvents. However, for most biological applications, in which the small and monodisperse particles are demanded, colloidal stability in water is crucial and follow-up treatment of the prepared nanoparticles is required.

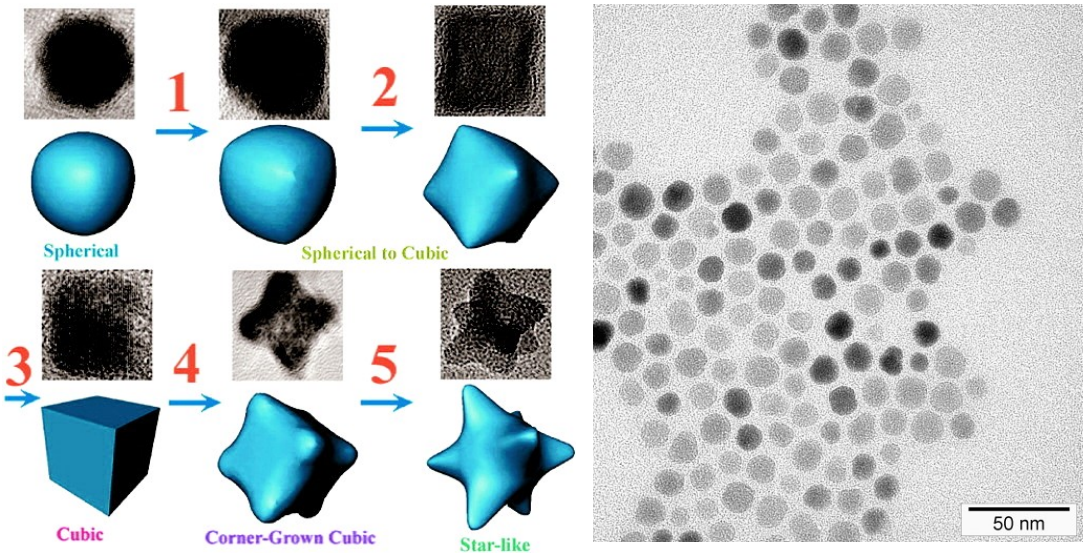

Figure 3-2. Left: Schematic representation of shape evolution of spinel $CoFe_2O_4$ nanocrystals prepared by the thermal decomposition method. The particles formed at the initial stage are mostly spherical, whereas later the particles transform into cubes. If slow growth continues, the reacting species bind preferentially to the corners of the cubes, because the corners have the highest surface energy and concentration of defects, and thus star-like particles are formed. Adapted from [154]. Right: TEM micrograph of our Zn-doped magnetite ($Fe_{2.63}Zn_{0.37}O_4$) nanoparticles prepared by thermal decomposition [D8]. The more or less regular spatial separation of particles in the 2D array on the TEM grid is due to the capping agents (oleic acid and oleylamine).

3.1.2 Sol-gel synthesis

The main principle of sol-gel techniques is a gradual transformation of a homogeneous solution (sol) into a polymeric network (gel), which either forms the final product or provides a precursor for further processing. The synthesis of silica or titania nanoparticles and coatings epitomizes the former case and will be discussed in more detail in Section 3.2. In the latter case, which can be exemplified by the Pechini method, the process continues through a xerogel by combustion during calcination, and finally the formation of the target product during a subsequent thermal treatment.

As an example of a simple sol-gel process, we can mention hydrolysis of Fe(III) salts leading to ferrihydrite. For simplicity, we will assume that only salts with noncoordinating or weakly coordinating counterions (e.g., nitrates) are used and no complexation agents are added to the mixture. One can then consider primarily Fe^{3+} species with ligands originating from water, namely water molecules and hydroxide and oxide anions, to occur in the hydrolysis and polycondensation (see an example in Figure 3-3).

Generally, complex ions containing metal cations can condense in different ways under different conditions and create polymers through oxo and hydroxo bridges or added agents [156]. Depending on the conditions such as pH, concentration, temperature, complexation agents, properties of the metal or oxidation state, the complex precursors in the solution gradually form gels or gelatinous precipitates (as in the case of Fe^{3+} [157]), structurally ranging from small nuclei to complicated polymerous frameworks. The pH is usually adjusted to higher values to promote hydrolysis of simple metal salts, typically by adding NH_3, NaOH, Na_2CO_3, or any hydroxyl exchanger [157].

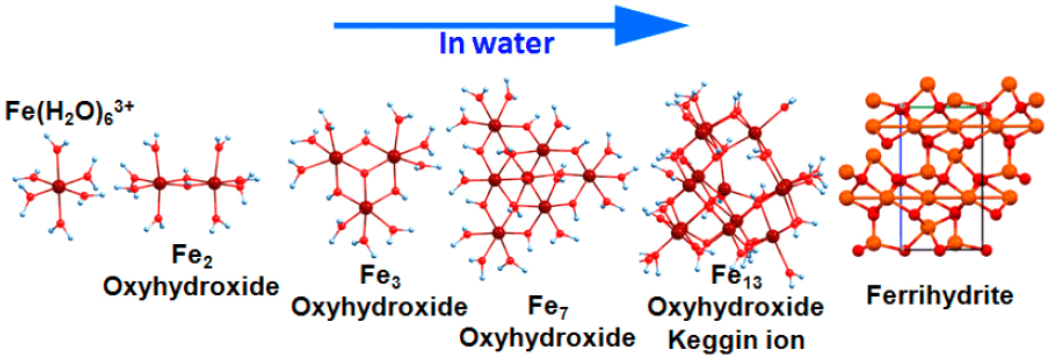

Figure 3-3. Scheme of one of the hydrolysis routes of Fe^{3+} ions in water and condensation through hydroxo and oxo bridges, starting from a mononuclear hexaaquairon(III) cation and resulting in polynuclear iron(III) oxyhydroxide clusters. Reproduced from [158].

We used the sol-gel synthesis to prepare La-Sr and La-Na manganite nanoparticles [D1], namely the Pechini process, in which citric acid was used as a chelating agent and ethylene glycol as a gelifying agent. The chelating agents form complexes with the dissolved metal cations and the diol enables cross-linking through esterification with carboxylic groups, which gives rise to a polymeric network, i.e., the gel. After drying, the xerogel is calcined – the organic constituents are removed by pyrolysis during this step – and a very fine inorganic precursor results. The target phase is then formed by solid-state reactions in the subsequent thermal treatment of the precursors, which does not require temperatures as high as the traditional ceramic route and thereby allows one to achieve a nanocrystalline product. Actually, the higher the temperature used, the larger crystallites are formed, which enables one to easily control the mean size of the prepared particles (see for example Figure 3-4). However, the as-grown product has to be subjected to mechanical processing, e.g., by milling or rolling, to break sintering bridges between the grains and obtain individual nanoparticles. Although the Pechini method and related techniques enable the preparation of diverse mixed-cation oxides, many of which are unreachable by other synthetic routes, the final product is characterized by broad

distributions of size and shape of nanoparticles, which is further increased by harsh mechanical processing [159].

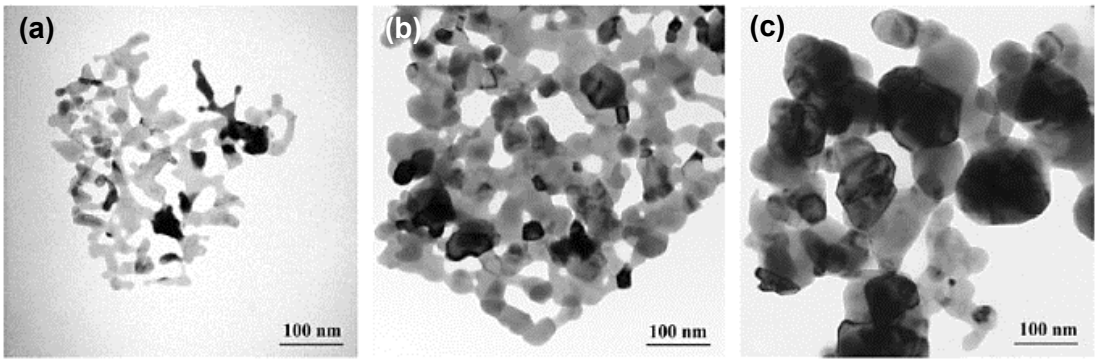

Figure 3-4. The as-grown nanocrystalline $La_{0.70}Sr_{0.30}MnO_3$ manganite before mechanical treatment, prepared by the Pechini method and annealed in oxygen at different temperatures: (a) 700 °C, (b) 800 °C, and (c) 900 °C for 3 h. Reproduced from [43].

3.1.3 Hydrothermal synthesis

Hydrothermal synthesis is based on chemical reactions that occur in aqueous solutions at elevated temperatures (higher than 100 °C) and pressures (higher than 1 bar). Such conditions are achieved in a closed pressure vessel, typically a sealed ampoule, a stainless-steel pressure vessel with a Teflon insert, or a more complex chemical reactor, which is heated externally. The pressure reached during the synthesis derives primarily from the applied temperature and the saturation pressure of water, which is generally affected by the ebullioscopic effect (but possible decomposition of reaction components and formation of gaseous byproducts have to be considered as well and rather avoided). Analogical procedures carried out in organic solvents are termed solvothermal syntheses. The hydrothermal method is inspired by hydrothermal mineral-forming processes in the Earth's crust and the technique has also proven very efficient for obtaining single crystals of diverse compounds including minerals. Therefore, it poses a natural choice for the synthesis of particles of iron oxides or sulfides. The method can provide effective control over the properties and morphology of the final product, furthermore, it is widely perceived as environmentally friendly due to the water solvent and relatively mild synthesis conditions compared to other methods. In our studies, we employed the hydrothermal method to synthesize magnetic nanoparticles of Mn-Zn ferrites [D1],[D2] and Co-Zn ferrites [D1],[D10], akageneite and maghemite [D4], and nanocrystalline greigite [D12] (see selected examples in Figure 3-5).

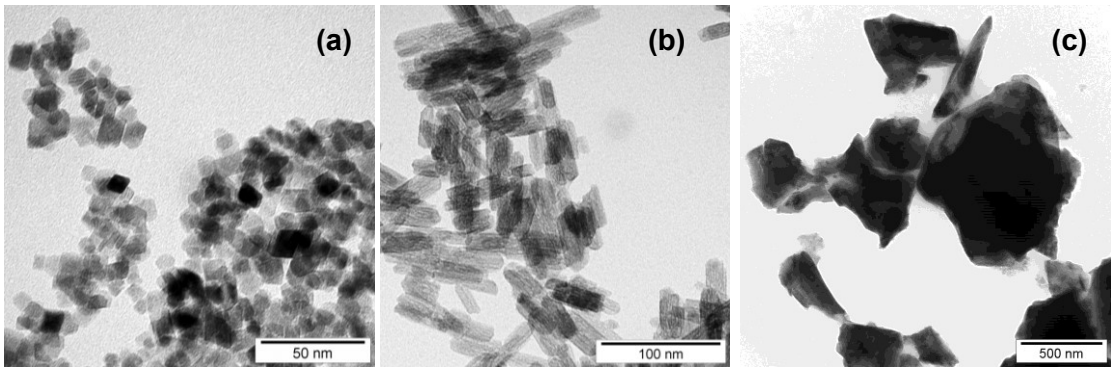

Figure 3-5. TEM images of particles prepared by the hydrothermal method: (a) $Co_{0.44}Zn_{0.70}Fe_{1.86}O_4$ ferrite [D10], (b) akaganeite β-FeO(OH,Cl), (c) nanocrystalline greigite Fe_3S_4.

In general, metal salts like nitrates, sulfates, halides, or acetates with high solubility in water are often used as starting materials in hydrothermal procedures. Aside from salt solutions, precipitated intermediates (e.g. metal oxide-hydroxide mixtures obtained at elevated pH) and powder dispersions are frequently employed as precursors [160]. During the heating period, the precursors dissolve or decompose and form reacting species. The following phases of nucleation and crystal growth can be again described by the LaMer mechanism. Particles formed at lower temperatures can dissolve and recrystallize upon further increase of temperature or during aging, typically when the system is kept at the elevated temperature [161]. If the concentration of reacting species drops below a certain critical value, Ostwald ripening can occur, during which smaller particles again dissolve while larger particles grow [160]. Sometimes, surfactants or specific agents are added to the reaction mixture to control the size or shape of the resulting particles and prevent their aggregation [162].

The density, viscosity, and surface tension of water diminish with increasing temperature (see Figure 3-6a for the T–ρ plot), which leads to greater mobility of the dissolved ions and molecules under hydrothermal conditions. The elevated temperatures and pressures increase the ionization constant of water (see Figure 3-6b) and promote the dissolution of materials otherwise insoluble at ambient conditions [163,164]. In the case of limited solubility of precursors in water at neutral pH even at hydrothermal conditions, the dissolution might be accomplished by adjusting pH by the addition of hydroxides or acids. At the same time, pH belongs to the crucial parameters defining the resulting product [165].

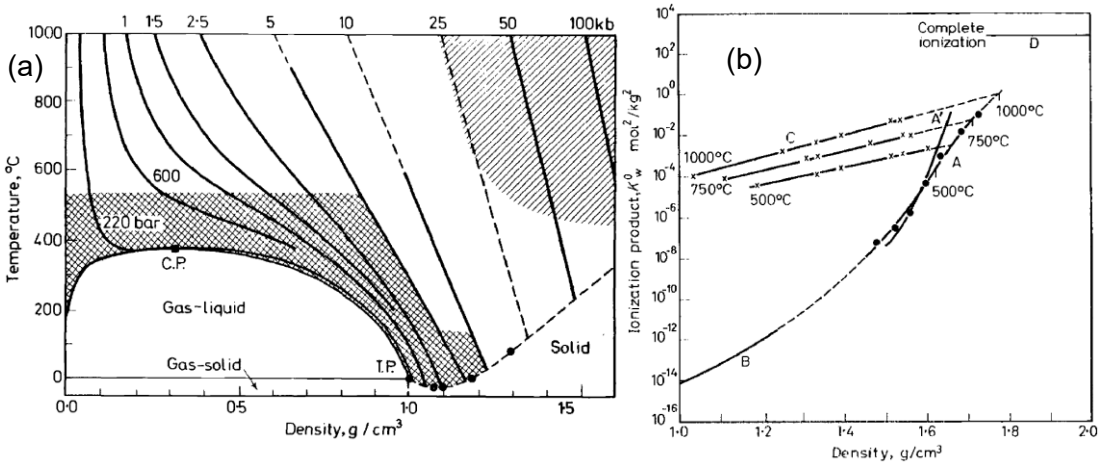

Figure 3-6. (a) Temperature-density diagram of water; full and dashed lines denote measured and interpolated isobars, T.P. and C.P. are the triple and critical points. The points to the right of the T.P. mark transitions between different polymorphs of ice. (b) The ionization product of water $K_w = [H^+][OH^-]$ (activities approximated with concentrations) as a function of density. Reproduced from [164].

3.1.4 Templated synthesis ("nanocasting")

An interesting method based on the application of a mesoporous silica template was used to prepare nanoparticles of ε-Fe_2O_3 and its substituted analogs, which we employed in our studies [D3],[D5],[D7],[D11],[O2] devoted above all to their efficiency in contrast enhancement in nuclear magnetic resonance imaging (MRI). The pores in the silica template provide spatial confinement to growing crystallites, which can stabilize metastable phases such as ε-Fe_2O_3. The pores can also determine the shape of the growing particles as "molds", as was demonstrated for example by growing MnO_2 nanowires [166]. Although the templated synthesis belongs to somewhat under-represented methods of synthesis of nanoparticles, it is a quite popular method of preparation of various nanocomposites. Moreover, functionalized mesoporous silica materials themselves have attracted considerable attention, e.g., in environmental and catalytic applications [167–170].

Our synthesis of the epsilon polymorph of iron oxide was based on [171] and consisted of the following steps: the preparation of a mesoporous SBA-15 silica template, its impregnation with metal nitrates, calcination at 1050-1100 °C, and removing the template by alkaline leaching.

The preparation of the SBA-15 template (SBA stands for "Santa Barbara Amorphous") was based on the approach described by Zhao et al. [172] and basically followed the procedure reported in [166]. The formation of the silica template with a highly ordered two-dimensional mesostructure of large pores (up

to 30 nm) is achieved by adding amphiphilic block copolymers to the reaction mixture. Nonionic block copolymers with distinct self-assembly characteristics act as structure-directing agents. At first, they form spherical micelles interacting with silicate species in the reaction mixture, then the micelles coalesce into larger cylindrical micelles. These large micelles make a self-assembled system, which serves as a template for condensation of silicate species and precipitation of silica [173–175] (see the scheme in Figure 3-7). In this specific case, the employed triblock copolymer consists of the more hydrophilic poly(ethylene oxide), more hydrophobic poly(propylene oxide), and again the poly(ethylene oxide) (PEO–PPO–PEO, P_{123}). Finally, the copolymer is removed from the sample by calcination at ~500 °C. The resulting pores have hexagonal symmetry, are uniform in size, and are separated by rather thick walls (~3–6 nm).

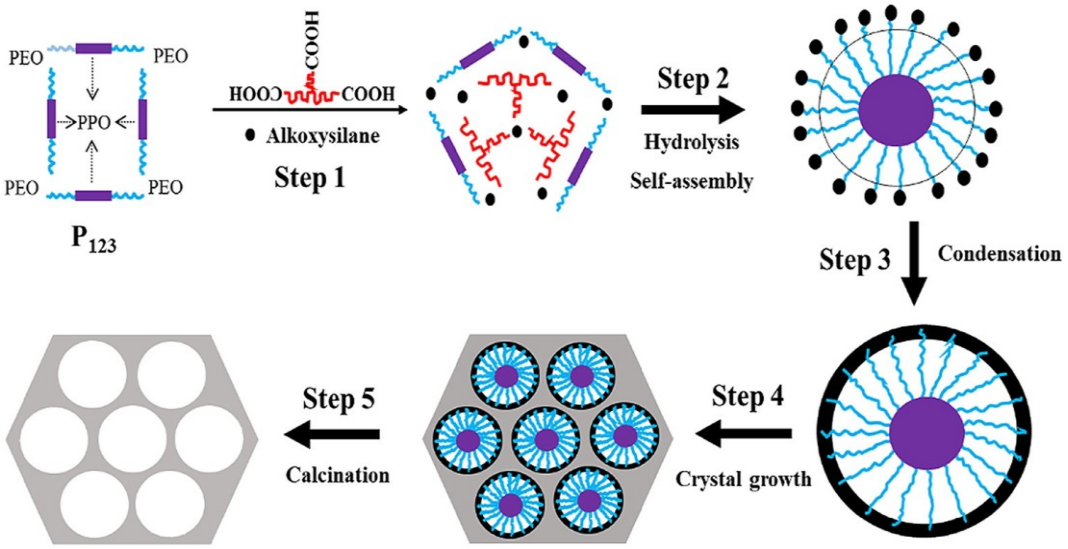

Figure 3-7. The preparation of SBA-15 mesoporous silica (in this case, the citric acid is used instead of the more common HCl to decrease pH). Reproduced from [175].

The impregnation of the prepared SBA-15 silica template with aqueous solutions of metal salts, usually metal nitrates, follows. The subsequent heat treatment produces nanoparticles of the oxides grown in the pores of the silica, as shown in Figure 3-8.

The character and initial concentration of the metal salts, potential presence of other species in the impregnation solution (e.g., sucrose [171]), the size of pores of the silica template, temperature of calcination of the impregnated intermediate, and the duration of the heat treatment influence the size of particles and modify the final ratio of the iron(III) oxide polymorphs in the sample [171,176].

Eventually, the silica template is removed by alkaline leaching, and the product is purified by multiple washing cycles.

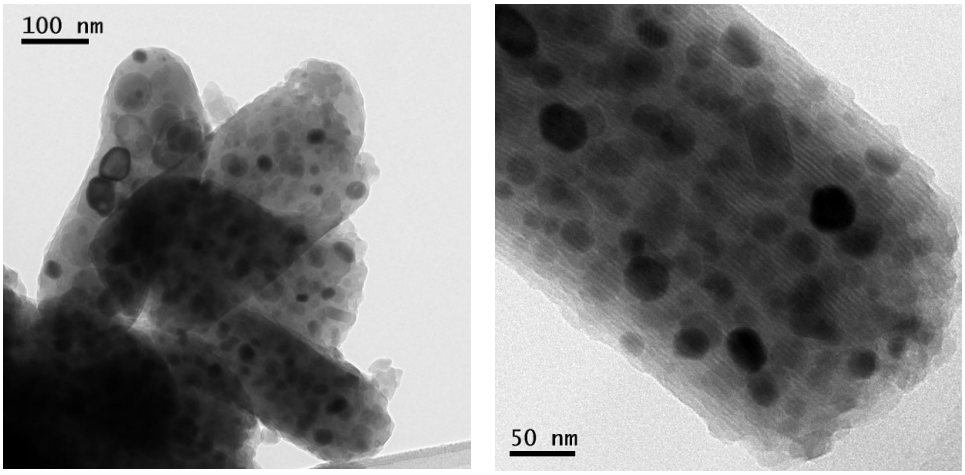

Figure 3-8. TEM images of the mesoporous SBA-15 silica template with ε-Fe_2O_3 nanoparticles grown in the pores.

3.1.5 Mechanochemical synthesis

The mechanochemical synthesis of nanoparticles relies on chemical reactions induced by the application of mechanical energy on reactants, for example by grinding the ingredients in a mortar or milling them in ball mills. In our studies [D6],[D9], high-energy ball milling of pure elements as starting materials in both laboratory and industrial mills was employed to prepare nanoparticles of Cu-Fe-S-based materials for thermoelectric applications. The samples were kindly provided by the group of Prof. Peter Baláž from the Institute of Geotechnics of the Slovak Academy of Sciences in Košice.

In a typical procedure, the reactants are mixed and fed into a milling vessel along with the milling medium – balls. Sometimes, other supporting agents can be added as well to achieve required properties, for example surfactants to prevent the particles from agglomeration [177]. Then, the milling vessel is sealed in an inert atmosphere and inserted into a mill, and after a chosen milling time at a desired milling frequency, the material is recovered.

In high-energy milling, two main types of ball mills are usually employed: i) in shaker or vibration mills, the vessel shakes back and forth in a curved trajectory and creates impact-related stresses in the material; ii) in planetary mills, the vessels are arranged on a rotating disk and, in addition, rotate around their own axes in the opposite direction. The counter-rotation enriches the range of mechanical effects acting in the grinding vessel with shear and friction. The mode of vessel

motion in both mill types is schematically sketched in Figure 3-9 along with main effects taking place in the planetary mill.

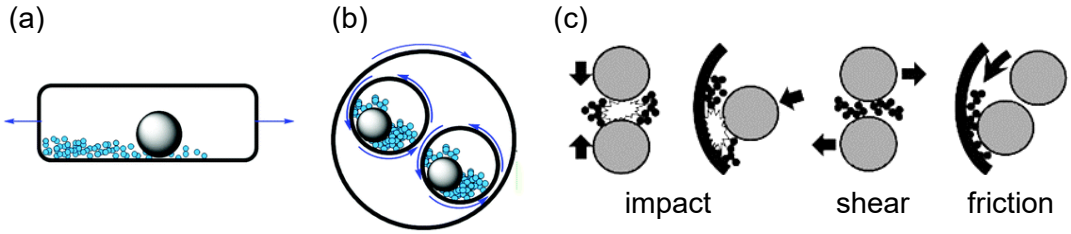

Figure 3-9. Schematic representation of a cross-section of (a) a shaker mill and (b) a planetary mill; (c) scheme of mechanisms dominating in the planetary mill. Adapted from [178] and [177].

The composition and properties of the resulting product depend not only on the starting material but also on many parameters of the mechanical process – the size and weight of balls and the ball-to-powder ratio, degree of vessel filling, the milling speed and time, and geometry of the mill. The mechanochemical synthesis aims to transfer as much energy to the treated material as possible and to induce defect formation, which enhances the chemical reactivity [179]. Another important parameter to consider is the material of the grinding vessel and balls because the product will most likely be, to some extent, contaminated by abrasion. Tungsten carbide, various types of stainless steel, and zirconia belong to the most widely used materials of grinding tools, though they can contain varying amounts of additional elements like Ni, Co, Ti, Mn, or Cu as binders in WC or additional alloying metals in steels [177]. The milling time should allow the reaction processes to finish but at the same time be as short as possible to minimize contamination and amorphization [180]. An example of mechanochemically synthesized nanoparticles and their structure is shown in Figure 3-10.

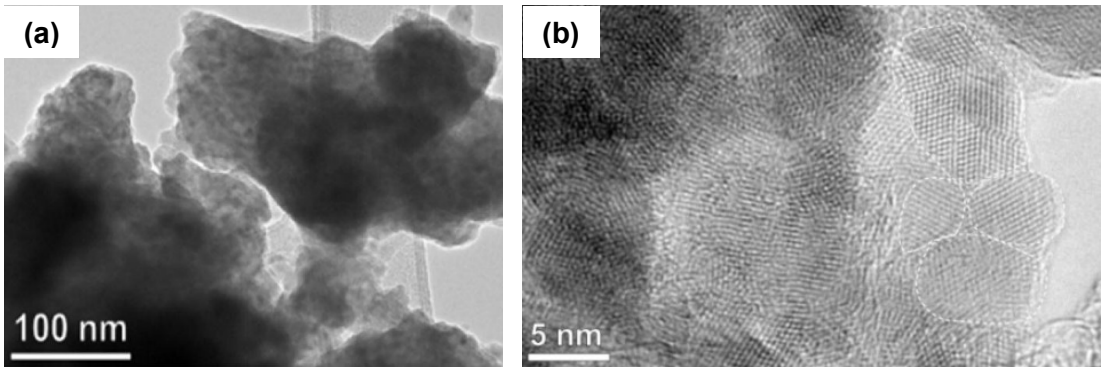

Figure 3-10. Nanoparticles synthesized by high-energy milling: (a) $CuFeS_2$ nanoparticles [D6], (b) HRTEM of ZnS nanoparticles [181].

As a huge amount of kinetic energy is deposited at the contact spot of colliding particles, the mechanically activated processes inherently take place under

nonequilibrium conditions and are highly localized. The surface of particles at the contact spot gets highly disordered, the collision is accompanied by the emission of excited fragments of the solid, electrons, and photons over a short period, and the local "instant temperature" can increase to thousands of kelvins. A cascade of processes related to various excitation energies and characteristic times follows, induces lattice defects and chemical mixing, and can trigger also self-propagating chemical reactions. The large concentration of defects together with high local pressure and temperature can, in certain cases, result in the formation of metastable polymorphs. Finally, after the milling ends, relaxation processes bring the product to equilibrium [180].

Due to the high complexity of the mechanically activated processes, which are not yet completely understood, precise control of the synthesis is often unfeasible. The final product then often comprises a multiphase system of nanoparticles, which can have a metastable distribution of atoms, usually have a high level of disorder, or can even comprise further nanocomposite structures. Nevertheless, a crucial advantage of this method is the ease of production and feasibility of scaling up to large volumes, which make mechanosynthesis felicitous for industrial applications.

3.2 Coating and functionalization of nanoparticles

Most applications of magnetic nanoparticles require specific surface modification of the magnetic cores, which protect the magnetic phase from chemical leaching, oxidation, or other changes due to aggressive environment, ensure colloidal stability in aqueous suspensions, provide additional functionalities (e.g., specific targeting, stealth character allowing the particle to evade immune recognition, etc.) or even enable physical effects unavailable for the magnetic cores (e.g. magnetoelectric nanoparticles, stimuli-responsive systems, etc.). The possibilities of various coatings are tremendous and offer a vast territory for fine-tuning of the nanoarchitectures to achieve the desired properties; however, with the increasing complexity, the reproducibility of such structures and their properties might be difficult to attain. In the following, we will focus only on three basic types of surface modification of nanoparticles that were important for our studies, namely stabilization with citrate and coating with silica and titania.

3.2.1 Citrate stabilization

Any type of the coating procedure aiming to encapsulate individual particles into some material must first ensure that the particles are colloidally stable in the reaction mixture, i.e., they do not aggregate during the process of encapsulation. In aqueous suspensions, an effective and facile method of stabilization of certain metal

oxide nanoparticles is the chemisorption of citrate [182]. We employed this stabilization in all studies engaging encapsulation in silica (see Section 3.2.2 below), as well as those concerning aqueous suspensions of "uncoated" particles stabilized just with a citrate monolayer [D1],[D5].

The citric acid, if added to the suspension of iron oxide nanoparticles, can adsorb on their surface via the $–COO^-$ groups and the $–O^-$ group (see the scheme in Figure 3-11). The central carboxyl group deprotonates preferentially compared to the terminal –COOH groups due to the negative inductive effect of the hydroxyl group [184]. Therefore, at a lower pH, there is a higher probability of adsorption of the citrate monoanion through the central carboxylate [185]. At higher pH, or after neutralization with a base such as ammonia, the doubly and triply deprotonated citrate anions become more abundant and bind to the surface with higher probability with two carboxyl groups [186]. Then the remaining $–COO^-$ group can be exposed to the solution, providing a negative charge, and stabilizing the particles in the suspension through the Coulomb repulsion. The effect of steric repulsion of the citrate layers also plays a role in particle stabilization [185,187].

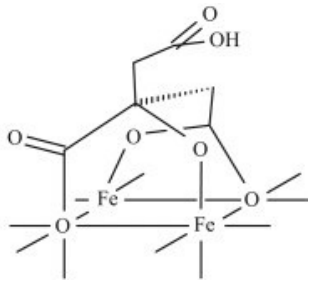

Figure 3-11. Idealized geometry of citrate adsorbed on an iron oxide surface; reproduced from [183].

3.2.2 Encapsulation in silica

Coating the particles with inorganic and chemically stable silica, which can be described by the formula of $SiO_{2-x}(OH)_{2x}$, where x depends on the degree of "structural hydration", i.e., the content of silanol groups, provides the necessary protection and colloidal stability in aqueous suspensions. As silica is nontoxic and biologically inert for most organisms, it represents an excellent coating material for biological and medical applications. Furthermore, silica coating can be easily functionalized with different chemical groups and molecules and, at the same time, prevents unwanted interaction of these moieties with the magnetic core, such as luminescence quenching of attached dyes [152]. Besides the common amorphous silica shells, mesoporous silica coatings can be achieved by various template-assisted procedures. Both types of silica coatings are illustrated in Figure 3-12. Whereas the increased porosity of the latter offers a higher specific surface or enables the loading of specific cargo such as drugs in controlled drug delivery [D2], the relatively simple and well-defined amorphous silica with a smooth surface poses an excellent choice for model studies [D7].

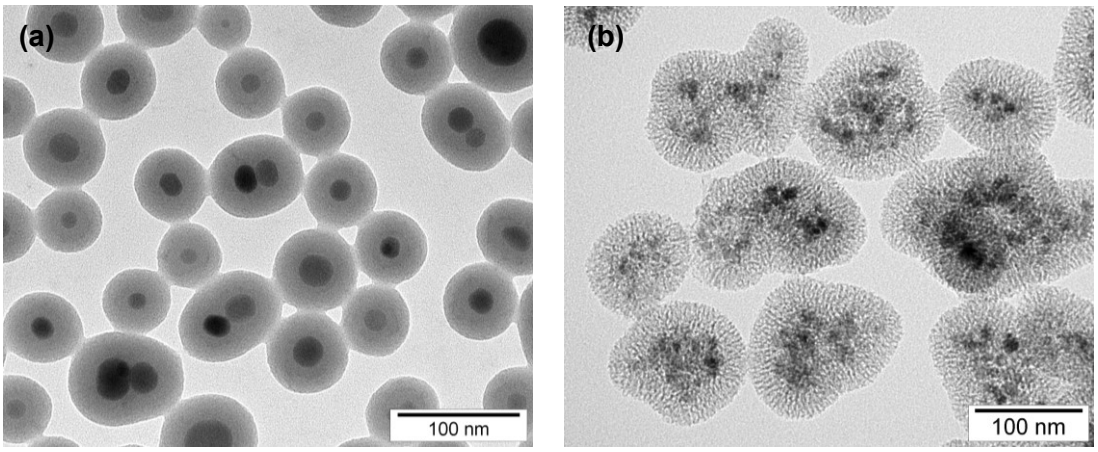

Figure 3-12. TEM micrographs of (a) ε-$Al_{0.23}Fe_{1.77}O_3$ nanoparticles encapsulated in amorphous silica (sample ε-AlFe-s21 in [D5]) and (b) $Mn_{0.4}Zn_{0.6}Fe_{1.8}O_4$ nanoparticles coated with mesoporous silica.

The most common methods of encapsulation of nanoparticles into silica are based on hydrolytic polycondensation of silicon alkoxides, most frequently tetraethoxysilane – TEOS or tetramethoxysilane – TMOS, in a mixture of water, alcohol (usually ethanol), and ammonia, which acts as a catalyst. These methods are denoted as the Stöber process because they are derived from the prototypical preparation of monodisperse silica particles by Stöber et al. [188]. The underlying reactions are schematically depicted in Figure 3-13. At first, the alkoxy group of the silicon alkoxide is replaced by the hydroxy group by hydrolysis while an alcohol molecule is released. The subsequent polycondensation through the –OH group results in Si–O–Si bond formation by either dehydration (the –O– bridge originates from the reaction of two –OH groups of two different entities) or dealcoholation (transfer of the proton from the –OH group of one entity to the alkoxy group of another entity). Chain reactions involving precursor molecules and already formed oligomers create a polymerous network, in which the silicon bonds are either participating in the oxo bridges or are terminated by hydroxy/alkoxy groups. Upon full dehydroxylation, the resulting network would provide pure and stoichiometric SiO_2.

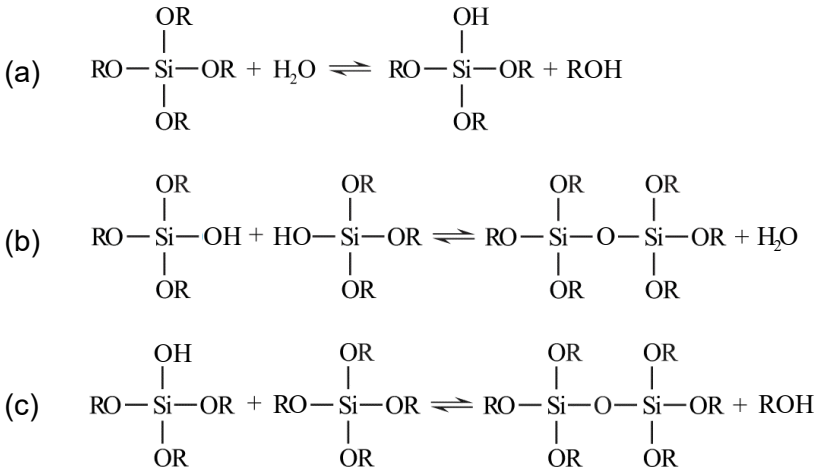

Figure 3-13. Reactions describing (a) the hydrolysis of the silicon alkoxide and polycondensation through (b) dehydration and (c) dealcoholation; R denotes the alkyl group. Adapted from [189].

When the Stöber method is applied in the encapsulation, nanoparticles act as seeds, at which the silica grows [190]. We employed this method in most of our studies [D1],[D2],[D3],[D4],[D5],[D7],[D10],[D11], the presence of cetyltrimethylammonium bromide (CTAB) in the starting solution induced formation of mesoporous silica coating [D2], [D4]. As shown in the pH dependence of ζ-potential of silica-coated particles in Figure 3-14, the highly negative ζ-potential at neutral pH suggests that silanol groups Si–OH are at least partially deprotonated due to the acid-base equilibrium and the silica surface has a negative charge. The aggregation of the coated particles is then prevented by Coulomb repulsion, leading to enhanced colloidal stability of the aqueous suspension [191,192].

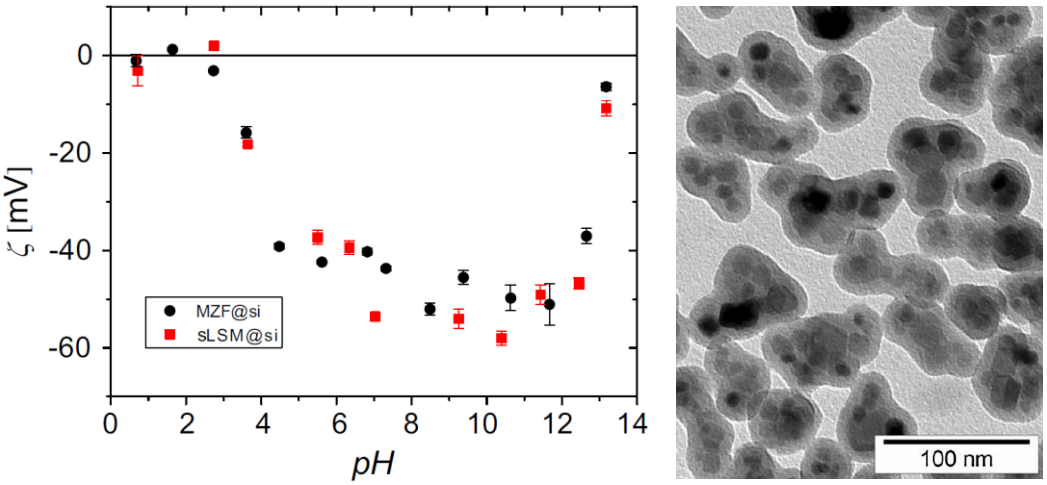

Figure 3-14. The pH dependence of ζ-potential for an aqueous suspension of silica-coated nanoparticles of $Mn_{0.61}Zn_{0.42}Fe_{1.97}O_4$ prepared by hydrothermal synthesis (MZF@si, TEM micrograph shown on the right) and $La_{0.63}Sr_{0.37}MnO_3$ prepared by sol-gel (sLSM@si). Adapted from [191].

3.2.3 Encapsulation in titania

Titanium dioxide or titania represents a chemically stable and biologically inert material with unique photocatalytic properties [193], which provides an interesting alternative to the widely used silica coating. The encapsulation procedure applied in [D1] and described in more detail in [194,195] is more or less analogous to the silica encapsulation above, being based on hydrolytic polycondensation of titanium alkoxides. Nevertheless, these processes are much faster than for the respective silicon alkoxides, which complicates the control of both the nucleation and growth processes [194]. The hydrolysis and condensation are slower for alkoxides with higher and more bulky alkyl groups, as well as their diffusion in the solution, whose rate affects the degree of polymerization [196].

To slow down the hydrolysis of titania precursors in our surfactant-assisted procedure, a solution of titanium butoxide was continuously applied over a prolonged period to simulate high dilution conditions. The nanoparticles were stabilized in the suspension with the CTAB surfactant, which also enabled the deposition of titania but induced certain porosity of the final coating [194]. Such encapsulation leads to amorphous titania shells, which are not as smooth and with uniform thickness as the silica coatings due to the higher speed of the hydrolytic polycondensation (see Figure 3-15). Analogically to silica, the titania coating bears a negative surface charge because of the deprotonated titanol groups Ti–O^- and provides colloidal stability to the particles through the Coulomb repulsion (see the pH dependence of ζ-potential in Figure 3-15).

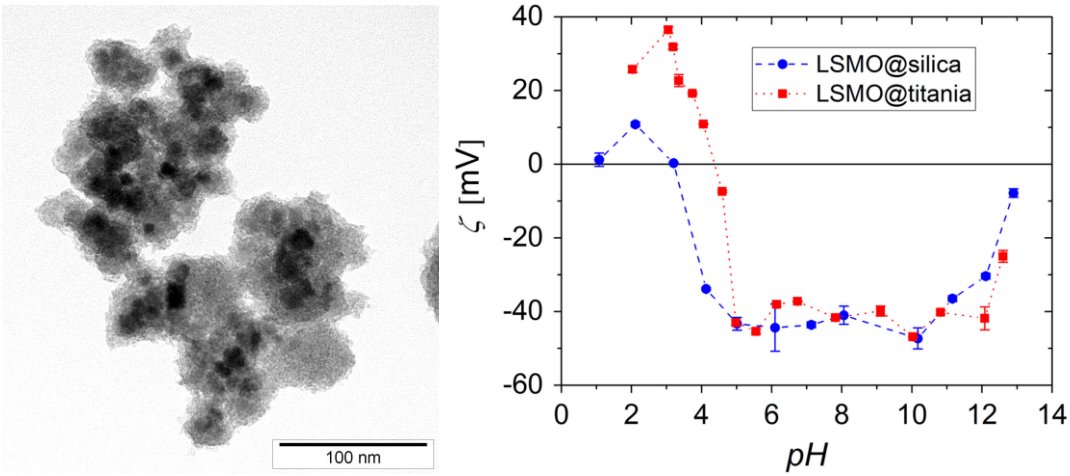

Figure 3-15. TEM micrograph of titania-coated $Mn_{0.61}Zn_{0.42}Fe_{1.97}O_4$ nanoparticles (left; from [D1]), and the comparison of the pH dependence of ζ-potential for $La_{0.65}Sr_{0.35}MnO_3$ nanoparticles coated with silica and titania (right; reproduced from [194]).

4 Selected iron-containing compounds

This chapter introduces selected materials studied in this thesis in more detail, highlighting peculiarities of individual compounds as well as more general phenomena inherent to such compounds. The core of this work is focused on iron-containing oxides – ferrites, magnetite, and various polymorphs of iron(III) oxide. The set of studied materials is further enriched with oxyhydroxides (akageneite) and sulfides (greigite, chalcopyrite). Perovskite manganites, which are interesting as heating agents for self-regulated magnetic hyperthermia and as MRI contrast agents, as shown also in our relaxivity study [D1], are mentioned only peripherally. Most of the studied compounds have a crystal structure of the spinel type. Involving both magnetite, Fe_3O_4, and its thiospinel analog greigite, Fe_3S_4, provides a complementary perspective on the role of anion properties, such as lower electronegativity of sulfur than oxygen and a closely related higher degree of covalence of the Fe–S bonding. The broader scope of this work offers an insight into the nuances of magnetism of multiple transition metal compounds with different exchange pathways and into the ways how the local magnetic structure affects the magnetic behavior of their nanoparticles. Importantly, it enables us to understand the control of magnetic properties by means of chemical composition and size of particles and utilize it when tuning the materials for the intended applications.

4.1 Spinel-type compounds

The compounds of the spinel type hold a fundamental position in Earth sciences, as well as material research. They are frequent accessory minerals of igneous and metamorphic rocks, usually with various compositions within the $(Mg,Fe^{2+})(Al,Cr,Fe^{3+})_2O_4$ oxyspinel series [197], some of them are frequent in sediments (e.g., magnetite or greigite, often of biogenic origin as mentioned in Chapter 2), they can guide the mining explorations (e.g., zincian spinel for sulfide ores [198]), many of them are important ores, such as magnetite for iron and violarite $FeNi_2S_4$ for nickel, or even gemstones based on the prototypical spinel $MgAl_2O_4$ [199] – probably the most famous examples are the Black Prince's Ruby, the focal stone of the Imperial State Crown, and Timur Ruby in the necklace, both being part of the Crown Jewels of the United Kingdom, or the red spinel in the Imperial Crown of Russia. In solid-state science, various compounds of the spinel type have attracted great interest thanks to their electric and magnetic properties accompanied by a rich spectrum of physical phenomena.

The compounds of the spinel type can be represented by a general formula AB_2X_4, in which A and B stand for different cations and in a more general case possibly for vacancies, and X is the anion. The atomic ratio of cations (A + B, including vacancies) to anions X must be 3:4. Most natural minerals of the spinel type belong to so-called oxyspinels ($X = O^{2-}$), whereas thiospinels (S^{2-}) and selenospinels (Se^{2-}) are quite rare. Nevertheless, synthetic tellurospinels and other compounds with the spinel structure where $X = F^-$, Cl^-, $(CN)^-$, and N^{3-} have been also prepared [200]. According to the oxidation state of the A and B, the minerals of the oxyspinel group can be further divided into (i) the spinel subgroup "2-3", i.e., $A^{2+}(B^{3+})_2O_4$, comprising not only the mineral spinel $MgAl_2O_4$ but also magnetite, maghemite, jacobsite $MnFe_2O_4$ or franklinite $ZnFe_2O_4$; and (ii) ulvöspinel subgroup "4-2", $A^{4+}(B^{2+})_2O_4$, named after ulvöspinel $TiFe_2O_4$ [200]. In the thiospinel and selenospinel groups, some uncertainties regarding the oxidation state of cations prevail and the assignment of formal valences can have little sense due to higher cation-anion covalent mixing and collective behavior of d-electrons [201]. The practice is further complicated by their tendency to nonstoichiometry. Nevertheless, the formal division leads to two subgroups within each of these groups: in the thiospinel group, they are (i) the carrollite subgroup "1-3.5", $A^+(B^{3.5+})_2S_4$ comprising mostly copper-bearing minerals ($A = Cu^+$) inclusive of carrollite $CuCo_2S_4$; and (ii) linnaeite subgroup "2-3", including, besides linnaeite Co_3S_4, also greigite and violarite. Similarly, the selenospinel group is divided into (i) "tyrrellite subgroup" "1-3.5" and (ii) bornhardtite subgroup "2-3" [200].

Due to its relative simplicity, the spinel structure was among the first crystal structures determined after the discovery of X-ray diffraction [199,202,203]. The spinel crystal structure represents one of the basic structures derived from the cubic close-packed structure of anions, with eight formula units in the unit cell (see Figure 4-1). Out of 64 tetrahedral and 32 octahedral voids of the close-packed anionic arrangement in the unit cell, A and B cations occupy 1/8 of tetrahedral and 1/2 of octahedral voids. Each X anion coordinates one cation in the tetrahedral site and three cations in the octahedral sites. If we view the atom layers perpendicularly to the triad axes ⟨111⟩, layers of anions and cations alternate; at the same time, layers of cations in octahedral sites alternate with layers containing cations in both tetrahedral and octahedral sites [204].

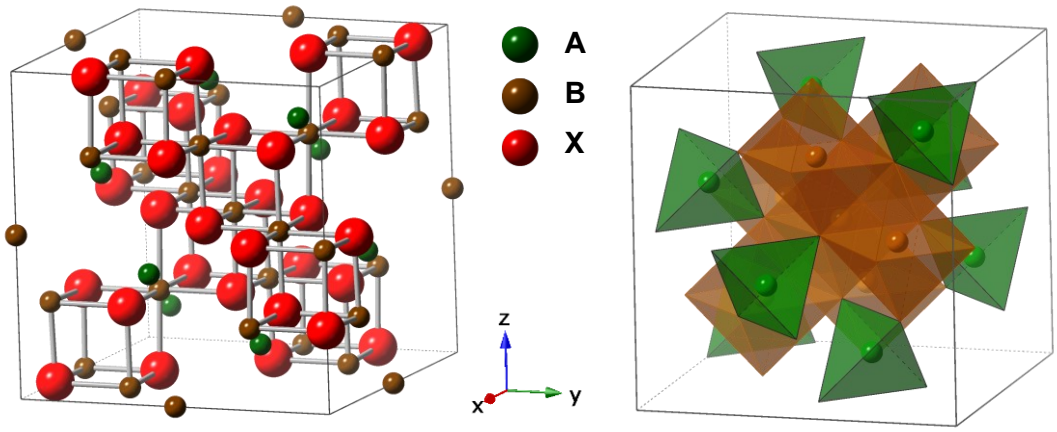

Figure 4-1. A unit cell of a structure of a normal spinel (see below) – ball-and-stick model (left) emphasizing the bonding of octahedral sites (occupied by B cations) with the anions and polyhedral model (right) emphasizing the coordination of the ions in octahedral and tetrahedral (occupied by A cations) sites. The crystal structure was visualized based on one of the ICSD magnetite records (ICSD code 84611, published in [205]; single-crystal XRD, T = 296 K, $Fd\bar{3}m$ space group, u = 0.2555(2)).

Another view on the spinel structure is provided by the polyhedral network, as visualized in Figure 4-1b. The tetrahedra are isolated from each other and share corners (X anions) with their neighboring octahedra. If we disregard the anions and octahedrally coordinated cations, the tetrahedral sites are arranged in a diamond lattice (see Figure 4-2a). The octahedra share six of their twelve X–X edges with their adjacent octahedra, forming a rutile-like array of edge-sharing chains along the six ⟨110⟩ directions. Again, if we focus exclusively on the cations in octahedral sites, it becomes apparent that the octahedral sites form a network of corner-sharing tetrahedra, giving rise to the pyrochlore lattice (Figure 4-2b). Looking at the sublattice formed by the octahedral sites along the ⟨111⟩ direction exposes two types of alternating layers – a 2D triangular lattice composed of apical cations of the tetrahedra, and a 2D kagome lattice built by triangles of cations at the base of the tetrahedra formed by octahedral sites (Figure 4-2c). Both the diamond lattice and, most importantly, the pyrochlore lattice are recognized to generate strong geometrical frustration effects, which have been indeed observed in many magnetic spinel-type compounds, such as ACr_2O_4 and AV_2O_4 (nonmagnetic A = Mg, Zn, Cd) and have been suggested also for some ferrites AFe_2O_4 [206].

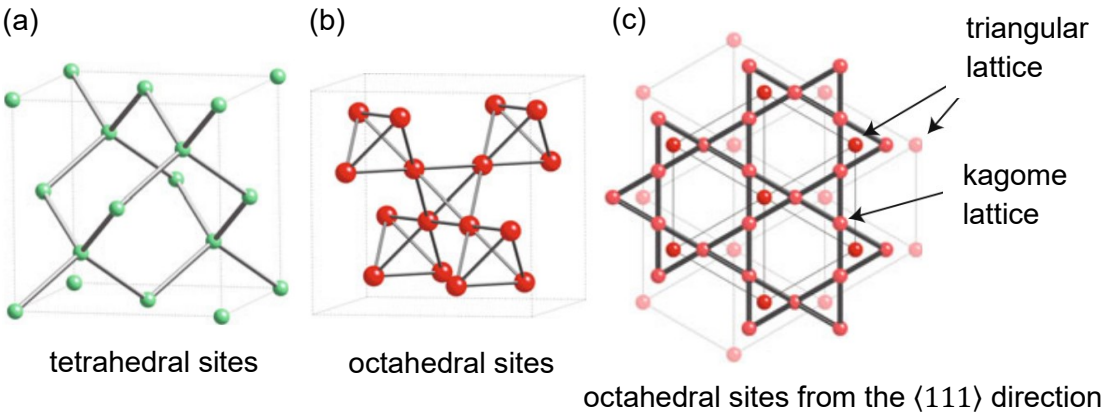

Figure 4-2. Cation sublattices of the spinel structure: (a) the diamond lattice of tetrahedral sites and (b,c) the pyrochlore lattice of octahedral sites. Adapted from [206].

The spinel structure as described above is consistent with several space groups, from the high-symmetry cubic group $Fd\bar{3}m$ to lower-symmetry groups like $P4_132$ or $R3$ [200]. In the highly symmetrical $Fd\bar{3}m$ group, cations in tetrahedral sites occupy 8*a* Wyckoff positions (1/8, 1/8, 1/8) with point symmetry $\bar{4}3m$, meaning that the tetrahedra (with X anions in the corners) are regular. However, the octahedra allow a trigonal distortion (along the ⟨111⟩ directions) since the cations in octahedral sites occupy 16*d* positions (1/2, 1/2, 1/2) with point symmetry $.\bar{3}m$. Anions in 32*e* positions (symmetry $.3m$) require an additional parameter for their complete description, the fractional coordinate *u*, which describes the position of the anion nearest to the origin (chosen here in the vacant octahedral site) by the coordinates (*u*, *u*, *u*). The anion lattice can easily accommodate around the tetrahedral and octahedral sites and thereby embrace large range of cations of different sizes, which endows the spinel structure with enormous chemical flexibility. The distortion of the spinel lattice as well as the octahedra can be described by the *u* parameter because the anions shift along the ⟨111⟩ directions to maintain the symmetry. Whereas $u = 0.25$ for the ideal cubic close packing of anions when the octahedra are regular, $u < 0.25$ represents compression and $u > 0.25$ elongation of the octahedra along the ⟨111⟩ trigonal axes. The empirical values of *u* fall in the range 0.2301–0.2703 [207], the distances between anions and cations are prolonged in the tetrahedral and shortened in the octahedral sites with an increase in *u*, and *vice versa* upon a decrease in *u*. The distortion from the ideal cubic close-packed lattice impacts among other also magnetic properties, for example by modifying the angle determinative for the superexchange interaction between the tetrahedral and octahedral sublattices (125.3° in the ideal case of regular octahedra) [207].

Traditionally, following the cation distribution in the prototypical spinel $MgAl_2O_4$ with Mg^{2+} in tetrahedral sites and Al^{3+} in octahedral sites, two limiting cases are distinguished: (i) *normal* spinels, whose divalent A^{2+} cations reside in tetrahedral sites and trivalent B^{3+} cations in octahedral sites; and (ii) *inverse* spinels, in which tetrahedral sites are occupied by trivalent B^{3+} ions and octahedral sites by both trivalent B^{3+} and divalent A^{2+} ions. The relation between the A^{2+}, B^{3+} cations and individual sites is characterized by the *inversion parameter i*. Based on the formula $(A_{1-i}B_i)[A_iB_{2-i}]X_4$, where we mark the tetrahedral sites with parentheses ( ) and octahedral sites with brackets [ ], the inversion parameter describes the ratio of A ions, which would "normally" be in tetrahedral sites but are found in octahedral sites, i.e., $i = 0$ in the normal spinels and $i = 1$ in the inverse spinels. The value of i is an outcome of both thermodynamics and kinetics, depending on the conditions during the crystallization process – temperature and program applied, oxygen fugacity – as well as inherent properties of the system, such as size, charge, covalence effects, or crystal field stabilization energies (CFSE) [200]. As a consequence, spinel-type compounds can exhibit a large degree of cation disorder, the random ordering being characterized with $i = 2/3$.

At this point, let us introduce the general concept of CFSE, originating in the crystal field theory. As briefly sketched in Section 2.1, the orbital energy levels of a transition metal atom are modified by anions (or other ligands) in its surroundings, the decisive factors are the symmetry and the intensity of the electrostatic field produced by the anions (*crystal field*). A detailed scheme of the coordination in octahedral and tetrahedral sites is depicted in Figure 4-3a for the sake of the following discussion. Whereas in an isolated transition metal ion, all five d-orbitals are degenerate, in the nonspherical crystal field of anions, the degeneracy is lifted and the d-orbital energy levels split about the "center of gravity" of the originally unsplit levels. In regular tetrahedral coordination with anions situated along the diagonals of the Cartesian coordinate system, the d-levels split into low-lying doubly degenerate e_g ($d_{x^2-y^2}$, d_{z^2} orbitals) and triply degenerate t_{2g} orbital levels (d_{xy}, d_{yz}, d_{xz} orbitals), as indicated in Figure 4-3b. The energy difference between these two levels is called the crystal field splitting and is denoted as Δ_t. To fulfill the "center of gravity" rule, e_g orbital levels lie $0.6\ \Delta_t$ below the barycenter (each electron in e_g "stabilizes" the transition metal cation by $0.6\ \Delta_t$) and t_{2g} levels lie $0.4\ \Delta_t$ above the barycenter. In the regular octahedral coordination with anions situated at the Cartesian axes, the same splitting of the d-levels occurs as in the regular tetrahedron, though with interchanged t_{2g} (d_{xy}, d_{yz}, d_{xz} orbitals pointing "between" the anions) and e_g ($d_{x^2-y^2}$, d_{z^2} orbitals pointing "towards" the anions) levels [208]. The larger crystal field splitting $\Delta_{oct} = 9/4\ \Delta_t$ again follows the

"center of gravity" rule (see Figure 4-4). The trigonal distortion of the octahedron splits further the t_{2g} levels into one a_{1g} (the orbital pointing towards the tetrahedral sites in spinels) and two e_g' (perpendicular to the a_{1g} orbital), as indicated in Figure 4-4. The CFSE then characterizes the resulting net stabilization energy after accommodating all d-electrons.

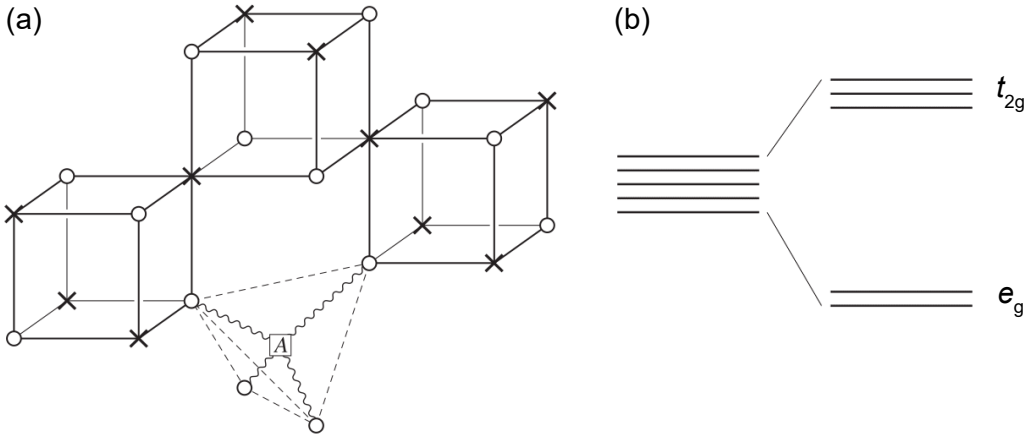

Figure 4-3. (a) Detailed view of the interconnection of the octahedral sites (crosses) and the tetrahedral site (A) in the spinel structure; (b) crystal field splitting of energy levels of d-orbitals of a transition metal cation/atom in the tetrahedral coordination. Adapted from [49].

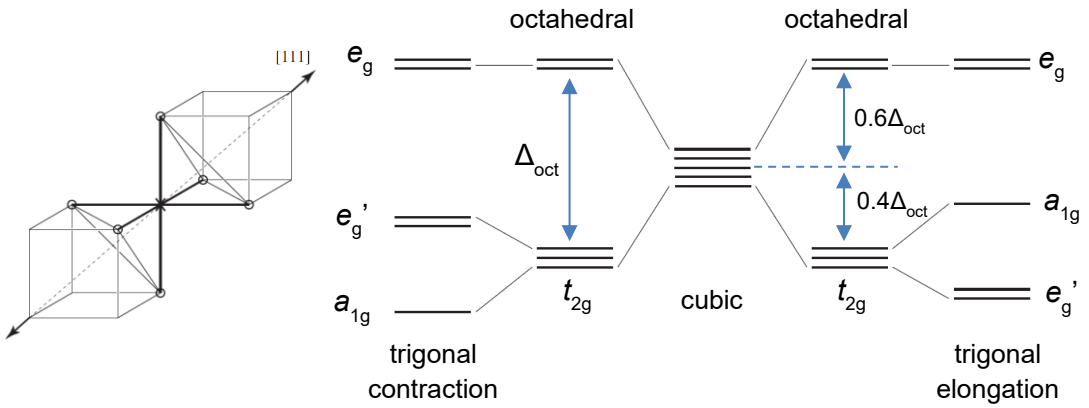

Figure 4-4. Trigonal distortion of the octahedron along the [111] direction (left) and the corresponding splitting of energy levels of d-orbitals (right). Adapted from [49].

The preference of transition metal cations for the octahedral sites is determined by the difference between the CFSE in octahedral and tetrahedral sites and is termed the octahedral site preference energy (OSPE). While OSPE suggests large octahedral affinity for, e.g., chromium ions Cr^{3+} and Cr^{2+} (157.8 and 71.1 kJ mol^{-1}, respectively), Mn^{3+} (95.4 kJ mol^{-1}), Ni^{2+} (86.2 kJ mol^{-1}) or Co^{3+} (79.5 kJ mol^{-1}), for Co^{2+} and Fe^{2+} it is smaller (31.0 and 16.7 kJ mol^{-1}, respectively). For metal ions with an empty (d^0; Ca^{2+}, Ti^{4+}, etc.), half-filled (d^5; Fe^{3+}, Mn^{2+}, etc.) or filled d-shell (d^{10}; Zn^{2+}, Ga^{3+}, etc.), OSPE reaches zero and their position, therefore, depends on the preferences of other ions in the structure [208].

Finally, let us note that the final distribution of electrons into d-orbitals must consider two competing tendencies: (i) the crystal field splitting, which aims to populate the lowest levels; and (ii) the Coulomb repulsion and exchange interactions, which comply with the Hund's first rule and aim to distribute electrons over as many d-orbitals as possible with parallel spins. The competition between the energy required to pair two electrons in the same orbital and the CFSE loss can lead to distinct electron configurations: the *low-spin* or *high-spin* configuration if the former or the latter is more favorable [208] (see an example of Fe^{2+} and Fe^{3+} configuration in octahedral coordination in Figure 4-5).

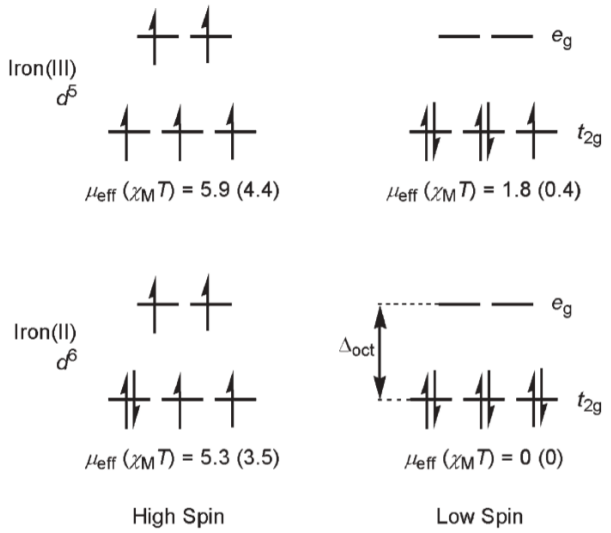

Figure 4-5. Occupancies of d-orbitals and typical effective magnetic moments in μ_B ($\chi_M T$ in cm^3 mol^{-1} K) in the high-spin and low-spin configuration of Fe^{3+} and Fe^{2+} in an octahedral crystal field. Reproduced from [209].

In the following section, we will describe in more detail the magnetic phases with the spinel structure that were studied within this thesis.

4.1.1 Mn-Zn and Co-Zn ferrites

The term ferrite in a narrow sense denotes any compound with a composition of $A^{II}Fe_2O_4$. As was discussed above, various degrees of inversion might occur depending on the character of the cations (e.g., CFSE) and the formation process of the material. The magnetic properties of these compounds highly depend on the delicate interplay of exchange interactions and the magnetic nature of the A cation. If A is magnetically active, the ferrite is usually ferrimagnetic – due to a strong

antiferromagnetic interaction between tetrahedral and octahedral sublattices, magnetic moments of the cations in the two sublattices are oriented antiparallel while they are parallel within each sublattice. Varying the composition of ferrites allows tuning their properties with regard to the intended application, for which the ternary ferrites, comprising two other elements in addition to iron, are particularly suitable. Tailoring the properties is facilitated by the fact that ferrites can form solid solutions with practically continuous composition between selected endmembers.

In this section, we will briefly introduce the endmembers of the series, whose members were studied in our work, namely $MnFe_2O_4$ (jacobsite, Figure 4-6a), $CoFe_2O_4$, and $ZnFe_2O_4$ (franklinite, Figure 4-6b,c). Formally, magnetite Fe_3O_4 also belongs to ferrites, however, it will be introduced in more detail in Section 4.1.2.

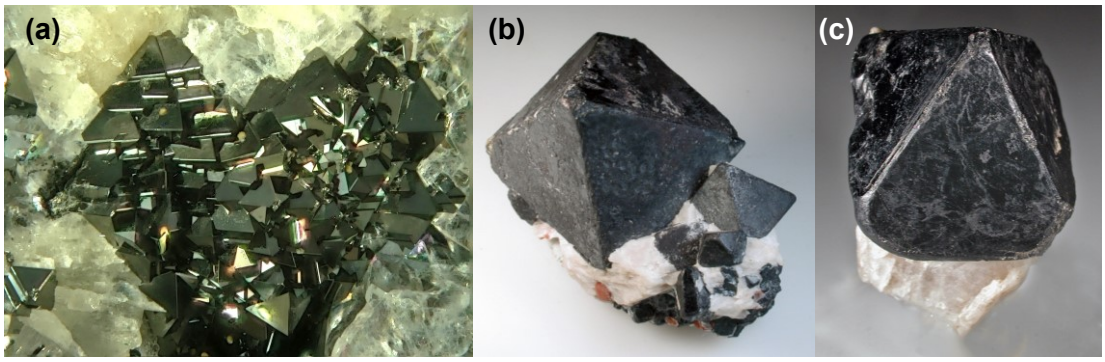

Figure 4-6. (a) Jacobsite crystals, the field of view 2.3 mm, Kuruman, South Africa (photograph by W. Windisch, released to the public domain); (b) franklinite in a marble matrix, the largest crystal with a size roughly 3.5 cm (corner-to-corner), Sterling Mine, USA (photograph by K. Nash, licensed under CC BY 3.0); (c) a franklinite crystal with dimensions 3.3 x 3.2 x 3.0 cm^3 on a calcite matrix, Franklin Mine, USA (photograph by K. Nash, licensed under CC BY 3.0). Photographs from [210,211].

Jacobsite, **$MnFe_2O_4$**, is believed to be predominantly a normal spinel, as confirmed from the lowest energy for this cation arrangement in DFT calculations [212], though the usual degree of inversion observed in single crystals is around $i \sim 0.2$ [213] and can be even higher for polycrystalline samples and especially nanoparticles. The lattice parameter is $a \sim 8.511$ Å [214] with variations depending on the actual stoichiometry and degree of inversion. Whereas the valence of atoms in the tetrahedral sites is Mn^{2+} and Fe^{3+}, both of which have the $3d^5$ electron configuration with $S = 5/2$, the valence states of cations at octahedral sites are less straightforward due to possible switching of valences to Mn^{3+} and Fe^{2+} [215]. Neither Mn^{2+} nor Fe^{3+} are Jahn-Teller-active ions so no transitions of the Verwey-type similar to magnetite are expected. Jacobsite is a ferrimagnet with the easy axis

of magnetization in the [111] direction and with Curie temperature ~470–570 K [216,217].

The **cobalt ferrite**, **$CoFe_2O_4$**, has an inverse spinel structure with Co^{2+} predominantly randomly distributed over the octahedral sites and $a \sim 8.39$ Å [218]. Since Co^{2+} has the $3d^7$ electron configuration, it participates in the magnetic interactions with $S = 3/2$. Cobalt ferrite has a collinear long-range ferrimagnetic order, possibly with a local spin canting, and high Curie temperature $T_C \sim 860$ K [219]. Its easy axis lies in the [100] direction, and the cobalt ferrite is characterized with large anisotropy energy compared to the other ferrites, ascribed to the Co^{2+} anisotropy in the low-symmetry environment, which arises from the distribution of Co^{2+} and Fe^{3+} over the nearest octahedral sites [220].

Franklinite, **$ZnFe_2O_4$**, is a normal spinel with $a \sim 8.447$ Å [214], in which the nonmagnetic Zn^{2+} with $3d^{10}$ electron configuration occupies mostly the tetrahedral sites, although a certain degree of inversion is also possible depending on the preparation procedure. In the ideal normal spinel, only weak superexchange interaction between Fe^{3+} in the octahedral sites applies, leading to a low temperature of antiferromagnetic ordering $T_N \sim 10$–13 K. In this case, the frustration effects related to the pyrochlore lattice formed by the octahedral sites play an important role in determining the magnetic ground state. Already far above T_N (at ~100 K), domains of a size ~3 nm with a short-range magnetic order are formed, which show signs of antiferromagnetic ordering at a larger scale. They have been evidenced only by methods with a sufficiently short time window, such as neutron methods or muon spin rotation, due to their fast fluctuations of the order of GHz [221]. Below T_N, the short-range and long-range order coexist at least down to 1.5 K, the former transforms into the latter upon decreasing the temperature, both being incommensurate [221]. Later, the observed long-range order was attributed to a chemical disorder since it was not found for single crystals of higher quality [222]. The neutron scattering experiments were interpreted in the framework of weak temperature-dependent interaction between Fe nearest neighbors J_1 competing with the antiferromagnetic interaction with the third neighbors J_3, leading possibly to a spin-liquid state [223,224]. Finally, a "spin molecule" model was proposed [225], in which Fe ions form spin dodecamers in the kagome plane (see Figure 4-7). In this model, the third-neighbor interactions are either antiferromagnetic for the superexchange path Fe–O–Fe–O–Fe with $J_3^{(Fe)}$, or ferromagnetic for the path Fe–O–Zn–O–Fe with $J_3^{(Zn)}$. Interestingly, the $J_3^{(Fe)}$ network forms diamond squares, which are not frustrated. The dodecamer then

originates by coupling the antiferromagnetic diamond subunits "as ferromagnetically as possible in accordance with the ferromagnetic J_1" [225].

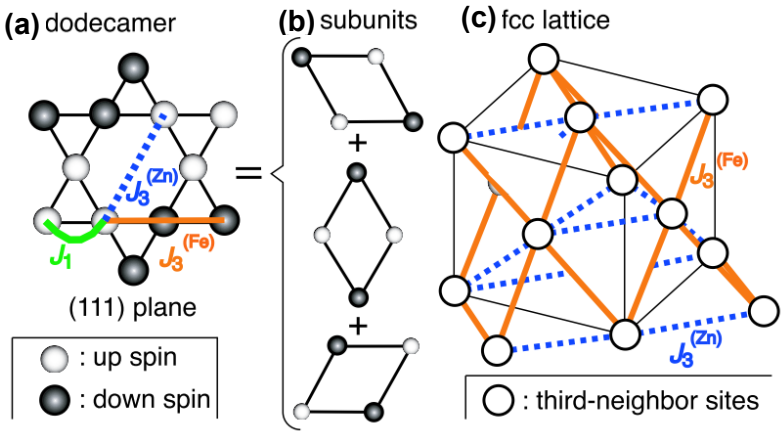

Figure 4-7. Dodecamer model of $ZnFe_2O_4$. The exchange interactions between nearest neighbors, J_1, and third neighbors via Fe and Zn, $J_3^{(Fe)}$ and $J_3^{(Zn)}$, are highlighted. In (a), the kagome star formed by Fe in the (111) plane is shown, formed by third-neighbor diamond subunits indicated in (b). The third-neighbor Fe sites form an fcc lattice, as indicated in (c). Reproduced from [225].

As already hinted above, the long-range magnetic order can evolve in nonideal crystals of $ZnFe_2O_4$ due to structural disorder, cation inversion, or O^{2-} defects. The defects might relieve the frustration or create new competing interaction paths, which might result in various spin arrangements, even ferrimagnetism [226]. In general, the ordering temperature increases with an increasing degree of inversion due to the strong antiferromagnetic interaction between Fe^{3+} in tetrahedral and octahedral sites. Naturally, the defects largely determine the magnetic state of $ZnFe_2O_4$ nanoparticles, which also tend to have a higher degree of cation inversion. As a consequence, the disorder in exchange interactions and magnetic dilution due to Zn^{2+} ions can result in the formation of, e.g., spin glass or spin-glass-like states in nanoparticle ensembles [227].

The **"magnetic dilution"** provided by diamagnetic ions such as Zn^{2+} can be used to increase the magnetization of the ferrimagnetic spinel ferrites – Zn^{2+} enters preferentially the tetrahedral site, decreasing the magnetization of the tetrahedral sublattice and increasing thus the overall magnetization. Through weakening the magnetic anisotropy, the incorporation of diamagnetic ions reduces both the coercive field and the Curie temperature, in the case of nanoparticles also the blocking temperature. We used the latter fact in our study on the influence of the magnetic state of Co-Zn ferrite nanoparticles on their performance in MRI [D10]. Solely by changing the ratio of Zn and Co, while keeping the size of the crystallites and the whole silica-coated particles practically the same, we shifted the onset of

the superparamagnetic state (see the ZFC-FC curves in Figure 2-14 and distribution of blocking temperatures in Figure 4-8a).

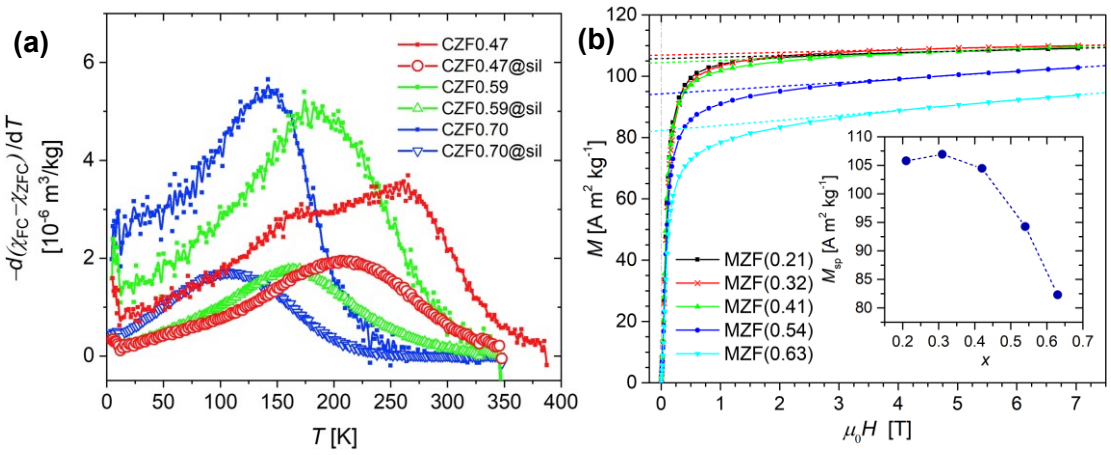

Figure 4-8. (a) Distribution of blocking temperatures from ZFC-FC curves (see Figure 2-14) of bare and silica-coated ("@sil") Co-Zn ferrite nanoparticles ($Co_yZn_xFe_{3-x-y}O_4$, $3–x–y = 1.86$, reproduced from [D10]); (b) virgin curves of Mn-Zn ferrite nanoparticles at 5 K, the spontaneous magnetization, obtained from extrapolation of high-field course to zero fields, is shown in the inset as a function of Zn content ($Mn_yZn_xFe_{3-x-y}O_4$, where $3–x–y = 1.94–1.99$; adapted from [O6]). The content of Zn, x, is indicated in sample codes.

Especially in the case of nanoparticles, each method of preparation requires finding the optimum doping with diamagnetic ions to maximize the magnetization because of the nonequilibrium cation distribution over the tetrahedral and octahedral sites. The diamagnetic ions break the superexchange interaction pathways, which decreases the predictability of the magnitude of the resulting magnetization at room temperature as well. Therefore, it is useful to examine magnetic properties and the distribution of cations in a series of similarly prepared particles differing in the doping level. In our study [O6] (under review at the time of writing the thesis and therefore excluded from the primary list of articles) with results partly referred to in [D2], we attempted to analyze the magnetic behavior of Mn-Zn ferrite nanoparticles ($Mn_zZn_xFe_{3-z-x}O_4$) prepared by the hydrothermal method in relation to the Zn content. A powerful combination of the ^{57}Fe Mössbauer spectroscopy and neutron diffraction enabled us to analyze the cation distribution for a selected sample with composition $Mn_{0.63}Zn_{0.40}Fe_{1.97}O_4$. The refined cation distribution $(Mn_{0.25}Zn_{0.28}Fe_{0.47})[Mn_{0.38}Zn_{0.12}Fe_{1.50}]O_4$ showed practically random occupation of both tetrahedral and octahedral sites with Mn and even though 1/3 of Zn atoms were in octahedral sites, which is not at all negligible, the result was still consistent with the preference of Zn for the tetrahedral sites. Such distribution suggests a nonequilibrium state due to the hydrothermal synthesis performed at a relatively

low temperature of 180 °C. Moreover, the presence of Zn in both sites can explain the nonmonotonous dependence of low-temperature spontaneous magnetization on the Zn doping with the maximum around $x \sim 0.3$, as shown in Figure 4-8b. The magnetic dilution effect was manifested by the more rapid decay of magnetization on increasing temperature for samples with higher Zn content, which was related to the onset of superparamagnetism.

4.1.2 Magnetite (Fe_3O_4)

Magnetite (see Figure 4-9) is one of the most abundant iron-bearing minerals on Earth and the one at the root of the discovery of magnetism in ancient Greece. It has an inverse spinel structure containing divalent iron atoms at octahedral sites, $(Fe^{3+})[Fe^{2+}Fe^{3+}]O_4$. More precisely, above the Verwey transition at $T_V \sim 120$ K, the electron of Fe^{2+} is delocalized over octahedral sites, leading to the effectively mixed valence of $Fe^{2.5+}$ in octahedral sites due to the fast electron hopping. At this state, magnetite has a cubic crystal structure of the high-symmetry $Fd\bar{3}m$ group. On the other hand, at T_V, charge separation at octahedral sites together with the Jahn-Teller distortion of the structure occurs. The distortion also reduces the symmetry of the structure to the monoclinic Cc group with the monoclinic angle $\beta \sim 90.2°$.

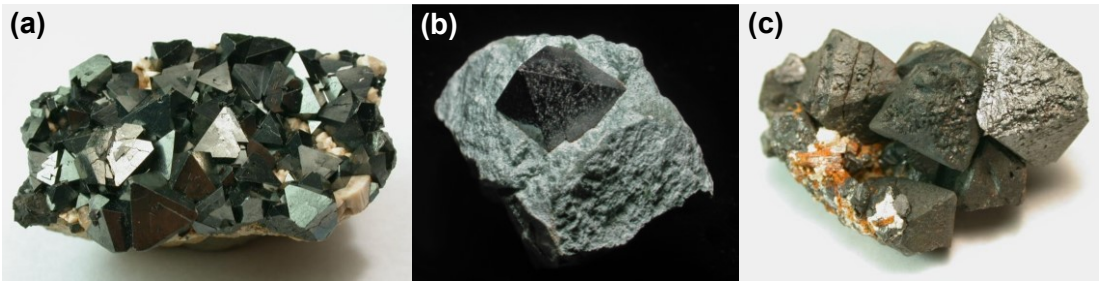

Figure 4-9. Magnetite: (a) a sample with dimensions roughly 4 cm x 2.6 cm in total, Cerro Huañaquino, Bolivia (photograph by J. Sobolewski, licensed under CC BY 3.0); (b) a 1.3 cm crystal on greenschist, Diamantina, Brazil (photograph by K. Nash, licensed under CC BY 3.0); (c) a sample with dimensions 4.4 cm x 2.4 cm, Spring Mountain Mining District, USA (photograph by J. Sobolewski, licensed under CC BY 3.0). Photographs from [228].

The physical nature of the Verwey transition rises questions even more than 80 years after its discovery. At low temperatures, magnetite is a Mott insulator with strongly correlated electrons, the Verwey transition being the first-order metal-to-insulator transition characterized by a sudden increase in resistivity upon cooling. Quite recently, a so-called trimeron model of the low-temperature magnetite structure has been proposed [229], in which charge localization occurs in the chains of three Fe in octahedral sites (see Figure 4-10). In such a chain, one Fe^{2+} donates the t_{2g} electron (minority-spin) density to two adjacent Fe^{3+} sites within

the trimeron, this charge transfer is accompanied by anomalous shortening of Fe-Fe bonds and accordingly also the displacement of oxygen atoms (see Figure 4-10b), and the formal oxidation state of Fe^{2+} sites rises to +2.4. Actually, the Fe^{3+} ions participate in a varying number of trimerons, and their formal oxidation state, remaining +3 only for two Fe^{3+} sites in the low-temperature unit cell which do not participate in any trimeron, decreases down to +2.4–2.6 for Fe^{3+} participating in three trimerons at the same time. Nevertheless, the distribution of the minority-spin density is different between the "Fe^{3+}" and "Fe^{2+}" sites, in which the high symmetry of the former and the orbital order of the latter are still preserved, which justifies using the formal values of +3 and +2 [229]. Although postulating the presence of trimerons also above T_V was tempting, short-range trimeron correlations above T_V have not been confirmed experimentally [230].

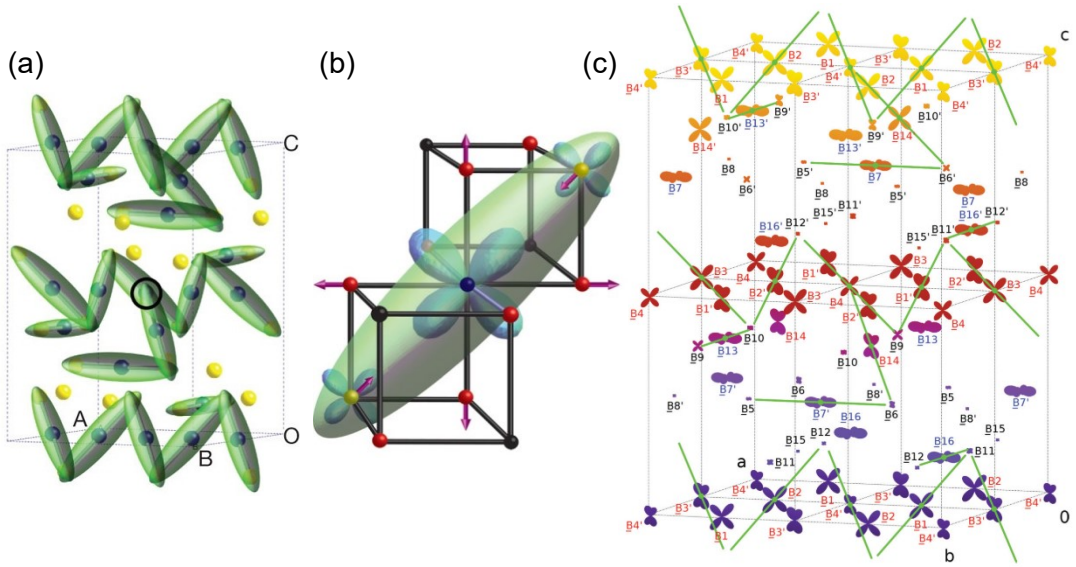

Figure 4-10. Low-temperature trimeron model at octahedral sites of magnetite: (a) structure showing trimeron chains (minority-spin electron density approximated by green ellipsoids), with Fe^{2+} marked in blue and Fe^{3+} in yellow, the black circle marks the only Fe^{2+} site being an end-member of a trimeron; (b) detailed view of a trimeron, atomic populations of the minority-spin electron are indicated by the size of t_{2g} orbitals shown in blue, the displacements of Fe and O (red) atoms are indicated by purple arrows; (c) minority-spin electron populations shown as angular dependence of electron density, trimerons marked with green lines. Pictures (a) and (b) reproduced from [229], (c) from [231].

Magnetite is a ferrimagnet with the Curie temperature of ~850 K. Interestingly, about 10 K above the Verwey temperature, T_S ~ 130 K, spin-reorientation occurs and the low-temperature easy axis of magnetization changes from the [100] to the [111] direction [232]. In this transition, the first magnetocrystalline anisotropy constant K_1 changes its sign from positive to negative upon heating (see Figure

2-5), therefore, T_S is sometimes referred to as the isotropy point [233]. This spin-reorientation transition produces a kink in temperature-variable magnetic data, which can be sometimes misinterpreted as the sign of the Verwey transition provided that no further confirmation by other methods (e.g., electric transport measurements) was done.

The Verwey transition is extremely sensitive to stoichiometry [234], which has led to conflicting reports in the literature. With increasing deviations δ from the ideal stoichiometry, $Fe_{3(1-\delta)}O_4$, T_V initially decreases (a linear dependence of T_V on δ was shown in [234]) and for larger deviations, the Verwey transition is suppressed [235]. Similar behavior was observed for doped magnetite, e.g., $Fe_{3-x}Ti_xO_4$ or $Zn_xFe_{3-x}O_4$. At around $3\delta = x \sim 0.012$, the nature of the Verwey transition changes from the first-order to the second-order transition, and the transition disappears for $3\delta = x > \sim 0.036$ [236]. By taking the example of $Zn_xFe_{3-x}O_4$, it was shown that in the doping range corresponding to the first-order transition, the lattice distortion due to the Verwey transition is practically constant with increasing x. However, in the higher range of doping, in which the transition is of the second order, the monoclinic distortion is much smaller and gradually diminishes with increasing doping. At the same time, the first-order transition is much sharper, whereas the second-order transition spreads over a broad range of temperatures [236,237].

The difficulties with controlling stoichiometry and sometimes even the lack of systematic effort to check the resulting stoichiometry have complicated the investigation of fundamental properties of magnetite nanoparticles. The degree of nonstoichiometry varies with the synthesis method and conditions, as well as with the size and shape of the particles. Therefore, it was often reported that the Verwey transition was absent in magnetite nanoparticles, and it was generally believed that it cannot occur even in stoichiometric particles below a certain size. Nevertheless, in the study on monodisperse particles with stoichiometry controlled by the CO/CO_2 atmosphere, J. Lee *et al.* [238] showed that the Verwey temperature was practically size-independent down to the size of particles ~20 nm, below which T_V decreased and the transition disappeared – at least in their case – for particles smaller than 6 nm. The authors also noticed that the disappearance of the Verwey transition coincided with the onset of superparamagnetism, i.e., the blocking temperature would fall below T_V for the smallest particles. However, in this study, no attention was devoted to shape anisotropy. Interestingly, A. Mitra *et al.* [239] demonstrated the presence of the Verwey transition for octahedral nanoparticles

of 6–14 nm in size and contrasted the data with similarly-sized (though probably less stoichiometric) spherical nanoparticles, for which the transition was absent.

Nevertheless, the absence of the monoclinic distortion, either due to nonstoichiometry or doping, preserves the cubic structure and facilitates thus the analysis of low-temperature data on magnetite nanoparticles by the probe methods which distinguish individual cation sites, such as Mössbauer and solid-state nuclear magnetic resonance (NMR) spectroscopy. Specifically, instead of 8 tetrahedral and 16 octahedral inequivalent iron sites in the monoclinic Cc structure, the cubic $Fd\bar{3}m$ structure contains only one tetrahedral and one (or two for charge-separated Fe^{2+}/Fe^{3+}) octahedral sites. Moreover, certain minority-spin electron localization allows us to distinguish between the Fe^{3+}-like and Fe^{2+}-like ions. We took considerable advantage of both phenomena in our Mössbauer analysis of Zn-doped magnetite nanoparticles (the mean size of crystallites from XRD 22 nm), trying to determine the actual stoichiometry and cation distribution over tetrahedral and octahedral sites [D8]. In this study, we showed that the nanoparticles prepared by the thermal decomposition method (sample "ZF") were stoichiometric magnetite with nonequilibrium cation distribution $(Fe^{3+}_{0.81}Zn^{2+}_{0.19})[Fe^{3+}_{1.19}Fe^{2+}_{0.63}Zn^{2+}_{0.18}]O_4$. During the subsequent pyrolysis of surfactants by thermal treatment of the nanoparticles at 500 °C for 2 h under argon flow, a carbon layer was formed at the surface of the nanoparticles (sample "ZF@C"). At the same time, a redistribution of cations towards the equilibrium took place, accompanied by slight oxidation and formation of vacancies ▢. The final stoichiometry was refined to $(Fe^{3+}_{0.72}Zn^{2+}_{0.28})[Fe^{3+}_{1.41}Fe^{2+}_{0.44}Zn^{2+}_{0.08}▢_{0.07}]O_4$. The respective ^{57}Fe Mössbauer spectra and hyperfine parameters of both samples are shown in Figure 4-11 and Table 4-1. In our model, each Fe site was fitted by two sextets to account for the distribution of Zn (and possibly cation vacancies) in the second coordination sphere.

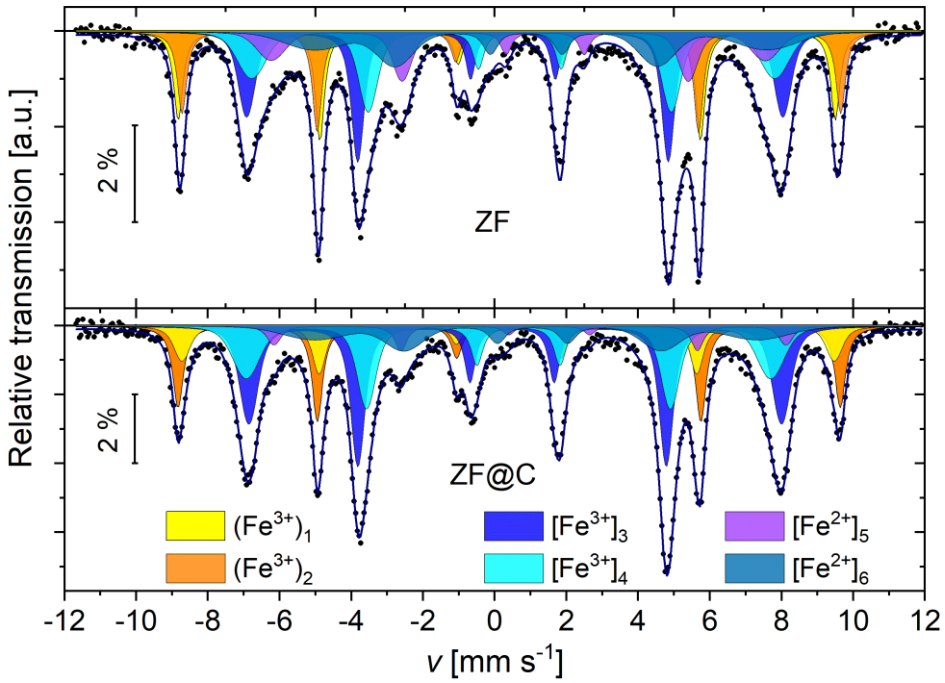

Figure 4-11. ^{57}Fe Mössbauer spectra of the as-prepared (ZF) and thermally treated (ZF@C, with a carbon layer at the surface) Zn-doped magnetite nanoparticles at 4.2 K and 6 T, which enabled us to refine their stoichiometry. Adapted from [D8].

Table 4-1. Hyperfine parameters from the fits of ^{57}Fe Mössbauer spectra of the ZF and ZF@C samples at 4.2 K in the magnetic field of B_{ext} = 6 T: δ – isomer shift, ε – quadrupole shift, B_{eff} – the effective hyperfine magnetic field ($\boldsymbol{B}_{eff} = \boldsymbol{B}_{hf} + \boldsymbol{B}_{ext}$, $\boldsymbol{B}_{hf}$ being the hyperfine field at the ^{57}Fe nuclei), A – the area fraction of the given component, () or [] denote the tetrahedral or octahedral sites, respectively. Data from [D8].

Sample	Component	δ [mm s^{-1}]	2ε [mm s^{-1}]	B_{eff} [T]	A
ZF	$(Fe^{3+})_1$	0.38(2)	-0.10(4)	56.9(2)	0.158(8)
	$(Fe^{3+})_2$	0.41(3)	0.10(4)	57.1(2)	0.15(2)
	$[Fe^{3+}]_3$	0.53(3)	0.05(3)	46.5(3)	0.24(2)
	$[Fe^{3+}]_4$	0.60(4)	-0.18(5)	45.3(4)	0.20(2)
	$[Fe^{2+}]_5$	1.03(4)	-0.75(7)	42.8(3)	0.12(1)
	$[Fe^{2+}]_6$	1.08(6)	0.4(1)	39.2(7)	0.14(2)
ZF@C	$(Fe^{3+})_1$	0.37(3)	0.00(4)	56.5(5)	0.10(5)
	$(Fe^{3+})_2$	0.41(2)	0.00(3)	57.4(2)	0.18(2)
	$[Fe^{3+}]_3$	0.53(3)	0.09(4)	46.2(2)	0.32(5)
	$[Fe^{3+}]_4$	0.52(3)	-0.28(6)	45.5(3)	0.23(4)
	$[Fe^{2+}]_5$	1.25(4)	-0.53(6)	44.4(4)	0.05(1)
	$[Fe^{2+}]_6$	1.10(6)	0.10(9)	38.4(6)	0.12(3)

4.1.3 Maghemite (γ-Fe_2O_3)

Maghemite (see Figure 4-12) is one of the five polymorphs of iron(III) oxide identified so far that can exist at ambient conditions. Besides ε-Fe_2O_3, to which we dedicate Section 4.2, and the thermodynamically most stable hematite, which was briefly mentioned in Section 2.3, two other polymorphs are known: the rare cubic β-Fe_2O_3 with the bixbyite structure [240,241] and monoclinic ζ-Fe_2O_3, which forms from β-Fe_2O_3 at high pressures and is also kinetically stable under ambient conditions [242]. Maghemite is structurally related to magnetite, in which the oxidation of Fe^{2+} to Fe^{3+} has to be compensated by cation vacancies to preserve electric neutrality. To better reflect the relation to the canonical spinel structure, the formula of maghemite was redefined by the International Mineralogical Association from Fe_2O_3 to $(Fe_{0.67}\square_{0.33})Fe_2O_4$, where □ marks a cation vacancy [200]. Nevertheless, a continuum of intermediate phases between magnetite and maghemite can exist due to incomplete oxidation and can be described by the general formula $Fe^{2+}_{1-3\delta}\square_{\delta}Fe^{3+}_{2(1+\delta)}O_4$ (this formula with $Fe^{2+} \rightarrow A^{2+}$, $Fe^{3+} \rightarrow B^{3+}$ is valid for any defective 2-3 spinel) [204].

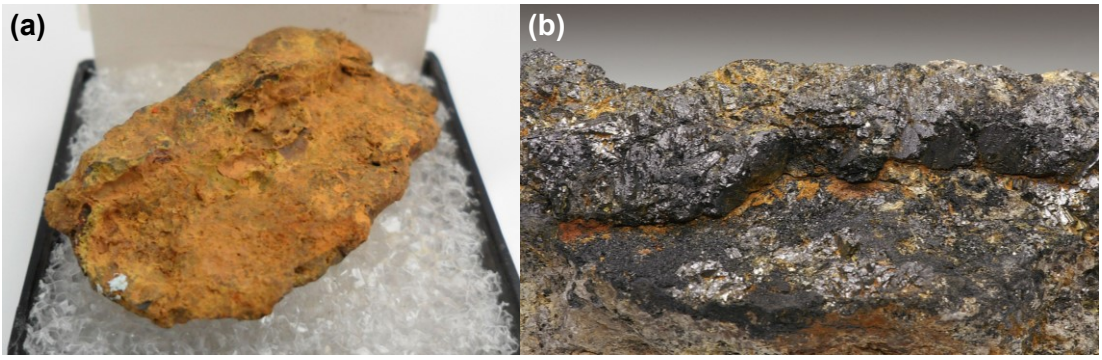

Figure 4-12. Maghemite: (a) maghemite often forms crusts on other minerals, Gancedo, Argentina (photograph by Rodrigosiev, licensed under CC BY-SA 3.0, cropped); (b) crust of brownish maghemite with black magnetite on gneiss, the field of view 5 cm, Hewitt Gem Quarry, USA (photograph by H. Moritz, licensed under CC BY-NC-SA 3.0, cropped). Photographs from [243,244].

For several decades, a certain ambiguity regarding the space group of maghemite prevailed, related to a certain degree of vacancy ordering in octahedral sites, and it was shown that experiments using powder samples provided inconsistent results due to material inhomogeneity [245]. Finally, the single-crystal electron diffraction shed more light on this issue. Depending on the degree of vacancy ordering, the space group of maghemite can range from the disordered cubic $Fd\bar{3}m$ with $a = 8.34$ Å, via an intermediate cubic enantiomorphous pair $P4_132/P4_332$ with partial vacancy ordering and a similar lattice parameter, to the tetragonal enantiomorphous pair $P4_12_12/P4_32_12$ with completely ordered vacancies

resulting in a tripled unit cell with a = 8.347 Å and c = 25.01 Å [246]. The group-subgroup relations of the disordered cubic and the ordered tetragonal structures are depicted and further discussed in [247].

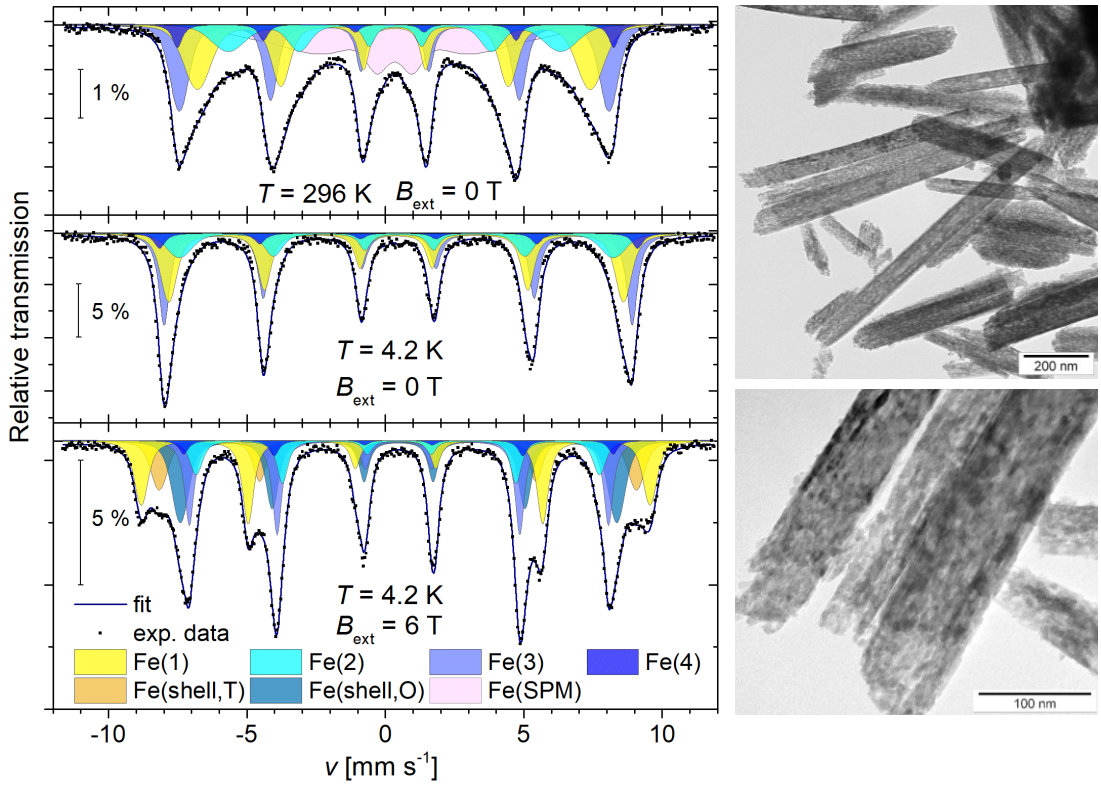

Figure 4-13. ^{57}Fe Mössbauer spectra (left) of nanocrystalline maghemite rods (right) prepared from an akaganeite precursor, fitted by the averaged model for the $P4_32_12$ space group; hyperfine parameters are provided in Table 4-2. Components representing tetrahedral sites are shown in yellow, octahedral sites in blue, Fe(4) represents the site with 33 % occupancy by Fe (and 66 % by vacancies). At room temperature, superparamagnetic relaxation manifests in the spectrum and Fe(SPM) characterizes the particles with the Néel time comparable to the characteristic time of the method. The core-shell model for the interior and the surface of the particles was used to interpret the in-field spectrum, all octahedral sites in the shell were approximated by one component. Partly adapted from [D4].

Vacancy ordering in maghemite nanoparticles was another topic examined as a part of this thesis. In our study [D4] on nanocrystalline maghemite rods prepared via akaganeite precursor under hydrothermal conditions, a certain degree of vacancy ordering was suggested from powder XRD patterns showing a superstructure diffraction peak. Several models were tested for fitting the Mössbauer data, describing different space groups of maghemite by adjusting the number and occupation of nonequivalent Fe sites and the number of vacancies among their nearest-neighbor sites. The best fit (see Figure 4-13 for spectra and Table 4-2 for hyperfine parameters) was obtained with the approximative model of the ordered

phase by Greaves [248], who used a subcell of the tripled $P4_32_12$ unit cell with 33 % occupancy of the appropriate sites for refinement of his powder neutron diffraction data. Such simplification largely reduces the number of nonequivalent iron sites (from nine to four) and thereby free parameters in the fitting procedure. The refinement of the XRD pattern with the $P4_32_12$ tetragonal structure provided lattice parameters $a = 8.327(5)$ Å and $c = 25.13(3)$ Å and size of crystallites 10–20 nm.

Table 4-2. Hyperfine parameters obtained from the Mössbauer spectra of maghemite rods in Figure 4-13. Fe(1) is the tetrahedral site and Fe(2)-Fe(4) are the octahedral sites, the Fe(SPM) component affected by the superparamagnetic relaxation is characterized by a broad distribution of magnetic hyperfine fields. Fixed parameters are marked by an asterisk. Data from [D4].

Conditions	Component	δ [mm s^{-1}]	2ε [mm s^{-1}]	B_{eff} [T]	A
T = 296 K B_{ext} = 0 T	Fe(1)	0.32(2)	-0.03(3)	44.1(3)	0.274*
	Fe(2)	0.35(3)	-0.04(4)	37.3(4)	0.137*
	Fe(3)	0.33(2)	0.03(3)	48.2(2)	0.274*
	Fe(4)	0.26(3)	0.21(4)	49.0(3)	0.046*
	Fe(SPM)	0.34(6)	-	-	0.27(1)
T = 4.2 K B_{ext} = 0 T	Fe(1)	0.39(2)	0.00(3)	51.0(3)	0.375*
	Fe(2)	0.45(3)	-0.10(5)	48.7(4)	0.1875*
	Fe(3)	0.47(2)	-0.04(3)	52.7(2)	0.375*
	Fe(4)	0.37(2)	0.21(6)	53.6(4)	0.0625*
T = 4.2 K B_{ext} = 6 T	Fe(1)	0.37(2)	0.01(3)	57.0(3)	0.217(5)
	Fe(2)	0.48(3)	-0.05(3)	45.4(3)	0.109(3)
	Fe(3)	0.49(2)	0.02(3)	47.1(2)	0.217(5)
	Fe(4)	0.37(5)	-0.04(6)	47.3(5)	0.036(1)
	Fe(shell,T)	0.45(3)	0.00*	53.5(3)	0.158(5)
	Fe(shell,O)	0.48(3)	0.00*	48.9(3)	0.26(2)

Finally, since the XRD patterns of both magnetite and maghemite with disordered vacancies are difficult to distinguish, Mössbauer spectroscopy offers an invaluable tool that enables determining the degree of oxidation of the prepared material, especially for nanoparticles. In our experience, many published reports on "magnetite" nanoparticles lack any estimation of the Fe^{2+} content in their samples and, in fact, most probably deal with ill-defined oxidized materials of a general stoichiometry Fe_xO_y or possibly even pure maghemite.

Similarly to other discussed spinel-type compounds, maghemite has a ferrimagnetic structure with the antiparallel ordering of spins in tetrahedral and octahedral sites. Its Curie temperature is difficult to obtain experimentally because maghemite tends to transform to hematite at temperatures around 700–800 K (or even at lower temperatures depending on the size of the particles), and T_C was estimated to lie somewhere between 820–986 K [246]. In a simplified view (see Section 2 for a more complicated view), nanoparticles of γ-Fe_2O_3 are often superparamagnetic at room temperature and form the basis of most so-called SPIONs ("superparamagnetic iron oxide nanoparticles") and USPIONs ("ultra-small" SPIONs) employed in the biomedical research.

4.1.4 Greigite (Fe_3S_4)

Finally, we will mention here the thiospinel analog of magnetite, greigite (Fe_3S_4, see Figure 4-14). Though its existence was expected, it was discovered in nature just in 1964, in lacustrine sediments in California [251]. Similarly to magnetite, greigite has an inverse spinel structure and its lattice is described by the $Fd\bar{3}m$ group. Nevertheless, before introducing the differences between both compounds, it will be illustrative to provide an idea about what it means to change the oxygen anions for sulfur.

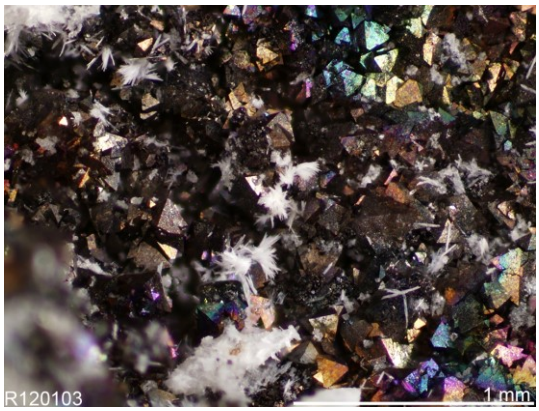

Figure 4-14. Small greigite octahedra, Alacrán mine, Chile (photograph by B. Jenkins, available in the RRUF database [249]). Photograph from [250].

Sulfur has a moderate electronegativity of 2.58 compared to 3.44 of oxygen, a larger Shannon effective ionic radius of 1.84 Å compared to 1.40 Å of O^{2-} and 2.6 times higher electric polarizability, i.e., $11.3 \cdot 10^{-40}$ C m^2 V^{-1} (10.2 Å^3) and $4.3 \cdot 10^{-40}$ C m^2 V^{-1} (3.88 Å^3) for S^{2-} and O^{2-}, respectively [252]. The polarizability, which describes the ability to displace the electron cloud with respect to the nucleus, is directly connected to the degree of covalence – higher polarizability of more loosely bound outer electrons of the larger S^{2-} anion results in bonding with a higher degree of covalence. Importantly, in contrast to transition metal oxides, 3d-electrons in transition metal sulfides can be partially or predominantly delocalized. For a suitable covalent mixing of the Fe–S bond, the coexistence of localized majority-spin d-electrons with itinerant minority-spin d-electrons is possible, as in the case of the Fe^{2+} with $3d^6$ configuration [253]. Due to the facile formation of the S–S bond, the sulfide stoichiometry is flexible with regard to

cation-deficiency, and nonstoichiometric compounds are easily formed. This, together with the higher degree of covalence and possible delocalization of d-electrons can even result in an ambiguous oxidation state of the transition metals.

The physical properties of greigite are not entirely settled since not only is it difficult to obtain pure and defect-free samples from the synthesis, but greigite is also prone to oxidation in air and easily decomposes at elevated temperatures [254]. It is a collinear ferrimagnet with the Curie temperature estimated from extrapolated dependences somewhere in the range of 590–800 K, though it probably starts to decompose somewhere around 500 K [252]. According to Mössbauer spectroscopy results, the tetrahedral sites are occupied by predominantly "Fe^{3+}" atoms, whereas fast electron hopping between the "Fe^{2+}" and "Fe^{3+}" leads to a mixed valence in the octahedral sites. Moreover, Mössbauer isomer shift points to partial charge transfer from octahedral sites to tetrahedral sites by superexchange [255]. Compared to magnetite, greigite has by $\sim 1/3$ smaller magnetization (~ 60 vs. ~ 90 A m^2 kg^{-1}) [256], which can be ascribed to the covalence effects and delocalization of d-electrons which contribute to σ-bonding between Fe and S [255]. It has also a much weaker exchange interaction between the magnetic sublattices than magnetite, resulting in different temperature dependences of the sublattice magnetization. No Verwey-like transition has been observed in greigite and no consensus has been accepted yet whether the transition should exist in perfect single crystals. Either all samples under previous studies have been "imperfect" so far (which might indeed be the case considering the difficulties mentioned above), or the lack of the Verwey-like transition is the inherent property of greigite itself. Even theoretical predictions do not provide a consistent view [257,258].

It is generally believed that the easy axis of magnetization lies in the [100] direction based on [259], though it seems that it has not been verified experimentally since then. In our study [D12], we used temperature-dependent Mössbauer spectra to analyze the direction of the easy axis and to check for the potential existence of the Verwey and spin-reorientation transitions in hydrothermally prepared nanocrystalline greigite (see Figure 3-5c for a TEM picture, Figure 4-15a–c for selected Mössbauer spectra and Table 4-3 for the values of their hyperfine parameters, Figure 4-15d–f shows the temperature dependences of hyperfine parameters of greigite components). The quadrupole shift ε of the Zeeman-split spectra depends as $\varepsilon \propto C(3\cos^2\vartheta - 1)$ on the angle ϑ between the local symmetry axis, which lies along the $\langle 111 \rangle$ directions in the octahedral sites of the spinel structure, and the local hyperfine magnetic field, which is antiparallel to the Fe

magnetic moment. Consequently, considering also the angular anisotropy of the hyperfine magnetic field, the sets of hyperfine parameters differ for ^{57}Fe nuclei with different orientations of the atomic magnetic moment with respect to the local symmetry axis. While these considerations do not manifest in the highly symmetrical tetrahedral sites, the spectral components of Fe in octahedral sites should, in principle, allow us to determine the easy axis of magnetization. If magnetic moments $\boldsymbol{m_0}$ are oriented parallel to one of the main crystallographic directions in the cubic cell, three different situations (and thereby three fitting models of the Mössbauer spectra) are possible. In the first case, $\boldsymbol{m_0} \parallel \langle 001 \rangle$, where ϑ = 54.74° for all Fe sites, $\varepsilon = 0$ and only one component for all octahedral sites is present in the spectrum. In the second situation, $\boldsymbol{m_0} \parallel \langle 011 \rangle$, in which case half of the Fe atoms have ϑ_1 = 90° and the other half ϑ_2 = 35.26°, resulting in two components with intensity ratio 2 : 2 and ε ratio $-C : C$. Finally, $\boldsymbol{m_0} \parallel \langle 111 \rangle$ means that a quarter of Fe atoms in octahedral sites have a parallel magnetic moment to the local axis ϑ_1 = 0° and for the rest ϑ_2 = 70.52°, therefore, the spectrum can be fitted with two components with intensities 1 : 3 and ε ratio $2C : (-\frac{2}{3}C)$. Our spectra did not support the first scenario, suggesting that the easy axis in our samples was other than along ⟨001⟩. By comparing the fits based on the two latter models, we concluded that a spin-reorientation transition probably takes place near ~100 K, during which the easy axis changes from the low-temperature ⟨111⟩ direction to ⟨011⟩ above ~100 K, which manifests in the quadrupole shift of the octahedral sites (see Figure 4-15e). Nevertheless, the spectral lines of the nanocrystalline material are broader than in the case of bulk samples, and a similar study performed on well-defined samples with larger grains would be required to confirm our findings. Finally, we did not observe any Verwey-like transition accompanied by a charge localization, which would have been evidenced by an abrupt change in the isomer shift of the components of octahedral sites (see Figure 4-15d).

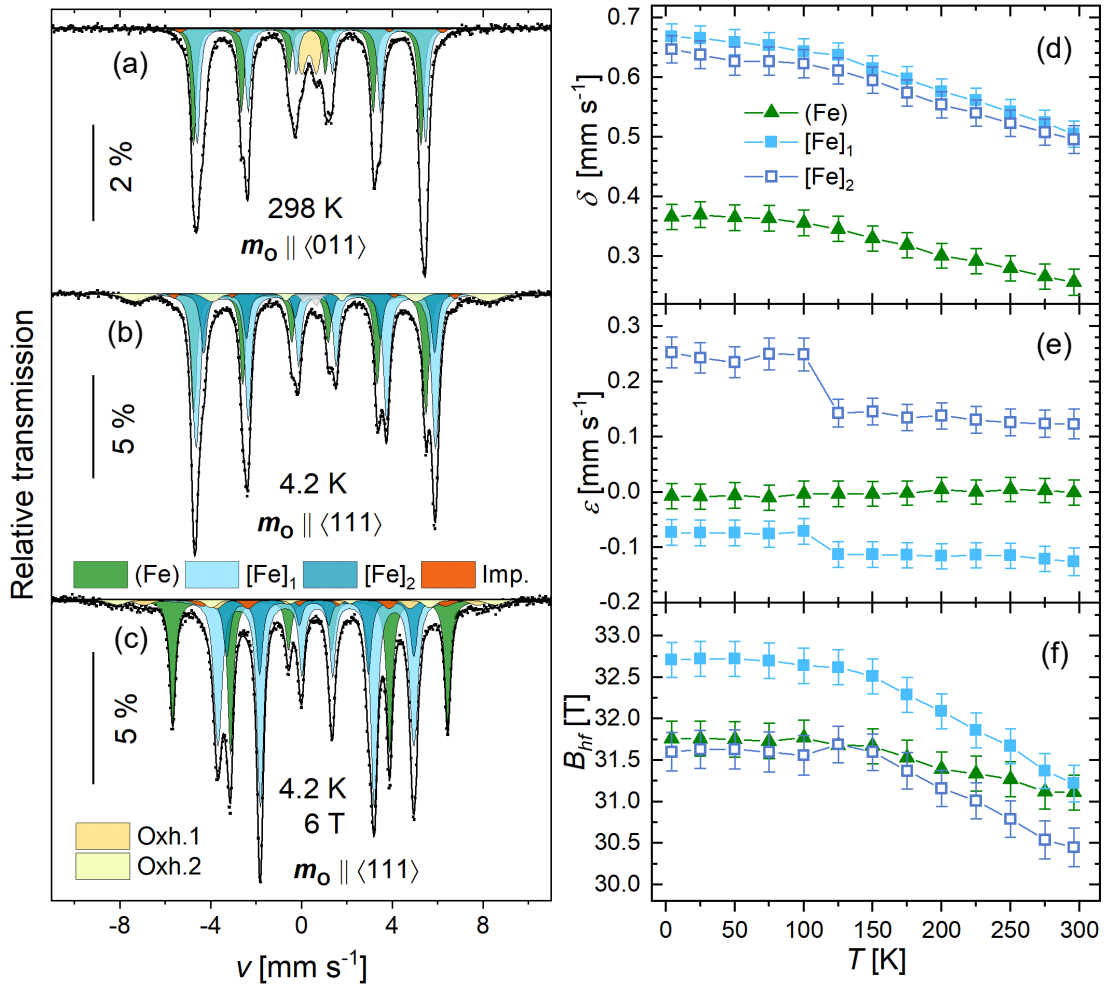

Figure 4-15. ^{57}Fe Mössbauer spectra of hydrothermally prepared nanocrystalline greigite at (a) room temperature where $\boldsymbol{m_o} \parallel \langle 011 \rangle$, (b) at 4.2 K in zero fields and (c) at 4.2 K and 6 T, where $\boldsymbol{m_o} \parallel \langle 111 \rangle$, with individual tetrahedral (Fe) and octahedral [Fe]$_i$ components of greigite and other impurities (mostly oxyhydroxides – Oxh.); the respective hyperfine parameters and areas of impurity components are provided in Table 4-3. Temperature dependence of (d) the isomer shift, (e) quadrupole shift and (f) hyperfine field of greigite components. Adapted from [D12].

Table 4-3. Hyperfine parameters of the Mössbauer spectra in Figure 4-15 of nanocrystalline greigite, data from [D12].

Conditions	Component	δ [mm s^{-1}]	2ε [mm s^{-1}]	B_{eff} [T]	A [%]
T = 296 K B_{ext} = 0 T $\boldsymbol{m_0} \parallel \langle 011 \rangle$	(Fe)	0.26(2)	0.00(3)	31.1(2)	30
	$[Fe]_1$	0.50(2)	-0.13(3)	31.2(2)	30
	$[Fe]_2$	0.50(2)	0.12(3)	30.5(2)	30
	Imp.	0.48(5)	-0.08(8)	35.8(5)	2
	Oxh.1+2	0.34(3)	0.64(4)	0	9
T = 4 K B_{ext} = 0 T $\boldsymbol{m_0} \parallel \langle 111 \rangle$	(Fe)	0.37(2)	-0.01(2)	31.8(2)	31
	$[Fe]_1$	0.67(2)	-0.07(2)	32.7(2)	46
	$[Fe]_2$	0.65(2)	0.25(3)	31.6(2)	15
	Imp.	0.54(4)	0.05(7)	38.4(4)	1
	Oxh.1+2	0.51(4)	-0.09(6)	48.3(4)	6
	Al-foil	0.39(4)	0.56(6)	0	1
T = 4 K B_{ext} = 6 T $\boldsymbol{m_0} \parallel \langle 111 \rangle$	(Fe)	0.38(2)	0.00(2)	37.6(2)	31
	$[Fe]_1$	0.67(2)	-0.06(3)	26.9(2)	46
	$[Fe]_2$	0.69(2)	0.28(4)	25.6(3)	15
	Imp.	0.87(7)	0.2(1)	33.3(6)	3
	Oxh.1	0.47(7)	-0.1(1)	45.8(6)	3
	Oxh.2	0.52(7)	-0.6(1)	51.6(7)	3

4.2 ε-Fe_2O_3

Leaving the compounds of the spinel type behind, we will move to materials of other structure types. Particular attention in pursuance of this thesis was devoted to the orthorhombic polymorph of iron(III) oxide, ε-Fe_2O_3, and its doped counterparts especially with regard to their magnetic properties and potential application as MRI contrast agents. Actually, ε-Fe_2O_3 remains in the blocked state at ambient temperature even in the nanosized form, and thus its nanoparticles behave as "nanomagnets".

The thermodynamically metastable ε-Fe_2O_3 crystallizes in the noncentrosymmetric $Pna2_1$ space group (see Figure 4-16), which is favorable for the manifestation of multiferroic properties – it is isomorphous to, e.g., $FeGaO_3$ and $AlFeO_3$, well-known multiferroics with large spontaneous magnetization, magnetoelectric coupling, and piezoelectric properties [260,261].

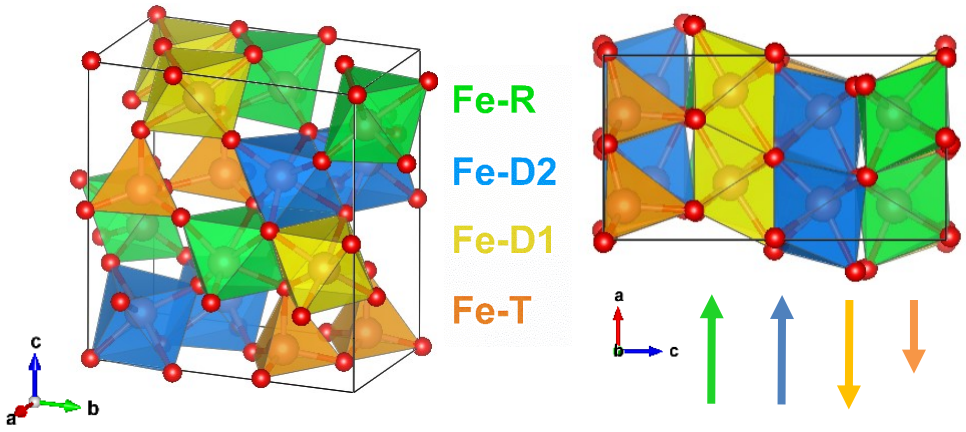

Figure 4-16. The orthorhombic unit cell of ε-Fe_2O_3 comprising 8 formula units, with four inequivalent Fe sites (distinguished by different colors) and ferrimagnetic ordering of Fe magnetic moments along the *a*-axis, whose directions and magnitudes are indicated by the arrows. Oxygen anions are shown in red.

Although the synthetic ε-Fe_2O_3 was first found already in 1934 [262] and named by Schrader and Buttner in 1963 [263], it was encountered only rarely in synthetic mixtures along with maghemite and hematite. Since the turn of the 21st century, with improved synthesis methods providing samples with higher purity, the epsilon polymorph has attracted considerable attention due to its giant coercivity and multiferroic behavior. Due to its low surface energy, which stabilizes ε-Fe_2O_3 and averts the formation of hematite below a certain size, ε-Fe_2O_3 has been prepared only in structures of reduced dimensions as nanoparticles [264], nanorods [265] and nanowires [266], and thin layers [267]. Moreover, in 2016, a new nano-mineral luogufengite analogous to ε-Fe_2O_3 was discovered in basaltic scoria from Idaho [268] (see Figure 4-17).

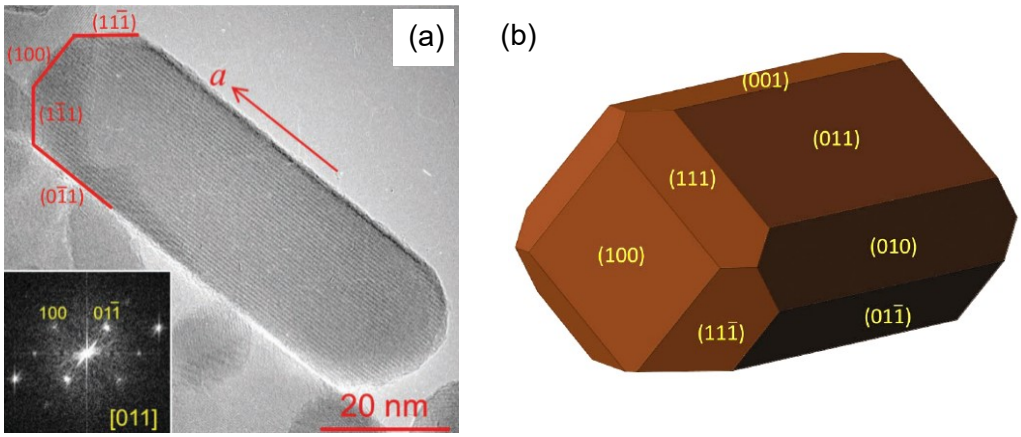

Figure 4-17. Luogufengite from basaltic scoria, Menan Volcanic Complex (USA): (a) HRTEM image of a luogufengite nanorod elongated along the *a*-axis, (b) ideal crystal morphology proposed based on HRTEM images. Adapted from [268].

The structure of ε-Fe_2O_3 consists of a combined hexagonal and cubic close-packed network of oxygen anions, which are supplemented with four crystallographically inequivalent Fe^{3+} sites, three of which are octahedral (Fe-D1, Fe-D2, Fe-R) and one tetrahedral (Fe-T). The four Fe sites form four magnetic sublattices, with magnetic moments oriented along the *a*-axis with magnitudes –3.9 μ_B, 3.9 μ_B, 3.7 μ_B and – 2.4 μ_B, respectively (according to [269] at 200 K). The predominant view is that at room temperature up to the Curie temperature of ~490–500 K, ε-Fe_2O_3 is a collinear ferrimagnet, though some canting or fluctuations of the moment of the tetrahedral sites were hypothesized to explain its somewhat lower value. The fluctuations would be, however, in contradiction to Mössbauer spectroscopy results, in which the tetrahedral site is distinguished by a decreased hyperfine field by ~19 T compared to octahedral sites, while having only slightly broader spectral lines [O1],[D3] (for a room-temperature Mössbauer spectrum see Figure 4-18 and Table 4-4 for the respective hyperfine parameters). Interestingly, a nonzero orbital component of the magnetic moment of the Fe^{3+} was reported [270], which was ascribed to the distortion of coordination polyhedra inducing a significant orbital mixing of 2p of oxygen and 3d of iron ions and charge transfer between them, producing the Fe electron configuration $3d^{5+q}$ [271]. The transferred charge *q*, together with ligand field effects and distortion of the polyhedra, then lifts the orbital degeneracy and leads to an orbital moment along the *a*-axis, which becomes the easy axis of magnetization due to a significant spin-orbit coupling [270]. The spin-orbit coupling induces large magnetocrystalline anisotropy $K \sim 5 \cdot 10^5$ J m^{-3} and results in a giant coercive field of ~2.1 T in the nanoparticles at room temperature [270],[D3]. The nanoparticles are single-domain and in the blocked state, which has captured the attention for their prospective application in magnetic recording media.

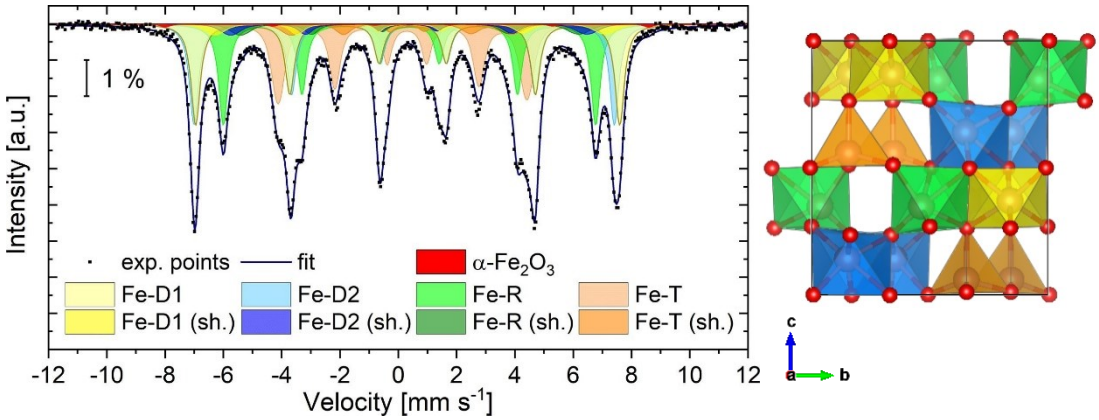

Figure 4-18. ^{57}Fe Mössbauer spectrum of ε-Fe_2O_3 nanoparticles at 296 K fitted by the core-shell model ("sh." mark shell components, the hyperfine parameters are summarized in Table 4-4; reproduced from [D3]) and the ε-Fe_2O_3 structure with corresponding colors of the individual Fe sites.

Table 4-4. Hyperfine parameters of ε-Fe_2O_3 nanoparticles obtained from the ^{57}Fe Mössbauer spectrum at 296 K (see Figure 4-18) fitted by the core-shell model. The intensities of core and shell components of individual Fe sites were fixed to be identical, the isomer shift of shell components was fixed to correspond to the respective core components, the quadrupole shift of the shell was assumed zero. Data from [D3].

Component	core				shell			
	δ [mm s^{-1}]	2ε [mm s^{-1}]	B_{eff} [T]	A [%]	δ [mm s^{-1}]	2ε [mm s^{-1}]	B_{eff} [T]	A [%]
ε-Fe_2O_3								
Fe-D1	0.41(3)	-0.17(4)	45.2(3)	21	0.41	0	41.6(5)	4
Fe-D2	0.36(3)	-0.32(4)	44.8(3)	21	0.36	0	38.0(6)	4
Fe-R	0.39(2)	-0.01(2)	39.7(2)	21	0.39	0	36.1(6)	4
Fe-T	0.22(2)	-0.15(3)	26.5(2)	21	0.21	0	23.4(5)	4
α-Fe_2O_3	0.40(2)	-0.21(2)	51.7(2)	0.4	-	-	-	-

Upon cooling, ε-Fe_2O_3 undergoes a two-step magnetic transition at temperatures ~150–80 K, manifested by a rapid decrease of magnetization and collapse of coercivity. It was interpreted as a second-order structural transition, in which the coordination polyhedra of Fe-D1 and Fe-T simultaneously distort accompanied by a small contraction of the lattice parameter c [270]. The Fe-T—O bond length increases, which reduces the charge transfer from O 2p to e_g d-orbitals of Fe-T. This transition is associated with a significant reduction of the orbital moment weakening the spin-orbit interaction and thereby also the magnetocrystalline anisotropy [270]. At the same time, the collinear commensurate magnetic structure

transforms to an incommensurate one, probably a square-wave-modulated structure [269] or a spiral structure [272]. Possibly, the decrease in anisotropy might lead to the increase of the domain-wall width that can extend beyond the particle size, from which the incommensurate magnetic state, or other inhomogeneous states such as the vortex state, can emerge [273,274].

When cooling the system below the transition temperature, the magnetic structure becomes stable at ~50 K [272], the orbital moment is restored and the anisotropy along with the coercive field increase again, though not as high as are the room-temperature values.

In our studies, we also devoted considerable attention to the low-temperature magnetic transition of ε-Fe_2O_3 by using Mössbauer spectroscopy [O1] and magnetization measurements [D3]. The temperature dependence of hyperfine parameters of individual Fe sites of ε-Fe_2O_3 is shown in Figure 4-19. The irregularities in the Fe-T isomer shift during the transition reflect the modifications in the Fe-T—O charge transfer. The changes in the quadrupole shift manifest the orientation of Fe magnetic moments with respect to the principal axes of the local EFG tensor, which can originate in the reorientation of either the magnetic moments or principal axes of the EFG tensor due to the site distortions (or both). The magnetic hyperfine field of Fe-T at temperatures below the transition is only slightly lower than that of octahedral sites, suggesting a similar value of the Fe-T magnetic moment. However, when crossing the transition during

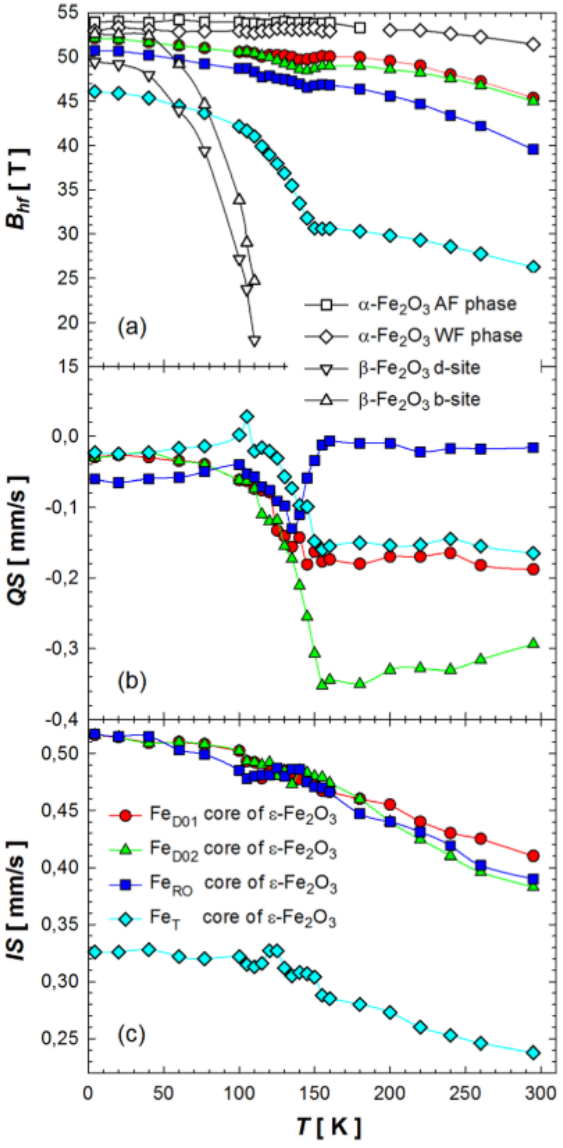

Figure 4-19. Temperature dependence of hyperfine parameters of ε-Fe_2O_3 nanoparticles with admixtures of α-Fe_2O_3 and β-Fe_2O_3 nanoparticles, B_{hf} denotes the hyperfine field, *QS* the quadrupole shift and *IS* the isomer shift. Reproduced from [O1].

heating, the Fe-T hyperfine field decreases by ~15 T together with the magnetic moment, which is mentioned above. Actually, the origin of such low values of both the hyperfine field and the magnetic moment in the tetrahedral site has not been satisfactorily explained yet.

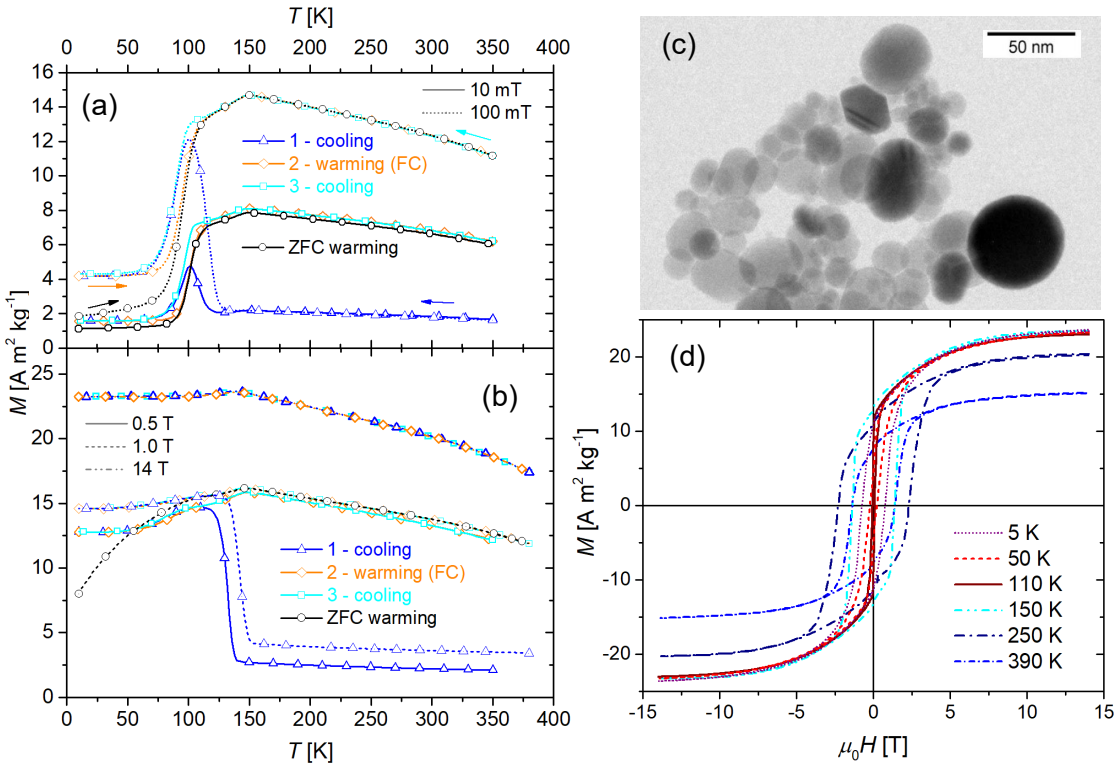

Figure 4-20. Magnetic data of ε-Fe_2O_3 nanoparticles shown in (c): temperature-dependent magnetization in various applied fields (a) and (b), measured in the applied field during: 1. cooling the pristine sample, 2. warming (FC curve), and 3. cooling again, moreover, a standard ZFC curve was measured as well. The color of the curves together with the tracking symbols refers to the respective type of scan, the style of the line to the applied magnetic field. In (d), hysteresis curves at selected temperatures are shown. Adapted from [D3].

The temperature scans of magnetization in various magnetic fields while heating/cooling, as well as the temperature dependence of coercive field with selected hysteresis curves, are depicted in Figure 4-20. During cooling in low fields, the pristine sample of randomly oriented nanoparticles remains demagnetized down to the temperature at which the applied field can overcome the anisotropy and the magnetization rises. Supposedly, the subsequent increase in coercivity with decreasing temperature along with the closure of magnetic domains inside the ensemble of particles results again in the decrease of the overall magnetization. Then during warming (FC curve), the typical two-step increase in magnetization due to the magnetic transition occurs, which is prone to hysteresis (by ~5–8 K). The magnetization scan at 14 T (reflecting the saturation magnetization, however,

a pronounced paraprocess is present as indicated by the high-field regions of magnetization curves in Figure 4-20d) still reveals some change of slope at the transition, though the second step of the transition seems to be suppressed. Interestingly, the coercive field starts to collapse already at temperatures below 200 K with a minimum at around 100 K (see Figure 4-21b), i.e., at ~50 K higher temperatures than the decrease in the magnetization.

The epsilon polymorph still rises challenging questions that remain unanswered. A general consensus about what exactly is happening during the low-temperature transition has not been achieved yet. Quite recently, several authors [275,276] have argued that the Curie temperature is, in fact, around ~800 K, much higher than the reported ~490 K at which, according to them, a different magnetic phase transition takes place. However, it is highly likely that the authors overlooked and misinterpreted minute impurities of γ-Fe_2O_3. The gamma polymorph can easily hide in the complex XRD pattern of the epsilon phase, especially if the pattern has broadened lines due to the small particle sizes. Moreover, the Mössbauer parameters of γ-Fe_2O_3 and ε-Fe_2O_3 are similar, therefore maghemite is difficult to detect. Despite that, its presence can be unambiguously deduced from a deformed hysteresis curve in the vicinity of the zero fields.

Similarly to spinel ferrites, the extraordinary properties of ε-Fe_2O_3 can be further tuned by suitable doping. For example, the rhodium-doped ε-$Rh_{0.14}Fe_{1.86}O_3$ nanoparticles have the largest coercive field among the known metal oxide magnets [277], namely 2.7 T at 300 K (3.5 T and 4.5 T at 300 K and 200 K when in a magnetically oriented thin film [278]). The large coercivity is attributed to the enhanced magnetocrystalline anisotropy through the Fe–O–Rh orbital mixing and also to the contribution of the Rh orbital momentum. The low-temperature transition characteristic of the epsilon phase is not suppressed by such degree of substitution, the coercive field rapidly decreases in the region ~170–80 K and continues to decrease down to 0.8 T at 10 K [278].

In our studies on the epsilon phase, we further focused on nanoparticles doped with trivalent diamagnetic cations, which are known for their preference for tetrahedral sites, namely Al^{3+} and Ga^{3+}. Due to the ferrimagnetic structure of ε-Fe_2O_3, the selective diamagnetic substitution in the single tetrahedral site enhances the overall magnetization, which is one of the crucial parameters that determine the efficiency of MRI contrast agents. We employed the compositions ε-$Al_{0.23}Fe_{1.77}O_3$ [D5] and ε-$Fe_{1.76}Ga_{0.24}O_3$ [D7],[D11] (alphabetical order of cations in the compound follows the convention), in which approximately half of the tetrahedral sites were occupied with the diamagnetic ions. These compositions also

enabled us to presume that all ions of the dopant occupy tetrahedral sites. Actually, an increasing fraction of Ga^{3+} ions was shown to occupy also the octahedral sites when the degree of substitution increases [279]. The substitution with diamagnetic cations indeed increased the magnetization of the samples compared to the undoped compound (see Figure 4-21a). The effect of magnetic dilution reduced the coercive field, as apparent from Figure 4-21b, but the single-domain character and blocked state of the nanoparticles were preserved. In both doped systems under study, neither the FC scans (see Figure 4-22) nor their derivatives showed any signs of the low-temperature transition. Neither did the coercivity of the ε-$Fe_{1.76}Ga_{0.24}O_3$, which increased with the decreasing temperature from the 1.2 T at 300 K up to 1.6 T at 5 K. Nevertheless, the coercive field of the ε-$Al_{0.23}Fe_{1.77}O_3$ nanoparticles decreased by more than 10 % on cooling between ~70 K and ~30 K roughly from almost 2.0 T to 1.7 T, which was still higher than the room-temperature value 1.5 T (see Figure 4-21b). The minor decrease hinted that the anisotropy was slightly reduced at this temperature range, but the decrease was not sufficient to induce the transition and manifest in the FC curve.

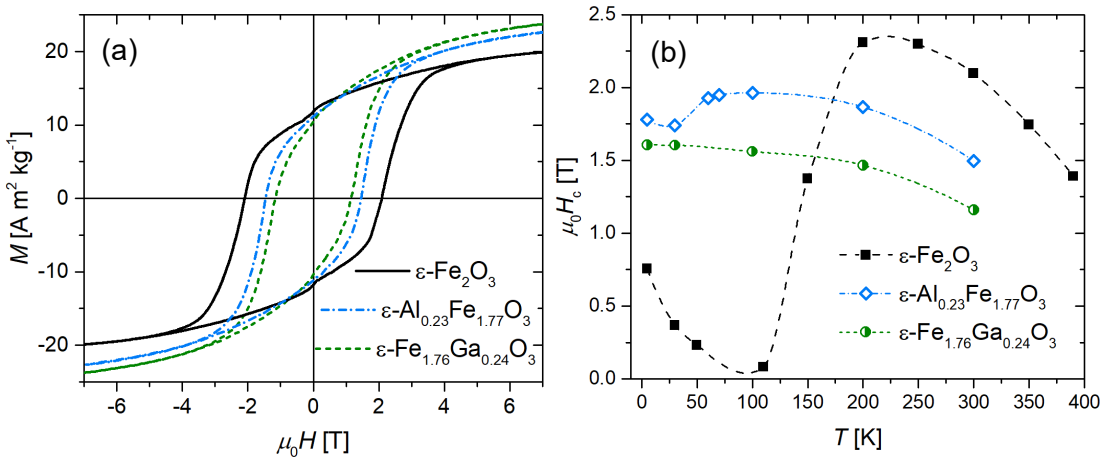

Figure 4-21. (a) Hysteresis curves of nanoparticles of the pure and doped epsilon phases at 300 K and (b) the temperature dependence of their coercive fields. Based on data published in [D3],[D5],[D11].

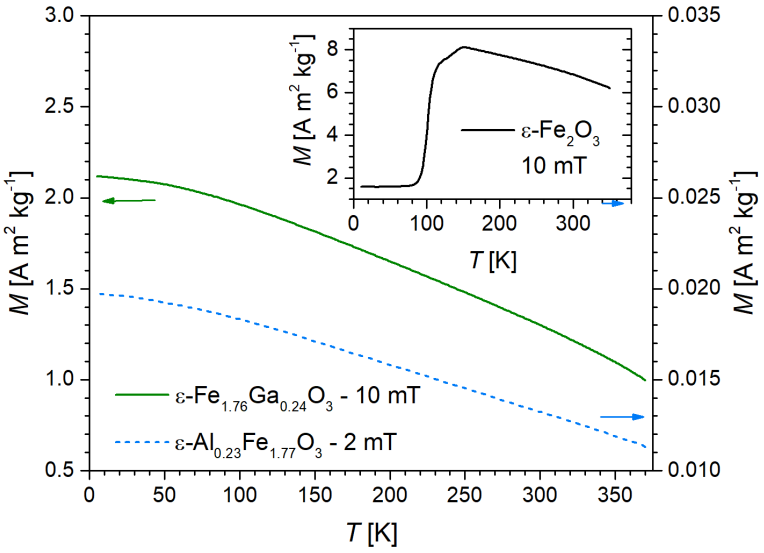

Figure 4-22. The temperature dependence of magnetization of ε-$Al_{0.23}Fe_{1.77}O_3$ and ε-$Fe_{1.76}Ga_{0.24}O_3$ nanoparticles measured in the FC regime, data for the undoped ε-Fe_2O_3 are shown in the inset. Data published in [D3],[D5],[D11].

The magnetic dilution effect modifies also the ^{57}Fe Mössbauer spectra of the doped compounds. The diamagnetic ions break the Fe–O–Fe superexchange interaction pathways and introduce different local environments to ^{57}Fe nuclei according to their number among nearest neighbors. Consequently, the hyperfine field at ^{57}Fe nuclei decreases in general and has broader distribution. In our samples, the diminishing intensity of the Fe-T component evidenced the successful substitution of the diamagnetic ions for Fe^{3+} ions in the tetrahedral sites. Since the nearest sites of the Fe-T are again two tetrahedral sites, the Fe-T component should be in fact fitted by three components differing in the number of diamagnetic ions as nearest neighbors. In the case of ε-$Fe_{1.76}Ga_{0.24}O_3$, the 0, 1, and 2 nearest neighbors provided intensities of the respective Fe-T components 27 %, 50 %, and 23 %. The decreased magnetic anisotropy due to Ga^{3+} ions leads to larger thermal fluctuations of the magnetic moments. An increase in temperature is first accompanied by the decreased hyperfine field and more pronounced fluctuations of magnetic moments at the Fe-T sites with two Ga^{3+} nearest neighbors, but at higher temperatures, the same occurs also at other Fe-T sites and at the octahedral sites with at least one Ga^{3+} nearest neighbor (see Figure 4-23 for Mössbauer spectra and Table 4-5 for the respective hyperfine parameters).

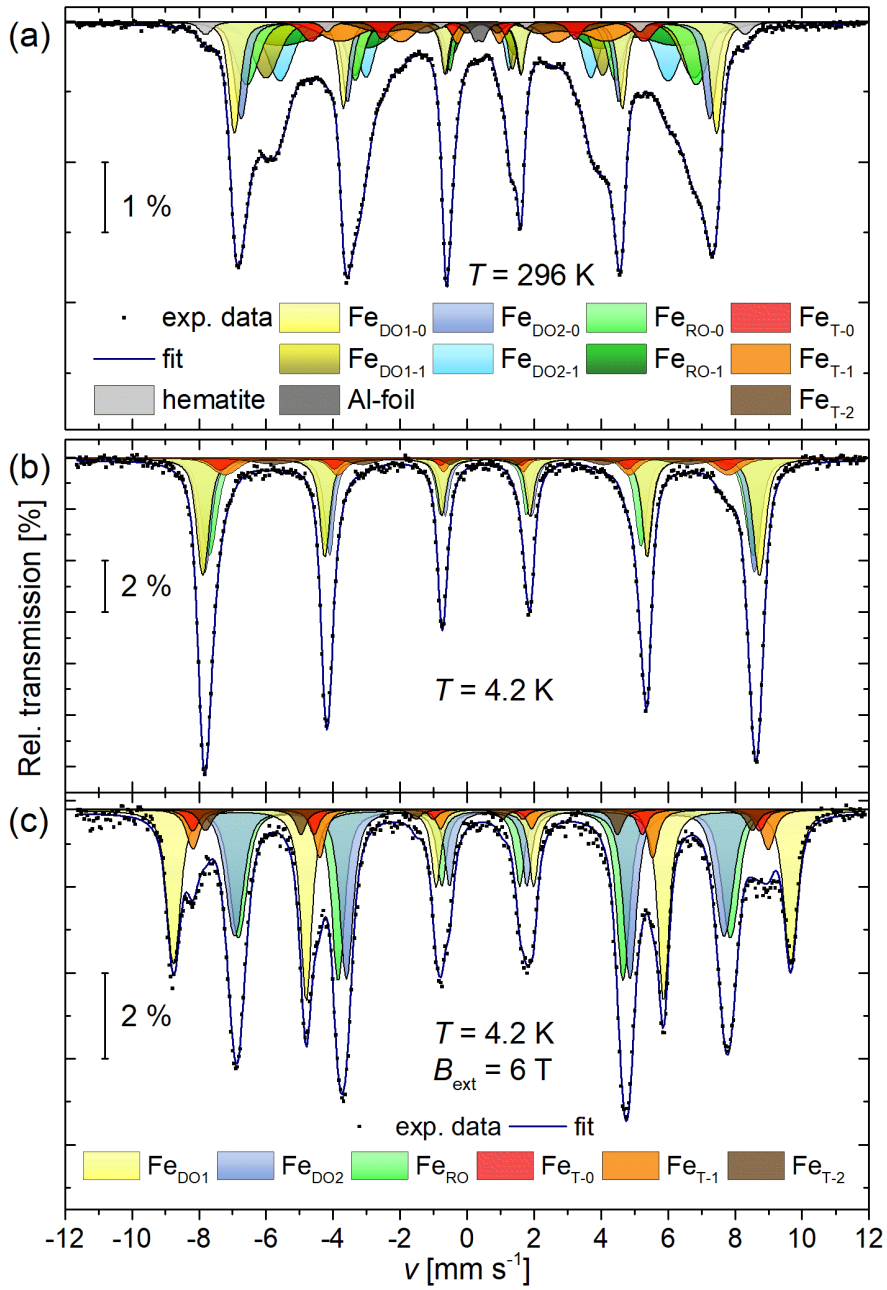

Figure 4-23. ^{57}Fe Mössbauer spectra of ε-$Fe_{1.76}Ga_{0.24}O_3$ nanoparticles at (a) room temperature, (b) at 4.2 K, both in zero fields, and (c) at 4.2 K and in the field of 6 T. The number after the hyphen in the designation of a component denotes the number of Ga^{3+} nearest neighbors, the hyperfine parameters are summarized inTable 4-5. Reproduced from [D11].

Table 4-5. Hyperfine parameters obtained from ^{57}Fe Mössbauer spectra of ε-$Fe_{1.76}Ga_{0.24}O_3$ nanoparticles; values marked with an asterisk were fixed during the fitting procedure, values with two asterisks were fixed to the values from the fits of the in-field spectra. Fe sites marked with ‡ in the room-temperature spectrum were assigned to the best of our knowledge, however, a certain ambiguity in the assignment of the octahedral sites should be retained.

Conditions	Fe sites	δ [mm s^{-1}]	2ε [mm s^{-1}]	B_{eff} [T]	A [%]
T = 296 K B_{ext} = 0 T	‡$Fe_{DO1\text{-}0}$	0.37(2)	-0.22(2)	44.7(2)	14*
	‡$Fe_{DO1\text{-}1}$	0.37(3)	0.03(4)	39.7(3)	14*
	‡$Fe_{DO2\text{-}0}$	0.37(2)	-0.23(3)	43.4(2)	14*
	‡$Fe_{DO2\text{-}1}$	0.27(3)	-0.13(3)	36.0(3)	14*
	‡$Fe_{RO\text{-}0}$	0.34(3)	-0.41(4)	41.7(3)	14*
	‡$Fe_{RO\text{-}1}$	0.43(4)	-0.12(6)	36.9(5)	14*
	$Fe_{T\text{-}0}$	0.34(3)	-0.05(4)	30.9(3)	4*
	$Fe_{T\text{-}1}$	0.26(3)	-0.16(5)	24.7(4)	7*
	$Fe_{T\text{-}2}$	0.4(2)	-0.09(6)	18.2(6)	4*
	hematite	0.37*	-0.24(4)	50.0*	2(1)
T = 4.2 K B_{ext} = 0 T	Fe_{DO1}	0.49**	-0.14(3)	51.6(3)	29*
	Fe_{DO2}	0.51(2)	-0.27(3)	50.9(3)	29*
	Fe_{RO}	0.46(2)	-0.06(3)	50.4(3)	29*
	$Fe_{T\text{-}0}$	0.30**	-0.23(8)	46.9(5)	4*
	$Fe_{T\text{-}1}$	0.39(4)	-0.20(7)	46.7(5)	7*
	$Fe_{T\text{-}2}$	0.4(2)	-0.18(8)	38.6(7)	4*
T = 4.2 K B_{ext} = 6 T	Fe_{DO1}	0.49(2)	-0.09(3)	57.2(2)	29*
	Fe_{DO2}	0.50(3)	-0.27(4)	45.4(2)	29*
	Fe_{RO}	0.46(3)	0.11(5)	45.6(2)	29*
	$Fe_{T\text{-}0}$	0.30(5)	-0.06(8)	52.6(4)	4*
	$Fe_{T\text{-}1}$	0.49(7)	-0.17(5)	53.3(3)	7*
	$Fe_{T\text{-}2}$	0.1(2)	0.59(6)	50.7(4)	4*

4.3 Chalcopyrite ($CuFeS_2$)

The last compound that we will mention in this chapter is chalcopyrite (see Figure 4-24), $CuFeS_2$, structurally related to sphalerite (cubic ZnS). The sphalerite cell comprises two penetrating face-centered cubic lattices of S^{2-} anions and of Zn^{2+} cations that are shifted so that the cations occupy tetrahedral interstices of the anionic lattice. In chalcopyrite, the tetrahedra of Fe are highly regular, whereas those of larger Cu are slightly distorted. The ordering of Cu and Fe in chalcopyrite

then results in the tetragonal unit cell (practically a double sphalerite cell) with the $I\bar{4}2d$ space group (see Figure 4-25) [252].

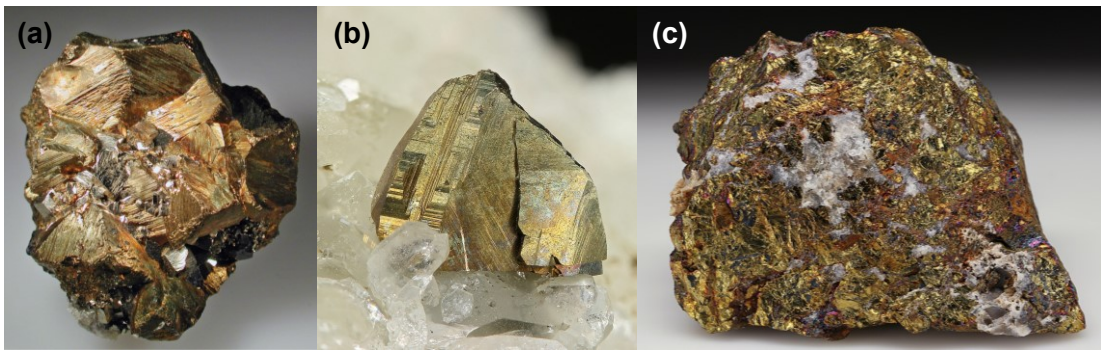

Figure 4-24. Chalcopyrite: (a) a crystal 2.2 x 2.2 x 1.2 cm^3 in size, Ground Hog Mine, USA (photograph by K. Nash, licensed under CC BY 3.0, cropped); (b) a 5 mm crystal embedded in quartz and datolite, Roncari Quarry, USA (photograph by H. Moritz, licensed under CC BY-NC-SA 3.0, cropped); (c) massive chalcopyrite with quartz, 6.5 x 4.5 x 4 cm^3, Newington, USA (photograph by H. Moritz, licensed under CC BY-NC-SA 3.0). Pictures from [280].

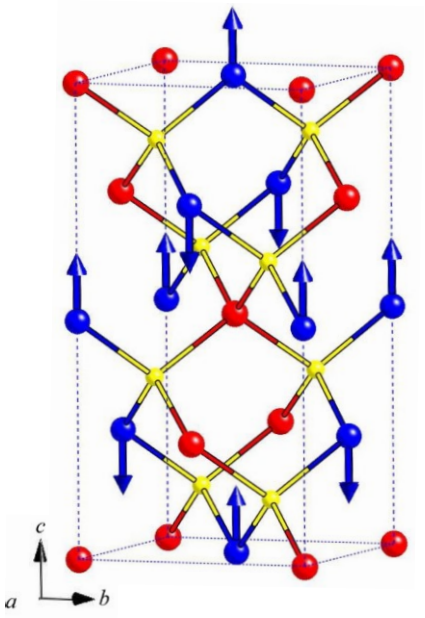

Figure 4-25. Chalcopyrite structure with indicated magnetic moments at Fe sites (blue), Cu shown in red, S in yellow. Reproduced from [281].

Interestingly, this most important copper ore has been a matter of debate about the valence state of the cations – hypothetically, both $Cu^{1+}Fe^{3+}S_2$ and $Cu^{2+}Fe^{2+}S_2$ are possible, and both can find some support in published data. The X-ray absorption near-edge structure (XANES) using the L-edge of Cu and K and L-edges of Fe concludes the latter [282], whereas X-ray photoelectron spectroscopy (XPS) [283,284] and Mössbauer spectroscopy [285,286] support the former. In general, the opinion prevails that copper is formerly monovalent with the number of d-electrons somewhere between nine and ten, i.e., with a little admixture of the formal Cu^{2+} state, and iron is formally trivalent, in the high-spin state. This assignment is rather formal, taking into account the strong covalent character of the bonds in chalcopyrite accompanied by a significant mixing of empty Fe 3d and occupied Cu 3d states, mediated by 3p states of sulfur [283].

Chalcopyrite is a collinear antiferromagnet with a Néel temperature in the range of 810-820 K [287,288], however, the measurement of the Néel temperature must be performed under a strictly inert atmosphere because chalcopyrite is prone to oxidation at elevated temperatures. The magnetic moments of Fe are oriented along the *c*-axis, and each sulfur atom connects two Fe with antiparallel moments (see Figure 4-25). The observed moment of 3.85 μ_B on Fe [289], lower than the theoretical value of 5 μ_B expected for high-spin Fe^{3+}, contributed to the confusion about the valence state of iron but can be attributed to the covalence effects. It is also consistent with the magnetic hyperfine field ~35 T obtained from Mössbauer spectra, significantly lower than, e.g., ~51 T of hematite. From an anomaly in magnetic susceptibility, it has been also speculated that an antiferromagnetic ordering of Cu ions with a very small moment occurs at low temperatures [290,291], which would presume the presence of Cu^{2+} since Cu^{+} with its $3d^{10}$ configuration is diamagnetic. Nevertheless, the magnetic ordering of copper has not been satisfactorily supported yet, and the observed anomalies were probably due to impurities. Moreover, neutron diffraction data provide zero magnetic moments of Cu within the experimental error [289,292], and the magnetic ordering of Cu sublattice was not even supported by DFT calculations [281]. It was also suggested that the anti-site Fe atoms can induce the formation of magnetically frustrated or ferromagnetic clusters and can lead to a considerable magnetization and exchange bias, shifted magnetization curves along the field axis [O4].

Chalcopyrite is an intriguing system for probing the magnetic properties of antiferromagnetic nanoparticles. In studies [D6],[D9] focused mainly on thermoelectric properties of mechanochemically prepared chalcopyrite nanoparticles, we dealt also with the degree of structural disorder and magnetic relaxation (see Figure 3-10a for TEM image and Figure 4-26 for Mössbauer spectra of a representative sample prepared by high-energy milling from elements). The Mössbauer spectra acquired at 3.5 K of chalcopyrite nanoparticles with the mean size of crystallites from XRD ~ 12 nm reflect the structural disorder, which modifies the magnetic hyperfine field at the ^{57}Fe nuclei (see Table 4-6 for hyperfine parameters) and leads to the broadening of the sextet lines. Room-temperature spectra showing sextets of the chalcopyrite phase (hyperfine parameters in Table 4-7) indicate that the particles strongly interact, as discussed in Section 2.4. The broadening of lines reflects, along with the structural disorder, also the size distribution of the particles. The narrow lines of the sextet S1 can be ascribed to larger, structurally well-ordered particles, whose magnetic moments appear static in the Mössbauer time window of 10^{-10}-10^{-7} s. In the case of medium-sized particles, superparamagnetic fluctuations of their magnetic moments decrease the effective

magnetic hyperfine field at the ^{57}Fe nuclei, resulting also in pronounced broadening of the sextet lines (approximated by S2-S4 sextets). Finally, the smallest nanoparticles (or those characterized with a higher degree of structural disorder weakening the magnetic exchange) with very fast fluctuations of magnetic moments are manifested by a collapsed sextet S5.

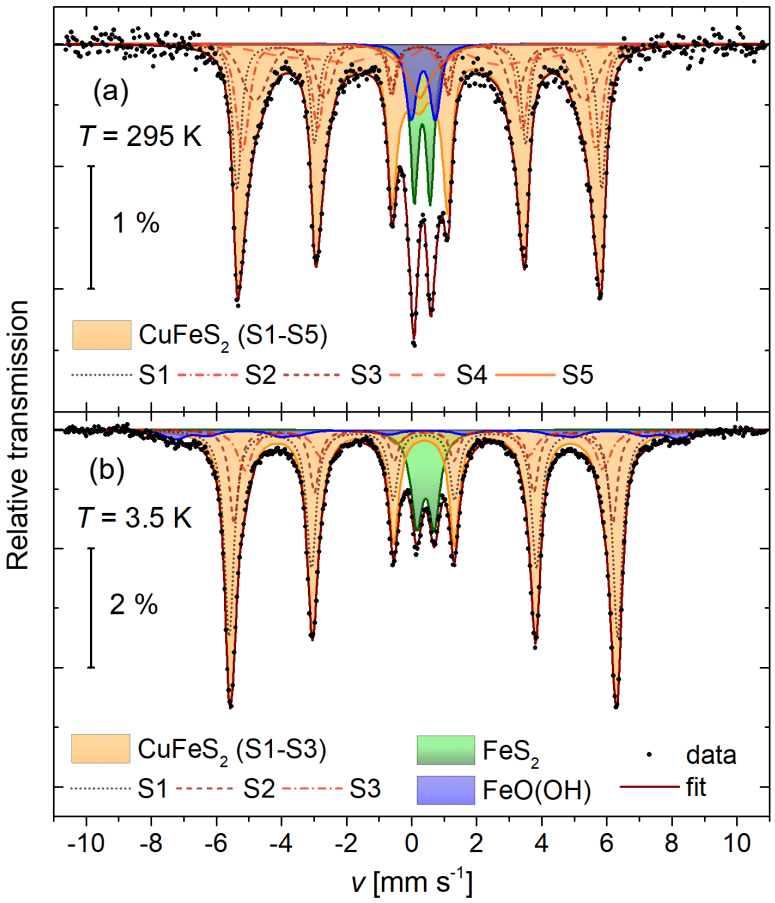

Figure 4-26. ^{57}Fe Mössbauer spectra at (a) 295 K and (b) 3.5 K of chalcopyrite nanoparticles prepared from elements by high-energy milling. The hyperfine parameters and the area of FeO(OH) and FeS_2 components are summarized in Table 4-6 and Table 4-7. Adapted from [D6].

Table 4-6. Hyperfine parameters of chalcopyrite nanoparticles prepared from elements by high-energy milling, obtained from ^{57}Fe Mössbauer spectra at 3.5 K (Figure 4-26a). The S1-S3 sextets of chalcopyrite model different degrees of the structural disorder in the local environment of ^{57}Fe nuclei, SO1 and SO2 sextets are ascribed to a surface layer of iron oxyhydroxides, D is a doublet of the pyrite admixture, whose quadrupole splitting Δ_Q is marked by the dagger. Data from [D6].

Component	Interpretation	δ [mm s^{-1}]	ε [mm s^{-1}]	B_{hf} [T]	A [%]
S1	$CuFeS_2$	0.372(8)	-0.02(1)	37.0(1)	46(1)
S2	$CuFeS_2$	0.37(1)	-0.02(2)	36.1(1)	20.3(8)
S3	$CuFeS_2$	0.39(2)	-0.02(3)	34.2(2)	14(1)
SO1	γ-FeO(OH)	0.45(16)	0.00(6)	42(1)	3(2)
SO2	β-FeO(OH)	0.47(7)	0.000(4)	48.0(6)	5(2)
D	FeS_2	0.43(1)	0.271(6)/0.54(1)†	-	12.1(3)

Table 4-7. Hyperfine parameters of chalcopyrite nanoparticles prepared from elements by high-energy milling, obtained from ^{57}Fe Mössbauer spectra at 295 K (Figure 4-26b). The spectra were fitted with distributions of B_{hf} (sextets) and Δ_Q (doublets). The S1-S4 sextets of chalcopyrite model different degrees of the structural disorder along with different superparamagnetic relaxation rates of nanoparticles of different sizes, the SP5 component of a collapsed sextet is most affected by the superparamagnetic relaxation; D1 denotes the doublet of the pyrite admixture, while D2 is the doublet of superparamagnetic/paramagnetic iron oxyhydroxides. Further, $\langle\varepsilon\rangle$ is the mean quadrupole shift (for the doublets, the mean quadrupole splitting $\langle\Delta_Q\rangle$ is marked by the dagger), $\langle B_{hf}\rangle$ the mean magnetic hyperfine field, σ_{QS} and σ_B denote the standard deviations related to the distributions of quadrupole shift/splitting and hyperfine magnetic field, respectively. Data from [D6].

Comp.	Interpr.	δ [mm s^{-1}]	$\langle\varepsilon\rangle$ [mm s^{-1}]	σ_{QS} [mm/s]	$\langle B_{hf}\rangle$ [T]	σ_B [T]	A [%]
S1	$CuFeS_2$	0.25(1)	-0.01(1)	-	34.8(1)	0.2(2)	22(6)
S2	$CuFeS_2$	0.25*	-0.01(1)	-	33.7(4)	0.8(3)	22(4)
S3	$CuFeS_2$	0.25*	0*	-	31.4(9)	2.0(5)	20(5)
S4	$CuFeS_2$	0.25*	-0.09(8)	-	23(3)	7(2)	12(4)
SP5	$CuFeS_2$	0.25*	0*	-	0(4)	4(2)	6(2)
D1	FeS_2	0.33(1)	0.25(1) /0.49(2)†	0.02(3) /0.04(6)	-	-	11(2)
D2	FeO(OH)	0.36(3)	0.37(4) /0.74(7)†	0.08(4) /0.17(7)	-	-	6.6(7)

Finally, let us mention that apart from the more thermodynamically stable tetragonal α-phase of $CuFeS_2$ described in the text above, chalcopyrite can exist also in a cubic β-phase with a sphalerite structure, in which the Cu and Fe atoms are randomly distributed over the metal site. Moreover, the α-phase can contain inclusions of the β-phase. At higher temperatures, chalcopyrite tends to lose sulfur and gradually transforms to the (possibly sulfur-deficient) β-phase. At temperatures above T_N, the transformation to the β-phase is completed, which coincides with the loss of the magnetic ordering [293].

5 Magnetic nanoparticles in medicine

Over the decades of research, ideas and concepts of applications of magnetic nanoparticles have mushroomed in various areas of science, medicine, industry, and other fields, bringing the necessity of a multidisciplinary approach. The most important field with high societal relevance, which the nanoparticles have been prospected to revolutionize, is medicine. Magnetic nanoparticles have opened a way to the development of novel medical methods for sensitive detection, accurate diagnosis, and efficient treatment of, for example, cancer, cardiovascular or neurological diseases. Whereas most of this chapter will be devoted to MRI contrast agents and assessing their performance, which was the main focus of the author of this thesis, medicine could benefit – at least in the future – from several other applications of magnetic nanoparticles such as tracers for magnetic particle imaging (MPI), contrast agents for multimodal imaging, heating agents for magnetic fluid hyperthermia, or drug carriers in targeted drug delivery and remotely triggered drug release [294–296]. From these applications, only magnetic fluid hyperthermia has found its way into clinical practice so far when a heating agent based on aminosilane-coated iron oxide nanoparticles, NanoTherm, was finally approved in 2010 by the European Medicines Agency (EMA) for glioblastoma treatment by local hyperthermia [297].

Medical applications require nanoparticles that form a colloidally stable suspension in water, or more precisely under physiological conditions. Moreover, most of the applications would assume special functionalization, for example, to avoid fast clearance through the reticuloendothelial system (RES), to achieve specific interactions with cells, or to couple them with cargo. Besides the careful evaluation of the material properties, the evaluation of the *in vitro* and, eventually, for highly promising cases also *in vivo* toxicity should be an integral part of medically oriented studies.

Although our principal focus has been on the fundamental research devoted to the properties of diverse nanoparticles and testing theoretical models, we assessed the cytotoxicity of most of the studied nanoparticles as well, and therefore general considerations regarding the evaluation of toxicity of magnetic nanoparticles will close this section.

5.1 Contrast agents for MRI

A considerable part of our research was devoted to the analysis of the efficacy of magnetic nanoparticles to create contrast effects in MRI, i.e., their **relaxivity**. The

noninvasive and nonionizing MRI presents an important tool for clinical diagnosis, and specific enhancement of the image contrast of certain regions/structures is often desirable for better identification and specification of pathological alterations.

5.1.1 NMR and relaxation times

MRI builds on the principles of NMR, which combines the effects of static and radiofrequency (rf) magnetic fields on a system of atomic nuclei with nonzero spins, in MRI mostly ^{1}H with $I = 1/2$. The basic principles of NMR and MRI can be found elsewhere [298,299], in the following text we will point out only several aspects necessary for the discussion of relaxivity.

A nucleus with a magnetic moment $\boldsymbol{\mu} = \gamma_N \boldsymbol{I}$, where γ_N is the nuclear gyromagnetic ratio ($\gamma_N/(2\pi) \cong 42.58$ MHz T^{-1} for ^{1}H) and $\boldsymbol{I}$ the nuclear spin, inserted in a magnetic field $\boldsymbol{B}_0$ shows some analogy to a gyroscope and precesses with the *Larmor frequency*

$$\omega_0 = \gamma_N B_0. \tag{5.1}$$

The system of ^{1}H nuclei creates a nonzero magnetization when inserted into a magnetic field due to the difference in the thermal population of levels of two possible orientations according to the Boltzmann distribution. This magnetization can be manipulated by suitable rf pulses, whose choice and timing are the subject of a vast field of NMR pulse sequence design. After the magnetization of the ^{1}H ensemble $\boldsymbol{M}_0$ is rotated from its original orientation along the applied magnetic field $\boldsymbol{B}_0$ ($\boldsymbol{B}_0 \parallel z$-axis) to the perpendicular *xy*-plane, it relaxes back again to Boltzmann equilibrium. The longitudinal component of magnetization increases with time t during the relaxation as

$$M_z(t) = M_0\left(1 - e^{-\frac{t}{T_1}}\right), \tag{5.2}$$

whereas the transverse component of magnetization gradually decays as

$$M_\perp(t) = M_0 e^{-\frac{t}{T_2}}. \tag{5.3}$$

In these expressions, T_1 and T_2 denote the *longitudinal* (*spin-lattice*) and *transverse* (*spin-spin*) *relaxation time*. Their reciprocals, R_1 and R_2, are the respective relaxation rates. In the *spin-lattice* (*longitudinal,* T_1-)*relaxation*, the spin returns to equilibrium by exchanging energy with its surroundings, chiefly by interaction with local fluctuating magnetic fields, which originate mostly in the intra- and intermolecular dipole-dipole interactions with other spins in the vicinity. *Spin-spin* (*transverse,* T_2-)*relaxation* describes the process of losing the phase coherence

in the ensemble of precessing spins. Due to the local fluctuations of the magnetic field, the spins precess with slightly different Larmor frequencies, and $M_\perp$ diminishes due to their dephasing. The T_2 -relaxation can be enhanced by macroscopic field inhomogeneities, for example, due to instrumental reasons or distortions caused by large differences in susceptibilities in the sample. Such accelerated relaxation time is formally denoted T_2^* and determines the *free induction decay* (FID) of the magnetization signal observed after a rf π/2-pulse is applied.

After applying a π/2-pulse rotating the magnetization by 90° to the *xy*-plane, the FID signal diminishes as $\propto \exp(t/T_2^*)$. To determine T_2, which will be crucial for our further discussion, a more complex procedure has to be applied. If a π-pulse is applied at t_e after the first pulse, the spins are rotated by 180° and again refocused at $2t_e$, giving rise to a *spin echo*. The intensity of the spin echo decays with time after the initiating π/2-pulse as $\propto \exp(t/T_2)$. Therefore, it is possible to apply a series of π-pulses to collect a series of spin-echo signals to measure T_2. This approach has been established in the *Carr-Purcell* (CP) [300] and further improved in the *Carr-Purcell-Meiboom-Gill* (CPMG) [301] *methods* (see Figure 5-1). Let us imagine that the π/2-pulse rotated the magnetization from *z* to the *y*-axis (in the rotating reference frame). In the former method, the initial π/2-pulse and the subsequent π-pulses share the same phase (the magnetic field of the rf pulses points in the same direction), the π-pulses flip the spins by 180° around the *x*-axis, and the magnetization in spin echoes points alternately in the -*y* and *y* directions. This procedure leads to the accumulation of experimental errors in the course of the π-pulse series from an imprecise setting of the pulses. In contrast, the phase of the π/2-pulse in the CPMG sequence differs by π/2 from the phase of the π-pulses, which flip the spins by 180° around the *y*-axis so that the magnetization has the same phase in all spin echoes and the error is canceled with every even π-pulse [301].

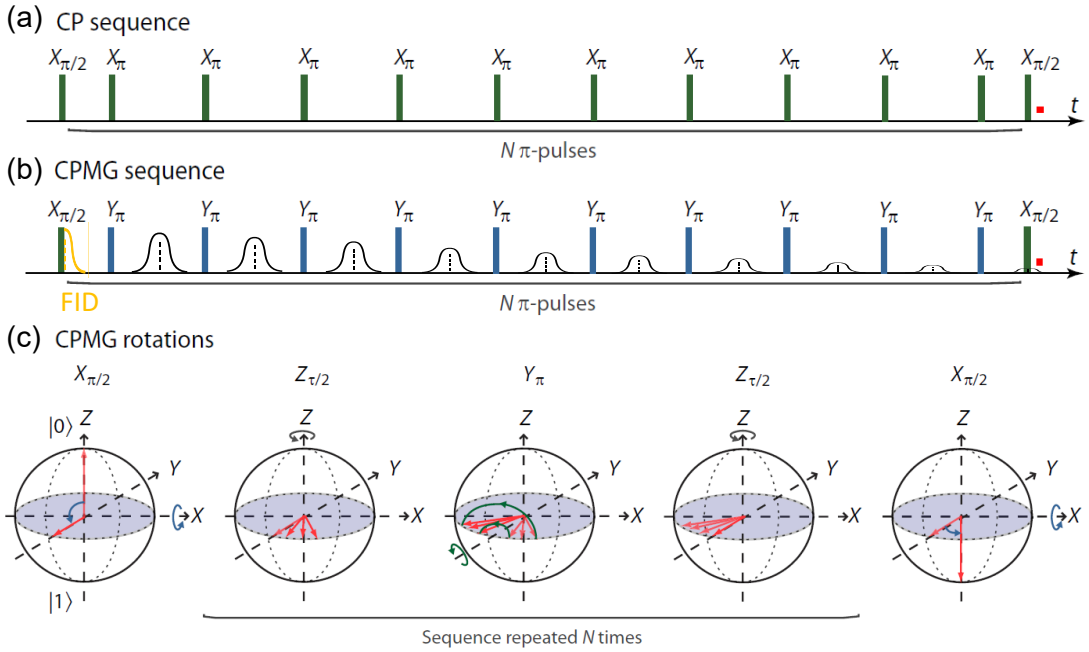

Figure 5-1. Schematic representation of the (a) CP and (b) CPMG sequences for measuring the T_2 relaxation time by using spin echos, the FID signal and spin echos, whose intensity decreases as $\propto \exp(t/T_2)$, are also indicated in (b); $X_{\pi/2}$ marks the π/2-pulse rotating the spin magnetization by 90° around the x-axis, X_π (Y_π) denote the π-pulses rotating the spins by 180° around the $x(y)$-axis in the CP (CPMG) sequence. In (c), the evolution of the spin system in the CPMG sequence from the initiating π/2-pulse ($X_{\pi/2}$) over the flipping π-pulse (Y_π) to the spin echo and the readout pulse ($X_{\pi/2}$) rotating the magnetization again to the z-axis is indicated. Adapted from [302].

5.1.2 MRI and contrast generation

Briefly, MRI shifts the NMR principles towards 2D imaging by encoding the space information by magnetic field gradients $\frac{\partial B_z}{\partial x_i}$ applied during the imaging sequence along each coordination axis x_i in addition to the static field [303]. The image contrast is generated by a delicate interplay of the local ^{1}H density ρ together with local T_1 and T_2 relaxation times. The resulting signal (spin-echo induction voltage) can be described by

$$\Sigma(t) = k\rho\left(1 - e^{-\frac{\mathrm{TR}}{T_2}}\right)e^{-\frac{\mathrm{TE}}{T_2}}, \tag{5.4}$$

where k is the instrumental proportionality factor, which comprises all instrumental parameters including the amplification or sensitivity of rf coils. The *repetition time* TR marks the time between consecutive repetitions of the sequence, and the *echo-time* $\mathrm{TE} = 2t_e$ is the time when the spin echo appears after the initiating π/2-pulse. By varying TE and TR, one can select among different types of image weighting which enable visualization with the emphasis on

different structures. Whereas the proton-density weighting (long TR, short TE) simply maps the abundance of ^{1}H nuclei, T_1-weighting (short TE, TR $\sim T_1$) differentiates between structures based on their T_1 and displays tissues with short T_1 of ^{1}H nuclei, such as fat, as brighter fields and fluids with long T_1 as dark areas. Practically the opposite effect is achieved in T_2-weighted images (long TR, long TE), in which areas with fast T_2 relaxation provide only little signal, in contrast to fluids with long T_2.

A popular family of imaging sequences uses a set of opposite gradient pulses to manipulate the spin system and generate the *gradient echo*. They follow the T_2^*-relaxation because no rephasing π-pulses are employed, consequently, they are much faster than the sequences based on the spin echo [304].

5.1.3 Relaxivity

Although certain contrast in the MRI images is generated by the differences in relaxation times and proton density because of different composition of the tissues, sometimes it is useful to enhance the contrast between tissues that are quite similar – for example, to distinguish healthy and pathological tissues. The MRI contrast agents (CAs) are designed to improve the early detection of tumors and metastases and their diagnostic prospects. The performance of a CA is characterized by its **relaxivity** r_i, i.e., its ability to increase the relaxation rate R_i of ^{1}H nuclei in the system per unit concentration of the agent (usually in moles of formula units or magnetically active ions). Relaxivity of a CA in a solution/suspension is defined by the following expression

$$R_i = r_i c_{\mathrm{CA}} + R_{i,0}\,, i = 1,2 \qquad (5.5)$$

in which c_{CA} denotes the concentration of the CA and $R_{i,0}$ is the relaxation rate of pure medium, most often water. Whereas linear regression of a concentration series $R_i(c_{\mathrm{CA}})$ represents a more precise way to measure the relaxivity, the relaxation rate is sometimes measured at a single and sufficiently high concentration (especially when testing various dependencies) and approximated with $R_i \approx r_i c_{\mathrm{CA}}$ under the condition of $R_{i,0} \ll R_i$.

The CAs with high **longitudinal relaxivity** r_1 induce brighter areas in T_1-weighted imaging, therefore they are labeled as "positive" CAs. All T_1-CAs currently available for clinical use are Gd-based complexes (see, for example, Gd-DOTA in Figure 5-2a). Although free Gd^{3+} ions are toxic, they form stable complexes with suitable chelating ligands, which should prevent the toxic effect of the ions. Gd-based CAs have been widely applied since 1988 [305] though the first studies were born already at the beginning of the 1980s [306,307]. However, 20 years later,

a link between the application of these CAs and nephrogenic systemic fibrosis was suggested [308,309]. It has been shown quite recently that in patients, with normal renal function and even without intracranial abnormalities, which were administered a common intravenous contrast agent gadodiamide (see Figure 5-2b), Gd is deposited in neuronal tissue, it crosses the blood-brain barrier and accumulates in the brain [310,311]. Moreover, increased concentration of Gd found in natural waters and even in tap water in large cities and their vicinity has been ascribed to the clinical use of Gd-based compounds, as most of the applied agent is excreted by the urinal tract unchanged [312,313]. All these findings raise health and environmental concerns and have renewed the interest in Gd-free MRI CAs.

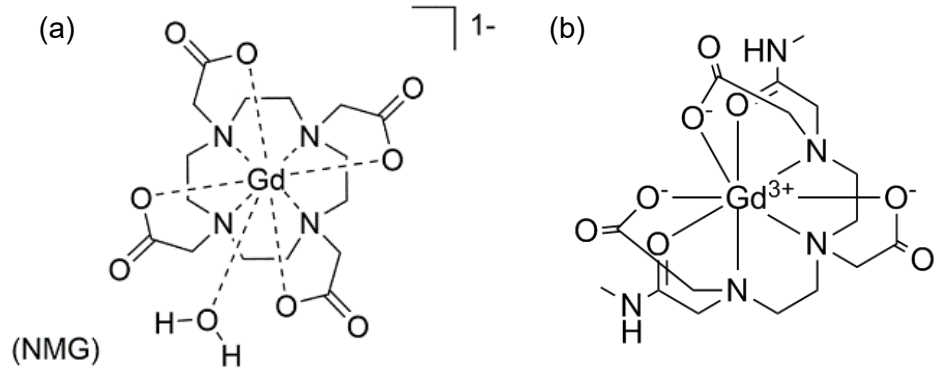

Figure 5-2. Examples of Gd-based positive MRI CAs: (a) gadoteric acid (Gd-DOTA, generic name gadoterate meglumine, trade name Dotarem or Clariscan), NMG = meglumine; (b) gadodiamide (Gd-DTPA-BMA, trade name Omniscan). Adapted from [314,315].

Magnetic nanoparticles containing transition metals present an efficient alternative. In the rest of this section, the discussion will be limited to **transverse relaxivity** r_2 of **CAs based on magnetic nanoparticles**, which influence chiefly the R_2 relaxation and are therefore mostly studied as "negative" CAs for T_2-weighted imaging.

Since the relaxivity is determined both by the material characteristics of the CA and its interaction with ^{1}H nuclei in the medium, it depends on numerous parameters of the system. Among the decisive CA parameters, one can name for example magnetization (and properties that determine it – composition, crystallinity, cation distribution, particle size, etc.) and the magnetic state (e.g., paramagnetic, SPM, or blocked state), distribution of particle sizes directly related to the distribution of magnetic moments of the particles, particle shape, aggregation, or type and thickness of the coating. Other relevant parameters are the characteristics of the medium (self-diffusion, hydrogen bonding, etc.) and other macroscopic parameters such as temperature or applied magnetic field. Despite the

enormous complexity of the system, several theoretical models have been introduced attempting to capture the relation between these parameters and the resulting relaxivity.

5.1.4 Models of transverse relaxivity

For simplicity, let us further focus on the aqueous suspensions of magnetic nanoparticles. The theoretical models on relaxation of the ^{1}H system induced by magnetic nanoparticles build on mechanisms originally established for CAs based on paramagnetic complexes: (i) the *inner-sphere relaxation* dealing with ^{1}H protons that temporarily bind to a nanoparticle, and (ii) the *outer-sphere relaxation* considering protons diffusing in the surroundings of a nanoparticle [316]. In nanoparticle suspensions, the latter usually dominates and the former is then neglected. The application of the paramagnetic outer-sphere theory to magnetic nanoparticles was first introduced in [317].

^{1}H nuclei in water molecules diffusing in the vicinity of a magnetic particle experience fluctuations of the magnetic field due to the combined effect of its free diffusion through the local field inhomogeneities (the outer-sphere mechanism, Figure 5-3), and the effective relaxation of the nanoparticle according to the expression (2.19). However, several initial assumptions must be taken into account before discussing the individual models [318]: (i) the particle size in the expressions relates to the distance of the closest approach of water molecules, i.e., including the coating; (ii) the nanoparticles are distributed homogeneously in the suspension at very low concentration; (iii) only uniaxial anisotropy of the nanoparticles is considered for simplicity; (iv) the particle magnetic moments are subjected to Néel and Brownian relaxation (if applicable), and the SPM moments precess with Larmor frequency; (v) the SPM moment follows Boltzmann distribution and tends to get aligned with the applied field.

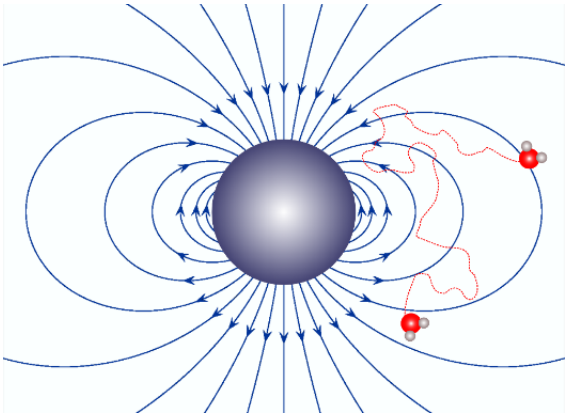

Figure 5-3. Scheme of a water molecule diffusing in the dipolar magnetic field of a nanoparticle in the outer-sphere relaxation.

The theoretical description of r_2 based on the outer-sphere relaxation depends on the mutual comparison of characteristic times of the diffusion of water molecules and frequency shifts in the precession of ^{1}H nuclei in the vicinity of a particle. The

models also differentiate between the "long-echo" and "short-echo" limits according to the comparison of the aforementioned characteristic times with the echo time t_e of the pulse sequence employed.

Assuming that the Brownian relaxation of nanoparticles is much slower than the diffusion of water molecules, one can define the *diffusion correlation time*

$$\tau_D = \frac{d^2}{4D}\,, \tag{5.6}$$

where d is the diameter of the particle and D is the self-diffusion coefficient of water. The time τ_D describes the time which a water molecule needs to diffuse the distance of $d/\sqrt{2}$ [316].

The changes in Larmor precession of ^{1}H spins are described by the *dispersion of ^1H Larmor frequency shifts* $\Delta\omega$. In a suspension, the ^{1}H Larmor frequency ω_0 in an external field from the expression (5.1) is modified by the dipolar field of the nanoparticles $\boldsymbol{B}_{\mathrm{dip}}(\boldsymbol{r})$ as $\omega_{\mathrm{tot}}(\boldsymbol{r}) = \gamma_N\left|\boldsymbol{B}_0 + \boldsymbol{B}_{\mathrm{dip}}(\boldsymbol{r})\right|$. By assuming $B_{\mathrm{dip}} \ll B_0$, one can write $\omega_{\mathrm{tot}} \approx \gamma_N\left(B_0 + B_{\mathrm{dip}}\cos\beta + \cdots\right) = \omega_0 + \omega(\beta)$, where β is the angle between $\boldsymbol{B}_{\mathrm{dip}}(\boldsymbol{r})$ and $\boldsymbol{B}_0$. If we consider an experiment where $\boldsymbol{B}_0$ is oriented along the z-axis and the particle moments are aligned with the external field, we need to take into account the z-component of the dipolar field of a particle

$$B_{\mathrm{dip},z}(R,\theta) = \frac{\mu_0 M r_c^3}{3}\frac{3\cos^2\theta - 1}{R^3}. \tag{5.7}$$

In this expression, r_c denotes the radius of the magnetic core of the particle (excluding nonmagnetic coating) and R, θ are spherical coordinates. The dispersion $\Delta\omega(R)$ over the full solid angle at the distance R from the center of the nanoparticle can be calculated as

$$\Delta\omega(R) = \frac{\gamma_N}{4\pi}\left(\int_0^{2\pi}\int_0^{\pi}\left[B_{\mathrm{dip},z}(R,\theta) - \bar{B}_{\mathrm{dip},z}\right]^2 \sin\theta\,\mathrm{d}\theta\mathrm{d}\varphi\right)^{1/2}, \tag{5.8}$$

where the average field $\bar{B}_{\mathrm{dip},z} = 0$. The dispersion $\Delta\omega$ over all space is usually approximated by the shift at the equator of the particle ($R = r_c, \theta = \pi/2$)

$$\Delta\omega \approx \frac{\gamma_N \mu_0 M}{3}, \tag{5.9}$$

or from the expression (5.8) at the nanoparticle surface ($R = r_c$), which differs from the formula (5.9) by the factor $2/\sqrt{5} \approx 0.89$ [316],[D11].

Based on the ratio of τ_D and $(\Delta\omega)^{-1}$, the theoretical models can be categorized into three regimes: the motional averaging regime, static dephasing regime, and partial refocusing model [319].

The **motional averaging regime (MAR)** [316,320,321] applies if the *Redfield condition* $\Delta\omega\tau_D \ll 1$ is fulfilled. In this regime considering small nanoparticles, water molecules diffuse rapidly among the particles and experience a wide spread of local magnetic fields. However, the corresponding Larmor shift of water ^{1}H is effectively time-averaged during the measurement (long-echo limit). The relaxation rate is given by the quantum-mechanical outer-sphere theory, $R_{2,\mathrm{MAR}} = R^*_{2,\mathrm{MAR}}$ and the transverse relaxivity is then

$$r_{2,\mathrm{MAR}} = \frac{R_{2,\mathrm{MAR}}}{c_{\mathrm{CA}}} = \frac{16}{45}\frac{f}{c_{\mathrm{CA}}}\tau_D(\Delta\omega)^2, \qquad (5.10)$$

where f is the volume fraction that the particles occupy in the suspension, and the ratio f/c_{CA} denotes, in the case of single-phase nanoparticles and c_{CA} in formula units, the molar volume of the particles.

When $\Delta\omega\tau_D$ rises and the MAR condition breaks down, the system reaches the **static dephasing regime (SDR)** [320,322–324]. This regime leaves the conditions of outer-sphere relaxation behind and can be achieved only for high magnetization of the nanoparticles. In SDR, the ^{1}H spins are regarded as motionless in a nonuniform magnetic field of randomly distributed magnetic dipoles, and SDR thus places the absolute upper limit to r_2 while $t_e \to \infty$. Since the SDR model does not consider the effect of refocusing pulses, the description is valid only for the FID relaxation with

$$r^*_{2,\mathrm{SDR}} = \frac{R^*_{2,\mathrm{SDR}}}{c_{\mathrm{CA}}} = \frac{2\sqrt{3}}{9}\frac{f}{c_{\mathrm{CA}}}\Delta\omega\,. \qquad (5.11)$$

However, it is considered to be a good approximation of r_2 if $5 < \Delta\omega\tau_D < 20$ [325]. By comparing the expressions (5.10) and (5.11), one can conclude that SDR becomes effective for $\Delta\omega\tau_D > 5\sqrt{3}\pi/8 \cong 3.40$ under the condition $\tau_D < 2.25t_e$ [320]. Similarly, the critical size of a spherical particle which marks the transition from MAR to SDR can be calculated as

$$d_{\mathrm{SDR}} = \left(\frac{5\sqrt{3}\pi D}{2\Delta\omega}\right)^{1/2}. \qquad (5.12)$$

The dependence of the parameter $\Delta\omega\tau_D$, decisive for MAR and SDR, on temperature and size of the particles is shown in Figure 5-4 for an example of ε-$Al_{0.23}Fe_{1.77}O_3$ nanoparticles.

If $\tau_D > t_e$, the refocusing by the π-pulses becomes partially effective and the **partial refocusing model (PRM)** [320] must be considered. In PRM, the area around the particle is divided into two regions. First, in the inner region close to the particle, the spins of ^{1}H nuclei experience magnetic field gradients so strong that they get

rapidly dephased by a single encounter and the corresponding signal decays so fast that it is unobservable in MRI. Second, the spins in the outer region are sufficiently far from the particle to experience only weak gradients, they can be effectively refocused. Therefore, $r_{2,\mathrm{PRM}}$ decreases compared to the FID relaxation $r^*_{2,\mathrm{PRM}} = r^*_{2,\mathrm{SDR}}$. The boundary between the two regions can be formally defined by the radius r' and $\Delta\omega'$ at the respective distance, for which $\Delta\omega'\tau_\mathrm{D} = 1$. The relaxivity in PRM is given by the formula [319],[D1]

$$r_{2,\mathrm{PRM}} = \frac{1.8}{\tau_\mathrm{D}}\frac{f}{c_\mathrm{CA}}(\Delta\omega t_\mathrm{e})^{1/3}(1.52 + f\Delta\omega t_\mathrm{e})^{5/3}. \qquad (5.13)$$

The transition from SDR to PRM can be observed already for $\Delta\omega t_\mathrm{e} > 20$ [325]. In general, this model applies for particles that are even larger than in SDR, i.e., which exceed the size [323]

$$d_\mathrm{PRM} = 2\left(\frac{1.49D}{\Delta\omega}(\Delta\omega t_\mathrm{e})^{1/3}(1.52 + f\Delta\omega t_\mathrm{e})^{5/3}\right)^{1/2}. \qquad (5.14)$$

The predicted ranges of validity of the discussed regimes are shown in Figure 5-5, which depicts the dependence of transverse relaxivity on particle size and specific magnetization.

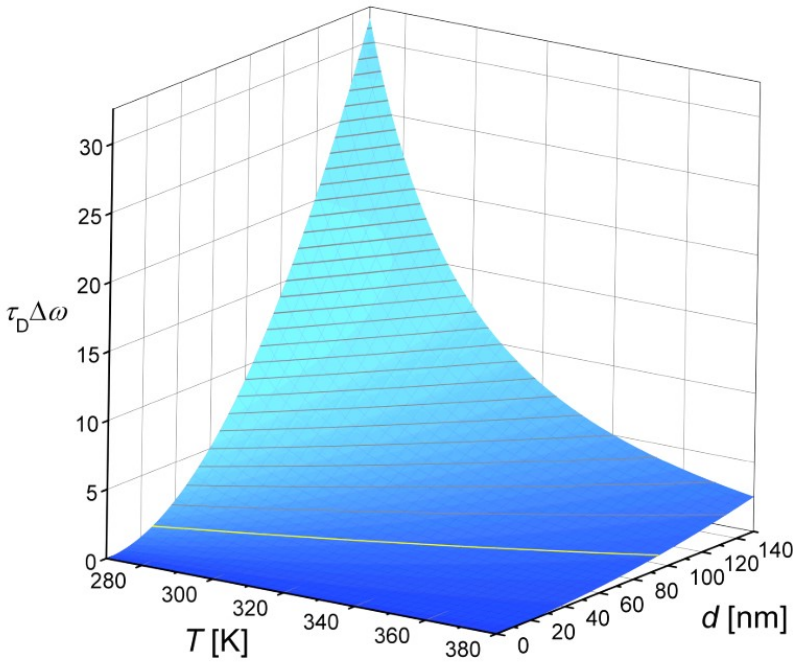

Figure 5-4. The parameter $\Delta\omega\tau_\mathrm{D}$ as a function of temperature and size of particles for ε-$Al_{0.23}Fe_{1.77}O_3$ nanoparticles, the light-yellow line marks $\Delta\omega\tau_\mathrm{D} = 1$. The temperature dependence of self-diffusion coefficient of water was approximated by the Speedy-Angell power law [326], the dependence of magnetization on temperature was determined experimentally on bare nanoparticles at 0.5 T. Reproduced from [D5].

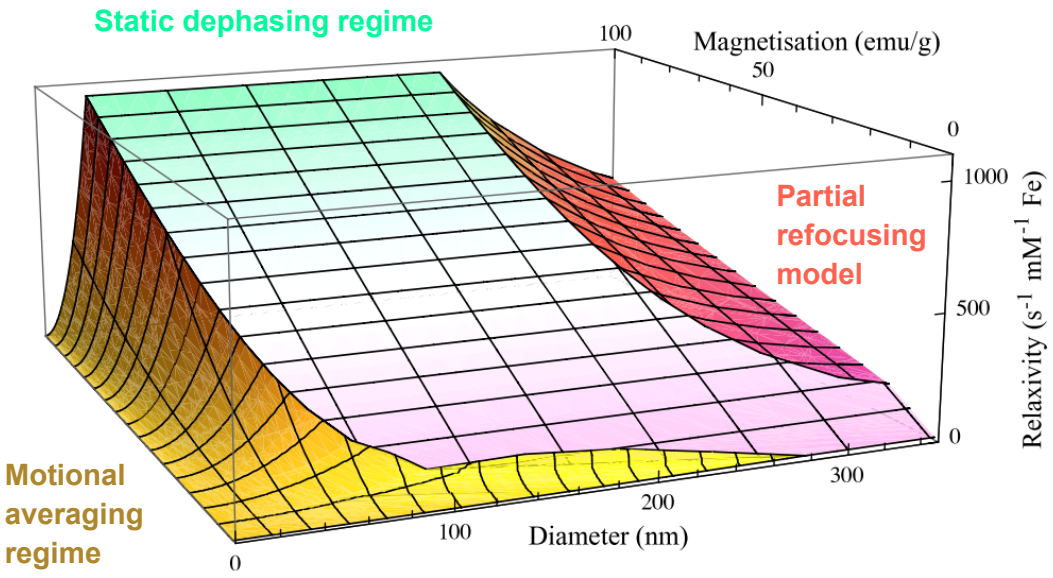

Figure 5-5. A graph showing the different regimes of transverse relaxivity depending on the diameter and specific magnetization, the boundary between SDR and PRM corresponds to t_e = 1 ms (in PRM, r_2^* remains at the maximum value corresponding to the SDR one). Adapted from [319].

Many other models have been proposed dealing mostly with the relaxivity at low magnetic fields to explain the nuclear magnetic relaxation dispersion (NMRD) profiles, which characterize the ^{1}H relaxation rates measured by the field cycling method over a broad range of low Larmor frequencies. However, most of these models usually converge to one of the three models above at the high-field limit. For example, the two-site *chemical exchange model* describes the relaxation in the transition between MAR and SDR for particles of the intermediate size through a *visit-limited regime*, analogically to a chemical exchange between regions with strong gradients close to particles and farther regions with weaker gradients (defined similarly to PRM) [327,328]. Another interesting approach is the *rigid dipole model* for particles with high anisotropy and negligible Néel relaxation [329,330].

Standard models assume that the particles are formed by single crystals, however, **aggregation** of such nanocrystals can have a significant impact on the relaxivity, both positive and negative. The effect of clustering and the shape of aggregates have attracted considerable attention [319,325,331,332] and have been analyzed mostly with the help of Monte Carlo simulations. Examples of mostly studied shapes of aggregates of spherical particles (e.g., in [331]) are depicted in Figure 5-6. The relaxivity of dense spherical aggregates of small SPM nanoparticles, which would fall within MAR if considered individually, increases with the number of particles N_{ag} in the aggregate as $r_2 \propto N_{ag}^{\alpha}$ with $\alpha = 0.18–0.55$ [331,333,334] (in [334], $\alpha =$

0.44). Such an aggregate can be regarded in the analysis as a similarly sized single particle. As regards the density of the aggregate, if both the individual particles and the whole aggregate are in MAR, the relaxivity of the aggregate decreases with increasing distance between the particles. The opposite situation arises for larger particles that would fall within PRM. The analysis of low-dense aggregates might, however, require allowing diffusion of water among the particles in the aggregate [323,331]. If the particles form a dense shell, their relaxivity is comparable to a dense spherical aggregate of the same radius. In linear aggregates, the relaxivity in MAR decreases with the increasing interparticle distance, whereas it increases in PRM. In general, spherical/spherical-shell aggregates provide higher relaxivity than linear ones. Nevertheless, in all studied cases, the relaxivity of an aggregate that falls within SDR does not depend on the aggregate type and shows only weak dependence on the aggregate parameters, such as the interparticle distance [331].

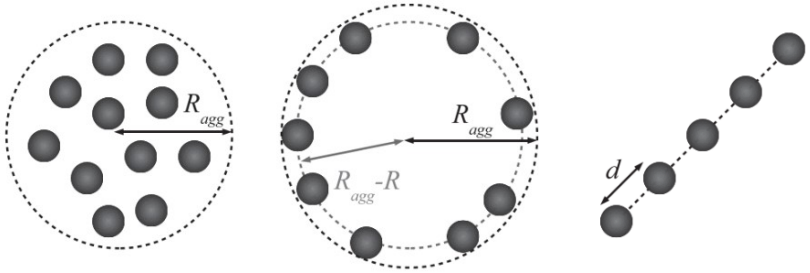

Figure 5-6. Different types of aggregates studied in [331]: spherical, spherical-shell, and linear aggregates. Adapted from [331].

Interestingly, it has been demonstrated that irregular **shapes**, such as those in Figure 3-2, enhance the relaxivity of nonspherical nanoparticles. The particles have not only a higher surface-to-volume ratio compared to spherical particles of the same volume, but they also reach inhomogeneous magnetic states (see Figure 2-11) that introduce additional magnetic field inhomogeneities experienced by water molecules. The same mechanism applies also in the case of nonhomogeneous aggregates of the particles [335] (for an example of the magnetic field around an asymmetrical pair of a nonspherical particle and a smaller sphere see Figure 5-7).

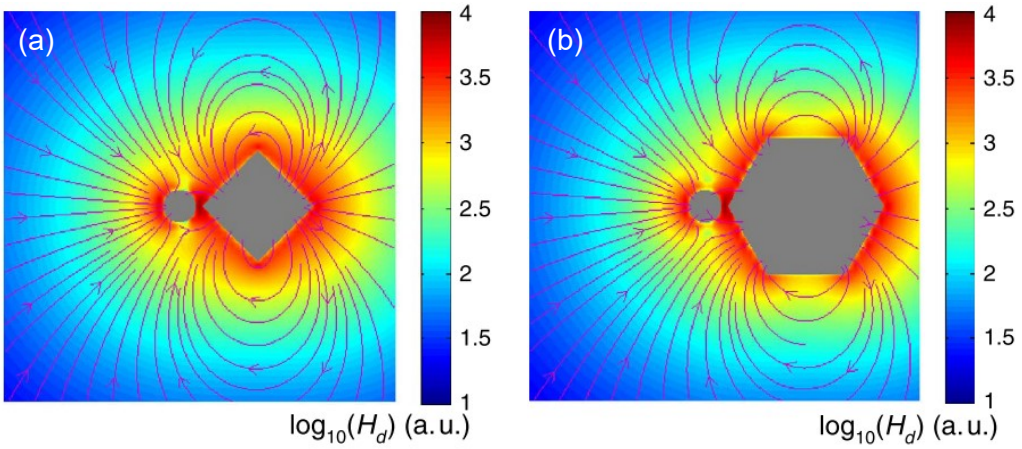

Figure 5-7. Calculated demagnetizing fields around a pair of a 5 nm spherical particle and (a) a cube and (b) a hexagonal plate with 12 nm edges, in the external field of 7 T (applied from left to right). The distance between the particles is 1 nm. Adapted from [335].

Moreover, as the surface of the nanoparticles should ensure their colloidal stability and enhance biocompatibility, the particle **coating** can play a crucial role in the resulting relaxivity. The coating represents the contact zone of the particles and the medium and modifies the interaction between them. It enlarges the distance of the closest approach, pushing the water molecules farther from the magnetic cores to regions with a lower dipolar magnetic field, which decreases as $\sim R^{-3}$ according to the expression (5.7). At a larger distance, also the magnetic field gradients are weaker and the field of an irregular particle has a more dipolar character. The related decrease in $\Delta\omega$ and the increase in apparent particle size (while keeping the same magnetic moment of the core) reduce the relaxivity and shift it towards the MAR. In contrast, the coating can prolong the residence times of water molecules closer to the particle and slow down the diffusion, or provide available binding sites for water molecules, which could increase the relaxivity [336]. This mechanism was demonstrated for example on nanoparticles functionalized with casein – a milk protein with high affinity to water, which both enhances the retention time of water molecules and contains hydrated functional groups that can exchange with the bulk water [337]. To conclude, the enormous complexity of the system and relaxation mechanisms involved does not allow a simple interpretation of the data based on the aforementioned theoretical models. For example, in [338], the authors demonstrated identical relaxivity of $La_{0.75}Sr_{0.25}MnO_3$ nanoparticle clusters with the average size of the cluster 34-51 nm coated with amorphous silica of thicknesses 15-38 nm, whereas the relaxivity of the clusters with the silica thickness of 54 nm decreased only mildly compared with the sample with the thinnest shell (see Fig. 4b in [338]).

5.1.5 Results regarding the relaxivity

We devoted particular attention to the analysis of various parameters influencing the transverse relaxivity and comparison of the experimental data with theoretical models. Our data were obtained for aqueous suspensions of nanoparticles, which were either largely SPM (ferrites) or in the blocked state (pure and doped epsilon polymorph of Fe_2O_3). The examined nanoparticles provided values of transverse relaxivity that were comparable to once commercially approved CAs or even exceeded them [339], e.g., in the case of titania or silica-coated Mn-Zn ferrites [D1]. The combination of the particle sizes and echo times that we employed restricted our discussion to MAR and SDR models. In the following, we will briefly mention selected results obtained within this thesis.

Temperature dependence

The analysis of the temperature dependence of relaxivity has been one of the main topics of this thesis. According to expressions (5.10) and (5.11), two main temperature-dependent parameters define the behavior of relaxivity: (i) magnetization of the particles, which decreases with rising temperature, and (ii) the self-diffusion coefficient of water, which increases with temperature and can be modeled by the Speedy-Angell power-law $D(T) = D_0 \left(\frac{T}{T_s} - 1\right)^{\gamma_{SA}}$. Here, $D_0 = 1.635(2)\cdot10^{-8}$ m^2 s^{-1}, $T_s = 215.1(12)$ K and $\gamma_{SA} = 2.06(5)$ [340]. As MAR and SDR follow different temperature dependence, $r_{2,MAR}(T) \propto M^2(T)/D(T)$ and $r_{2,SDR}(T) \propto M(T)$, it should be possible to determine the individual contributions of the two regimes based on the shape of $r_2(T)$. Moreover, the parameters determining the transition between the MAR and SDR regimes are temperature-dependent as well (see Figure 5-4). The combination of the regimes within one system can arise due to the size distribution of particles in real samples, which is never as sharp as the delta function but usually follows the log-normal distribution [341], or even in a system of monodisperse particles on the verge of the transition between the regimes.

The available instrumentation enabled us to measure the temperature dependence of relaxivity in the external magnetic fields of 0.47 T (Bruker Minispec 20mq relaxometer with the corresponding ^{1}H Larmor frequency of 20 MHz) and 11.75 T (Bruker Avance III HD NMR spectrometer, 500 MHz), whereas the temperature range was limited to ~5–70 °C by technical factors and fast evaporation at higher temperatures.

In the first publication on this topic included in this thesis [D1], we compared the absolute values of relaxivities of different magnetic phases coated with similarly

thick silica layers ($e \approx 14$–19 nm): La-Sr and La-Na manganites (LSMO, LNMO, the size of magnetic cores d_c – clusters of crystallites – roughly ~50 nm), Mn-Zn and Co-Zn ferrites (MZFO, CZFO, $d_c \sim 30$ nm), and further MZFO with different types of surface coating (citrate, silica, titania; see Figure 5-8a-c); for relaxivities and compositions see Figure 5-8 and its caption. The measured relaxivity was further qualitatively compared to the evolution of the temperature-dependent parameters in MAR and SDR (see Figure 5-9 for selected samples). The magnitude of relaxivity of different magnetic phases correlated well with their magnetization, MZFO and LSMO having both the highest magnetization and relaxivity. LSMO consisted of larger particles, which, together with the high magnetization, shifted the sample practically into SDR. In contrast, LNMO has a Curie temperature of 36 °C, which results in a rapid decrease of its relaxivity above room temperature. The influence of the coating on the relaxivity, taking an example of MZFO, reflected the different character of the resulting core-shell nanoparticles. Citrate forms only a monomolecular layer (see Section 3.2.1) at the surface of individual nanoparticles, allowing water molecules the closest approach to the magnetic cores. Coating the MZFO particles with uniform silica shells with a thickness of 19 nm led to an increase in the distance of water molecules from the magnetic cores, which shifted r_2 to lower values and closer to MAR (see Figure 5-9). The rapid process of encapsulation in titania leads to larger aggregates of MZFO particles with a broad size distribution, which placed the system into the SDR, possibly even the PRM regime.

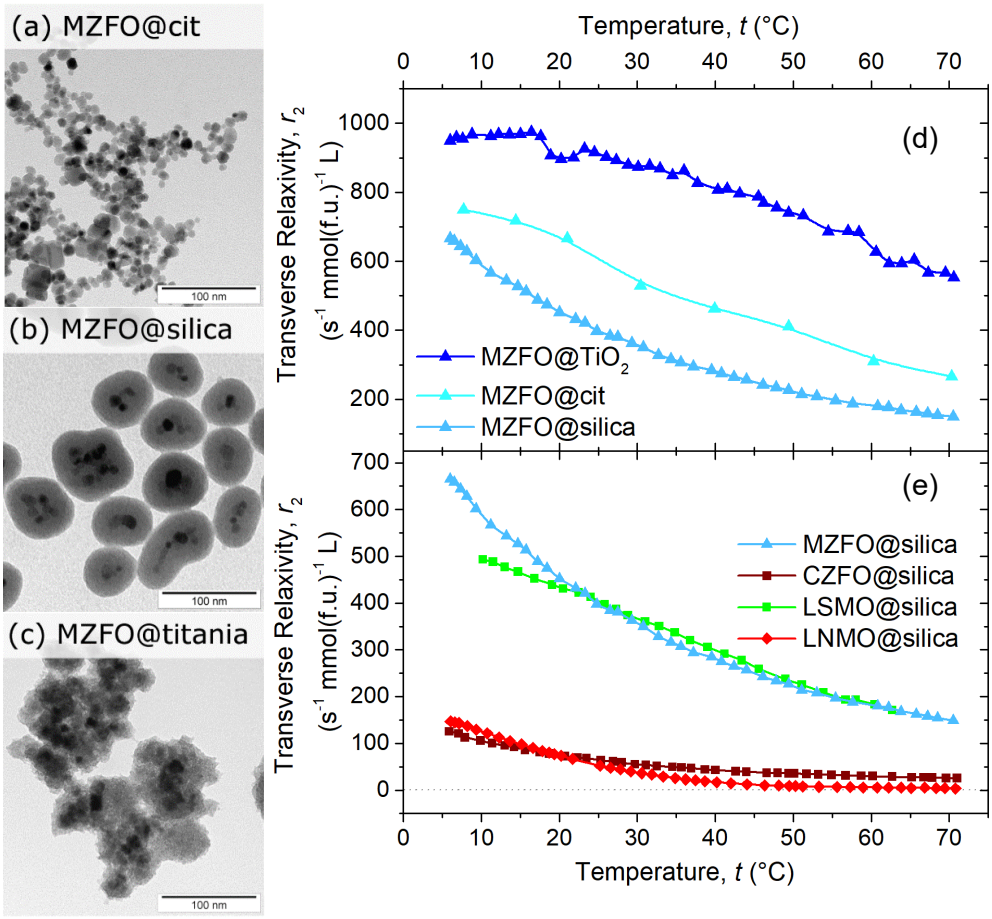

Figure 5-8. TEM images of $Mn_{0.61}Zn_{0.42}Fe_{1.97}O_4$ (MZFO) nanoparticles (a) stabilized with citrate, (b) encapsulated in silica and (c) in titania (the scale marks 100 nm). The comparison of transverse relaxivity at 0.47 T of (d) MZFO with different coatings and (e) different nanoparticles coated with silica (CZFO – $Co_{0.44}Zn_{0.70}Fe_{1.86}O_4$, LSMO – $La_{0.65}Sr_{0.35}MnO_3$, LNMO – $La_{0.8}Na_{0.2}MnO_3$). Adapted from [D1].

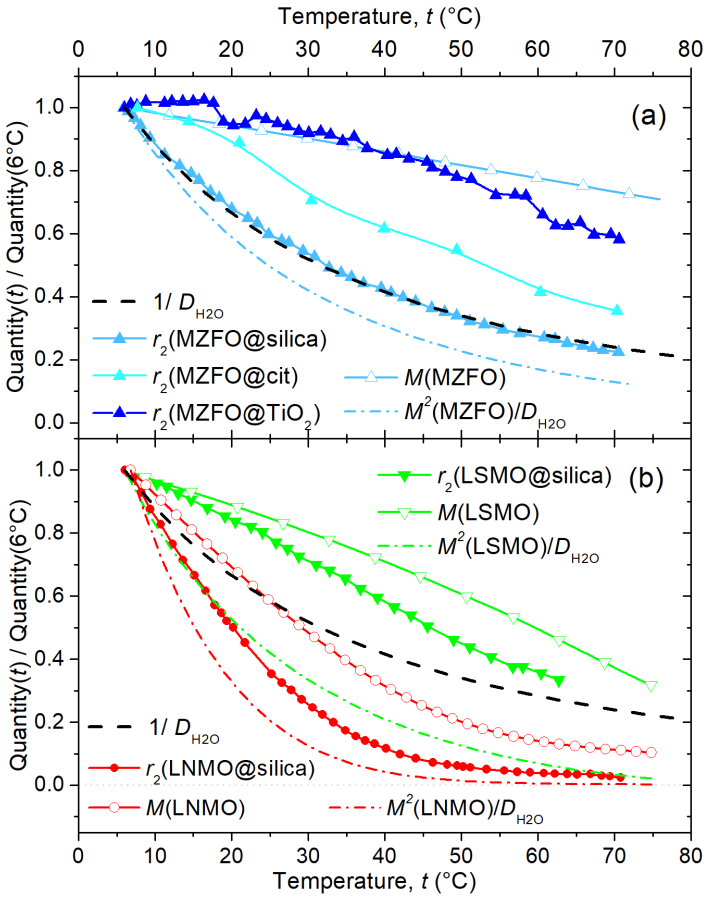

Figure 5-9. Example of the analysis of $r_2(T)$ at 0.47 T of (a) MZFO with various coatings, (b) manganites in amorphous silica. The measured relaxivity and dependences $r_{2,\mathrm{MAR}}(T) \propto M^2/D$, $r_{2,\mathrm{SDR}}(T) \propto M$ and for comparison also $1/D$, were rescaled to $r_2(6\ °\mathrm{C})$. Adapted from [D1].

In several studies, we chose the ε-Fe_2O_3 system and its doped counterparts as an interesting material with high coercivity, unprecedented in relaxometry studies and biomedical research in general. We were interested in the impact of the blocked state, i.e., nonexistent Néel relaxation at the NMR time scale, on the transverse relaxivity, which is manifested most importantly in the field dependence (see below). Specifically, we studied the relaxivity of ε-Fe_2O_3 [D3] and its analogs doped with aluminum [D5] and gallium [D11], [D7] and we developed a regression model to fit the temperature dependence of r_2 by the combination of MAR and SDR. This model, presented in detail in our recent study [D11], is derived based on expressions for relaxivity in MAR and SDR, (5.10) and (5.11), and parameters τ_D and $\Delta\omega$, (5.6) and (5.9). Further, we assume that $r_{2,\mathrm{SDR}} \cong r^*_{2,\mathrm{SDR}}$ and that the samples are comprised of spherical particles. Then the relaxivity of the sample can be written as

$$r_2(T) = s'\left[w_{\mathrm{MAR}}(T) r_{2,\mathrm{MAR}}(T) + w_{\mathrm{SDR}}(T) r_{2,\mathrm{SDR}}(T)\right], \qquad (5.15)$$

where s' is a refinable parameter scaling the fit to the experimental values, $w_{\mathrm{MAR}}(T) = a + bT$ is a temperature-dependent weight of MAR described by empirical coefficients a and b, whereas $w_{\mathrm{SDR}}(T) = 1 - w_{\mathrm{MAR}}(T)$ is the weight of SDR. By substituting the quantities in (5.15) for the expressions mentioned above, we arrive at

$$r_2(T) = s\left[A \frac{M_{\mathrm{core}}^2(T)}{(T/T_{\mathrm{S}} - 1)^{\gamma_{\mathrm{SA}}}} w_{\mathrm{MAR}}(T) + M_{\mathrm{core}}(T)\left(1 - w_{\mathrm{MAR}}(T)\right)\right], \qquad (5.16)$$

$$s = s' \frac{4\pi\mu_0 \gamma M_{\mathrm{w}} d_{\mathrm{c}}^3}{9\sqrt{15}(d_{\mathrm{c}} + 2e)^3},$$

$$A = \frac{4\mu_0 \gamma \rho d_{\mathrm{c}}^3}{15\sqrt{15}\pi D_0 (d_{\mathrm{c}} + 2e)}.$$

Here, s is the overall refinable scale, M_{w} and ρ the molar mass and the density of the magnetic phase, d_{c} is the size of the magnetic core (an individual crystallite or their cluster) and e the thickness of the coating, $M_{\mathrm{core}}(T)$ is the magnetization of the magnetic phase (in the case of particles with high coercivity such as the epsilon phase, magnetization measured in a suspension or obtained by extrapolation from high fields in a powder sample). This model enables a quantitative estimate of the contributions of MAR and SDR. Although it might be improved by introducing the log-normal size distribution of magnetic cores combined with the temperature-dependent critical size d_{SDR} according to formula (5.12), the complexity of such a model would extend beyond the information comprised in the simple monotonous curve.

We employed this model (5.16) to analyze the temperature dependence of transverse relaxivity of ε-$Fe_{1.76}Ga_{0.24}O_3$ nanoparticles coated with an amorphous silica layer of various thicknesses (~6–24 nm) in two magnetic fields [D11]. Figure 5-10 both depicts the measured data of $r_2(T)$ and shows the fit of the data by the expression (5.16) in two extreme examples.

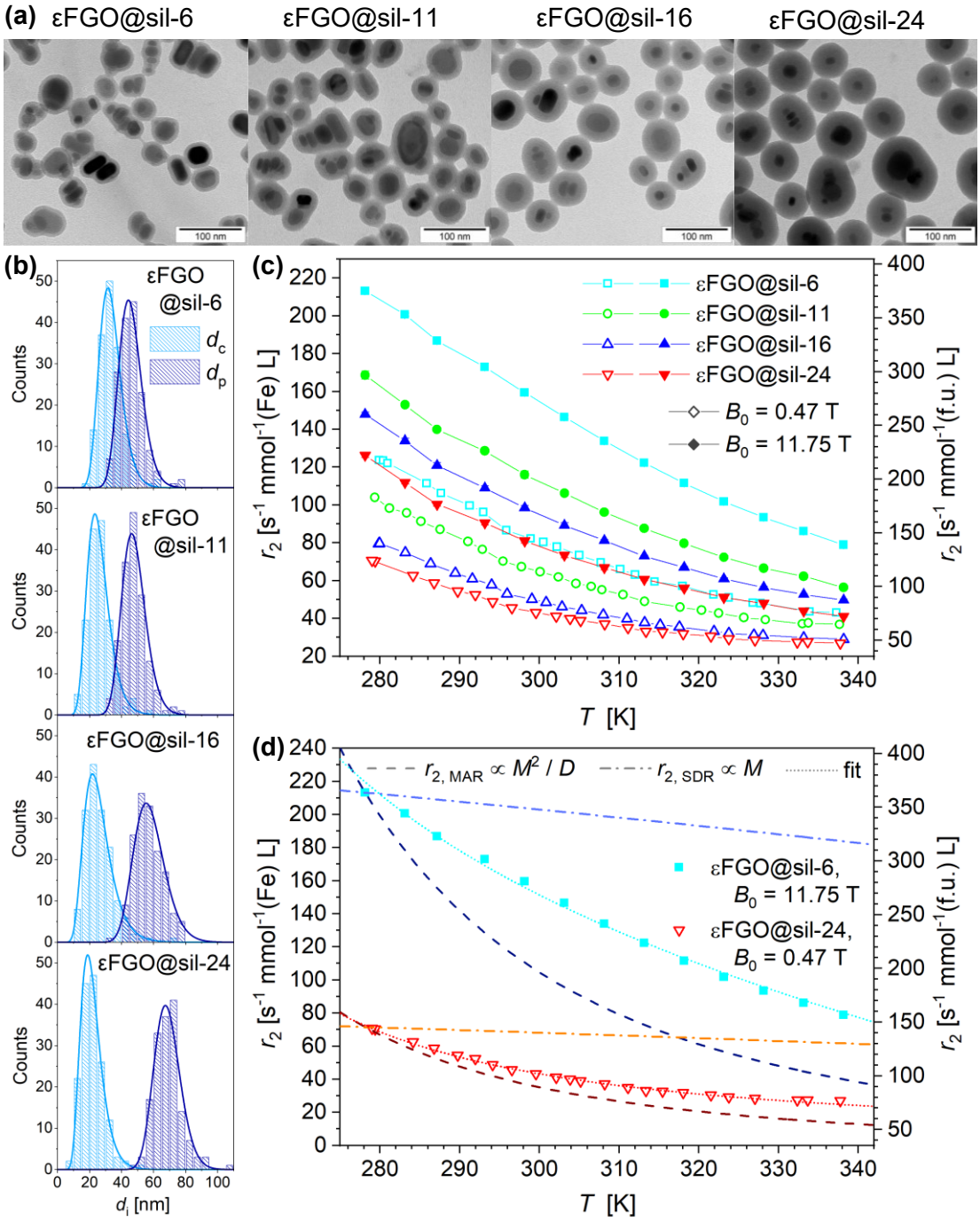

Figure 5-10. Silica-coated ε-$Fe_{1.76}Ga_{0.24}O_3$ nanoparticles (the number in the sample code indicates the coating thickness in nanometers) and their transverse relaxivity: (a) TEM micrographs, (b) size distributions of magnetic cores d_c (possibly containing several crystallites) and whole coated particles d_p obtained from the analysis of TEM micrographs and fitted with the log-normal function, the mean size of individual crystallites was 11 nm; (c) the experimentally determined temperature dependence of r_2 at 0.47 T (empty symbols) and 11.75 T (filled symbols), and (d) application of the model (5.16) for analysis of the samples with the largest weight of MAR (εFGO@sil-24 at 0.47 T) and SDR (εFGO@sil-6 at 11.75 T). Similarly to Figure 5-9, the limiting theoretical curves of $w_{MAR}(T) = 1$ and $w_{SDR}(T) = 1$ are shown, rescaled to r_2(278 K). Adapted from [D11].

By using the regression model (5.16), several general conclusions can be drawn from our datasets on the ε-Fe_2O_3 system:

(i) These particles are mostly in MAR in the examined range of temperatures and magnetic fields.

(ii) Even a small fraction of particles acting in SDR can significantly influence the shape of $r_2(T)$ since the relaxivity in SDR is much larger, for example, ~10–60 times larger than in MAR in the system of ε-$Fe_{1.76}Ga_{0.24}O_3$ nanoparticles at 278 K [D11].

(iii) The ratio of particles in SDR increases with decreasing thickness of the coating (combined effect of more coated clusters and increasing the parameter $\Delta\omega\tau_D \propto d_c^3/(d_c + 2e)$).

(iv) Increasing temperature shifts the system rapidly towards MAR due to the accelerated self-diffusion of water – higher temperature facilitates the fast motion of the molecules among the magnetic particles and promotes the averaging of local field inhomogeneities experienced by ^1H nuclei.

(v) MAR strongly prevails at the low magnetic field (0.47 T), probably because of the limited contribution of coated clusters (see below).

(vi) At high fields (11.75 T), the magnetic moments of individual crystallites in the clusters are aligned along the applied field (see hysteresis curves in Figure 4-21a, Figure 5-11b, and Figure 5-12b) and the larger overall moment of the clusters increases the weight of SDR.

(vii) The above-mentioned points correlate well with the changes in d_{SDR} (Eq. (5.12)) compared to the size distribution of the coated particles (see, e.g., Figure 5-10b) – d_{SDR} increases with the rising temperature and thickness of the silica coating; consequently, more particles fulfill the Redfield condition and act in MAR. At the same time, d_{SDR} decreases at higher applied magnetic fields, cutting a larger fraction of particles off to SDR.

Dependence on the external magnetic field

In the relaxivity models, the only field-dependent quantity is the particle magnetization contained in the $\Delta\omega$ expression, i.e., $r_{2,MAR}(B_0) \propto M^2(B_0)$ and $r_{2,SDR}(B_0) \propto M(B_0)$. Nevertheless, the actual magnetic moments of individual particles or clusters are of higher relevance than the magnetization of a powder sample. While SPM nanoparticles in a powder generate a Langevin-like magnetization curve with negligible hysteresis, particles in the blocked state such as ε-Fe_2O_3 exert a large hysteresis. For this reason, it is particularly useful to

measure the magnetization curve of a suspension of blocked particles, which can provide deeper insight into changes in the magnetization of individual particles in the suspension. Since the external magnetic field in standard NMR and MRI instrumentation is fixed, each point in the field dependence of relaxivity requires using a different instrument – in the studies included in this thesis, we employed two relaxometers Bruker Minispec 20mq (0.47 T, 20 MHz) and 40mq (0.94 T, 40 MHz), clinical MRI scanners Siemens Magnetom Avanto (1.5 T, 64 MHz) and Trio (3.0 T, 128 MHz), a MRI experimental scanner for laboratory animals Bruker Biospec 47/40 USR (4.7 T, 200 MHz), and in some cases also a NMR spectrometer Bruker Avance III HD (11.75 T, 500 MHz). Because obtaining data for a field dependence of transverse relaxivity in higher magnetic fields, which are more relevant for the clinical practice than fractions of tesla, is not that straightforward, the r_2 field dependence of nanoparticle CAs is strongly underrepresented in the literature (from the notable exceptions let us mention for example [342], where the authors use a similar strategy employing several relaxometers at low fields and a 300 MHz NMR spectrometer, or [343] employing a recently emerged NMRD instrumentation modified for T_2 measurements by the fast-field-cycling technique).

The dependence of relaxivity on the external magnetic field was particularly interesting within the series of the epsilon polymorph of Fe_2O_3 and related phases with high magnetocrystalline anisotropy and large hysteresis in their powder forms. In [D3] and [D5], we measured both the magnetization curves of suspensions of silica-coated particles and the field dependence of their relaxivity, as shown in Figure 5-11 (ε-Fe_2O_3) and Figure 5-12 (ε-$Al_{0.23}Fe_{1.77}O_3$). To understand these results, one must take into account that the coating procedure provides not only individually coated crystallites but also a certain fraction of clusters of crystallites coated as a whole (see for example TEM images in Figure 5-11a or Figure 5-12a). In the virgin sample, the magnetic moments of individual crystallites that form the clusters adopt the most favorable orientation to minimize the magnetostatic energy of the cluster, decreasing thus the overall magnetic moment of the cluster. If we follow the virgin curves of the aqueous suspensions (Figure 5-11b and Figure 5-12b), the practically discrete rise at very low fields marks the reorientation of the magnetic particles (including the coated clusters according to their overall moment) to the direction of the external field. In a rather simplified view, the magnitude of this initial rise negatively correlates with the relative occurrence of nonlinear clusters, as more crystallites can be found in clusters in samples with thinner silica shells. Upon increasing the applied field, the particles undergo magnetization processes as in the immobilized particles (see Figure 5-12a for the

virgin curve of the powder sample). In clusters, the magnetic moments of individual crystallites, originally oriented along their easy axes, first reorient within the system of their easy axes to a direction more favorable in the applied field, and when the magnitude of the field increases further, the moments gradually tilt into the direction of the field. After reaching the irreversibility limit, the magnetization loops further follow the anhysteretic Langevin-like curves, dominated by the reorientation of the freely rotating particles when the direction of the field is altered. Notably, a substantial paraprocess present in the immobilized sample is preserved also in particles in the suspensions. The presence of irreversible processes, which enhance the overall magnetic moment of the clusters consisting of magnetically blocked particles, indicates that relaxivity at lower fields up to ~4 T should depend on the magnetization history. Interestingly, the transverse relaxivity of ε-$Al_{0.23}Fe_{1.77}O_3$ nanoparticles stabilized with citrate (see Figure 5-12c) follows a different trend than the silica-coated counterparts. The absence of tightly bound clusters results in higher relaxivity at low fields than in the case of the silica-coated samples because the virgin curve of individually rotating crystallites already follows the Langevin-like curve. Moreover, the lack of clusters might also lead to lower relaxivity at high fields than for the sample with the thinnest silica coating since, as discussed above, the presence of clusters increases the relaxivity. However, in the other silica-coated samples from the same series, the ratio of crystallites in clusters decreases with the increasing thickness of the coating, and the enhancement of r_2 by the clusters is also counterbalanced by the corresponding increase in the distance of the closest approach of water molecules.

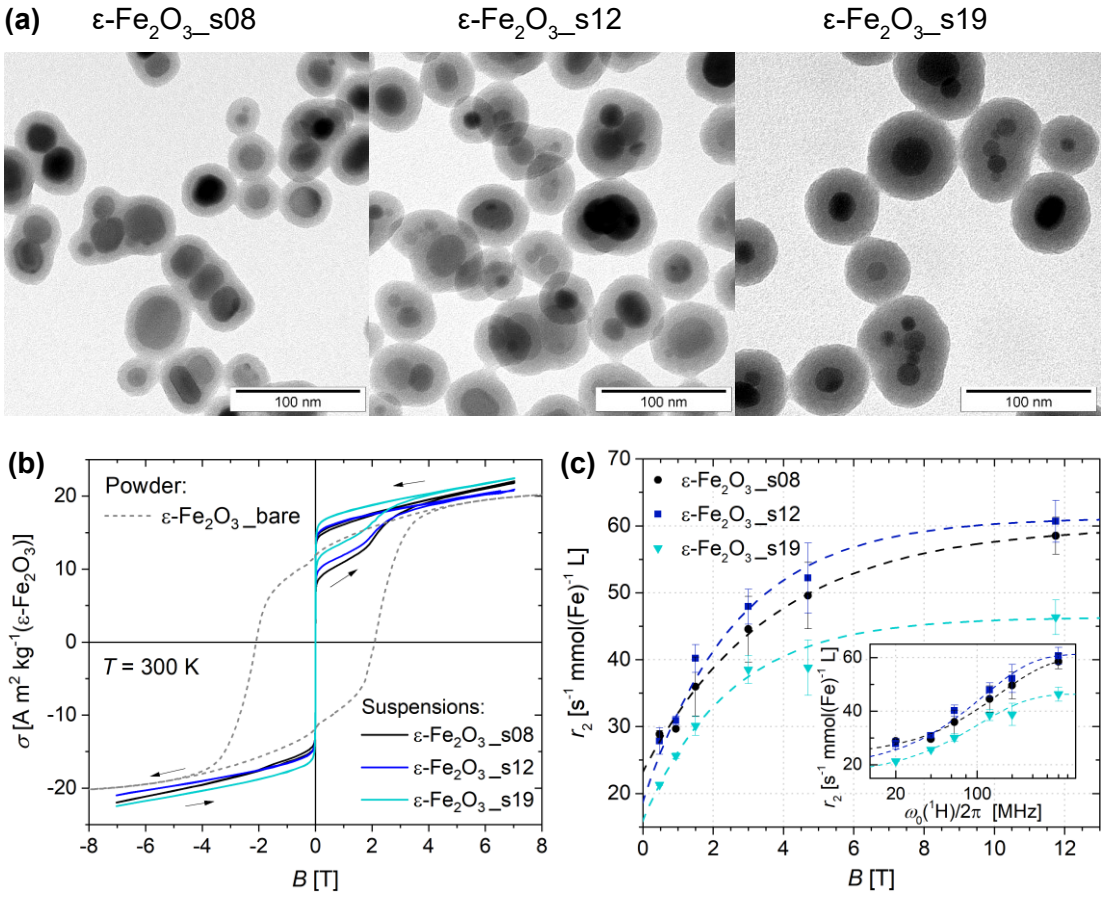

Figure 5-11. (a) TEM micrographs of ε-Fe_2O_3 nanoparticles coated with silica (the number in the sample code indicates the thickness of silica in nanometers), which reveal a certain fraction of clusters coated as a whole; (b) virgin and magnetization curves of their suspensions at 300 K, accompanied with the hysteresis curve of the bare powder sample (dashed line); (c) field dependence of transverse relaxivity of virgin suspensions at 313 K (the dashed lines provide only guidelines to the eye). The relaxivity data plotted against the ^{1}H Larmor frequency in the logarithmic scale are shown in the inset for straightforward comparison with NMRD data in the literature. Adapted from [D3].

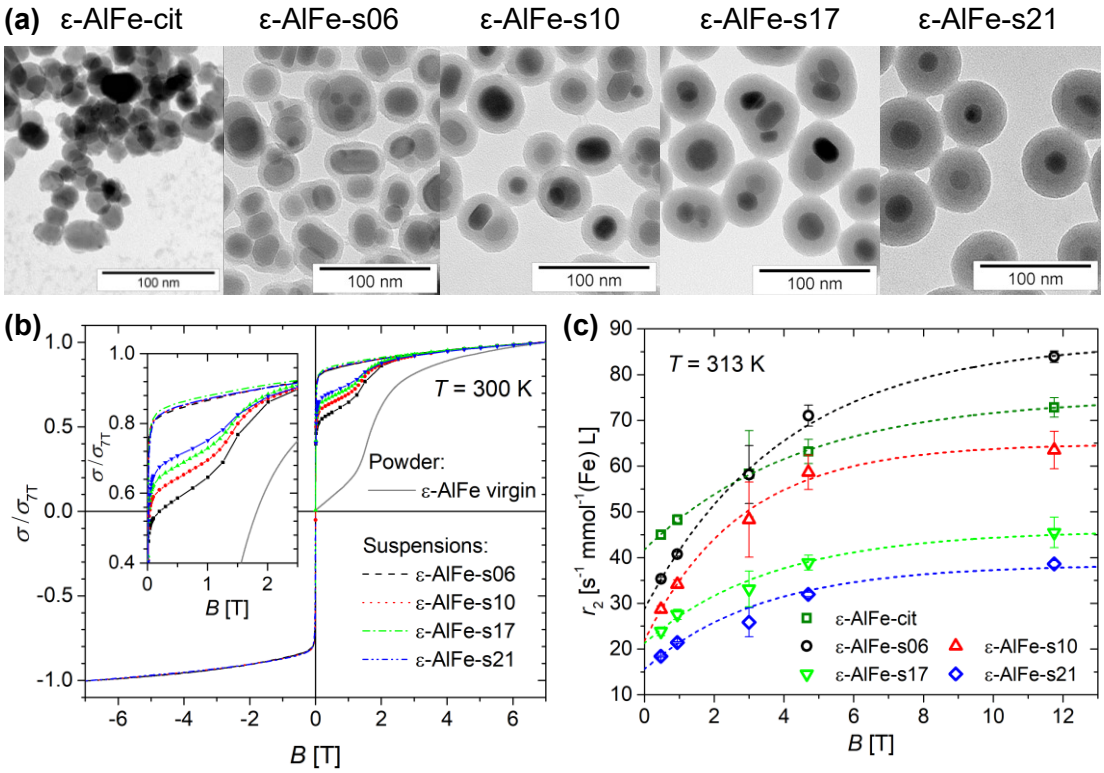

Figure 5-12. (a) TEM micrographs of ε-$Al_{0.23}Fe_{1.77}O_3$ nanoparticles stabilized with citrate (ε-AlFe-cit) or coated with silica (the number in the sample code indicates the thickness of silica in nanometers); (b) the virgin and magnetization curves of suspensions of silica-coated particles at 300 K, with the virgin curve of the bare powder sample (grey line); (c) field dependence of transverse relaxivity of virgin suspensions at 313 K (the dashed lines provide only guidelines to the eye). Adapted from [D5].

Finally, in our study [D10], we focused on the influence of the magnetic state of nanoparticles on transverse relaxivity. As a model system, we chose magnetic nanoparticles based on $Co_xZn_yFe_{3-x-y}O_4$ spinel ferrites, prepared in the form of 10 nm-sized crystallites and coated with silica under the strictly same conditions to obtain particles with comparable sizes ($d_c \approx 31$ nm, $e \approx 11$ nm). This system enabled us to tailor magnetic behavior of the particles from the blocked ferrimagnetic state, over the SPM regime to the vicinity of the paramagnetic state by adjusting the zinc content in the ferrite phase, while keeping all other parameters identical (for ZFC-FC curves and distribution of blocking temperatures see Figure 2-14 and Figure 4-8a). The comparative analysis of the three distinct magnetic behaviors revealed similar trends in temperature and field dependences of relaxivity, only differing in magnitude (for the temperature dependence see Fig. 5b in the study [D10], for the dependence on the magnetic field see Figure 5-13c). Specifically, the increase in relaxivity of the samples was related to the increase in magnetic moments of individual crystallites due to the paraprocess. The field

dependence of transverse relaxivity fell between the limits of MAR and SDR. On this system unrelated to ε-Fe_2O_3, we confirmed that the magnitude of magnetization is of higher importance for the transverse relaxivity than the magnetic state of particles in magnetic fields relevant for clinical MRI.

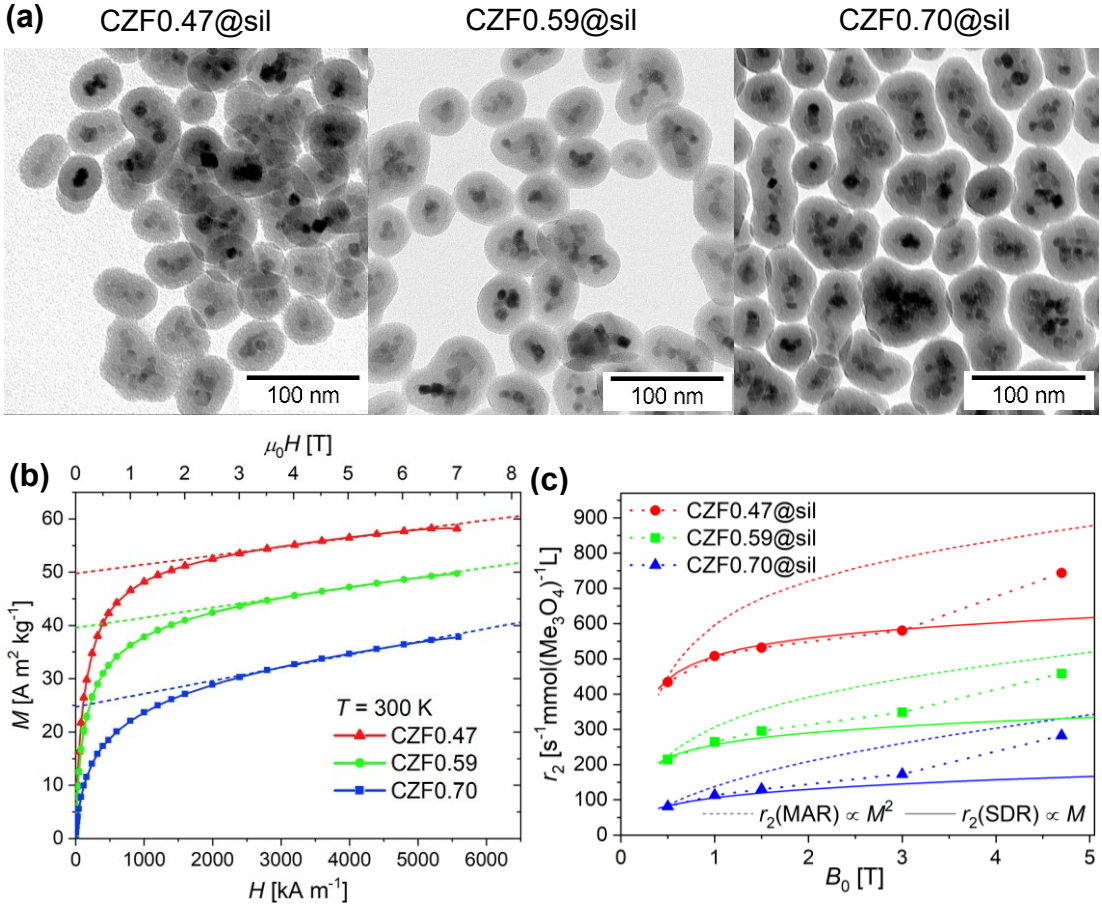

Figure 5-13. (a) TEM micrographs of silica-coated $Co_xZn_yFe_{3-x-y}O_4$ ferrite nanoparticles (denoted CZFy, 3-x-y = 1.96); (b) a detailed view of their magnetization curves at 300 K with linear extrapolation showing the high-field paraprocess; (c) field dependence of transverse relaxivity at room temperature, the boundaries set by MAR and SDR rescaled to r_2(0.47 T) are marked with short-dashed and solid lines, respectively. Adapted from [D10].

Dependence of r_2 on the thickness of the silica shell

Finally, in the series of the doped epsilon phases in [D5], [D7], and [D11], we examined whether the decrease in relaxivity of silica-coated nanoparticles with the increasing coating thickness corresponds to the increase in the distance of the closest approach of water molecules according to the theoretical models. We can approximate the size of the particle in τ_D in the formula (5.6) by $d_c + 2e$ and rescale the dispersion $\Delta\omega$ by $d_c^3/(d_c + 2e)^3$ according to the formulas (5.7) and

(5.8). The relaxivity in MAR then depends on e as $r_{2,\mathrm{MAR}}(e) \propto d_\mathrm{c}^6/(d_\mathrm{c}+2e)^4$ and in SDR as $r_{2,\mathrm{SDR}}(e) \propto d_\mathrm{c}^3/(d_\mathrm{c}+2e)^3$.

The measured dependences for ε-$Al_{0.23}Fe_{1.77}O_3$ and ε-$Fe_{1.76}Ga_{0.24}O_3$ nanoparticles are shown in Figure 5-14, along with rescaled calculated curves. The experimental relaxivity decreases much slower with the increasing silica thickness than predicted by the models. Even considering larger magnetic cores at the tail of the log-normal size distribution acting in SDR does not explain the results, as indicated by the calculated curve for the 9$^{\mathrm{th}}$ decile of d_c in Figure 5-14b. The gradual shift from SDR to MAR expected with increasing coating thickness, as well as the lower ratio of coated clusters in samples with thicker shells, would lead to an even faster reduction of r_2. Speculating about possible enhancement of the relaxivity beyond the simple models described above, we should consider that any relevant process enhancing the relaxivity would have to take place at a time scale comparable to $(\Delta\omega)^{-1}$, i.e., ~1–10 μs ($\Delta\omega \sim$ 0.1–1 MHz) in our case. Molecular dynamics simulations showed that in the vicinity of a silica surface, water up to three molecular layers (~9 Å) has properties distinct from bulk water, especially, the self-diffusion coefficient decreases by an order of magnitude [344]. Nevertheless, the self-diffusion of water at the solid-liquid interface is still fast enough to contribute to relaxivity [D5]. The observed slow decrease of $r_2(e)$ might also indicate that silica does not form an impenetrable barrier for water molecules and the relaxivity is further enhanced by slow diffusion in the coating layers, which effectively reduces the apparent shell thickness.

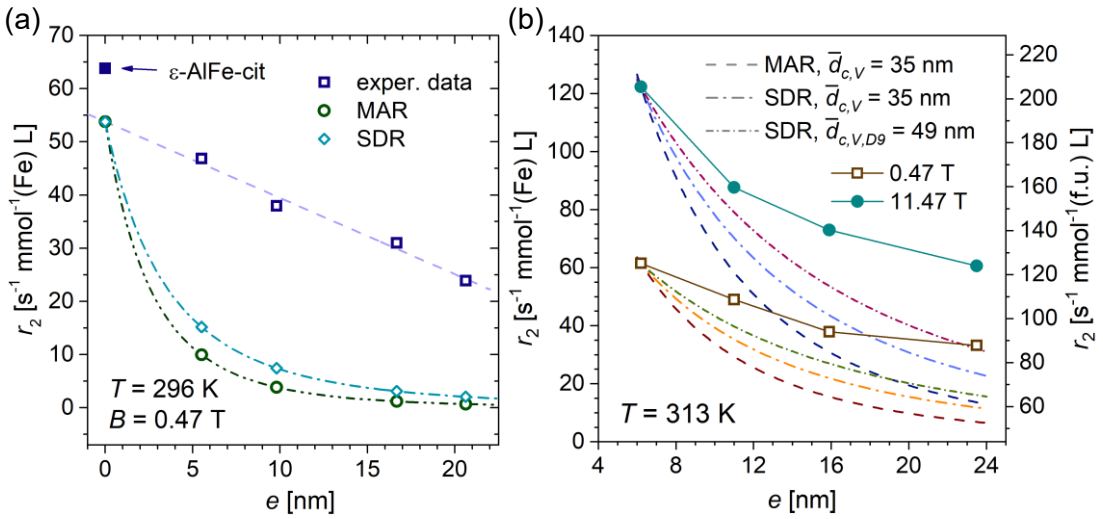

Figure 5-14. The dependence of transverse relaxivity on the thickness of the silica coating e in the (a) ε-$Al_{0.23}Fe_{1.77}O_3$ and (b) ε-$Fe_{1.76}Ga_{0.24}O_3$ systems for selected temperatures and fields. In (a), the data are fitted by purely empirical linear dependence and accompanied by theoretical MAR and SDR curves. These curves were calculated based on the median size of the crystallites from TEM and further rescaled to $r_2(0)$, which was obtained by extrapolation of the experimental points; adapted from [D5]. In (b), $r_2(e)$ is shown for two magnetic fields, the MAR and SDR theoretical curves based on the volume-averaged size of magnetic cores 35 nm and the ninth decile 49 nm are rescaled to r_2(6 nm); adapted from [D11].

MRI experiments

Although MRI scanners (1.5, 3.0, and 4.7 T) were primarily involved to achieve additional points in the field dependence of relaxivity, we performed also a few MRI experiments just for imaging. Within the ε-Fe_2O_3-based series of [D3], [D5], and [D11], we wanted to visualize the contrast effect generated by the magnetically blocked nanoparticles in an ultra-high-field MRI at 11.75 T. An example of MRI scans of aqueous suspensions of silica-coated ε-$Fe_{1.76}Ga_{0.24}O_3$ nanoparticles in capillaries, supplemented by the comparison to the traditional contrast agent Resovist and pure water, is shown in Figure 5-15.

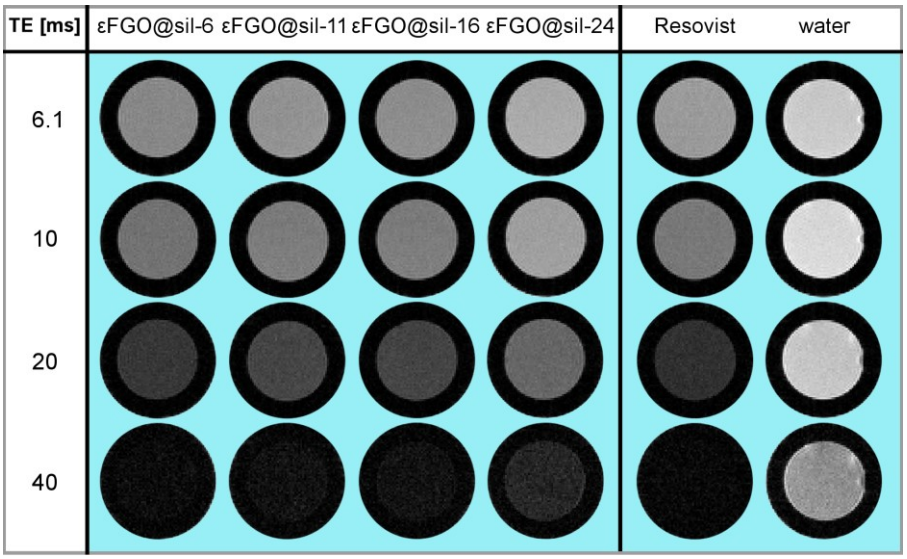

Figure 5-15. Ultra-high-field MRI of aqueous suspensions of silica-coated ε-$Fe_{1.76}Ga_{0.24}O_3$ nanoparticles and Resovist of the identical concentration 0.4 mmol(Fe) L^{-1} in capillaries. All samples were scanned together, the scans were acquired at 11.75 T with the T_2-weighted multi-slice-multi-echo pulse sequence and TR = 3 s. Reproduced from [D11].

In the framework of [D5], we performed also a pilot study probing the contrast generation *in vivo* in a mouse model by ε-$Al_{0.23}Fe_{1.77}O_3$ nanoparticles coated with a silica layer of 17 nm. The mice were scanned at 1 T, 30 min after intravenous application of 100 μL of the particle suspension. The images are shown in Figure 5-16. Although the low dose of CA led to a negligible contrast change (Figure 5-16b), with the increasing dose the hypointensity in the liver was more pronounced (Figure 5-16c), and at 20 mmol(Fe) L^{-1}, the enhanced relaxation decreased the signal in the whole body (Figure 5-16d). Considering the rather low magnetic field and that the suspension of these magnetically blocked particles was not exposed to high fields before the administration, we expect a markedly stronger effect in clinical MRI scanners with fields typically 1.5–3.0 T (but possibly up to 7 T).

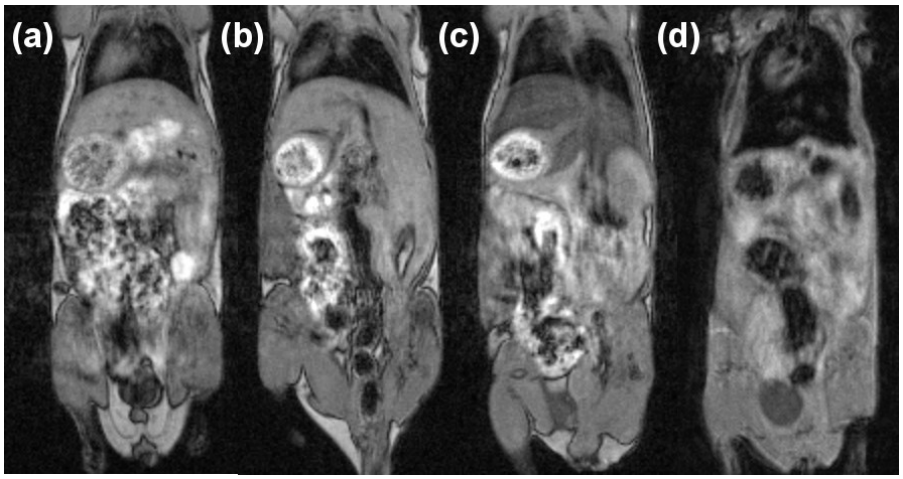

Figure 5-16. *In vivo* MRI scans of mice at 1 T acquired with a strongly T_2^*-weighted gradient-echo sequence (a) before the CA administration, and 30 min after the intravenous administration of the suspension of ε-$Al_{0.23}Fe_{1.77}O_3$ nanoparticles coated with 17 nm silica with concentrations (b) 5 mmol(Fe) L^{-1}, (c) 10 mmol(Fe) L^{-1}, and (d) 20 mmol(Fe) L^{-1}. Reproduced from [D5].

5.1.6 Magnetic nanoparticles as CAs in clinical practice

The general disadvantage of magnetic nanoparticles as primarily T_2-CAs consists in generating negative contrast, i.e., the lack of signal. The loss of signal might be sometimes ambiguous and instrumental sources of such hypointensity should be excluded. With an example of liver lesions, it was also illustrated that a combined analysis of SPION-enhanced and nonenhanced images is more accurate than the analyses of enhanced images alone [345]. Nevertheless, the disadvantage of generating the hypointensity has been circumvented by targeting tissue in which the healthy cells accumulate the nanoparticles and the malignant cells do not. The SPIONs are removed very fast from the bloodstream by the RES, mostly phagocytic Kupffer cells in the liver. Since the RES cells in the liver are distributed rather homogeneously, the healthy tissue with internalized nanoparticles turns dark. Consequently, the pathologic tissue, which generally does not contain Kupffer cells, appears as light areas. Because no specific targeting modifications, such as advanced organic functionalization or attachment of antibodies, are required, the SPIONs have been widely used for clinical liver imaging for more than 30 years [346].

The first clinical trial using SPIONs for imaging of liver lesions in 15 patients was run in 1988 at the Massachusetts General Hospital in Boston and confirmed increased sensitivity – higher number of detected lesions – and resolution of the images [347]. Since then, two types of SPION formulas have been approved for clinical use in liver imaging: (i) Feridex (Feridex I.V. in the USA, Endorem in

Europe), with the formula known as ferumoxides and coated with dextran, was referred to as AMI-25; (ii) Resovist ([348], also known as Cliavist) with the generic name ferucarbotran and coated with carboxydextran was available in Europe and Japan and referred to as SH U 555A [349]. Nevertheless, both agents were discontinued due to a limited number of applications and concerns about side effects. Feridex, the first approved organ-specific MRI CA, was finally abandoned in 2008 and Resovist remains available only in Japan [346].

Eventually, farmaceutical companies have prioritized the USPION-based CAs, which circulate in the bloodstream for a longer time and thereby offer a broader range of clinical applications. Due to their small size, they can cross the capillary walls more easily and enter a broader range of tissue types, including other components of RES such as lymph nodes and bone marrow. Although their transverse relaxivity is generally lower than in the case of larger SPIONs, their comparatively higher longitudinal relaxivity provides an enhanced T_1 contrast and enables simultaneous analysis of both T_1 and T_2 -weighted images. Basing on a similar mechanism as in the case of liver lesions, USPIONs can be used to visualize the metastases in lymph nodes as well [350,351] (see Figure 2-1a). Other clinical applications comprise, for example, angiography [352] (see Figure 2-1b,c), visualization of inflammation [353], tumor perfusion [354], and the delineation of tumor boundaries, e.g., in the brain [355]. The Clariscan (NC100150, PEG-fero, Feruglose) stabilized with a carbohydrate polyethylene glycol, Resovist S Supravist (USPION analog of Resovist, SH U 555C), and dextran-coated ferumoxtran-10 (AMI-227, Combidex, Sinerem) belonged to clinically applied MRI contrast agents [346,356], however, analogically to SPION CAs, their production has been discontinued. Interestingly, the only USPION currently available for clinical use is ferumoxytol (Feraheme), which was approved as a food supplement, originally to treat iron-deficiency anemia in patients with chronic kidney disease. However, it has been widely used “off-label” as a MRI CA as well, for example, in patients with kidney failure to whom CAs based on gadolinium cannot be administered [354,357].

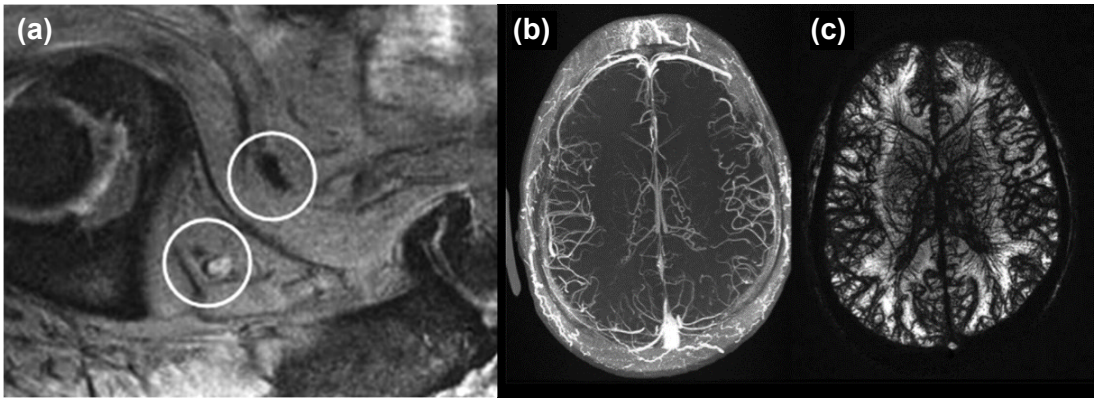

Figure 5-17. USPION-enhanced contrast in MRI: (a) a T_2^*-weighted gradient-echo image showing a normal (top circle) and a metastatic (bottom circle) lymph node in a prostate cancer patient 24 h after the administration of ferumoxtran-10; adapted from [358]. (b) T_1-weighted and (c) T_2-weighted axial images of the brain of a volunteer, obtained by a spoiled gradient-recalled-echo sequence 1–2 hours after intravenous injection of ferumoxytol (dose of 6 mg iron per kilogram of body weight); adapted from [346].

5.1.7 Cell tracking by MRI

Although clinical applications of negative MRI CAs in tumor imaging have recently receded into the background, new imaging opportunities emerge with the technological advances in MRI. One of the promising areas is the tracking of cells *in vivo*, which not only enables imaging of cells in their native environment to improve the fundamental knowledge but can also serve as an important technique accompanying present-day cell therapy. Although most of the related research still pivots on preclinical studies using animal models, since the very first clinical study in 2005 devoted to the tracking of SPION-labeled dendritic cells in melanoma patients [359], numerous clinical studies have been performed mostly under the framework of cell-based therapies [360,361]. For example, novel methods of treatment of chronic conditions such as cancer or autoimmune diseases employ immune cells, whose biodistribution, motility, and viability after the injection belong to crucial factors that determine the success of the therapy, and, at the same time, can be followed upon labeling with negative CAs by MRI [362]. Another type of cell therapy, which can profit from *in vivo* cell tracking, uses stem cells and has already shown encouraging results, e.g., in the treatment of cardiovascular or neurological diseases requiring restoration of function of damaged tissue, such as heart and brain strokes [363].

In principle, the cells of interest can be labeled with magnetic nanoparticles by two distinct approaches. First, the cells are labeled *ex vivo*, outside of the body in cell culture. Some phagocytic cell types such as T-cells can be labeled easily by mere

incubation of the cells in a medium with dispersed nanoparticles, more or less, irrespective of their functionalization. On the other hand, specific surface modification or functionalization can be employed before the incubation with other cell types to facilitate the internalization of particles into cells, e.g., coating with antibodies or polycationic transfection agents such as poly-L-lysine increasing the interaction with the cell membrane [363]. Alternatively, the internalization of nanoparticles into cells can be achieved by disrupting the cell membrane, for example by electroporation, which uses electrical pulses to induce changes in the permeability of the membrane [364], or sonoporation employing ultrasound waves [365]. Although these methods based on a temporary enhancement of membrane permeability are much faster than conventional incubation (several minutes compared to 24/48 h of incubation), they require careful optimization to prevent an increased death rate of treated cells [363].

The second method of cell labeling takes place *in vivo* and relies on phagocytosis of the injected CA by immune cells of the RES, i.e., mostly by monocytes circulating in blood or macrophages in the tissues. These cells tend to cumulate in inflammatory sites, which then enables localization of the inflammation in the body by using MRI [362]. This approach is also behind the clinical imaging of lymph nodes and liver lesions discussed in Section 5.1.6. Another interesting method of *in vivo* cell labeling to monitor processes after a vaccine injection, "magnetovaccination", was introduced in [366]. The authors injected irradiated tumor cells, labeled with SPIONs and modified to express antigens to induce antitumor activities, into a mouse. The dying tumor cells were then captured by dendritic cells, whose migration to lymph nodes and delivery of the antigens could be tracked by MRI. A similar mechanism may distort the results in the tracking of cells labeled *ex vivo* that eventually die and are captured by the immune cells, which follow different migration paths.

MRI enables tracking the target cells noninvasively and in real time, in contrast to biopsies, which are limited to *ex vivo* information at a certain time point. Contrary to nuclear imaging (including positron emission tomography, PET) using radionuclide labeling and requiring a complementary imaging method, MRI readily provides an anatomical context of the cell environment and MRI CAs do not raise concerns about the effect of radiation on the long-term viability of the therapeutic cells [362]. Furthermore, the detection limit of CA-enhanced MRI tracking reaches down to a single cell, as was demonstrated already in 2006 by using micrometer-sized iron oxide particles [367]. However, MRI is not able to distinguish between living and dead cells. In the case of proliferating cells such as

stem cells, either the CA is progressively diluted when distributed rather evenly between daughter cells, which leads to fading signal over time [368], or only a certain fraction of the daughter cell population can be visualized if the distribution of CA during cell division is asymmetrical [369]. Consequently, the MRI tracking employing magnetic nanoparticles as the tracking agent is more suitable for short-term and real-time experiments at the initial stages of the treatment [363].

5.2 Comments on cytotoxicity of magnetic nanoparticles

In size, nanoparticles can be compared to viruses, proteins, or just a couple of pitches of the DNA helix. As such, they can reach intracellular structures and interact with biomolecules [370], for example, disrupt the conformation and functionality of proteins [371]. The evaluation of toxicity of magnetic nanoparticles is one of the necessary steps in the transfer from research laboratories to clinical practice, though it remains the most challenging one. The *in vitro* studies of cytotoxicity in cell cultures provide the first assessment of potential risks and help to determine the safe dose for individual cells. The *in vivo* studies on laboratory animals ensue, aiming to test the dose range derived from *in vitro* experiments in the context of a "useful" dose for the intended application. Moreover, other side effects such as skin and eye irritation, chronic toxicity, or carcinogenicity are assessed [372]. In our studies, we targeted preliminary evaluation of cytotoxicity, therefore we employed only the *in vitro* experiments.

The analysis of cytotoxicity of nanoparticles is a multifactorial problem, and most studies in the literature provide insufficient data in terms of the studied material and biological experiments, while methodical issues are often even more questionable. Not only chemical composition and the crystal phase but also the actual size, shape, or degree of agglomeration and the colloidal stability in the cell medium of the tested nanoparticles play a significant role, though in the analyzed sample they are often a matter of distribution. The surface properties of the coating codetermine the fate of the particles together with their degradation rate. Importantly, different cell types react to identical nanoparticles differently, triggering various reaction pathways and showing different sensitivity, which might lead to conflicting results on cytotoxicity in published studies. A crucial, though sometimes neglected parameter is the purity and sterility of the employed suspension since any impurities can cover the real effect of the nanoparticles under study. Similarly, the aging of the suspension accompanied, e.g., by particle aggregation or leaching of metal ions might distort the results compared to freshly prepared suspensions. The composition of the medium in the cell culture determines the composition and dynamics of protein corona formed around the

nanoparticles. The protein corona is a layer of proteins adsorbed onto the particle surface under physiological conditions (or in a medium that mimics them) and can modify the cellular response to the nanoparticles. The apparent cytotoxicity can also vary significantly based on the incubation period and concentration of the nanoparticles (cell viability determined after a short incubation, for example after 24 h, can be high although significant cytotoxic effects might occur within 48 h or later), as well as the method used to evaluate the viability and condition of the cells.

As no unifying protocol on cytotoxicity evaluation has been established yet, the published studies differ considerably in the aforementioned issues and sometimes even studies by the same authors of the same material can deliver conflicting conclusions [373,374]. Regrettably, even the method for precise determination of the particle concentration in the suspension, one of the crucial parameters, has not been unified and consistently demanded. Moreover, as a rule of thumb, biologically oriented studies do not always provide sufficient material characterization of the nanoparticle system itself and vice versa – the studies focused primarily on material properties tend to oversimplify or disregard biological issues.

In our studies [D4] and [D5], we ran a preliminary evaluation of cytotoxicity by assessing the viability and proliferation of cells incubated with the nanoparticles by the *trypan blue exclusion test*. In this method, the cells after incubation are transferred into a suspension containing trypan blue. Viable cells have intact cell membranes that exclude the dye, whereas the membrane of dead cells lacks integrity and is permeable for the dye, which stains their cytosol blue [375]. The viability is then calculated as the ratio of unstained to all cells observed in light microscopy.

In [D5], rat mesenchymal stem cells were incubated for 48 h with silica-coated ε-$Al_{0.23}Fe_{1.77}O_3$ nanoparticles at 0.35 mmol(Fe) L^{-1} (0.20 mmol(f.u.) L^{-1}). The viability of adherent cells v was evaluated and rescaled to assign 100 % viability to the untreated negative control. The proliferation was characterized by cell gain, $\Gamma = vN_{\mathrm{smp}}/N_{\mathrm{cnt}}$, in which N_{smp} and N_{cnt} is the number of harvested adherent cells treated with the particles and in the negative control, respectively. The viability was high in general (exceeding 84 %) considering the delicate nature of stem cells. In experiments at an identical concentration of Fe (the same content of magnetic cores), the cell gain decreased on average by 3 % per 1 nm of the coating thickness, which might indicate that the increasing amount of silica disturbs either the cell proliferation or the adhesion of the cells. The viability and cell gain are shown in Figure 5-18, together with the evolution of the total mass of the nanoparticles as a function of the coating thickness. Specifically, particles with the

thickest coating of 21 nm weigh roughly six times more than the particles with a 6 nm silica shell.

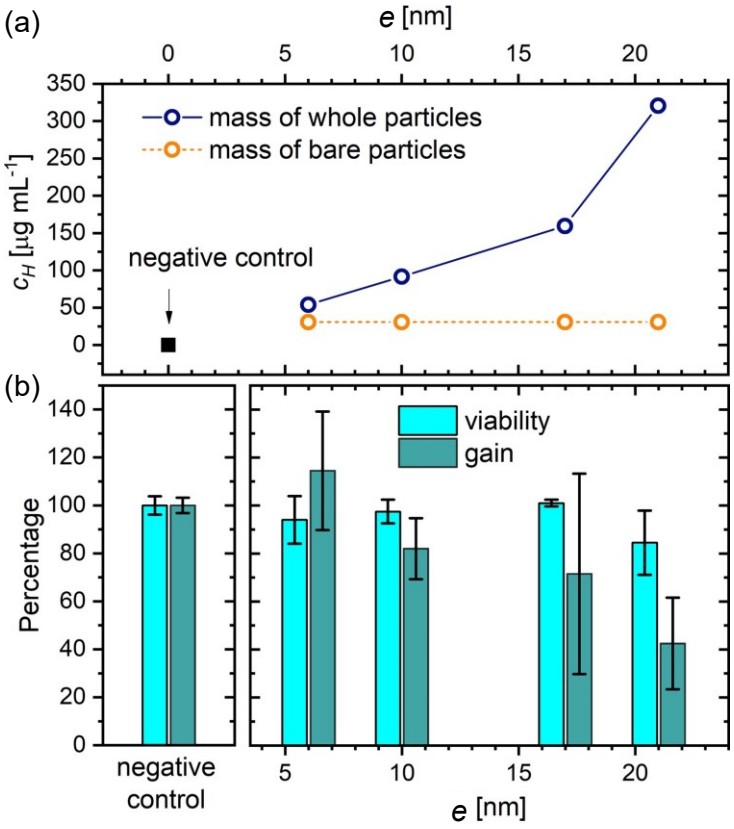

Figure 5-18. The evaluation of cytotoxicity of silica-coated ε-$Al_{0.23}Fe_{1.77}O_3$ nanoparticles: (a) the mass of particles applied to cells as a function of the shell thickness *e* at a constant concentration of 0.35 mmol(Fe) L^{-1} (calculated from magnetization data); (b) cell viability and gain after 48 h of incubation of rat mesenchymal stem cells with the samples at the concentration of 0.35 mmol(Fe) L^{-1}, the error bars mark the standard deviation from duplicates. Reproduced from [D5].

In [D4], we tested the preparation of silica-coated maghemite rods from akageneite precursor, intended for biomedical applications. The length of the rods reached several hundred nm, the average thickness was ~85 nm, and the coating thickness ~15 nm. The larger size of these particles should facilitate MRI detection in cell tracking (see Section 5.1.7) and magnetic manipulation with cells (see Section 6.1). Moreover, the elongated shape of the particles could be used in the newly emerging therapies that attempt to improve tissue regeneration, employing magnetic particles as scaffolds, e.g., in the regeneration of damaged spinal cord [376]. To analyze the cytotoxicity of the silica-coated maghemite rods, we selected the human lung adenocarcinoma cell line A549 and the human breast adenocarcinoma cell line MCF-7 as suitable models and treated the cells with the rods at final concentration 0.1–0.42 mmol(Fe) L^{-1} in the medium. This time, the viability from

the trypan blue exclusion test was assessed after 24 and 48 h not only for the adherent cells but also for those floating in the medium. The viability of pooled cells exceeded in all cases 95 % (see Figure 5-19), the number of harvested cells was not significantly different from the control either.

Another method, which enabled us to monitor cell viability, proliferation, and adherent properties continuously in real time, was the measurement of *impedance changes* by the *xCELLigence system* [377]. In this method, the cells are seeded onto platelets with golden electrodes and incubated in the medium. An increasing area covered by the proliferating cells adhered to the electrodes increases the measured impedance, and changes in proliferation, adhesion ability, or cell death can be deduced from the measured impedance curve. The results are presented in arbitrary units called "Cell Index" – CI, a difference of impedance of the platelet with and without the cells normalized to the same value for all individual experiments at the time of the treatment. We used the xCELLigence system in [D4] for comparison with the results of the trypan blue exclusion test. Interestingly, this comparison revealed only a mild decrease in the cell adhesion of the MCF-7 cells at the highest concentration of rods 0.42 mmol(Fe) L^{-1} (see Figure 5-20).

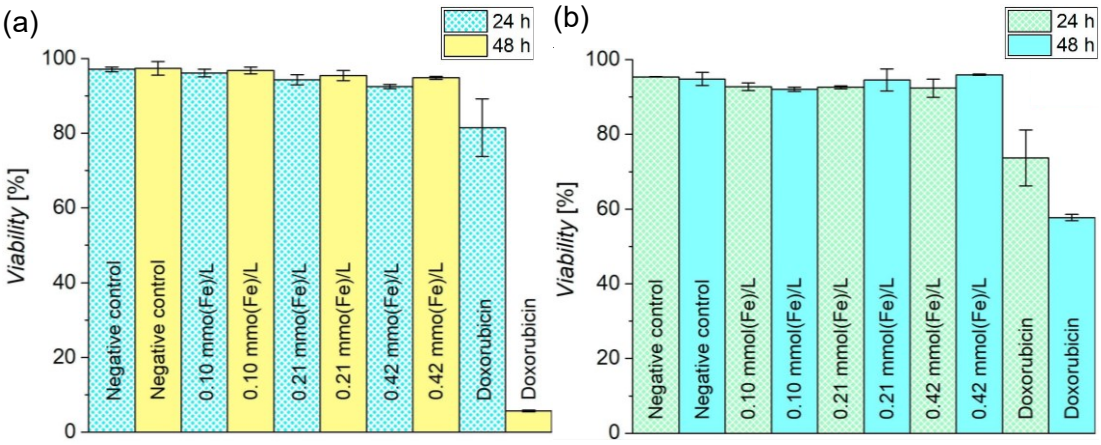

Figure 5-19. Viability of (a) A549 cells and (b) MCF-7 cells 24 and 48 h after the treatment with silica-coated maghemite rods at the given concentration, obtained by the trypan blue exclusion test. The negative control was treated with deionized water, whereas the cells treated with 1 μmol L^{-1} of doxorubicin were used as a positive control; the error bars indicate standard deviation from two experiments. Adapted from [D4].

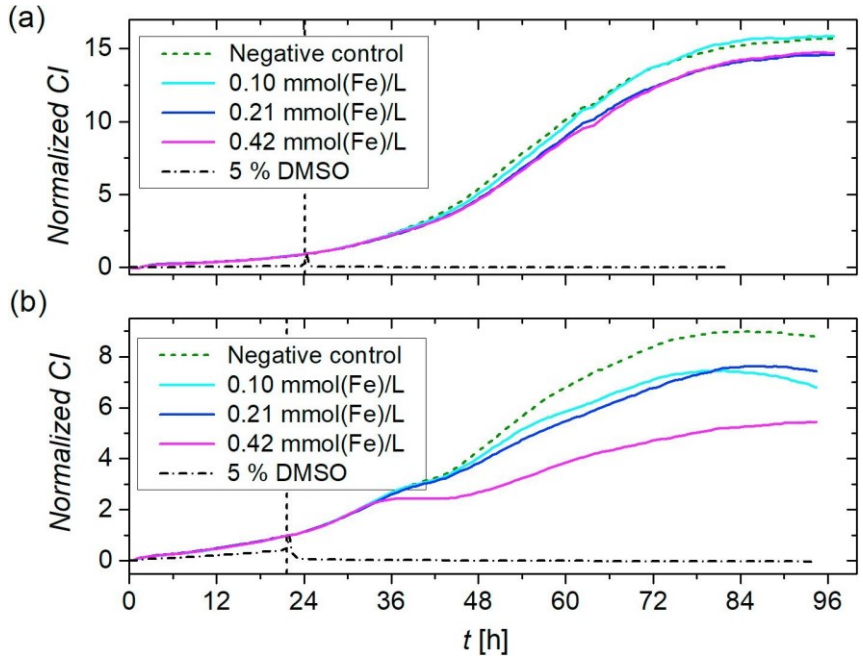

Figure 5-20. The real-time monitoring of cell viability, proliferation, and adhesion by the xCELLigence system of (a) A549 and (b) MCF-7 cell lines incubated with silica-coated maghemite rods; the cells treated with deionized water and 5 % DMSO were used as a negative control and a positive control, respectively. The vertical dashed line marks the introduction of the particles to the culture, the cells were monitored for 72 h after the treatment. Reproduced from [D4].

In [D7], we performed an extensive study of the interaction of silica-coated ε-$Fe_{1.76}Ga_{0.24}O_3$ nanoparticles (εFGO) with cells, namely their influence on cell viability, proliferation, cytoskeletal network, and distribution of cell cycle stages. For this purpose, we chose both A549 and MCF-7 cell lines, and employed particle concentrations 0.15–0.61 mmol(f.u.) L^{-1}. By a combination of the trypan blue exclusion test and impedance measurement by the xCELLigence system, we confirmed that the εFGO nanoparticles do not alter the viability (see Figure 5-21 for viabilities by the trypan blue test) and proliferation of these cells in the examined range of concentrations; however, the nanoparticles with the thickest coatings at higher concentrations impaired cell adhesion. The subsequent experiments were performed at the highest concentration of suspensions of 0.61 mmol(f.u.) L^{-1} to see the strongest effects induced by the particles. No clear difference from the untreated control in the distribution of the cell cycle was observed in the A549 cells for any sample, which indicates that the particles neither retard the growth of cells nor interfere with mechanisms responsible for cell cycle progression (see Figure 5-22). However, the immunofluorescence microscopy (see Figure 5-23) showed disrupted orientation of actin cytoskeleton and a loss of actin stress fibers in cells treated with nanoparticles coated with thicker silica layers (16

and 24 nm). The ability of the cells to adhere to the substrate is provided by focal adhesions, macromolecular structures linking the cell to the extracellular matrix. Since the focal adhesions connect to the actin cytoskeletal network, its disruption results in a decreased area of the focal adhesions, as observed in the case of cells treated with the two samples with the thicker silica coating (see Figure 5-24). Because similar effects were not observed for samples with thinner coatings at the same concentration, we concluded that the described effect was rather mechanical than chemical because the amount of material internalized into cells increases rapidly with the increasing thickness of the coating (see Figure 5-18a). Importantly, our results showing the negligible toxicity of this system can be generalized to the undoped and, by considering the results of [D5], also to the Al-doped epsilon polymorph of the iron(III) oxide.

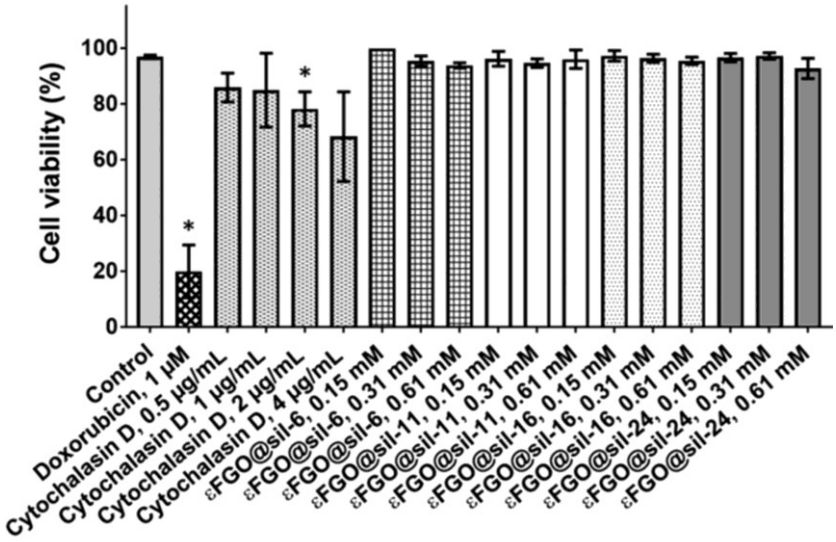

Figure 5-21. The effect of silica-coated ε-$Fe_{1.76}Ga_{0.24}O_3$ nanoparticles (εFGO, the number in the sample code denotes the mean thickness of silica shell) on the viability of A549 cells, determined after 48 h of incubation with the particles by the trypan blue exclusion test; the error bars mark the standard deviation based on three experiments. The negative control received sterile deionized water, while treatment with cytostatic doxorubicin and actin polymerization disruptor cytochalasin D was used for the positive controls. The asterisks mark results that were significantly different from the negative control (p-value < 0.05). Reproduced from [D7].

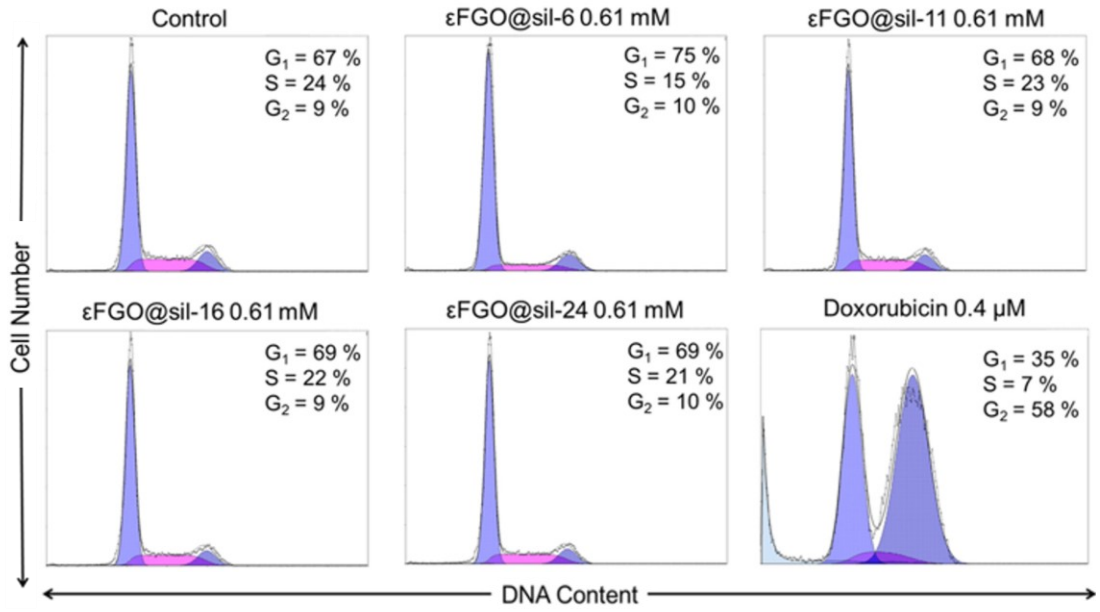

Figure 5-22. Representative histograms showing the distribution of the cell cycle in A549 cells treated with silica-coated ε-$Fe_{1.76}Ga_{0.24}O_3$ nanoparticles at a concentration of 0.61 mmol(f.u.) L^{-1}, after 48 h incubation with the nanoparticles. The negative control treated with sterile deionized water and the positive control treated with cytotoxic doxorubicin are shown for comparison. Adapted from [D7]. (In the G_1 phase, "gap 1", the proliferating cell is metabolically active and grows, and is in this case diploid – has two sets of chromosomes. During the S phase, "synthesis", the cell replicates its DNA and becomes tetraploid, whereas during the G_2 phase, "gap 2", the tetraploid cell further grows and prepares for mitosis and cytokinesis – nuclear and cellular division [378].)

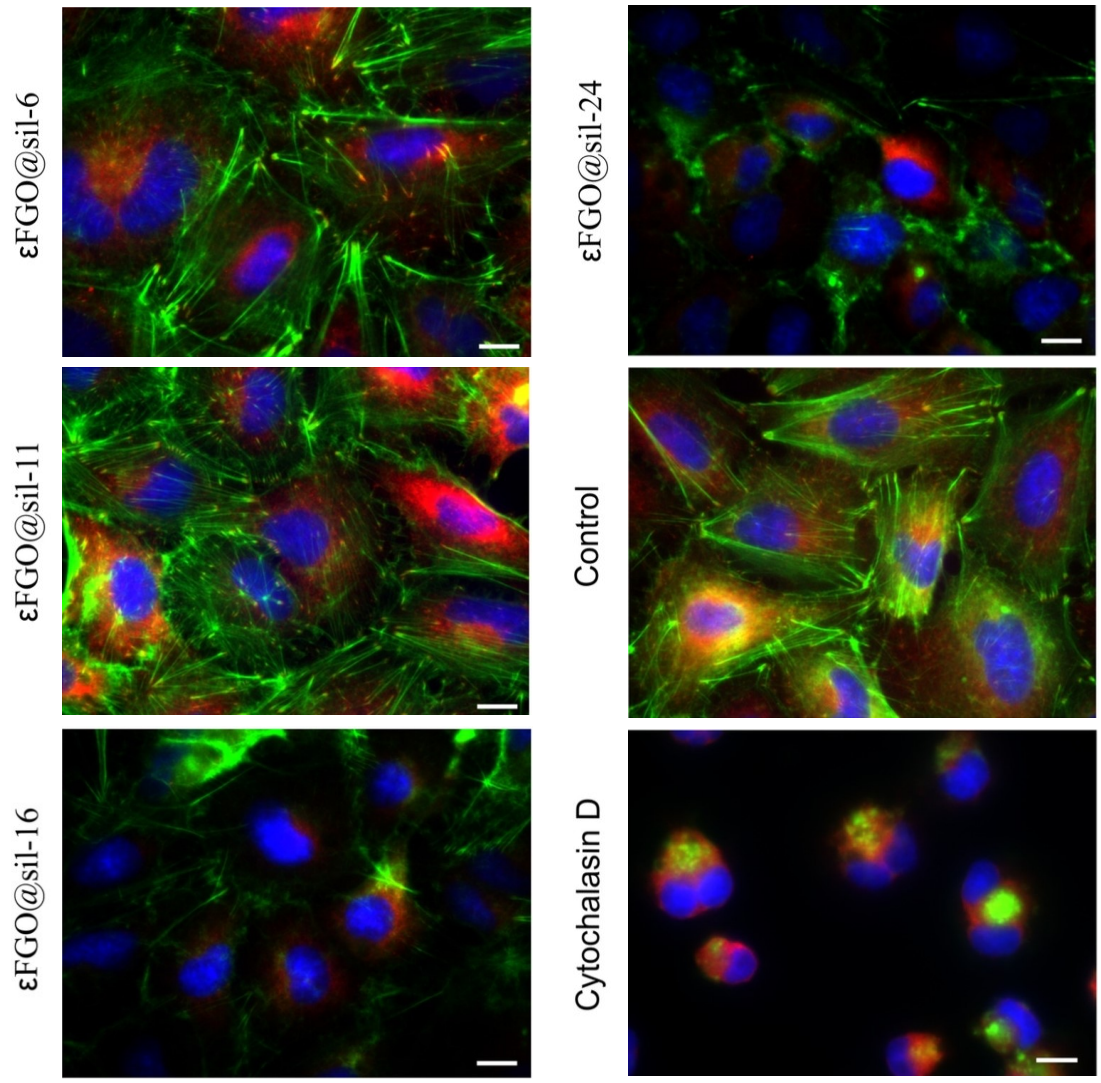

Figure 5-23. Fluorescence microscopy images of A549 cells treated with silica-coated ε-$Fe_{1.76}Ga_{0.24}O_3$ nanoparticles at a concentration of 0.61 mmol(f.u.) L^{-1}, after 24 h of incubation. The negative control was sham-treated with the phosphate-buffered saline, and the positive control was treated with 2 mg L^{-1} of cytochalasin D, an alkaloid inhibiting actin polymerization. The blue signal marks the nuclei (DAPI staining), filamentous actin is stained green (Alexa Fluor 488 phalloidin), and paxillin, a protein associated with focal adhesions, is stained red (monoclonal antibody anti-paxillin); the scale bars represent 10 μm. Adapted from [D7].

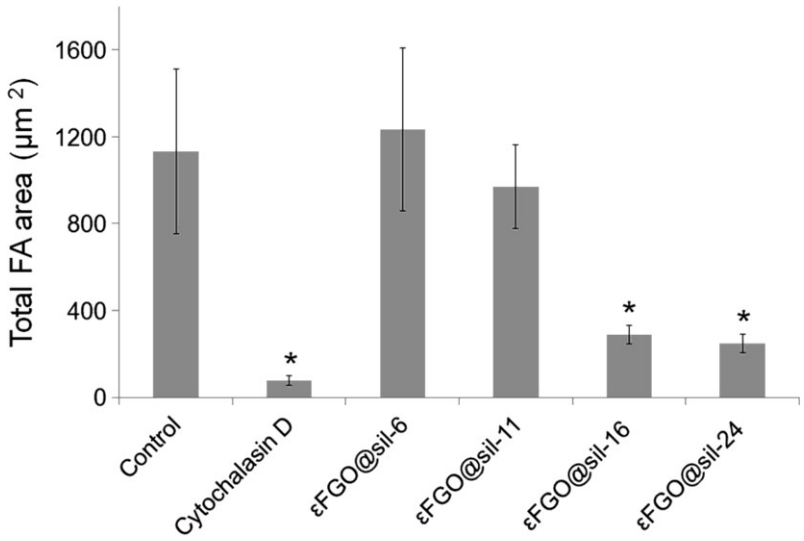

Figure 5-24. The total area of focal adhesion contacts per cell, calculated from paxillin-stained microscopy images of A549 cells treated with silica-coated ε-$Fe_{1.76}Ga_{0.24}O_3$ nanoparticles (0.61 mmol(f.u.) L^{-1}, after 24 h incubation; see Figure 5-23). Cells treated with 2 mg L^{-1} of cytochalasin D were used as a positive control, the error bars mark the standard deviation from the image analysis of 10 cells, the asterisk marks the results significantly different from the negative control ($p < 0.05$). Reproduced from [D7].

6 Other applications

Though applications in analytical chemistry partly overlap with the applications in medical diagnostics, we will devote a separate section to one of the most significant analytical applications of magnetic particles, namely magnetic solid-phase extraction. As a prominent example of how magnetic microparticles or nanoparticles can contribute to a sustainable future, thermoelectric applications are briefly introduced, including the effects brought by nanostructuring.

6.1 Magnetic separation

Magnetic nanoparticles can be used in medicine not only inside the living body but also for the detection and analysis of various analytes in biological samples such as urine or blood. The goal of separation techniques is to isolate the analyte, i.e., the species to be detected or quantified, from the matrix of a sample, which might be too dilute or too complex for the intended chemical analysis. In the case of highly dilute samples, they raise the possibility to concentrate the analyte to beat the detection limits and improve the reliability of the analysis. The examination of complex biological samples can be extremely difficult because various biomolecules or the admixtures in the matrix usually strongly interfere with the analysis. The traditional methods of sample preparation, i.e., analyte isolation and preconcentration struggle considerably. The electrophoresis is usually slow and has insufficient reproducibility, the ultrafiltration can suffer from the adsorption of biological macromolecules on the membrane fibers, and precipitation can deactivate the targeted biological macromolecules [379].

Magnetic solid-phase extraction (MSPE) is one of the separation techniques based on solid-phase extraction, which uses a magnetic sorbent, such as magnetic nanoparticles or microparticles with suitable surface coatings or specific molecular functionalization, for separation of the analyte. In a typical MSPE process (see the scheme in Figure 6-1), the sorbent exerting an affinity to the target species, either via specific interactions (hybridization of single-stranded nucleic acids, molecular recognition, complexation of metal ions) or through nonspecific adsorption, is mixed with the primary sample containing the analyte. During a certain incubation time, the analyte binds to the sorbent and then the whole complex is separated from the matrix by a magnetic field. The bound analyte can be further purified and eventually eluted for the subsequent analysis, which might employ for example high-performance liquid chromatography, mass spectroscopy, UV-Vis spectroscopy, surface-enhanced Raman spectroscopy (SERS), or polymerase chain reaction (PCR). The sorbents can be recovered for repeated use.

The high surface-to-volume ratio of nanoparticles together with suitable surface modifications and the possibility to separate the sorbent with an external magnetic field combine in synergy to make MSPE a highly efficient method for the sample preparation. Moreover, it largely speeds up the separation process, if employed as a part of a chain of several methods, and can be easily used on a larger scale. Naturally, MSPE is not limited to biomedical analysis, it can be generally applied in analytical chemistry, but also in other fields such as biochemistry, catalysis, or wastewater treatment.

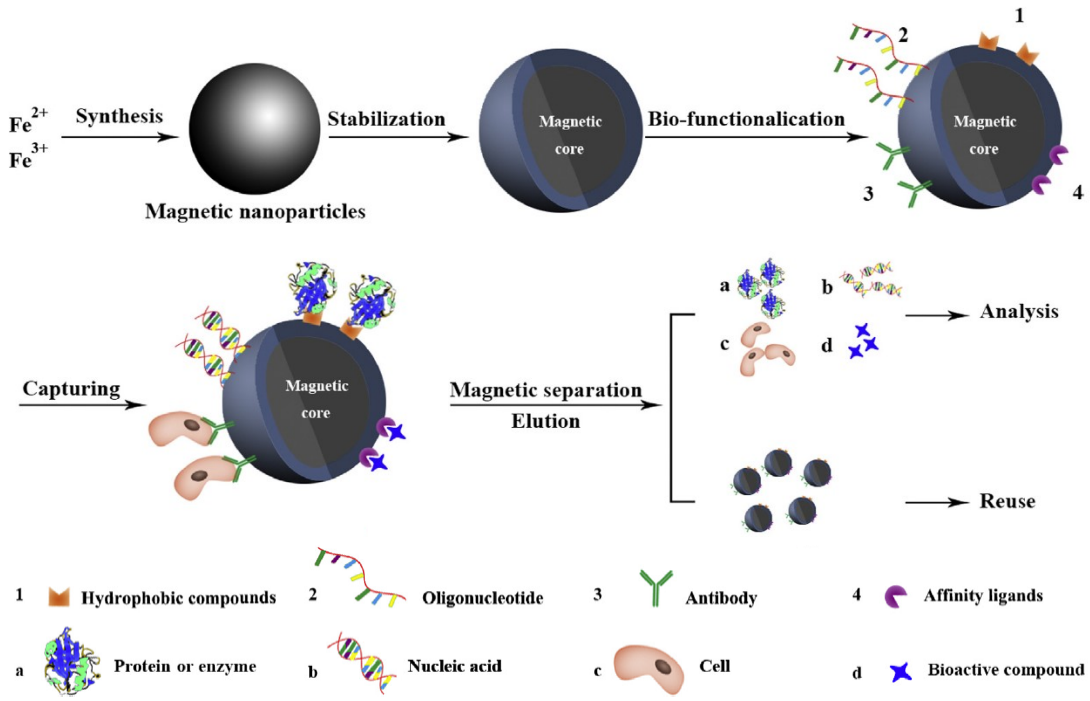

Figure 6-1. The general scheme of magnetic separation in the analysis of biological samples, including cell sorting and separation. Adapted from [379].

The most important parameters for optimization at the nanoparticle level are the size of the particles and especially their magnetic moment. A magnetic force acts on a nanoparticle with a nonzero magnetic moment only at the presence of a magnetic field gradient

$$\boldsymbol{F}_{\mathrm{m}} = (\boldsymbol{m} \cdot \boldsymbol{\nabla})\boldsymbol{B}, \tag{6.1}$$

where the magnetic moment can be written as $\boldsymbol{m} = V\boldsymbol{M} = V\Delta\chi\boldsymbol{H}$, $\Delta\chi = \chi_{\mathrm{p}} - \chi_{\mathrm{s}}$ is the difference in susceptibility of the particle and the solvent. In the case of an aqueous suspension of nanoparticles, we can approximate $\boldsymbol{H} \approx \mu_0\boldsymbol{B}$. After an algebraic simplification, one can get the expression [380]

$$F_{\mathrm{m}} = V\Delta\chi\nabla\left(\frac{B^2}{2\mu_0}\right). \tag{6.2}$$

To separate the nanoparticles with the analyte from the suspension, the hydrodynamic drag force given by Stokes' law has to be taken into account

$$F_{\mathrm{d}} = 6\pi\eta dv, \tag{6.3}$$

where η is the dynamic viscosity of the solvent, d the diameter of the particle, and v velocity of the particle in the fluid. Combining the formulas (6.2) and (6.3), we can get a simple expression for the equilibrium velocity of a spherical particle when the magnetic force is counterbalanced by the hydrodynamic drag force

$$v = \frac{\xi_{\mathrm{m}}}{\mu_0}\nabla(B^2) \tag{6.4}$$

with the magnetophoretic mobility $\xi_{\mathrm{m}} = d^2\Delta\chi/(9\eta)$. This parameter characterizes how well the given nanoparticles in a given solvent can be manipulated by external magnetic fields [380].

Nevertheless, the crucial part of the design of the sorbent for MSPE is surface modification. To achieve the high specificity required for most biological and biomedical applications, the surface must be functionalized with biomolecules targeting the required analyte, as indicated in Figure 6-1. Typically, specific affinity ligands, which have high affinity to corresponding moieties through molecular recognition interactions, or antibodies can be used to separate proteins, enzymes, or other biomolecules of interest, while grafting of specific oligonucleotide sequences enables separation of complementary nucleic acids through base pairing [379,381]. MSPE can be used also for the separation of whole cells including selected cell types if the magnetic particles are coated with appropriate immunospecific agents. However, for such a purpose, larger micrometer-sized particles with greater magnetophoretic mobility are more suitable. The "immunomagnetic separation" of both procaryotic and eucaryotic cells using specific antibodies against specific antigens produced by the target cells has been demonstrated in numerous studies. For example, in [382], the folic acid (vitamin B9) was used as the affinity ligand for the folic acid receptor, which is overexpressed in many types of human cancer cells, to provide MSPE of tumor cells. In [383], the authors used monoclonal antibodies to target both leukemia and prostate cancer cells with high efficiency (>96 %) and sensitivity (0.01 % of cancer cells in the sample). The MSPE has been employed also to detect and isolate bacteria cells, for example, both gram-positive and gram-negative pathogenic bacteria by using the vancomycin antibiotic interacting with the cell wall [384], or *Escherichia coli* and *Salmonella enterica* pathogens from food samples by using specific antibodies [385].

In other applications, such as wastewater and groundwater cleaning, rather cheap and easily prepared sorbents are preferred due to their high efficiency and facile employment in larger amounts. The main mechanism of binding the analyte in this case is nonspecific **adsorption**, which might occur either as chemical adsorption (chemisorption) through chemical bonds, physical adsorption (physisorption) mainly via Van der Waals forces or hydrogen bonds, or ion exchange [386] (see Figure 6-2). An extensively applied approach to characterize adsorption is based on adsorption isotherms, which describe the relationship between the equilibrium concentration of the analyte in the solution, c_e, and adsorbed amount of analyte on the solid sorbent, Q_e, at a certain temperature (and a given pH and ionic strenght) [386]. Numerous isotherm models have been proposed covering different situations and derived under different assumptions, and some of them will be introduced in the following text.

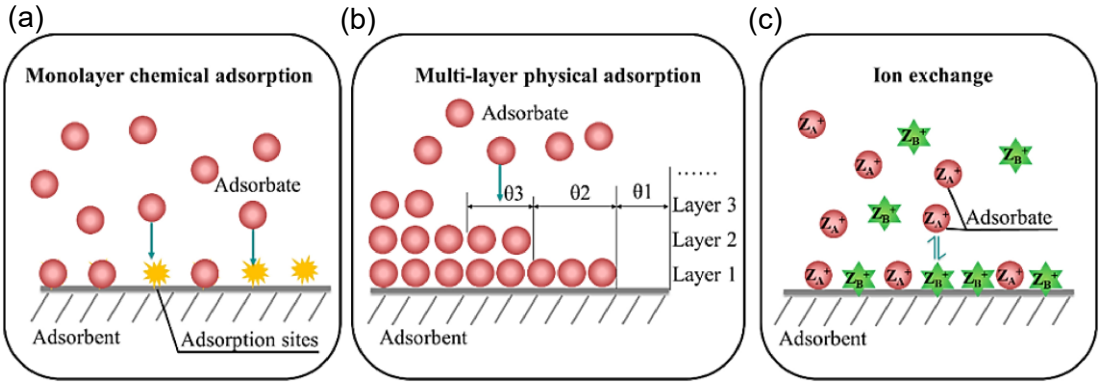

Figure 6-2. Three basic types of adsorption: (a) chemical adsorption of the analyte – adsorbate – leading to a single layer at the surface of the sorbent, (b) physical adsorption leading to multiple layers of the analyte, and (c) the ion exchange, in which ions of the analyte exchange for ions of the same or different (but of the same sign) charge at the adsorbent surface. Reproduced from [386].

The simplest model is *linear adsorption* (analogy of the linear Henry's law for the amount of dissolved gas in liquids [387]), which applies to monolayer adsorption at a very low surface coverage of the adsorbent. It neglects the interaction between adsorbed molecules and can be used also as the low-concentration limit of the other models. A more sophisticated and commonly used model is the *Freundlich isotherm* [388], an empirical model which can be described by

$$Q_e = \kappa_F c_e^{1/n}, \tag{6.5}$$

in which κ_F and n are constants. It was shown that the Freundlich isotherm describes well chemical adsorption with an approximately 50 % equilibrium coverage fraction of the adsorbent [386,389]. The model has been further modified to include the effect of competition between multiple adsorbates, often only on an

empirical basis [390]. The most widely used adsorption model is the *Langmuir isotherm* [391,392] depicted in Figure 6-3, which was originally proposed for the adsorption of gas molecules at a solid surface. This theoretical model describes the chemical adsorption of a monolayer of adsorbate molecules under the following conditions: (i) the adsorption sites are equivalent and distributed homogeneously on the surface of the adsorbent, (ii) the adsorbate molecules do not interact, (iii) each site can accommodate only one adsorbate molecule, and (iv) a dynamic reversible equilibrium is established during the experiment [393]. The Langmuir isotherm is described by

$$Q_\mathrm{e} = \frac{Q_\mathrm{s}\kappa_\mathrm{L}c_\mathrm{e}}{1+\kappa_\mathrm{L}c_\mathrm{e}}, \tag{6.6}$$

in which Q_s is the maximum adsorption capacity of the sorbent and $\kappa_\mathrm{L} = k_\mathrm{a}/k_\mathrm{d}$ is the ratio of kinetic rate constants of adsorption and desorption, which describes the affinity of the sorbate to the sorbent. Although it might seem that the conditions mentioned above are oversimplifying at the microscopic scale, they are often valid at low concentrations of the adsorbate if the whole macroscopic system is considered. Moreover, many adsorption processes rely, in principle, on monolayer chemisorption. Interestingly, the Freundlich isotherm can be conceptualized as a sum of Langmuir isotherms with a log-normal distribution of κ_L [390].

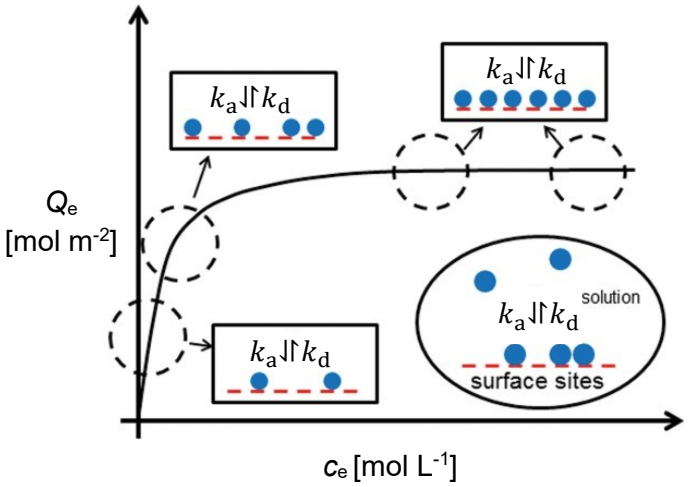

Figure 6-3. Langmuir isotherm. The adsorbate forms a monolayer, each point of the isotherm describes a dynamic equilibrium of adsorbing and desorbing species with constant values of k_a and k_d. Adapted from [393].

The industrial and environmental importance of understanding the adsorption processes has encouraged the efforts to describe the adsorption under various conditions, and many other adsorption models have been proposed [386]. We will mention just a few examples: the empirical *Toth isotherm* extending the Langmuir isotherm for the application in heterogeneous systems [394], empirical *Temkin isotherm* for multilayer adsorption at a medium concentration of the sorbate [395], empirical *Redlich-Peterson* [396] and *Sips* [397] *isotherms* approaching the

Langmuir and Freundlich isotherms as the limiting cases, or the theoretical *Brunauer-Emmett-Teller* (BET) *model* describing the physical multilayer adsorption [398].

Although any solid material can be used as a sorbent, the higher the surface area, the more efficient the separation process. Moreover, nanoparticles have high surface energy and to decrease it, they tend to adsorb the accessible molecules with higher affinity than in the case of larger particles. This property makes them excellent adsorbents, however, the desorption of the analyte might require harsher conditions than it would in the case of a traditional sorbent [399].

In our study [D8], we wanted to demonstrate a fast and facile way for the preparation of a nonspecific and thus universal sorbent based on magnetic nanoparticles for MSPE. As a core material, we used Zn-doped magnetite nanoparticles, which were prepared by the thermal decomposition method. Importantly, as follows from the description of the method in Section 3.1.1, the resulting nanoparticles are capped with organic surfactants, namely with oleic acid and oleylamine. The Zn-doped magnetite cores with high crystallinity have large magnetization, which ensures high magnetic separation efficiency for the given size of particles. Exposing surfactant-capped nanoparticles to elevated temperatures results in pyrolysis of the surfactants and the formation of a carbon layer at the particle surface, as shown in Figure 6-4. The heat treatment of the nanoparticles was performed at 500 °C for two hours and, apart from the pyrolysis of surfactants, resulted in slight oxidation of the magnetite and redistribution of the Zn and Fe over the tetrahedral and octahedral sites closer to the thermodynamic equilibrium (see Mössbauer spectra in Figure 4-11 with the respective hyperfine parameters in Table 4-1).

The sorption capacity of the resulting carbon-coated nanoparticles was tested by using methylene blue, a water-soluble organic cationic dye, as a model. Methylene blue was the first fully synthetic drug in medicine originally proposed for malaria treatment [400,401] and is the most commonly used dye to color cotton, silk, and wood [402]. The adsorption capacity obtained from the Langmuir isotherm (expression (6.6), Figure 6-4) and recalculated to the carbon content in the sorbent agreed well with the adsorption capacity of commercial activated carbons [402,403]. As a proof of principle, the efficiency of the sorbent in MSPE was analyzed in a model solution of a highly diluted β-estradiol. This steroid compound is the most important estrogen, i.e., one of the hormones directly responsible for the regulation of the female reproductive system. However, at the same time, β-estradiol represents a disturbing environmental pollutant because it can interfere

with the endocrinal system of wild animals as well as humans and disrupt their hormone levels, and block or mimic the normal function of their natural hormones [404,405]. In our experiments, the magnetic sorbent was applied to an aqueous β-estradiol solution and then separated by a permanent magnet. Thereafter, the steroid was eluted and determined, and the particles recovered for repeated use over 5 cycles in total. As shown in the inset of Figure 6-4, the efficiency of the sorbent did not decline with the increasing number of cycles. In another experiment, we tested the preconcentration capabilities of the sorbent. By applying mere 5 mg of the sorbent to a highly diluted β-estradiol solution (0.27 mg L^{-1}, V = 1 L) and subsequent elution, a solution with a 35times higher concentration was obtained (9.5 mg L^{-1}, V = 5 mL).

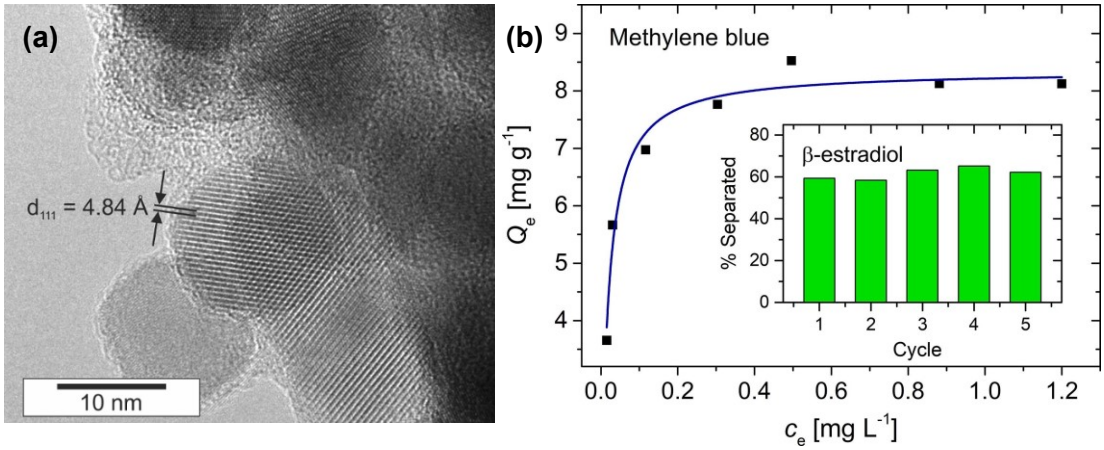

Figure 6-4. The Zn-doped iron oxide nanoparticles with surface carbon layer prepared by pyrolysis of surfactants (sample ZF@C): (a) HRTEM image, and (b) the adsorbed amount of methylene blue per gram of the sorbent Q_e as a function of the equilibrium concentration of the dye c_e in solution, fitted by the Langmuir isotherm. Preliminary experiments on the MSPE of β-estradiol in the inset show the percentage of the steroid separated from solution in each of five cycles during repeated use of the sorbent. Reproduced from [D8].

6.2 Thermoelectric applications

The attractive idea of direct thermal-to-electrical energy conversion is the cornerstone of thermoelectric (THE) applications. The need to search for sustainable sources of energy and the effort to utilize the inevitable heat losses have triggered the research in the area of thermoelectrics as one of the promising directions which might help to decrease our environmental impact and lead to higher efficiency in energy use. The thermoelectric devices are solid-state, without moving parts, and produce no greenhouse emissions or noises when in operation. Nevertheless, the efficiency of these devices is lower than other conventional energy-conversion technologies due to the low performance of the THE materials.

Therefore, they have been used so far in applications that appreciate reliability and predictability over the efficiency and cost, such as pacemakers, remote wireless sensors, or radioisotope thermoelectric generators (RTGs) for deep-space probes. The pivot of the contemporary THE research is the effort to enhance the performance of THE materials to such a level that would make them a truly competitive energy-conversion technology suitable for large-scale employment in the everyday life. Furthermore, to make the THE technology truly environmentally friendly, it is necessary to base it on nontoxic materials composed of abundant elements.

6.2.1 Characterizing thermoelectric performance

In the assessment of THE materials, three important parameters are monitored. The first parameter, dimensionless *figure of merit*, ZT, characterizes the efficiency of the material:

$$ZT = \frac{\alpha^2 \sigma T}{\kappa} = \frac{PF\ T}{\kappa}. \tag{6.7}$$

Here, α is the Seebeck coefficient (the thermopower), σ is electrical conductivity, $\kappa = \kappa_\mathrm{l} + \kappa_\mathrm{e}$ is the thermal conductivity consisting of the lattice (phonon and magnon) component κ_l and charge-carrier component κ_e, $PF = \alpha^2\sigma$ is the power factor. The thermopower α is positive for hole (p-type) and negative for electron (n-type) conduction. While high α provides large voltage output and high σ reduces losses by Joule heating, low κ maintains a large temperature gradient. However, optimizing these parameters for maximum performance is a matter of compromises – typically, increasing σ is accompanied by the decrease of α, as well as it is troublesome to enhance σ but not κ at the same time [406]. Moreover, all these parameters are temperature-dependent.

The THE device can be regarded as a thermodynamic heat engine with charge carriers as the working medium. Then, the maximum power-generation efficiency of the THE device can be calculated as

$$\eta_\mathrm{max} = \eta_\mathrm{Car} \frac{\sqrt{1 + ZT_\mathrm{m}} - 1}{\sqrt{1 + ZT_\mathrm{m}} + \left(\frac{T_\mathrm{cold}}{T_\mathrm{hot}}\right)}, \tag{6.8}$$

in which $\eta_\mathrm{Car} = (T_\mathrm{hot} - T_\mathrm{cold})/T_\mathrm{hot}$ denotes the Carnot efficiency, T_hot and T_cold are the temperatures of the hot and cold sides of the THE device, and ZT_m is the average value of ZT between T_cold and T_hot. Larger ZT_m brings the system closer to the ideal Carnot efficiency. In terms of the desired efficiency for more widespread use, ZT_m of the material should reach at least 3–4 [407].

The second parameter, the *THE quality factor* $\mathcal{B}$, includes also microscopic properties derived from the band structure such as the carrier mobility μ_c or the effective mass of the carriers m^*. In a one-band nondegenerate semiconductor,

$$\mathcal{B} \propto \frac{\mu_c (m^*)^{3/2}\, T^{5/2}}{\kappa_l}. \tag{6.9}$$

This expression hints at directions to follow when optimizing the THE performance on the microscopic scale. One must remain cautious though since the carrier mobility decreases with increasing m^*. For a given scattering mechanism, higher $\mathcal{B}$ results in a higher ZT [407].

The last parameter, the *THE compatibility factor* S_{THE}, relates to the design of a segmented THE device. It is defined by macroscopic quantities

$$S_{\mathrm{THE}} = \frac{\sqrt{1+ZT}-1}{\alpha T}. \tag{6.10}$$

The S_{THE} characterizes the relative current density, the ratio of the electric current density to the heat flux by thermal conduction, which maximizes the efficiency relative to η_{Car}. In the case of a segmented THE device, the closer the compatibility factors of the employed THE materials, the higher the combined efficiency. In contrast, if S_{THE} of these materials differs by a factor of 2 or more, the segmentation can decrease the overall efficiency compared to if the materials were used separately [408].

6.2.2 Enhancing THE materials by overcoming traditional trade-offs

The path to high-performance THE materials zig-zags around several degrees of freedom – charge, orbital, lattice, and spin – which need to be optimized [407]. Most of the materials investigated for THE applications are semiconductors because they have just the right number of charge carriers to maximize the power factor and the figure of merit. At the same time, the electronic part of the thermal conductivity increases with the increasing number of charge carriers. The relationship between the concentration of charge carriers and α, σ, power factor, and κ is schematically depicted in Figure 6-5.

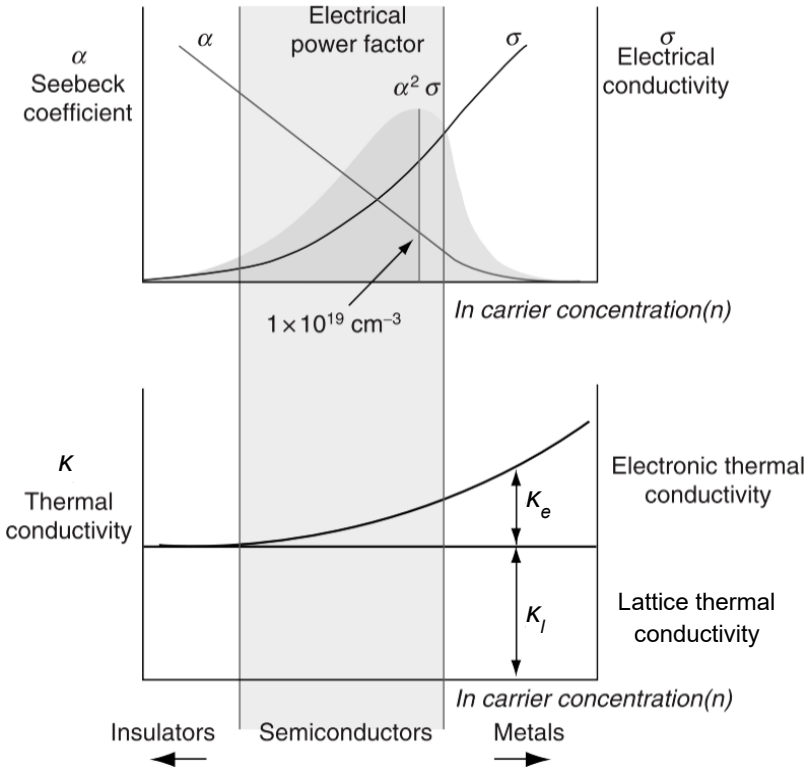

Figure 6-5. The dependence of quantities decisive for the thermoelectric figure of merit on the concentration of charge carriers, including the lattice and charge-carrier (here electronic) components of thermal conductivity. Adapted from [409].

Nevertheless, the lattice thermal conductivity depends on other parameters of the material. Since it describes the heat carried by phonons (or magnons), the means to manipulate its magnitude are the scattering mechanisms. It can be calculated as $\kappa_\mathrm{l} = \frac{1}{3} C_V l_\mathrm{p} v_\mathrm{s}$, where C_V denotes the isochoric heat capacity, l_p the phonon mean free path and v_s the mean speed of sound [410]. Since the phonons have largely varying wavelengths and mean free paths (below 1 nm up to 10 μm), it is crucial to provide scattering centers for phonons at various length scales [411], and, at the same time, not disrupt the electric conductivity by scattering the charge carriers [412]. A powerful method how to achieve this goal is **nanostructuring**, which reduces the size of grains of the material and thereby limits the phonon mean free path. A simple model based on the effective medium approximation describes the lattice thermal conductivity of a polycrystalline material with spherical grains of identical size by

$$\frac{1}{\kappa_\mathrm{l}} = \frac{1}{\kappa_0} + \frac{2R_\mathrm{K}}{d}, \tag{6.11}$$

where κ_0 is the thermal conductivity of the bulk, R_K the Kapitza resistance at the grain boundary and d the size of the grains [413]. Since the Kapitza resistance is difficult both to measure and to modify, the main focus remains on decreasing the

size of the grains, again with caution towards maintaining the electrical conductivity as high as possible [406].

Further, the nanostructuring introduces grain boundaries with a high density of lattice defects as additional scattering centers. Actually, defect engineering is another highly efficient method of reducing the lattice thermal conductivity. Dense dislocation arrays at grain boundaries together with point defects inside the grains scatter phonons of different wavelengths compared to the whole grains, covering thus a broader range of the phonon spectrum. Similarly, doping the material with selected atoms not only optimizes the concentration of charge carriers, but the dopants also represent extrinsic point defects, which further facilitate the formation of intrinsic point defects such as vacancies, antisites, or interstitials in their surroundings. There are also other mechanisms to reduce κ_l, for example, by limiting the lifetime of the phonons by a strong anharmonicity of chemical bonds, which enhances phonon-phonon interactions and Umklapp processes [414]. Interestingly, the idea behind decreasing κ_l through anharmonicity has led to the phonon-glass-electron-crystal (PGEC) concept of an ideal THE material [415,416]. In the PGEC approach, the maximum electron mean free path enabling the electron transport is achieved by high crystallinity of the material ("electron single crystal"), whereas its large and complex unit cells containing weakly bound atoms with highly different masses reduce the phonon mean free path to a minimum, i.e., down to the interatomic distance ("phonon glass"). The PGEC concept has been applied with success for example in clathrates and skutterudites, which contain cage-like structures enclosing guest atoms or molecules ("rattlers") acting as efficient phonon scatterers by the "rattling effect" [417,418].

Apart from reducing κ_l, an important issue is the enhancement of the power factor $\alpha^2\sigma$. The use of magnetic semiconductors has been proposed as one of the strategies allowing to manipulate also the spin degree of freedom. The carrier belonging to a magnetic ion changes the spin of the ion by 1/2 and thereby modifies the magnetic entropy. Furthermore, the interaction between the carrier and the surrounding magnetic sites may strengthen the exchange interaction between the sites. These two effects may produce competing contributions to the Seebeck coefficient, the first one dominates at high temperatures, whereas the second one at temperatures well below the magnetic ordering temperature [409,419]. The magnetic interactions also increase the effective mass of the carriers, which enhances α.

Chalcopyrite represents a model example of a THE magnetic semiconductor with high PF. Due to its antiferromagnetic structure with high Néel temperature (see

Section 4.3), a strong coupling between the charge carriers and the magnetic moments exists, which largely increases α. Moreover, it has been proposed that the large Seebeck coefficient originates in the electron-magnon scattering and the *magnon-drag effect* [420,421]. If the magnetic material is exposed to a temperature gradient, a magnon flux can be generated besides the carrier flux. The magnon flux then sweeps the carriers from the high-temperature to the low-temperature region due to the electron-magnon interaction and results in the magnon drag [422]. To explain the temperature dependence of α in the chalcopyrite system, the authors in [421] developed the magnon-drag expression

$$\alpha = \alpha_0 + \alpha_{3/2} T^{3/2} + \alpha_4 T^4, \tag{6.12}$$

in which α_0 is the Seebeck coefficient at 0 K, $\alpha_{3/2} T^{3/2}$ characterizes the carrier-magnon scattering, and $\alpha_4 T^4$ is related to the spin-wave fluctuations in the antiferromagnet. The second term dominates the temperature dependence ($\alpha_{3/2}$ is virtually by six orders of magnitude larger than α_4) and was found to depend on the Fe content in the nonstoichiometric $Cu_{1+x}Fe_{1-x}S_2$.

6.2.3 Nanostructured chalcopyrite for thermoelectric applications

In our studies [D6],[D9], we focused on THE properties of chalcopyrite prepared in the nanosized form by high-energy milling and then compacted by spark plasma sintering or eventually hot pressing. In [D6], we compared the THE performance of three distinct samples: (i) chalcopyrite prepared from pure elements by milling (sample denoted as S), (ii) material obtained by milling of natural chalcopyrite, (N), and (iii) material prepared by co-milling of the same natural mineral together with pure elements in the weight ratio of 1:1 (SN). Whereas the mechanosynthesis from elemental precursors relies primarily on the nanostructuring principle, the milling of the natural mineral leads to its mechanical activation and introducing defects into the structure. Further, co-milling of pure elements together with the mineral was based on the idea that the natural chalcopyrite grains would serve as seeds triggering the growth of the chalcopyrite phase. In contrast, during the mechanochemical synthesis from pure elements, mainly the binary sulfide CuS is formed at first and acts as seeds for the formation of the chalcopyrite phase, into which the remaining Fe is incorporated [423]. We also observed a larger amount of pyrite, FeS_2, in the Mössbauer spectra of sample S (see Figure 4-26 with hyperfine parameters in Table 4-6 and Table 4-7) than in other samples, which points towards the larger content of copper in other components of the sample. Interestingly, the N and NS samples tended to over-stoichiometry of iron in the $CuFeS_2$ formula, which was also consistent with the negative Seebeck coefficient and predominantly n-type character of the samples (see Figure 6-6). It is also important

to note that to improve its THE applicability, $CuFeS_2$ has to be doped either through an excess of Fe, S deficiency ($CuFeS_{2-x}$) or substituting Cu^{1+} for divalent species such as Zn^{2+}, Pd^{2+}, etc. [D9].

Besides α, the other basic THE properties of the samples are depicted in Figure 6-6 as well. The lattice thermal conductivity dominated over the electronic part, as suggested by the large electrical resistivity. Therefore, we used the Debye-Callaway model of phononic thermal conductivity [424,425]

$$\kappa = \frac{k_B}{2\pi^2 v_s}\left(\frac{k_B T}{\hbar}\right)^3 \int_0^{\theta_D/T} \tau(x)\frac{x^4 e^x}{(e^x-1)^2}dx \qquad (6.13)$$

to fit the data. In the expression (6.13), ħ is the reduced Planck constant, θ_D the Debye temperature, τ the relaxation time, $x = \hbar\omega/(k_B T)$ and ω is the phonon frequency. The relaxation time comprises contributions from different scattering mechanisms, which are summed as

$$\frac{1}{\tau} = \frac{v_s}{d} + A'\omega^4 + B'\omega^2 T e^{-\theta_D/3T} + C'\omega \qquad (6.14)$$

where d is the grain size and A', B' and C' are adjustable parameters. More details of the fitting procedure can be found in [D6] and its Supplementary Material. The first three contributions are present also in the polycrystalline mineral before mechanical activation and describe the grain-boundary, point-defect, and Umklapp scattering, respectively. However, the nanostructuring by high energy milling did not sufficiently reduce the phonon mean free path below the grain size, otherwise, κ would decrease at low temperatures as $\propto T^3$ and would have a much lower value, which was not observed. Therefore, to fit the data correctly, the last term leading to the T^2 dependence of κ and containing a free parameter C' was added to describe the weaker scattering of longwave phonons. This term can result from various scattering mechanisms, including scattering by magnetic fluctuations, structural disorder, or dislocation strain field, which might be the most probable one. Whereas sample S had practically zero ZT due to its low electrical conductivity and high κ, the other samples could be taken as n-type thermoelectrics with reasonable performance, whose main advantage lies in the very simple preparation method.

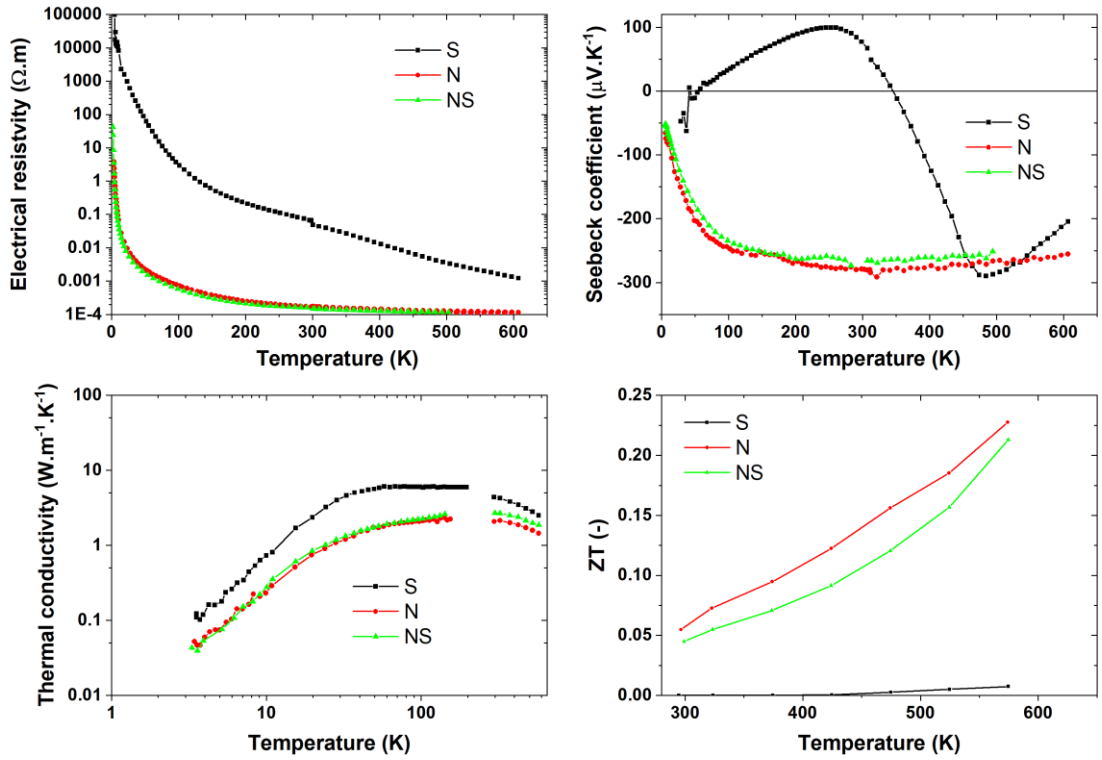

Figure 6-6. The temperature dependence of basic THE properties of chalcopyrite nanomaterials prepared by mechanochemical synthesis from pure elements (S), by milling of a mineral (N), and co-milling of the mineral with pure elements (NS). Adapted from [D6].

Recent achievements of our colleagues from the group of Prof. P. Baláž and his collaborators in the field of mechanochemically prepared copper-based sulfides, supplemented by our measurements, are summarized in [D9]. Here, the comparison between samples synthesized from pure elements in a laboratory mill and in an industrial mill showed a higher *ZT* for the latter sample, probably due to a higher structural disorder suggested also by Mössbauer spectra.

7 Conclusion

This thesis aimed to guide the reader through some of the results on iron-containing magnetic nanoparticles and present them in a broader context from the viewpoint of the structure, magnetic properties, and intended applications of the studied systems. The text should provide at least some insight into the nuances of magnetism of selected transition metal compounds with various exchange pathways and into the ways how the local magnetic structure affects the magnetic behavior of their nanoparticles.

Magnetic phenomena emerging at the nanoscale such as superparamagnetism offer novel possibilities that can be employed in diverse applications. As such, these phenomena spread through our work, and we devoted particular attention to their theoretical treatment. We also strived to stress that the applied synthesis method determines the resulting properties of nanoparticles, such as their size, shape, cation distribution, or surface modification, and that these properties are just as important as the chemical composition or crystal structure of the materials employed. Selected magnetic phases studied in this thesis were introduced together with their characteristic properties, which were complemented with original results, illustrating for example magnetic transitions (spin-reorientation transition in Fe_3S_4 or ε-Fe_2O_3) or the influence of doping on their magnetic behavior.

The core of this thesis was formed by a thorough analysis of nanoparticle properties that influence relaxivity, which describes the efficiency of magnetic nanoparticles as contrast agents in MRI. Understanding the individual parameters involved can enable targeted synthesis of contrast agents with higher efficiency that can be applied in lower doses and thus pose a lower health risk in clinical practice. The presented studies intended to provide reliable experimental data on the transverse relaxivity of magnetic nanoparticles that would enable the verification of theoretical predictions. We also attempted to fill the knowledge gap present in the literature, where for example the field and temperature dependences of relaxivity were lacking.

All nanomaterials that we studied as potential contrast agents in MRI, except for the systems at the verge of the transition to the paramagnetic state ($Co_{0.44}Zn_{0.70}Fe_{1.86}O_4$ [D10] and $La_{0.80}Na_{0.20}MnO_3$ [D1] nanoparticles), demonstrated comparable or even higher transverse relaxivities relative to contrast agents approved for use in clinical practice. The nanoparticles based on the less-known ε-Fe_2O_3 have not been tested for any medical applications before, and we hope to trigger further experimental work in this respect, especially in the recently

expanding area of ultra-high-field MRI. Moreover, the nanoparticles that we subjected to *in vitro* studies, namely the γ-Fe_2O_3 rods, and ε-$Al_{0.23}Fe_{1.77}O_3$ and ε-$Fe_{1.76}Ga_{0.24}O_3$ nanoparticles demonstrated negligible cytotoxicity – at least in the analyzed ranges of concentration with the examined cell lines employed as suitable models. These findings are not surprising, considering the chemical composition of these materials where primarily Fe^{3+} ions and possibly also the biologically tolerated Ga^{3+} ions are involved, but they suggest that these nanoparticles might be a reasonable choice for biomedical or medical applications. Further studies should consider above all advanced surface functionalization that would comply with specific requirements of the targeted applications, such as functionalization with folic acid or monoclonal antibodies for active targeting, or organic functionalization providing the so-called stealth character, which is essential for any intravenous applications if RES is not specifically targeted. If real clinical applications are envisaged, evaluation of toxicity both *in vitro* on multiple types of cells and eventually *in vivo* in laboratory animals inevitably follows.

As a proof-of-concept, we presented a facile method of preparation of magnetic nanoparticles covered by a carbon layer as a sorbent for the magnetic solid-phase extraction. We also demonstrated the efficiency of such a sorbent in sample preparation of a representative environmental pollutant for the subsequent analysis, i.e., adsorption of the analyte on the sorbent, followed by separation by a magnetic field, and elution of the analyte for the analysis. Although some optimization would be desirable, this method can provide an inexpensive and universal tool at hand for laboratory analyses.

Finally, we probed the influence of various precursors employed in the preparation of nanoparticles of chalcopyrite by high-energy milling on the thermoelectric performance of the product. Starting material can influence the range of processes occurring during the milling, such as the sequence of emerging intermediates/products during the milling, and modify thus the distribution of available charge carriers in the resulting composite. Future studies in this direction could focus on the search for suitable dopants that would adjust the number of charge carriers and would lead to the improvement of the figure of merit, while optimizing the milling process.

References

[1] E. Carretti, M. Bonini, L. Dei, B.H. Berrie, L. V Angelova, P. Baglioni, R.G. Weiss, New frontiers in materials science for art conservation: Responsive gels and beyond, Acc. Chem. Res. 43 (2010) 751–760. doi:10.1021/ar900282h.

[2] P. Baglioni, D. Chelazzi, eds., Nanoscience for the Conservation of Works of Art, The Royal Society of Chemistry, 2013. doi:10.1039/9781849737630.

[3] M. Bonini, S. Lenz, R. Giorgi, P. Baglioni, Nanomagnetic sponges for the cleaning of works of art, Langmuir. 23 (2007) 8681–8685. doi:10.1021/la701292d.

[4] D. Peer, J.M. Karp, S. Hong, O.C. Farokhzad, R. Margalit, R. Langer, Nanocarriers as an emerging platform for cancer therapy, Nat. Nanotechnol. 2 (2007) 751–760. doi:10.1038/nnano.2007.387.

[5] S.M. Moghimi, A.C. Hunter, J.C. Murray, Nanomedicine: current status and future prospects, FASEB J. 19 (2005) 311–330. doi:10.1096/fj.04-2747rev.

[6] T.M. Allen, P.R. Cullis, Drug delivery systems: Entering the mainstream, Science. 303 (2004) 1818–1822. doi:10.1126/science.1095833.

[7] C. Buzea, I.I. Pacheco, K. Robbie, Nanomaterials and nanoparticles: Sources and toxicity, Biointerphases. 2 (2007) MR17–MR71. doi:10.1116/1.2815690.

[8] V. Srivastava, D. Gusain, Y.C. Sharma, Critical review on the toxicity of some widely used engineered nanoparticles, Ind. Eng. Chem. Res. 54 (2015) 6209–6233. doi:10.1021/acs.iecr.5b01610.

[9] ISO/TS 80004-6:2013(en), Nanotechnologies — Vocabulary — Part 6: Nano-object characterization, (n.d.). https://www.iso.org/obp/ui/#iso:std:iso:ts:80004:-6:ed-1:v1:en:term:2.1 (accessed February 1, 2021).

[10] W. Huang, M.J. Jackson, M.J. Dekkers, P. Solheid, B. Zhang, Z. Guo, L. Ding, Nanogoethite as a potential indicator of remagnetization in red beds, Geophys. Res. Lett. 46 (2019) 12841–12850. doi:10.1029/2019GL084715.

[11] H. Mouritsen, Long-distance navigation and magnetoreception in migratory animals, Nature. 558 (2018) 50–59. doi:10.1038/s41586-018-0176-1.

[12] J.L. Kirschvink, M.M. Walker, C.E. Diebel, Magnetite-based magnetoreception, Curr. Opin. Neurobiol. 11 (2001) 462–467. doi:10.1016/S0959-4388(00)00235-X.

[13] W. Wiltschko, R. Wiltschko, Magnetic orientation and magnetoreception in birds and other animals, J. Comp. Physiol. A. 191 (2005) 675–693. doi:10.1007/s00359-005-0627-7.

[14] J. Shaw, A. Boyd, M. House, R. Woodward, F. Mathes, G. Cowin, M. Saunders, B. Baer, Magnetic particle-mediated magnetoreception, J. R. Soc. Interface. 12 (2015) 20150499. doi:10.1098/rsif.2015.0499.

[15] P.N. Fleischmann, R. Grob, W. Rössler, Magnetoreception in Hymenoptera: importance for navigation, Anim. Cogn. 23 (2020) 1051–1061. doi:10.1007/s10071-020-01431-x.

[16] S. Mann, N.H. Sparks, M.M. Walker, J.L. Kirschvink, Ultrastructure, morphology and organization of biogenic magnetite from sockeye salmon, *Oncorhynchus nerka*: implications for magnetoreception, J. Exp. Biol. 140 (1988) 35–49. doi:10.1242/jeb.140.1.35.

[17] C.E. Diebel, R. Proksch, C.R. Green, P. Neilson, M.M. Walker, Magnetite defines a vertebrate magnetoreceptor, Nature. 406 (2000) 299–302. doi:10.1038/35018561.

[18] L.C. Naisbett-Jones, N.F. Putman, M.M. Scanlan, D.L.G. Noakes, K.J. Lohmann, Magnetoreception in fishes: The effect of magnetic pulses on orientation of juvenile Pacific salmon, J. Exp. Biol. 223 (2020) jeb222091. doi:10.1242/jeb.222091.

[19] K.R. Caspar, K. Moldenhauer, R.E. Moritz, P. Němec, E.P. Malkemper, S. Begall, Eyes are essential for magnetoreception in a mammal, J. R. Soc. Interface. 17 (2020) 20200513. doi:10.1098/rsif.2020.0513.

[20] L. Tian, W. Lin, S. Zhang, Y. Pan, Bat head contains soft magnetic particles: Evidence from magnetism, Bioelectromagnetics. 31 (2010) 499–503. doi:10.1002/bem.20590.

[21] M. Zapka, D. Heyers, C.M. Hein, S. Engels, N.L. Schneider, J. Hans, S. Weiler, D. Dreyer,

D. Kishkinev, J.M. Wild, H. Mouritsen, Visual but not trigeminal mediation of magnetic compass information in a migratory bird, Nature. 461 (2009) 1274–1277. doi:10.1038/nature08528.

[22] J.L. Kirschvink, A. Kobayashi-Kirschvink, B.J. Woodford, Magnetite biomineralization in the human brain., Proc. Natl. Acad. Sci. U. S. A. 89 (1992) 7683–7687. doi:10.1073/pnas.89.16.7683.

[23] M. Miglierini, J. Dekan, M. Kopani, A. Lancok, J. Kohout, M. Cieslar, Iron in spleen tissues, AIP Conf. Proc. 1489 (2012) 107–114. doi:10.1063/1.4759478.

[24] J.R. Dunn, M. Fuller, J. Zoeger, J. Dobson, F. Heller, J. Hammann, E. Caine, B.M. Moskowitz, Magnetic material in the human hippocampus, Brain Res. Bull. 36 (1995) 149–153. doi:10.1016/0361-9230(94)00182-Z.

[25] J. Dobson, Magnetic iron compounds in neurological disorders, Ann. N. Y. Acad. Sci. 1012 (2004) 183–192. doi:10.1196/annals.1306.016.

[26] R.B. Frankel, R.P. Blakemore, R.S. Wolfe, Magnetite in freshwater magnetotactic bacteria, Science. 203 (1979) 1355–1356. doi:10.1126/science.203.4387.1355.

[27] S. Mann, N.H.C. Sparks, R.B. Frankel, D.A. Bazylinski, H.W. Jannasch, Biomineralization of ferrimagnetic greigite (Fe_3S_4) and iron pyrite (FeS_2) in a magnetotactic bacterium, Nature. 343 (1990) 258–261. doi:10.1038/343258a0.

[28] M. Farina, D.M.S. Esquivel, H.G.P.L. De Barros, Magnetic iron-sulphur crystals from a magnetotactic microorganism, Nature. 343 (1990) 256–258. doi:10.1038/343256a0.

[29] C.T. Lefèvre, D.A. Bazylinski, Ecology, diversity, and evolution of magnetotactic bacteria, Microbiol. Mol. Biol. Rev. 77 (2013) 497–526. doi:10.1128/mmbr.00021-13.

[30] R.E. Kopp, T.D. Raub, D. Schumann, H. Vali, A. V Smirnov, J.L. Kirschvink, Magnetofossil spike during the Paleocene-Eocene thermal maximum: Ferromagnetic resonance, rock magnetic, and electron microscopy evidence from Ancora, New Jersey, United States, Paleoceanography. 22 (2007) PA4103. doi:10.1029/2007PA001473.

[31] I. Vasiliev, C. Franke, J.D. Meeldijk, M.J. Dekkers, C.G. Langereis, W. Krijgsman, Putative greigite magnetofossils from the Pliocene epoch, Nat. Geosci. 1 (2008) 782–786. doi:10.1038/ngeo335.

[32] E. Natan, R.R. Fitak, Y. Werber, Y. Vortman, Symbiotic magnetic sensing: raising evidence and beyond, Philos. Trans. R. Soc. B. 375 (2020) 20190595. doi:10.1098/rstb.2019.0595.

[33] C.M. Pieters, L.A. Taylor, S.K. Noble, L.P. Keller, B. Hapke, R. V. Morris, C.C. Allen, D.S. McKay, S. Wentworth, Space weathering on airless bodies: Resolving a mystery with lunar samples, Meteorit. Planet. Sci. 35 (2000) 1101–1107. doi:10.1111/j.1945-5100.2000.tb01496.x.

[34] J.F. Einsle, A.S. Eggeman, B.H. Martineau, Z. Saghi, S.M. Collins, R. Blukis, P.A.J. Bagot, P.A. Midgley, R.J. Harrison, Nanomagnetic properties of the meteorite cloudy zone, Proc. Natl. Acad. Sci. U. S. A. 115 (2018) E11436–E11445. doi:10.1073/pnas.1809378115.

[35] T. Hoang, A. Lazarian, Polarization of magnetic dipole emission and spinning dust emission from magnetic nanoparticles, Astrophys. J. 821 (2016) 91. doi:10.3847/0004-637x/821/2/91.

[36] B.T. Draine, B. Hensley, The submillimeter and millimeter excess of the Small Magellanic Cloud: Magnetic dipole emission from magnetic nanoparticles?, Astrophys. J. 757 (2012) 103. doi:10.1088/0004-637X/757/1/103.

[37] D.S. McKay, E.K. Gibson, K.L. Thomas-Keprta, H. Vali, C.S. Romanek, S.J. Clemett, X.D.F. Chillier, C.R. Maechling, R.N. Zare, Search for past life on Mars: Possible relic biogenic activity in martian meteorite ALH84001, Science. 273 (1996) 924–930. doi:10.1126/science.273.5277.924.

[38] D. Faivre, D. Schüler, Magnetotactic bacteria and magnetosomes, Chem. Rev. 108 (2008) 4875–4898. doi:10.1021/cr078258w.

[39] V. Uskokovic, S. Pernal, V.M. Wu, Earthicle: The design of a conceptually new type of particle, ACS Appl. Mater. Interfaces. 9 (2017) 1305–1321. doi:10.1021/acsami.6b14047.

[40] S.P. Gubin, ed., Magnetic nanoparticles, Wiley-VCH, Weinheim, 2009.

[41] I. Canton, G. Battaglia, Endocytosis at the nanoscale, Chem. Soc. Rev. 41 (2012) 2718–2739.

doi:10.1039/c2cs15309b.
[42] C. Kinnear, T.L. Moore, L. Rodriguez-Lorenzo, B. Rothen-Rutishauser, A. Petri-Fink, Form follows function: Nanoparticle shape and its implications for nanomedicine, Chem. Rev. 117 (2017) 11476–11521. doi:10.1021/acs.chemrev.7b00194.
[43] P. Žvátora, M. Veverka, P. Veverka, K. Knížek, K. Závěta, E. Pollert, V. Král, G. Goglio, E. Duguet, O. Kaman, Influence of surface and finite size effects on the structural and magnetic properties of nanocrystalline lanthanum strontium perovskite manganites, J. Solid State Chem. 204 (2013) 373–379. doi:10.1016/j.jssc.2013.06.006.
[44] R. Skomski, Nanomagnetics, J. Phys. Condens. Matter. 15 (2003) R841–R896. doi:10.1088/0953-8984/15/20/202.
[45] J.B. Goodenough, Theory of the role of covalence in the perovskite-type manganites [La,*M*(II)]MnO_3, Phys. Rev. 100 (1955) 564–573. doi:10.1103/PhysRev.100.564.
[46] J.B. Goodenough, An interpretation of the magnetic properties of the perovskite-type mixed crystals $La_{1-x}Sr_xCoO_{3-\lambda}$, J. Phys. Chem. Solids. 6 (1958) 287–297. doi:10.1016/0022-3697(58)90107-0.
[47] J. Kanamori, Superexchange interaction and symmetry properties of electron orbitals, J. Phys. Chem. Solids. 10 (1959) 87–98. doi:10.1016/0022-3697(59)90061-7.
[48] P.W. Anderson, New approach to the theory of superexchange interactions, Phys. Rev. 115 (1959) 2–13. doi:10.1103/PhysRev.115.2.
[49] D.I. Khomskii, Transition metal compounds, Cambridge University Press, 2014. doi:10.1017/CBO9781139096782.
[50] M.A. Ruderman, C. Kittel, Indirect exchange coupling of nuclear magnetic moments by conduction electrons, Phys. Rev. 96 (1954) 99–102. doi:10.1103/PhysRev.96.99.
[51] T. Kasuya, A theory of metallic ferro- and antiferromagnetism on Zener's model, Prog. Theor. Phys. 16 (1956) 45–57. doi:10.1143/ptp.16.45.
[52] K. Yosida, Magnetic properties of Cu-Mn alloys, Phys. Rev. 106 (1957) 893–898. doi:10.1103/PhysRev.106.893.
[53] C. Zener, Interaction between the d shells in the transition metals, Phys. Rev. 81 (1951) 440–444. doi:10.1103/PhysRev.81.440.
[54] S. Krupička, Fyzika feritů a příbuzných magnetických kysličníků, Academia, Praha, 1969.
[55] C.J. O'Connor, Magnetochemistry - Advances in Theory and Experimentation, in: Prog. Inorg. Chem., John Wiley & Sons, Ltd, 1982: pp. 203–283. doi:10.1002/9780470166307.ch4.
[56] I. Dzyaloshinsky, A thermodynamic theory of "weak" ferromagnetism of antiferromagnetics, J. Phys. Chem. Solids. 4 (1958) 241–255. doi:10.1016/0022-3697(58)90076-3.
[57] T. Moriya, Anisotropic superexchange interaction and weak ferromagnetism, Phys. Rev. 120 (1960) 91–98. doi:10.1103/PhysRev.120.91.
[58] I. Sosnowska, T.P. Neumaier, E. Steichele, Spiral magnetic ordering in bismuth ferrite, J. Phys. C Solid State Phys. 15 (1982) 4835–4846. doi:10.1088/0022-3719/15/23/020.
[59] R. Skomski, Simple Models of Magnetism, Oxford University Press, New York, 2008. doi:10.1093/acprof:oso/9780198570752.001.0001.
[60] A.R. Muxworthy, E. McClelland, Review of the low-temperature magnetic properties of magnetite from a rock magnetic perspective, Geophys. J. Int. 140 (2000) 101–114. doi:10.1046/j.1365-246X.2000.00999.x.
[61] L.R. Bickford, J.M. Brownlow, R.F. Penoyer, Magnetocrystalline anisotropy in cobalt-substituted magnetite single crystals, Proc. IEE - Part B Radio Electron. Eng. 104 (1957) 238–244. doi:10.1049/pi-b-1.1957.0038.
[62] Y. Syono, Magnetocrystalline anisotropy and magnetostriction of Fe_3O_4-Fe_2TiO_4 series: with special application to rock magnetism, Japanese J. Geophys. 4 (1965) 71–143.
[63] J.H. van Vleck, On the anisotropy of cubic ferromagnetic crystals, Phys. Rev. 52 (1937) 1178–1198. doi:10.1103/PhysRev.52.1178.
[64] W.F. Brown, Micromagnetics: Successor to domain theory?, J. Phys. Le Radium. 20 (1959) 101–104. doi:10.1051/jphysrad:01959002002-3010100.

[65] O. Petracic, Superparamagnetic nanoparticle ensembles, Superlattices Microstruct. 47 (2010) 569–578. doi:10.1016/j.spmi.2010.01.009.
[66] J.L. Dormann, D. Fiorani, E. Tronc, Magnetic relaxation in fine-particle systems, in: Adv. Chem. Phys., 1997: pp. 282–494. doi:10.1002/9780470141571.ch4.
[67] M. Jamet, W. Wernsdorfer, C. Thirion, V. Dupuis, P. Mélinon, A. Pérez, D. Mailly, Magnetic anisotropy in single clusters, Phys. Rev. B. 69 (2004) 024401. doi:10.1103/PhysRevB.69.024401.
[68] W. Wernsdorfer, E.B. Orozco, K. Hasselbach, A. Benoit, B. Barbara, N. Demoncy, A. Loiseau, H. Pascard, D. Mailly, Experimental evidence of the Néel-Brown model of magnetization reversal, Phys. Rev. Lett. 78 (1997) 1791–1794. doi:10.1103/PhysRevLett.78.1791.
[69] R.H. Victora, Predicted time dependence of the switching field for magnetic materials, Phys. Rev. Lett. 63 (1989) 457–460. doi:10.1103/PhysRevLett.63.457.
[70] X. Batlle, A. Labarta, Finite-size effects in fine particles: magnetic and transport properties, J. Phys. D. Appl. Phys. 35 (2002) 15–42. doi:10.1088/0022-3727/35/6/201.
[71] M. Knobel, W.C. Nunes, L.M. Socolovsky, E. De Biasi, J.M. Vargas, J.C. Denardin, Superparamagnetism and other magnetic features in granular materials: a review on ideal and real systems., J. Nanosci. Nanotechnol. 8 (2008) 2836–57. doi:10.1166/JNN.2008.017.
[72] E.C. Stoner, E.P. Wohlfarth, A mechanism of magnetic hysteresis in heterogeneous alloys, Philos. Trans. R. Soc. A. 240 (1948) 599–642. doi:10.1098/rsta.1948.0007.
[73] S. Bedanta, W. Kleemann, Supermagnetism, J. Phys. D. Appl. Phys. 42 (2009) 013001. doi:10.1088/0022-3727/42/1/013001.
[74] W.F. Brown, Thermal fluctuations of a single-domain particle, Phys. Rev. 130 (1963) 1677–1686. doi:10.1103/PhysRev.130.1677.
[75] W.T. Coffey, D.S.F. Crothers, J.L. Dormann, L.J. Geoghegan, Y.P. Kalmykov, J.T. Waldron, A.W. Wickstead, The effect of an oblique magnetic field on the superparamagnetic relaxation time, J. Magn. Magn. Mater. 145 (1995) L263–L267. doi:10.1016/0304-8853(94)00863-9.
[76] L. Néel, Theorie du tramage magnetique des ferromagnetiques aux grains fins avec applications aux terres cuites, Ann. Géophysique. 5 (1949) 99–136.
[77] W.F. Brown, Relaxational behavior of fine magnetic particles, J. Appl. Phys. 30 (1959) S130–S132. doi:10.1063/1.2185851.
[78] A. Furrer, ed., Introduction to Neutron Scattering: Lecture Notes of the Introductory Course of the 1st European Conference on Neutron Scattering (ECNS '96), Paul Scherrer Institut, Villigen, 1996.
[79] N.N. Greenwood, T.C. Gibb, Mössbauer Spectroscopy, Springer Netherlands, Dordrecht, 1971. doi:10.1007/978-94-009-5697-1.
[80] I.J. Bruvera, P. Mendoza Zélis, M. Pilar Calatayud, G.F. Goya, F.H. Sánchez, Determination of the blocking temperature of magnetic nanoparticles: The good, the bad, and the ugly, J. Appl. Phys. 118 (2015) 184304. doi:10.1063/1.4935484.
[81] J.S. Micha, B. Dieny, J.R. Régnard, J.F. Jacquot, J. Sort, Estimation of the Co nanoparticles size by magnetic measurements in Co/SiO_2 discontinuous multilayers, J. Magn. Magn. Mater. 272–276 (2004) e967–e968. doi:10.1016/j.jmmm.2003.12.268.
[82] H. Mamiya, M. Ohnuma, I. Nakatani, T. Furubayashim, Extraction of blocking temperature distribution from zero-field-cooled and field-cooled magnetization curves, IEEE Trans. Magn. 41 (2005) 3394–3396. doi:10.1109/TMAG.2005.855205.
[83] R.F.L. Evans, R.W. Chantrell, O. Chubykalo-Fesenko, Surface and interface effects in magnetic core–shell nanoparticles, MRS Bull. 38 (2013) 909–914. doi:10.1557/mrs.2013.231.
[84] P. Bruno, Tight-binding approach to the orbital magnetic moment and magnetocrystalline anisotropy of transition-metal monolayers, Phys. Rev. B. 39 (1989) 865–868. doi:10.1103/PhysRevB.39.865.
[85] P.A. Lindgård, P. V Hendriksen, Estimation of electronic and structural influence on the thermal magnetic properties of clusters, Phys. Rev. B. 49 (1994) 12291–12294.

doi:10.1103/PhysRevB.49.12291.
[86] L. Néel, Anisotropie magnétique superficielle et surstructures d'orientation, J. Phys. Le Radium. 15 (1954) 225–239. doi:10.1051/jphysrad:01954001504022500.
[87] B. Issa, I.M. Obaidat, B.A. Albiss, Y. Haik, Magnetic nanoparticles: Surface effects and properties related to biomedicine applications, Int. J. Mol. Sci. 14 (2013) 21266–21305. doi:10.3390/ijms141121266.
[88] I.M.L. Billas, A. Chatelain, W.A. de Heer, Magnetism from the atom to the bulk in iron, cobalt and nickel clusters, Science. 265 (1994) 1682–1684.
[89] F. Liu, M.R. Press, S.N. Khanna, P. Jena, Magnetism and local order: Ab initio tight-binding theory, Phys. Rev. B. 39 (1989) 6914–6924. doi:10.1103/PhysRevB.39.6914.
[90] M.B. Stearns, Origin of the hyperfine fields in pure Fe and at solute atoms in Fe, Phys. Rev. B. 4 (1971) 4081–4091. doi:10.1103/PhysRevB.4.4081.
[91] C.S. Wang, A.J. Freeman, Surface states, surface magnetization, and electron spin polarization: Fe(001), Phys. Rev. B. 24 (1981) 4364–4371. doi:10.1103/PhysRevB.24.4364.
[92] U. Herr, J. Jing, R. Birringer, U. Gonser, H. Gleiter, Investigation of nanocrystalline iron materials by Mössbauer spectroscopy, Appl. Phys. Lett. 50 (1987) 472–474. doi:10.1063/1.98177.
[93] A.E. Berkowitz, W.J. Schuele, P.J. Flanders, Influence of crystallite size on the magnetic properties of acicular γ-Fe_2O_3 particles, J. Appl. Phys. 39 (1968) 1261–1263. doi:10.1063/1.1656256.
[94] J.M.D. Coey, Noncollinear spin arrangement in ultrafine ferrimagnetic crystallites, Phys. Rev. Lett. 27 (1971) 1140–1142. doi:10.1103/PhysRevLett.27.1140.
[95] R.. Kodama, Magnetic nanoparticles, J. Magn. Magn. Mater. 200 (1999) 359–372. doi:10.1016/S0304-8853(99)00347-9.
[96] A. Ochi, K. Watanabe, M. Kiyama, T. Shinjo, Y. Bando, T. Takada, Surface magnetic properties of γ-Fe_2O_3 by ^{57}Fe Mössbauer emission spectroscopy, J. Phys. Soc. Japan. 50 (1981) 2777–2778. doi:10.1143/JPSJ.50.2777.
[97] K. Haneda, H. Kojima, A.H. Morrish, P.J. Picone, K. Wakai, Noncollinearity as a size effect of CrO_2 small particles, J. Appl. Phys. 53 (1982) 2686–2688. doi:10.1063/1.330893.
[98] A.H. Morrish, K. Haneda, Surface magnetic properties of fine particles, J. Magn. Magn. Mater. 35 (1983) 105–113. doi:10.1016/0304-8853(83)90468-7.
[99] T. Okada, H. Sekizawa, F. Ambe, S. Ambe, T. Yamadaya, Magnetic and Mössbauer studies of Co adsorbed γ-Fe_2O_3, J. Magn. Magn. Mater. 31–34 (1983) 903–904. doi:10.1016/0304-8853(83)90732-1.
[100] R.H. Kodama, S.A. Makhlouf, A.E. Berkowitz, Finite size effects in antiferromagnetic NiO nanoparticles, Phys. Rev. Lett. 79 (1997) 1393–1396. doi:10.1103/PhysRevLett.79.1393.
[101] R.H. Kodama, A.E. Berkowitz, E.J. Mc Niff, S. Foner, Surface spin disorder in $NiFe_2O_4$ nanoparticles, Phys. Rev. Lett. 77 (1996) 394–397. doi:10.1103/PhysRevLett.77.394.
[102] B. Martínez, X. Obradors, L. Balcells, A. Rouanet, C. Monty, Low temperature surface spin-glass transition in γ-Fe_2O_3 nanoparticles, Phys. Rev. Lett. 80 (1998) 181–184. doi:10.1103/PhysRevLett.80.181.
[103] M. Garcia Del Muro, X. Batlle, A. Labarta, Surface effects in barium hexaferrite nanoparticles, J. Magn. Magn. Mater. 196 (1999) 138–139. doi:10.1016/S0304-8853(98)00692-1.
[104] A.E. Berkowitz, R.H. Kodama, S.A. Makhloul, F.T. Parker, F.E. Spada, E.J. McNiff, S. Foner, Anomalous properties of magnetic nanoparticles, J. Magn. Magn. Mater. 196 (1999) 591–594. doi:10.1016/S0304-8853(98)00845-2.
[105] J.R.L. De Almeida, D.J. Thouless, Stability of the Sherrington-Kirkpatrick solution of a spin glass model, J. Phys. A. Math. Gen. 11 (1978) 983–990. doi:10.1088/0305-4470/11/5/028.
[106] H. Maletta, W. Zinn, Spin glasses, in: K.A. Gschneidner, L. Eyring (Eds.), Handb. Phys. Chem. Rare Earths, 1st ed., Elsevier, 1989: pp. 213–356. doi:10.1016/S0168-1273(89)12008-X.
[107] D. Kubániová, P. Brázda, K. Závěta, T. Kmječ, M. Klementová, J. Kohout, Identification of

ferric oxide polymorphs in nanoparticles prepared by sol-gel method and maximization of ε-Fe_2O_3 content, J. Magn. Magn. Mater. 472 (2019) 96–103. doi:10.1016/j.jmmm.2018.09.107.

[108] S. Mørup, D.E. Madsen, C. Frandsen, C.R.H. Bahl, M.F. Hansen, Experimental and theoretical studies of nanoparticles of antiferromagnetic materials, J. Phys. Condens. Matter. 19 (2007) 213202. doi:10.1088/0953-8984/19/21/213202.

[109] S. Mørup, Spin-canting and transverse relaxation at surfaces and in the interior of ferrimagnetic particles, J. Magn. Magn. Mater. 266 (2003) 110–118. doi:10.1016/S0304-8853(03)00462-1.

[110] C.J. Serna, F. Bødker, S. Mørup, M.P. Morales, F. Sandiumenge, S. Veintemillas-Verdaguer, Spin frustration in maghemite nanoparticles, Solid State Commun. 118 (2001) 437–440. doi:10.1016/S0038-1098(01)00150-8.

[111] F.T. Parker, M.W. Foster, D.T. Margulies, A.E. Berkowitz, Spin canting, surface magnetization, and finite-size effects in γ-Fe_2O_3 particles, Phys. Rev. B. 47 (1993) 7885–7891. doi:10.1103/physrevb.47.7885.

[112] M.M. Savosta, V.N. Krivoruchko, I.A. Danilenko, V.Y. Tarenkov, T.E. Konstantinova, A. V Borodin, V.N. Varyukhin, Nuclear spin dynamics and magnetic structure of nanosized particles of $La_{0.7}Sr_{0.3}Mn_{0.3}O_3$, Phys. Rev. B. 69 (2004) 024413. doi:10.1103/PhysRevB.69.024413.

[113] Z. Jirák, E. Hadová, O. Kaman, K. Knížek, M. Maryško, E. Pollert, M. Dlouhá, S. Vratislav, Ferromagnetism versus charge ordering in the $Pr_{0.5}Ca_{0.5}MnO_3$ and $La_{0.5}Ca_{0.5}MnO_3$ nanocrystals, Phys. Rev. B. 81 (2010) 024403. doi:10.1103/PhysRevB.81.024403.

[114] J. Curiale, M. Granada, H.E. Troiani, R.D. Sánchez, A.G. Leyva, P. Levy, K. Samwer, Magnetic dead layer in ferromagnetic manganite nanoparticles, Appl. Phys. Lett. 95 (2009) 43106. doi:10.1063/1.3187538.

[115] A.G. Roca, L. Gutiérrez, H. Gavilán, M.E. Fortes Brollo, S. Veintemillas-Verdaguer, M. del P. Morales, Design strategies for shape-controlled magnetic iron oxide nanoparticles, Adv. Drug Deliv. Rev. 138 (2019) 68–104. doi:10.1016/j.addr.2018.12.008.

[116] J.C. Maxwell, A treatise on electricity and magnetism, The Clarendon Press, Oxford, 1873. https://archive.org/details/atreatiseonelec00maxwgoog (accessed March 8, 2021).

[117] G. Salazar-Alvarez, J. Qin, V. Šepelák, I. Bergmann, M. Vasilakaki, K.N. Trohidou, J.D. Ardisson, W.A.A. Macedo, M. Mikhaylova, M. Muhammed, M.D. Baró, J. Nogués, Cubic versus spherical magnetic nanoparticles: The role of surface anisotropy, J. Am. Chem. Soc. 130 (2008) 13234–13239. doi:10.1021/ja0768744.

[118] C. Gatel, F.J. Bonilla, A. Meffre, E. Snoeck, B. Warot-Fonrose, B. Chaudret, L.M. Lacroix, T. Blon, Size-specific spin configurations in single iron nanomagnet: From flower to exotic vortices, Nano Lett. 15 (2015) 6952–6957. doi:10.1021/acs.nanolett.5b02892.

[119] J.A. Osborn, Demagnetizing factors of the general ellipsoid, Phys. Rev. 67 (1945) 351–357. doi:10.1103/PhysRev.67.351.

[120] M.E. Schabes, H.N. Bertram, Magnetization processes in ferromagnetic cubes, J. Appl. Phys. 64 (1988) 1347–1357. doi:10.1063/1.341858.

[121] L. Néel, Superparamagnétisme des grains très fins antiferromagnétiques, C. R. Hebd. Seances Acad. Sci. 252 (1961) 4075–4080. https://hal.archives-ouvertes.fr/hal-02878431 (accessed March 10, 2021).

[122] L. Néel, Superantiferromagnétisme dans les grains fins, C. R. Hebd. Seances Acad. Sci. 253 (1961) 203–208. https://hal.archives-ouvertes.fr/hal-02878449 (accessed March 10, 2021).

[123] N.J.O. Silva, V.S. Amaral, L.D. Carlos, Relevance of magnetic moment distribution and scaling law methods to study the magnetic behavior of antiferromagnetic nanoparticles: Application to ferritin, Phys. Rev. B. 71 (2005) 184408. doi:10.1103/PhysRevB.71.184408.

[124] C. Gilles, P. Bonville, K.K.W. Wong, S. Mann, Non-Langevin behaviour of the uncompensated magnetization in nanoparticles of artificial ferritin, Eur. Phys. J. B. 17 (2000) 417–427. doi:10.1007/s100510070121.

[125] L. Néel, Propriétés magnétiques des grains fins antiferromagnétiques: Superparamagnétisme

et superantiferromagnétisme, J. Phys. Soc. Japan. 17 (1962) 676–685.
[126] T. Shinjo, M. Kiyama, N. Sugita, K. Watanabe, T. Takada, Surface magnetism of α-Fe_2O_3 by Mössbauer spectroscopy, J. Magn. Magn. Mater. 35 (1983) 133–135. doi:10.1016/0304-8853(83)90475-4.
[127] R.D. Zysler, D. Fiorani, A.M. Testa, M. Godinho, E. Agostinelli, L. Suber, Size effects in the spin-flop transition of hematite nanoparticles, J. Magn. Magn. Mater. 272–276 (2004) 1575–1576. doi:10.1016/j.jmmm.2003.12.1128.
[128] S. Mørup, Spin-flop in antiferromagnetic microcrystals, Surf. Sci. 156 (1985) 888–892. doi:10.1016/0039-6028(85)90263-8.
[129] Ö. Özdemir, D.J. Dunlop, T.S. Berquó, Morin transition in hematite: Size dependence and thermal hysteresis, Geochemistry, Geophys. Geosystems. 9 (2008) 10–11. doi:10.1029/2008GC002110.
[130] F.J. Morin, Magnetic susceptibility of αFe_2O_3 and αFe_2O_3 with added titanium, Phys. Rev. 78 (1950) 819–820. doi:10.1103/PhysRev.78.819.2.
[131] A.H. Morrish, Canted Antiferromagnetism: Hematite, World Scientific Publishing, Singapore, 1994. doi:10.1142/2518.
[132] F. Bødker, M.F. Hansen, C.B. Koch, K. Lefmann, S. Mørup, Magnetic properties of hematite nanoparticles, Phys. Rev. B. 61 (2000) 6826–6838. doi:10.1103/PhysRevB.61.6826.
[133] N. Amin, S. Arajs, Morin temperature of annealed submicronic α-Fe_2O_3 particles, Phys. Rev. B. 35 (1987) 4810–4811. doi:10.1103/PhysRevB.35.4810.
[134] A. Sanson, O. Mathon, S. Pascarelli, Local vibrational dynamics of hematite (α-Fe_2O_3) studied by extended x-ray absorption fine structure and molecular dynamics, J. Chem. Phys. 140 (2014) 224504. doi:10.1063/1.4882282.
[135] R.E. Vandenberghe, E. Van San, E. De Grave, G.M. Da Costa, About the Morin transition in hematite in relation with particle size and aluminium substitution, Czechoslov. J. Phys. 51 (2001) 663–675. doi:10.1023/A:1017697715646.
[136] G.J. Muench, S. Arajs, E. Matijević, The Morin transition in small α-Fe_2O_3 particles, Phys. Status Solidi. 92 (1985) 187–192. doi:10.1002/pssa.2210920117.
[137] M. Vasquez-Mansilla, R.. Zysler, C. Arciprete, M. Dimitrijewits, D. Rodriguez-Sierra, C. Saragovi, Annealing effects on structural and magnetic properties of α-Fe_2O_3 nanoparticles, J. Magn. Magn. Mater. 226–230 (2001) 1907–1909. doi:10.1016/S0304-8853(00)00858-1.
[138] M.F. Hansen, C. Koch, S. Mørup, Magnetic dynamics of weakly and strongly interacting hematite nanoparticles, Phys. Rev. B. 62 (2000) 1124–1135. doi:10.1103/PhysRevB.62.1124.
[139] C. Frandsen, S. Mørup, Spin rotation in α-Fe_2O_3 nanoparticles by interparticle interactions, Phys. Rev. Lett. 94 (2005) 027202. doi:10.1103/PhysRevLett.94.027202.
[140] S. Shtrikman, E.P. Wohlfarth, The theory of the Vogel-Fulcher law of spin glasses, Phys. Lett. A. 85 (1981) 467–470. doi:10.1016/0375-9601(81)90441-2.
[141] D. Fiorani, J.L. Dormann, R. Cherkaoui, E. Tronc, F. Lucari, F. D'Orazio, L. Spinu, M. Nogues, A. Garcia, A.M. Testa, Collective magnetic state in nanoparticles systems, J. Magn. Magn. Mater. 196 (1999) 143–147. doi:10.1016/S0304-8853(98)00694-5.
[142] M. García del Muro, X. Batlle, A. Labarta, Erasing the glassy state in magnetic fine particles, Phys. Rev. B. 59 (1999) 13584–13587. doi:10.1103/PhysRevB.59.13584.
[143] M. Sasaki, P.E. Jönsson, H. Takayama, H. Mamiya, Aging and memory effects in superparamagnets and superspin glasses, Phys. Rev. B. 71 (2005) 104405. doi:10.1103/PhysRevB.71.104405.
[144] O. Petracic, X. Chen, S. Bedanta, W. Kleemann, S. Sahoo, S. Cardoso, P.P. Freitas, Collective states of interacting ferromagnetic nanoparticles, J. Magn. Magn. Mater. 300 (2006) 192–197. doi:10.1016/j.jmmm.2005.10.061.
[145] S. Mørup, M. Bo Madsen, J. Franck, J. Villadsen, C.J.W. Koch, A new interpretation of Mössbauer spectra of microcrystalline goethite: "Super-ferromagnetism" or "super-spin-glass" behaviour?, J. Magn. Magn. Mater. 40 (1983) 163–174. doi:10.1016/0304-8853(83)90024-0.
[146] J.M. Luttinger, L. Tisza, Theory of dipole interaction in crystals, Phys. Rev. 70 (1946) 954–

964. doi:10.1103/PhysRev.70.954.
[147] J. Jordanovic, M. Beleggia, J. Schiøtz, C. Frandsen, Simulations of super-structure domain walls in two dimensional assemblies of magnetic nanoparticles, J. Appl. Phys. 118 (2015) 043901. doi:10.1063/1.4926730.
[148] M. Varón, M. Beleggia, T. Kasama, R.J. Harrison, R.E. Dunin-Borkowski, V.F. Puntes, C. Frandsen, Dipolar magnetism in ordered and disordered low-dimensional nanoparticle assemblies, Sci. Rep. 3 (2013) 1234. doi:10.1038/srep01234.
[149] X. Batlle, N. Pérez, P. Guardia, O. Iglesias, A. Labarta, F. Bartolomé, L.M. García, J. Bartolomé, A.G. Roca, M.P. Morales, C.J. Serna, Magnetic nanoparticles with bulklike properties, J. Appl. Phys. 109 (2011) 07B524. doi:10.1063/1.3559504.
[150] B.H. Kim, N. Lee, H. Kim, K. An, Y. Il Park, Y. Choi, K. Shin, Y. Lee, S.G. Kwon, H. Bin Na, J.G. Park, T.Y. Ahn, Y.W. Kim, W.K. Moon, S.H. Choi, T. Hyeon, Large-scale synthesis of uniform and extremely small-sized iron oxide nanoparticles for high-resolution *T*i magnetic resonance imaging contrast agents, J. Am. Chem. Soc. 133 (2011) 12624–12631. doi:10.1021/ja203340u.
[151] D. Kim, N. Lee, M. Park, B.H. Kim, K. An, T. Hyeon, Synthesis of uniform ferrimagnetic magnetite nanocubes, J. Am. Chem. Soc. 131 (2009) 454–455. doi:10.1021/ja8086906.
[152] A.H. Lu, E.L. Salabas, F. Schüth, Magnetic nanoparticles: Synthesis, protection, functionalization, and application, Angew. Chemie - Int. Ed. 46 (2007) 1222–1244. doi:10.1002/anie.200602866.
[153] V.K. LaMer, R.H. Dinegar, Theory, production and mechanism of formation of monodispersed hydrosols, J. Am. Chem. Soc. 72 (1950) 4847–4854. doi:10.1021/ja01167a001.
[154] N. Bao, L. Shen, W. An, P. Padhan, C. Heath Turner, A. Gupta, Formation mechanism and shape control of monodisperse magnetic $CoFe_2O_4$ nanocrystals, Chem. Mater. 21 (2009) 3458–3468. doi:10.1021/cm901033m.
[155] C.R. Groom, I.J. Bruno, M.P. Lightfoot, S.C. Ward, The Cambridge Structural Database, Acta Cryst. 72 (2016) 171–179. doi:10.1107/S2052520616003954.
[156] R.-R. Xu, Q. Su, High Temperature Synthesis, in: Mod. Inorg. Synth. Chem., Elsevier, 2017: pp. 9–43. doi:10.1016/B978-0-444-63591-4.00002-1.
[157] J. Livage, M. Henry, C. Sanchez, Sol-gel chemistry of transition metal oxides, Prog. Solid State Chem. 18 (1988) 259–341. doi:10.1016/0079-6786(88)90005-2.
[158] B. Das, Theoretical study of small iron–oxyhydroxide clusters and formation of ferrihydrite, J. Phys. Chem. A. 122 (2018) 652–661. doi:10.1021/acs.jpca.7b09470.
[159] O. Kaman, P. Veverka, Z. Jirák, M. Maryško, K. Knížek, M. Veverka, P. Kašpar, M. Burian, V. Šepelák, E. Pollert, The magnetic and hyperthermia studies of bare and silica-coated $La_{0.75}Sr_{0.25}MnO_3$ nanoparticles, J. Nanoparticle Res. 13 (2011) 1237–1252. doi:10.1007/s11051-010-0117-x.
[160] E. Suvaci, E. Özel, Hydrothermal Synthesis, in: M. Pomeroy (Ed.), Encycl. Mater. Tech. Ceram. Glas., Elsevier, 2021: pp. 59–68. doi:10.1016/B978-0-12-803581-8.12096-X.
[161] T. Adschiri, Y. Hakuta, K. Sue, K. Arai, Hydrothermal synthesis of metal oxide nanoparticles at supercritical conditions, J. Nanoparticle Res. 3 (2001) 227–235. doi:10.1023/A:1017541705569.
[162] J.A. Darr, J. Zhang, N.M. Makwana, X. Weng, Continuous hydrothermal synthesis of inorganic nanoparticles: Applications and future directions, Chem. Rev. 117 (2017) 11125–11238. doi:10.1021/acs.chemrev.6b00417.
[163] S. Feng, L. Guanghua, Hydrothermal and Solvothermal Syntheses, in: Mod. Inorg. Synth. Chem., Elsevier, 2011: pp. 63–95. doi:10.1016/B978-0-444-53599-3.10004-6.
[164] E.U. Franck, Water and aqueous solutions at high pressures and temperatures, Pure Appl. Chem. 24 (1970) 13–30. doi:10.1351/pac197024010013.
[165] M. Yoshimura, K. Byrappa, Hydrothermal processing of materials: Past, present and future, J. Mater. Sci. 43 (2008) 2085–2103. doi:10.1007/s10853-007-1853-x.
[166] M. Imperor-Clerc, D. Bazin, M.D. Appay, P. Beaunier, A. Davidson, Crystallization of β-

MnO_2 nanowires in the pores of SBA-15 silicas: In situ investigation using synchrotron radiation, Chem. Mater. 16 (2004) 1813–1821. doi:10.1021/cm035353m.

[167] B. Singh, J. Na, M. Konarova, T. Wakihara, Y. Yamauchi, C. Salomon, M.B. Gawande, Functional mesoporous silica nanomaterials for catalysis and environmental applications, Bull. Chem. Soc. Jpn. 93 (2020) 1459–1496. doi:10.1246/bcsj.20200136.

[168] S. Rostamnia, E. Doustkhah, Nanoporous silica-supported organocatalyst: a heterogeneous and green hybrid catalyst for organic transformations, RSC Adv. 4 (2014) 28238–28248. doi:10.1039/C4RA03773A.

[169] L.T. Gibson, Mesosilica materials and organic pollutant adsorption: part A removal from air, Chem. Soc. Rev. 43 (2014) 5163–5172. doi:10.1039/c3cs60096c.

[170] L.T. Gibson, Mesosilica materials and organic pollutant adsorption: part B removal from aqueous solution, Chem. Soc. Rev. 43 (2014) 5173–5182. doi:10.1039/C3CS60095E.

[171] P. Brázda, J. Kohout, P. Bezdička, T. Kmječ, α-Fe_2O_3 versus β-Fe_2O_3: Controlling the phase of the transformation product of ε-Fe_2O_3 in the Fe_2O_3/SiO_2 system, Cryst. Growth Des. 14 (2014) 1039–1046. doi:10.1021/cg4015114.

[172] D. Zhao, Q. Huo, J. Feng, B.F. Chmelka, G.D. Stucky, Nonionic triblock and star diblock copolymer and oligomeric surfactant syntheses of highly ordered, hydrothermally stable, mesoporous silica structures, J. Am. Chem. Soc. 120 (1998) 6024–6036. doi:10.1021/ja974025i.

[173] J.C. Vartuli, K.D. Schmitt, C.T. Kresge, W.J. Roth, M.E. Leonowicz, S.B. McCullen, S.D. Hellring, J.S. Beck, J.L. Schlenker, Effect of surfactant/silica molar ratios on the formation of mesoporous molecular sieves: Inorganic mimicry of surfactant liquid-crystal phases and mechanistic implications, Chem. Mater. 6 (1994) 2317–2326. doi:10.1021/cm00048a018.

[174] V.L. Zholobenko, A.Y. Khodakov, M. Impéror-Clerc, D. Durand, I. Grillo, Initial stages of SBA-15 synthesis: An overview, Adv. Colloid Interface Sci. 142 (2008) 67–74. doi:10.1016/j.cis.2008.05.003.

[175] L. Li, D. Liu, Z. Guo, Y. Liu, W. Chu, Improved facile synthesis of mesoporous SBA-15-CTA using citric acid under mild conditions, J. Solid State Chem. 282 (2019) 121079. doi:10.1016/j.jssc.2019.121079.

[176] E. Delahaye, V. Escax, N. El Hassan, A. Davidson, R. Aquino, V. Dupuis, R. Perzynski, Y.L. Raikher, "Nanocasting": using SBA-15 silicas as hard templates to obtain ultrasmall monodispersed γ-Fe_2O_3 nanoparticles, J. Phys. Chem. B. 110 (2006) 26001–26011. doi:10.1021/jp0647075.

[177] A.P. Amrute, J. De Bellis, M. Felderhoff, F. Schüth, Mechanochemical synthesis of catalytic materials, Chem. - A Eur. J. 27 (2021) 6819–6847. doi:10.1002/chem.202004583.

[178] D. Tan, F. García, Main group mechanochemistry: from curiosity to established protocols, Chem. Soc. Rev. 48 (2019) 2274–2292. doi:10.1039/c7cs00813a.

[179] P. Baláž, M. Achimovicová, M. Baláž, P. Billik, C.Z. Zara, J.M. Criado, F. Delogu, E. Dutková, E. Gaffet, F.J. Gotor, R. Kumar, I. Mitov, T. Rojac, M. Senna, A. Streletskii, W.C. Krystyna, Hallmarks of mechanochemistry: From nanoparticles to technology, Chem. Soc. Rev. 42 (2013) 7571–7637. doi:10.1039/c3cs35468g.

[180] P. Baláž, Mechanochemistry in Nanoscience and Minerals Engineering, Springer, Berlin, Heidelberg, 2008. doi:10.1007/978-3-540-74855-7.

[181] E. Dutková, N. Daneu, Z.L. Bujňáková, M. Baláž, J. Kováč, J. Kováč, P. Baláž, Mechanochemical synthesis and characterization of $CuInS_2/ZnS$ nanocrystals, Molecules. 24 (2019) 1031. doi:10.3390/molecules24061031.

[182] S. Mornet, C. Elissalde, V. Hornebecq, O. Bidault, E. Duguet, A. Brisson, M. Maglione, Controlled growth of silica shell on $Ba_{0.6}Sr_{0.4}TiO_3$ nanoparticles used as precursors of ferroelectric composites, Chem. Mater. 17 (2005) 4530–4536. doi:10.1021/cm050884r.

[183] G. Goloverda, B. Jackson, C. Kidd, V. Kolesnichenko, Synthesis of ultrasmall magnetic iron oxide nanoparticles and study of their colloid and surface chemistry, J. Magn. Magn. Mater. 321 (2009) 1372–1376. doi:10.1016/j.jmmm.2009.02.041.

[184] R.B. Martin, A complete ionization scheme for citric acid, J. Phys. Chem. 65 (1961) 2053–

2055. doi:10.1021/j100828a032.
[185] J.W. Park, J.S. Shumaker-Parry, Structural study of citrate layers on gold nanoparticles: Role of intermolecular interactions in stabilizing nanoparticles, J. Am. Chem. Soc. 136 (2014) 1907–1921. doi:10.1021/ja4097384.
[186] N. Kallay, E. Matijević, Adsorption at solid/solution interfaces. 1. Interpretation of surface complexation of oxalic and citric acids with hematite, Langmuir. 1 (1985) 195–201. doi:10.1021/la00062a003.
[187] S. Biggs, P. Mulvaney, C.F. Zukoski, F. Grieser, Study of anion adsorption at the gold-aqueous solution interface by atomic force microscopy, J. Am. Chem. Soc. 116 (1994) 9150–9157. doi:10.1021/ja00099a033.
[188] W. Stöber, A. Fink, E. Bohn, Controlled growth of monodisperse silica spheres in the micron size range, J. Colloid Interface Sci. 26 (1968) 62–69. doi:10.1016/0021-9797(68)90272-5.
[189] J.O. Kroll, B.J. Riley, J.S. McCloy, J.A. Peterson, Sol–gel synthesis of iodosodalite precursors and subsequent consolidation with a glass binder made from oxides and sol–gel routes, J. Sol-Gel Sci. Technol. 96 (2020) 564–575. doi:10.1007/s10971-020-05348-2.
[190] O. Kaman, Příprava, struktura a vlastnosti hybridních nanočástic s jádry perovskitového a spinelového typu, Charles University, 2009.
[191] O. Kaman, T. Dědourková, J. Koktan, J. Kuličková, M. Maryško, P. Veverka, R. Havelek, K. Královec, K. Turnovcová, P. Jendelová, A. Schröfel, L. Svoboda, Silica-coated manganite and Mn-based ferrite nanoparticles: a comparative study focused on cytotoxicity, J. Nanoparticle Res. 18 (2016) 100. doi:10.1007/s11051-016-3402-5.
[192] S. V Patwardhan, F.S. Emami, R.J. Berry, S.E. Jones, R.R. Naik, O. Deschaume, H. Heinz, C.C. Perry, Chemistry of aqueous silica nanoparticle surfaces and the mechanism of selective peptide adsorption, J. Am. Chem. Soc. 134 (2012) 6244–6256. doi:10.1021/ja211307u.
[193] Z. Fei Yin, L. Wu, H. Gui Yang, Y. Hua Su, Recent progress in biomedical applications of titanium dioxide, Phys. Chem. Chem. Phys. 15 (2013) 4844–4858. doi:10.1039/c3cp43938k.
[194] Z. Jirák, J. Kuličková, V. Herynek, M. Maryško, J. Koktan, O. Kaman, Titania-coated manganite nanoparticles: Synthesis of the shell, characterization and MRI properties, J. Magn. Magn. Mater. 427 (2017) 245–250. doi:10.1016/j.jmmm.2016.10.097.
[195] O. Kaman, J. Kuličková, M. Maryško, P. Veverka, V. Herynek, R. Havelek, K. Královec, D. Kubániová, J. Kohout, P. Dvořák, Z. Jirák, Mn-Zn ferrite nanoparticles with silica and titania coatings: Synthesis, transverse relaxivity, and cytotoxicity, IEEE Trans. Magn. 53 (2017) 5300908. doi:10.1109/TMAG.2017.2721365.
[196] B.E. Yoldas, Hydrolysis of titanium alkoxide and effects of hydrolytic polycondensation parameters, J. Mater. Sci. 21 (1986) 1087–1092. doi:10.1007/BF01117399.
[197] D.J.M. Burkhard, Accessory chromium spinels: Their coexistence and alteration in serpentinites, Geochim. Cosmochim. Acta. 57 (1993) 1297–1306. doi:10.1016/0016-7037(93)90066-6.
[198] P.G. Spry, S.D. Scott, Zincian spinel and staurolite as guides to ore in the Appalachians and Scandinavian Caledonides, Can. Mineral. 24 (1986) 147–163. https://pubs.geoscienceworld.org/canmin/article-abstract/24/1/147/11828/Zincian-spinel-and-staurolite-as-guides-to-ore-in (accessed July 8, 2021).
[199] C. Biagioni, M. Pasero, The systematics of the spinel-type minerals: An overview, Am. Mineral. 99 (2014) 1254–1264. doi:10.2138/am.2014.4816.
[200] F. Bosi, C. Biagioni, M. Pasero, Nomenclature and classification of the spinel supergroup, Eur. J. Mineral. 31 (2019) 183–192. doi:10.1127/ejm/2019/0031-2788.
[201] J.B. Goodenough, Descriptions of outer d electrons in thiospinels, J. Phys. Chem. Solids. 30 (1969) 261–280. doi:10.1016/0022-3697(69)90308-4.
[202] S. Nishikawa, Structure of some crystals of spinel group, Proc. Tokyo Math. Soc. 2nd Ser. 8 (1915) 199–209. doi:10.11429/ptmps1907.8.7_199.
[203] W.H. Bragg, The structure of the spinel group of crystals, London, Edinburgh, Dublin Philos. Mag. J. Sci. Ser. 6. 30 (1915) 305–315. doi:10.1080/14786440808635400.

[204] J.F.W. Bowles, R.A. Howie, D.J. Vaughan, J. Zussman, Non-Silicates: Oxides, Hydroxides, and Sulphides, The Geological Society, London, 2011. doi:10.3749/canmin.49.5.1335.
[205] S. Sasaki, Radial distribution of electron density in magnetite, Fe_3O_4, Acta Crystallogr. Sect. B. 53 (1997) 762–766. doi:10.1107/S0108768197007842.
[206] H. Takagi, S. Niitaka, Highly frustrated magnetism in spinels, in: C. Lacroix, P. Mendels, F. Mila (Eds.), Introd. to Frustrated Magn., Springer, Berlin, Heidelberg, 2011: pp. 155–175. doi:10.1007/978-3-642-10589-0_7.
[207] F. Bosi, Chemical and structural variability in cubic spinel oxides, Acta Crystallogr. Sect. B. 75 (2019) 279–285. doi:10.1107/S2052520619002282.
[208] R.G. Burns, Mineralogical Applications of Crystal Field Theory, 2nd ed., Cambridge University Press, New York, 1993. doi:10.1017/CBO9780511524899.
[209] M.A. Halcrow, Trapping and manipulating excited spin states of transition metal compounds, Chem. Soc. Rev. 37 (2008) 278–289. doi:10.1039/b701085k.
[210] Jacobsite, (n.d.). https://www.mindat.org/gm/2061 (accessed April 28, 2021).
[211] Franklinite, (n.d.). https://www.mindat.org/gm/1598 (accessed April 28, 2021).
[212] Z. Szotek, W.M. Temmerman, D. Ködderitzsch, A. Svane, L. Petit, H. Winter, Electronic structures of normal and inverse spinel ferrites from first principles, Phys. Rev. B. 74 (2006) 174431. doi:10.1103/PhysRevB.74.174431.
[213] Z. Jirák, S. Vratislav, Temperature dependence of distribution of cations in $MnFe_2O_4$, Czechoslov. J. Phys. 24 (1974) 642–647. doi:10.1007/BF01587300.
[214] M.G. Brik, A. Suchocki, A. Kamińska, Lattice parameters and stability of the spinel compounds in relation to the ionic radii and electronegativities of constituting chemical elements, Inorg. Chem. 53 (2014) 5088–5099. doi:10.1021/ic500200a.
[215] J.S. Kang, G. Kim, H.J. Lee, D.H. Kim, H.S. Kim, J.H. Shim, S. Lee, H. Lee, J.Y. Kim, B.H. Kim, B.I. Min, Soft x-ray absorption spectroscopy and magnetic circular dichroism study of the valence and spin states in spinel $MnFe_2O_4$, Phys. Rev. B. 77 (2008) 035121. doi:10.1103/PhysRevB.77.035121.
[216] R. Nepal, M. Saghayezhian, J. Zhang, R. Jin, Observation of three magnetic states in spinel $MnFe_2O_4$ single crystals, J. Magn. Magn. Mater. 497 (2020) 165955. doi:10.1016/j.jmmm.2019.165955.
[217] D. Levy, L. Pastero, A. Hoser, G. Viscovo, Thermal expansion and cation partitioning of $MnFe_2O_4$ (jacobsite) from 1.6 to 1276 K studied by using neutron powder diffraction, Solid State Commun. 201 (2015) 15–19. doi:10.1016/j.ssc.2014.10.001.
[218] G.D. Rieck, J.J.M. Thijssen, The cation distribution in $CoFe_2O_4$, Acta Crystallogr. Sect. B. 24 (1968) 982–983. doi:10.1107/s0567740868003559.
[219] J. Teillet, F. Bouree, R. Krishnan, Magnetic structure of $CoFe_2O_4$, J. Magn. Magn. Mater. 123 (1993) 93–96. doi:10.1016/0304-8853(93)90017-V.
[220] M. Tachiki, Origin of the magnetic anisotropy energy of cobalt ferrite, Prog. Theor. Phys. 23 (1960) 1055–1072. doi:10.1143/ptp.23.1055.
[221] W. Schiessl, W. Potzel, H. Karzel, M. Steiner, G. Kalvius, A. Martin, Magnetic properties of the $ZnFe_2O_4$ spinel, Phys. Rev. B. 53 (1996) 9143–9152. doi:10.1103/PhysRevB.53.9143.
[222] K. Kamazawa, Y. Tsunoda, H. Kadowaki, K. Kohn, Magnetic neutron scattering measurements on a single crystal of frustrated $ZnFe_2O_4$, Phys. Rev. B. 68 (2003) 024412. doi:10.1103/PhysRevB.68.024412.
[223] K. Kamazawa, Y. Tsunoda, K. Odaka, K. Kohn, Spin liquid state in $ZnFe_2O_4$, J. Phys. Chem. Solids. 60 (1999) 1261–1264. doi:10.1016/S0022-3697(99)00099-2.
[224] Y. Yamada, K. Kamazawa, Y. Tsunoda, Interspin interactions in $ZnFe_2O_4$: Theoretical analysis of neutron scattering study, Phys. Rev. B. 66 (2002) 064401. doi:10.1103/PhysRevB.66.064401.
[225] K. Tomiyasu, K. Kamazawa, A spin molecule model for geometrically frustrated spinel $ZnFe_2O_4$, J. Phys. Soc. Japan. 80 (2011) SB024. doi:10.1143/JPSJS.80SB.SB024.
[226] K.L. Salcedo Rodríguez, S.J. Stewart, P.M. Mendoza Zélis, G.A. Pasquevich, C.E. Rodríguez Torres, Role of defects on the magnetic behaviour of the geometrically frustrated spinel

$ZnFe_2O_4$, J. Alloys Compd. 752 (2018) 289–295. doi:10.1016/j.jallcom.2018.04.172.
[227] Y. Ying, L. Wang, W. Li, L. Qiao, J. Zheng, J. Yu, W. Cai, L. Jiang, S. Che, L. Zhang, L. Ling, Spin glass in a geometrically frustrated magnet of $ZnFe_2O_4$ nanoparticles, J. Supercond. Nov. Magn. 31 (2018) 3553–3558. doi:10.1007/s10948-018-4626-7.
[228] Magnetite, (n.d.). https://www.mindat.org/gm/2538 (accessed April 23, 2021).
[229] M.S. Senn, J.P. Wright, J. Cumby, J.P. Attfield, Charge localization in the Verwey structure of magnetite, Phys. Rev. B. 92 (2015) 24104. doi:10.1103/PhysRevB.92.024104.
[230] H. Elnaggar, R. Wang, S. Lafuerza, E. Paris, A.C. Komarek, H. Guo, Y. Tseng, D. McNally, F. Frati, M.W. Haverkort, M. Sikora, T. Schmitt, F.M.F. De Groot, Possible absence of trimeron correlations above the Verwey temperature in Fe_3O_4, Phys. Rev. B. 101 (2020) 085107. doi:10.1103/PhysRevB.101.085107.
[231] R. Řezníček, V. Chlan, H. Štěpánková, P. Novák, Hyperfine field and electronic structure of magnetite below the Verwey transition, Phys. Rev. B. 91 (2015) 125134. doi:10.1103/PhysRevB.91.125134.
[232] P. Novák, H. Štěpánková, J. Englich, J. Kohout, NMR in magnetite below and around the Verwey transition, Phys. Rev. B. 61 (2000) 1256–1260. doi:10.1103/PhysRevB.61.1256.
[233] D. Schmitz, C. Schmitz-Antoniak, A. Warland, M. Darbandi, S. Haldar, S. Bhandary, O. Eriksson, B. Sanyal, H. Wende, The dipole moment of the spin density as a local indicator for phase transitions, Sci. Rep. 4 (2014) 5760. doi:10.1038/srep05760.
[234] J.P. Shepherd, J.W. Koenitzer, R. Aragón, J. Spalek, J.M. Honig, Heat capacity and entropy of nonstoichiometric magnetite $Fe_{3(1-\delta)}O_4$: The thermodynamic nature of the Verwey transition, Phys. Rev. B. 43 (1991) 8461–8471. doi:10.1103/PhysRevB.43.8461.
[235] R. Aragan, D.J. Buttrey, J.P. Shepherd, J.M. Honig, Influence of nonstoichiometry on the Verwey transition, Phys. Rev. B. 31 (1985) 430–436. doi:10.1103/PhysRevB.31.430.
[236] A. Kozłowski, Z. Kąkol, R. Zalecki, K. Knight, J. Sabol, J.M. Honig, Powder neutron diffraction studies of Zn-doped magnetite, J. Phys. Condens. Matter. 11 (1999) 2749–2758. doi:10.1088/0953-8984/11/13/011.
[237] A. Kozłowski, Z. Kakol, R. Zalecki, J.M. Honig, Specific heat of low doped magnetite, $Fe_{3-x}Ti_xO_4$ and $Fe_{3-y}Zn_yO_4$, J. Magn. Magn. Mater. 140–144 (1995) 2083–2084. doi:10.1016/0304-8853(94)00583-4.
[238] J. Lee, S.G. Kwon, J.G. Park, T. Hyeon, Size dependence of metal-insulator transition in stoichiometric Fe_3O_4 nanocrystals, Nano Lett. 15 (2015) 4337–4342. doi:10.1021/acs.nanolett.5b00331.
[239] A. Mitra, J. Mohapatra, S.S. Meena, C. V. Tomy, M. Aslam, Verwey transition in ultrasmall-sized octahedral Fe_3O_4 nanoparticles, J. Phys. Chem. C. 118 (2014) 19356–19362. doi:10.1021/jp501652e.
[240] M.B. Svendsen, Beta-Fe_2O_3 - eine neue Eisen(III)oxyd-Struktur, Naturwissenschaften. 45 (1958) 542. doi:10.1007/BF00632057.
[241] O. Malina, J. Tuček, P. Jakubec, J. Kašlík, I. Medřík, H. Tokoro, M. Yoshikiyo, A. Namai, S. Ohkoshi, R. Zbořil, Magnetic ground state of nanosized β-Fe_2O_3 and its remarkable electronic features, RSC Adv. 5 (2015) 49719–49727. doi:10.1039/C5RA07484C.
[242] J. Tuček, L. Machala, S. Ono, A. Namai, M. Yoshikiyo, K. Imoto, H. Tokoro, S. Ohkoshi, R. Zbořil, Zeta-Fe_2O_3 – A new stable polymorph in iron(III) oxide family, Sci. Rep. 5 (2015) 15091. doi:10.1038/srep15091.
[243] Maghemite, (n.d.). https://www.mindat.org/gm/2533 (accessed April 8, 2021).
[244] Maghemite – Wikimedia Commons, (n.d.). https://commons.wikimedia.org/wiki/Category:Maghemite?uselang=de (accessed July 5, 2021).
[245] M. Boudeulle, H. Batis-Landoulsi, C. Leclercq, P. Vergnon, Structure of γ-Fe_2O_3 microcrystals: Vacancy distribution and superstructure, J. Solid State Chem. 48 (1983) 21–32. doi:10.1016/0022-4596(83)90055-5.
[246] R.M. Cornell, U. Schwertmann, The Iron Oxides, Wiley, Weinheim, 2003. doi:10.1002/3527602097.

[247] K. Kelm, W. Mader, The symmetry of ordered cubic γ-Fe_2O_3 investigated by TEM, Zeitschrift Für Naturforsch. B. 61 (2006) 665–671. doi:10.1515/znb-2006-0605.
[248] C. Greaves, A powder neutron diffraction investigation of vacancy ordering and covalence in γ-Fe_2O_3, J. Solid State Chem. 49 (1983) 325–333. doi:10.1016/S0022-4596(83)80010-3.
[249] B. Lafuente, R.T. Downs, H. Yang, N. Stone, The power of databases: The RRUFF project, in: T. Armbruster, R.M. Danisi (Eds.), Highlights Mineral. Crystallogr., De Gruyter, 2015: pp. 1–30.
[250] Greigite - RRUFF Database: Raman, X-ray, Infrared, and Chemistry, (n.d.). https://rruff.info/Greigite (accessed April 23, 2021).
[251] B.J. Skinner, R.C. Erd, F.S. Grimaldi, Greigite, the thio-spinel of iron; a new mineral, Am. Mineral. 49 (1964) 543–555. http://pubs.geoscienceworld.org/msa/ammin/article-pdf/49/5-6/543/4247536/am-1964-543.pdf (accessed May 3, 2021).
[252] D.J. Vaughan, ed., Sulfide mineralogy and geochemistry, Mineralogical Society of America, 2006. doi:10.2138/rmg.2006.61.
[253] J.B. Goodenough, Structural chemistry of iron sulfides, Mater. Res. Bull. 13 (1978) 1305–1314. doi:10.1016/0025-5408(78)90121-6.
[254] L. Chang, B.D. Rainford, J.R. Stewart, C. Ritter, A.P. Roberts, Y. Tang, Q. Chen, Magnetic structure of greigite (Fe_3S_4) probed by neutron powder diffraction and polarized neutron diffraction, J. Geophys. Res. 114 (2009) B07101. doi:10.1029/2008JB006260.
[255] J.B. Goodenough, G.A. Fatseas, Mössbauer ^{57}Fe isomer shift as a measure of valence in mixed-valence iron sulfides, J. Solid State Chem. 41 (1982) 1–22. doi:10.1016/0022-4596(82)90028-7.
[256] L. Chang, A.P. Roberts, Y. Tang, B.D. Rainford, A.R. Muxworthy, Q. Chen, Fundamental magnetic parameters from pure synthetic greigite (Fe_3S_4), J. Geophys. Res. Solid Earth. 113 (2008) B06104. doi:10.1029/2007JB005502.
[257] M. Wu, J.S. Tse, Y. Pan, Electronic structures of greigite (Fe_3S_4): A hybrid functional study and prediction for a Verwey transition, Sci. Rep. 6 (2016) 21637. doi:10.1038/srep21637.
[258] A.J. Devey, R. Grau-Crespo, N.H. De Leeuw, Electronic and magnetic structure of Fe_3S_4: GGA+U investigation, Phys. Rev. B - Condens. Matter Mater. Phys. 79 (2009) 195126. doi:10.1103/PhysRevB.79.195126.
[259] S. Yamaguchi, H. Wada, Magnetic anisotropy of Fe_3S_4 as revealed by electron diffraction, J. Appl. Phys. 41 (1970) 1873–1874. doi:10.1063/1.1659128.
[260] H. Wang, Y. Zhang, K. Tachiyama, Z. Xia, J. Fang, Q. Li, G. Cheng, Y. Shi, J. Yu, T. Katayama, S. Yasui, M. Itoh, Large polarization switching and high-temperature magnetoelectric coupling in multiferroic $GaFeO_3$ systems, Inorg. Chem. 60 (2021) 225–230. doi:10.1021/acs.inorgchem.0c02855.
[261] L.F. Cótica, S.N. De Medeiros, I.A. Santos, A. Paesano, E.J. Kinast, J.B.M. Da Cunha, M. Venet, D. Garcia, J.A. Eiras, Structural, magnetic, and dielectric investigations of the $FeAlO_3$ multiferroic ceramics, Ferroelectrics. 338 (2006) 241–246. doi:10.1080/00150190600740366.
[262] H. Forestier, G. Guiot-Guillain, Une nouvelle variété ferromagnétique de sesquioxyde de fer, C. R. Hebd. Seances Acad. Sci. 199 (1934) 720–723. https://gallica.bnf.fr/ark:/12148/bpt6k3151h/f720.item#.
[263] R. Schrader, G. Büttner, Eine neue Eisen(III)-oxidphase: ε-Fe_2O_3, Zeitschrift Für Anorg. Und Allg. Chemie. 320 (1963) 220–234. doi:10.1002/zaac.19633200503.
[264] E. Tronc, C. Chanéac, J.P. Jolivet, Structural and magnetic characterization of ε-Fe_2O_3, J. Solid State Chem. 139 (1998) 93–104. doi:10.1088/0953-8984/23/12/126003.
[265] S.-I. Ohkoshi, A. Namai, T. Yamaoka, M. Yoshikiyo, K. Imoto, T. Nasu, S. Anan, Y. Umeta, K. Nakagawa, H. Tokoro, Mesoscopic bar magnet based on ε-Fe 2 O 3 hard ferrite, (2016). doi:10.1038/srep27212.
[266] S. Sakurai, K. Tomita, K. Hashimoto, H. Yashiro, S. Ohkoshi, Preparation of the nanowire form of ε-Fe_2O_3 single crystal and a study of the formation process, J. Phys. Chem. C. 112 (2008) 20212–20216. doi:10.1021/jp806336f.
[267] K. Knížek, M. Pashchenko, P. Levinský, O. Kaman, J. Houdková, P. Jiříček, J. Hejtmánek,

M. Soroka, J. Buršík, Spin Seebeck effect in ε-Fe_2O_3 thin films with high coercive field, J. Appl. Phys. 124 (2018) 213904. doi:10.1063/1.5045304.

[268] H. Xu, S. Lee, H. Xu, Luogufengite: A new nano-mineral of Fe_2O_3 polymorph with giant coercive field, Am. Mineral. 102 (2017) 711–719. doi:10.2138/am-2017-5849.

[269] M. Gich, C. Frontera, A. Roig, E. Taboada, E. Molins, H.R. Rechenberg, J.D. Ardisson, W.A.A. Macedo, C. Ritter, V. Hardy, J. Sort, V. Skumryev, J. Nogues, High and low-temperature crystal and magnetic structures of ε-Fe_2O_3 and their correlation to its magnetic properties, Chem. Mater. 18 (2006) 3889–3897. doi:10.1021/cm0609931.

[270] Y.C. Tseng, N.M. Souza-Neto, D. Haskel, M. Gich, C. Frontera, A. Roig, M. Van Veenendaal, J. Nogués, Nonzero orbital moment in high coercivity ε-Fe_2O_3 and low-temperature collapse of the magnetocrystalline anisotropy, Phys. Rev. B. 79 (2009) 094404. doi:10.1103/PhysRevB.79.094404.

[271] M. Yoshikiyo, K. Yamada, A. Namai, S.I. Ohkoshi, Study of the electronic structure and magnetic properties of ε-Fe_2O_3 by first-principles calculation and molecular orbital calculations, J. Phys. Chem. C. 116 (2012) 8688–8691. doi:10.1021/jp300769z.

[272] Y. V Knyazev, A.I. Chumakov, A.A. Dubrovskiy, S. V Semenov, I. Sergueev, S.S. Yakushkin, V.L. Kirillov, O.N. Martyanov, D.A. Balaev, Nuclear forward scattering application to the spiral magnetic structure study in ε-Fe_2O_3, Phys. Rev. B. 101 (2020) 94408. doi:10.1103/PhysRevB.101.094408.

[273] M. Gich, A. Roig, C. Frontera, E. Molins, J. Sort, M. Popovici, G. Chouteau, D. Martín y Marero, J. Nogués, J. Nogús, Large coercivity and low-temperature magnetic reorientation in ε-Fe_2O_3 nanoparticles, J. Appl. Phys. 98 (2005) 044307. doi:10.1063/1.1997297.

[274] M.E. Schabes, Micromagnetic theory of non-uniform magnetization processes in magnetic recording particles, J. Magn. Magn. Mater. 95 (1991) 249–288. doi:10.1016/0304-8853(91)90225-Y.

[275] J.L. García-Muñoz, A. Romaguera, F. Fauth, J. Nogués, M. Gich, Unveiling a new high-temperature ordered magnetic phase in ε-Fe_2O_3, Chem. Mater. 29 (2017) 9705–9713. doi:10.1021/acs.chemmater.7b03417.

[276] A.A. Dubrovskiy, S. V. Semenov, Y. V. Knyazev, S.I. Popkov, S.S. Yakushkin, V.L. Kirillov, O.N. Martyanov, D.A. Balaev, The low-temperature magnetic state and magnetic ordering temperature of ε-Fe_2O_3 iron oxide nanoparticles, IEEE Magn. Lett. 10 (2019) 6110103. doi:10.1109/LMAG.2019.2956674.

[277] A. Namai, M. Yoshikiyo, K. Yamada, S. Sakurai, T. Goto, T. Yoshida, T. Miyazaki, M. Nakajima, T. Suemoto, H. Tokoro, S. Ohkoshi, Hard magnetic ferrite with a gigantic coercivity and high frequency millimetre wave rotation, Nat. Commun. 3 (2012) 1035. doi:10.1038/ncomms2038.

[278] S.I. Ohkoshi, K. Imoto, A. Namai, S. Anan, M. Yoshikiyo, H. Tokoro, Large coercive field of 45 kOe in a magnetic film based on metal-substituted ε-iron oxide, J. Am. Chem. Soc. 139 (2017) 13268–13271. doi:10.1021/jacs.7b07087.

[279] S.I. Ohkoshi, S. Kuroki, S. Sakurai, K. Matsumoto, K. Sato, S. Sasaki, A millimeter-wave absorber based on gallium-substituted epsilon-iron oxide nanomagnets, Angew. Chemie - Int. Ed. 46 (2007) 8392–8395. doi:10.1002/anie.200703010.

[280] Chalcopyrite, (n.d.). https://www.mindat.org/gm/955 (accessed May 8, 2021).

[281] S. Conejeros, P. Alemany, M. Llunell, I. de P.R. Moreira, V. Sánchez, J. Llanos, Electronic Structure and Magnetic Properties of $CuFeS_2$, Inorg. Chem. 54 (2015) 4840–4849. doi:10.1021/acs.inorgchem.5b00399.

[282] E.C. Todd, D.M. Sherman, J.A. Purton, Surface oxidation of chalcopyrite ($CuFeS_2$) under ambient atmospheric and aqueous (pH 2-10) conditions: Cu, Fe L- and O K-edge X-ray spectroscopy, Geochim. Cosmochim. Acta. 67 (2003) 2137–2146. doi:10.1016/S0016-7037(02)01371-6.

[283] M. Fujisawa, S. Suga, T. Mizokawa, A. Fujimori, K. Sato, Electronic structures of $CuFeS_2$ and $CuAl_{0.9}Fe_{0.1}S_2$ studied by electron and optical spectroscopies, Phys. Rev. B. 49 (1994) 7155–7164. doi:10.1103/PhysRevB.49.7155.

[284] C.I. Pearce, R.A.D. Pattrick, D.J. Vaughan, C.M.B. Henderson, G. van der Laan, Copper oxidation state in chalcopyrite: Mixed Cu d^9 and d^{10} characteristics, Geochim. Cosmochim. Acta. 70 (2006) 4635–4642. doi:10.1016/j.gca.2006.05.017.

[285] D.H. Choi, I.B. Shim, C.S. Kim, Mössbauer study of antiferromagnetic $CuFeO_2$, J. Magn. Magn. Mater. 320 (2008) e575–e577. doi:10.1016/j.jmmm.2008.04.018.

[286] C. Boekema, A.M. Krupski, M. Varasteh, K. Parvin, F. Van Til, F. Van Der Woude, G.A. Sawatzky, Cu and Fe valence states in $CuFeS_2$, J. Magn. Magn. Mater. 272–276 (2004) 559–561. doi:10.1016/j.jmmm.2003.11.206.

[287] T. Teranishi, Magnetic and electric properties of chalcopyrite, J. Phys. Soc. Japan. 16 (1961) 1881–1887. doi:10.1143/JPSJ.16.1881.

[288] H.N. Ok, C.S. Kim, Mössbauer study of antiferromagnetic $CuFeS_2$, Nuovo Cim. B. 28 (1975) 138–142. doi:10.1007/BF02722811.

[289] G. Donnay, L.M. Corliss, J.D.H. Donnay, N. Elliot, J.M. Hastings, Symmetry of magnetic structures: Magnetic structure of chalcopyrite, Phys. Rev. 112 (1958) 1917–1923. doi:10.1103/PhysRev.112.1917.

[290] A. Rais, A.M. Gismelseed, A.D. Al-Rawas, Magnetic properties of natural chalcopyrite at low temperature, Mater. Lett. 46 (2000) 349–353. doi:10.1016/S0167-577X(00)00199-3.

[291] J.C. Woolley, A.M. Lamarche, G. Lamarche, M. Quintero, I.P. Swainson, T.M. Holden, Low temperature magnetic behaviour of $CuFeS_2$ from neutron diffraction data, J. Magn. Magn. Mater. 162 (1996) 347–354. doi:10.1016/S0304-8853(96)00252-1.

[292] K.S. Knight, W.G. Marshall, S.W. Zochowski, The low-temperature and high-pressure thermoelastic and structural properties of chalcopyrite, $CuFeS_2$, Can. Mineral. 49 (2011) 1015–1034. doi:10.3749/canmin.49.4.1015.

[293] T.E. Engin, A.V. Powell, S. Hull, A high temperature diffraction-resistance study of chalcopyrite, $CuFeS_2$, J. Solid State Chem. 184 (2011) 2272–2277. doi:10.1016/J.JSSC.2011.06.036.

[294] M. Colombo, S. Carregal-Romero, M.F. Casula, L. Gutiérrez, M.P. Morales, I.B. Böhm, J.T. Heverhagen, D. Prosperi, W.J. Parak, Biological applications of magnetic nanoparticles, Chem. Soc. Rev. 41 (2012) 4306–4334. doi:10.1039/c2cs15337h.

[295] N. Panagiotopoulos, F. Vogt, J. Barkhausen, T.M. Buzug, R.L. Duschka, K. Lüdtke-Buzug, M. Ahlborg, G. Bringout, C. Debbeler, M. Gräser, C. Kaethner, J. Stelzner, H. Medimagh, J. Haegele, Magnetic particle imaging: current developments and future directions, Int. J. Nanomedicine. 10 (2015) 3097–3114. doi:10.2147/IJN.S70488.

[296] T.H. Shin, Y. Choi, S. Kim, J. Cheon, Recent advances in magnetic nanoparticle-based multi-modal imaging, Chem. Soc. Rev. 44 (2015) 4501–4516. doi:10.1039/c4cs00345d.

[297] H. Huang, W. Feng, Y. Chen, J. Shi, Inorganic nanoparticles in clinical trials and translations, Nano Today. 35 (2020) 100972. doi:10.1016/j.nantod.2020.100972.

[298] C.P. Slichter, Principles of Magnetic Resonance, Springer, Berlin, Heidelberg, 1990. doi:10.1007/978-3-662-09441-9.

[299] R.W. Brown, Y.-C.N. Cheng, E.M. Haacke, M.R. Thompson, R. Venkatesan, eds., Magnetic Resonance Imaging: Physical Principles and Sequence Design, 2nd ed., John Wiley & Sons, Hoboken, 2014. doi:10.1002/9781118633953.

[300] H.Y. Carr, E.M. Purcell, Effects of diffusion on free precession in nuclear magnetic resonance experiments, Phys. Rev. 94 (1954) 630–638. doi:10.1103/PhysRev.94.630.

[301] S. Meiboom, D. Gill, Modified spin-echo method for measuring nuclear relaxation times, Rev. Sci. Instrum. 29 (1958) 688–691. doi:10.1063/1.1716296.

[302] J. Bylander, S. Gustavsson, F. Yan, F. Yoshihara, K. Harrabi, G. Fitch, D.G. Cory, Y. Nakamura, J.S. Tsai, W.D. Oliver, Noise spectroscopy through dynamical decoupling with a superconducting flux qubit, Nat. Phys. 7 (2011) 565–570. doi:10.1038/nphys1994.

[303] P.J. Nacher, Magnetic resonance imaging: From spin physics to medical diagnosis, in: B. Duplantier, J.-M. Raimond, V. Rivasseau (Eds.), Spin Poincare Semin. 2007, Birkhäuser, Basel, 2009: pp. 159–193. doi:10.1007/978-3-7643-8799-0-6.

[304] K.D. Sattler, ed., Handbook of Nanophysics: Nanomedicine and Nanorobotics, CRC Press,

2011.
[305] A. Ranga, Y. Agarwal, K.J. Garg, Gadolinium based contrast agents in current practice: Risks of accumulation and toxicity in patients with normal renal function, Indian J. Radiol. Imaging. 27 (2017) 141–147. doi:10.4103/0971-3026.209212.
[306] D.H. Carr, J. Brown, G.M. Bydder, H.J. Weinmann, U. Speck, D.J. Thomas, I.R. Young, Intravenous chelated gadolinium as a contrast agent in NMR imaging of cerebral tumours, Lancet. 323 (1984) 484–486. doi:10.1016/S0140-6736(84)92852-6.
[307] D.H. Carr, J. Brown, G.M. Bydder, R.E. Steiner, H.J. Weinmann, U. Speck, A.S. Hall, I.R. Young, Gadolinium-DTPA as a contrast agent in MRI: Initial clinical experience in 20 patients, Am. J. Roentgenol. 143 (1984) 215–224. doi:10.2214/ajr.143.2.215.
[308] S.E. Cowper, H.S. Robin, S.M. Steinberg, L.D. Su, S. Gupta, P.E. LeBoit, Scleromyxoedema-like cutaneous diseases in renal-dialysis patients, Lancet. 356 (2000) 1000–1001. doi:10.1016/S0140-6736(00)02694-5.
[309] T. Grobner, Gadolinium - A specific trigger for the development of nephrogenic fibrosing dermopathy and nephrogenic systemic fibrosis?, Nephrol. Dial. Transplant. 21 (2006) 1104–1108. doi:10.1093/ndt/gfk062.
[310] R.J. McDonald, J.S. McDonald, D.F. Kallmes, M.E. Jentoft, D.L. Murray, K.R. Thielen, E.E. Williamson, L.J. Eckel, Intracranial gadolinium deposition after contrast-enhanced MR imaging, Radiology. 275 (2015) 772–782. doi:10.1148/radiol.15150025.
[311] R.J. McDonald, J.S. McDonald, D.F. Kallmes, M.E. Jentoft, M.A. Paolini, D.L. Murray, E.E. Williamson, L.J. Eckel, Gadolinium deposition in human brain tissues after contrast-enhanced MR imaging in adult patients without intracranial abnormalities, Radiology. 285 (2017) 546–554. doi:10.1148/radiol.2017161595.
[312] M. Bau, P. Dulski, Anthropogenic origin of positive gadolinium anomalies in river waters, Earth Planet. Sci. Lett. 143 (1996) 245–255. doi:10.1016/0012-821x(96)00127-6.
[313] S. Kulaksiz, M. Bau, Anthropogenic gadolinium as a microcontaminant in tap water used as drinking water in urban areas and megacities, Appl. Geochemistry. 26 (2011) 1877–1885. doi:10.1016/j.apgeochem.2011.06.011.
[314] J. Wahsner, E.M. Gale, A. Rodríguez-Rodríguez, P. Caravan, Chemistry of MRI contrast agents: Current challenges and new frontiers, Chem. Rev. 119 (2019) 957–1057. doi:10.1021/acs.chemrev.8b00363.
[315] Gadodiamide - MedChemExpress, (n.d.). https://www.medchemexpress.com/Gadodiamide.html (accessed July 17, 2021).
[316] R.A. Brooks, F. Moiny, P. Gillis, On T_2-shortening by weakly magnetized particles: The chemical exchange model, Magn. Reson. Med. 45 (2001) 1014–1020. doi:10.1002/mrm.1135.
[317] P.F. Renshaw, C.S. Owen, A.C. McLaughlin, T.G. Frey, J.S. Leigh, Ferromagnetic contrast agents: A new approach, Magn. Reson. Med. 3 (1986) 217–225. doi:10.1002/mrm.1910030205.
[318] Q.L. Vuong, P. Gillis, A. Roch, Y. Gossuin, Magnetic resonance relaxation induced by superparamagnetic particles used as contrast agents in magnetic resonance imaging: a theoretical review, Wiley Interdiscip. Rev. Nanomedicine Nanobiotechnology. 9 (2017) e1468. doi:10.1002/wnan.1468.
[319] M.R.J. Carroll, R.C. Woodward, M.J. House, W.Y. Teoh, R. Amal, T.L. Hanley, T.G. St Pierre, Experimental validation of proton transverse relaxivity models for superparamagnetic nanoparticle MRI contrast agents, Nanotechnology. 21 (2010) 035103. doi:10.1088/0957-4484/21/3/035103.
[320] P. Gillis, F. Moiny, R.A. Brooks, On T_2-shortening by strongly magnetized spheres: A partial refocusing model, Magn. Reson. Med. 47 (2002) 257–263. doi:10.1002/mrm.10059.
[321] Y. Ayant, E. Belorizky, J. Aluzon, J. Gallice, Calcul des densités spectrales résultant d'un mouvement aléatoire de translation en relaxation par interaction dipolaire magnétique dans les liquides, J. Phys. 36 (1975) 991–1004. doi:10.1051/jphys:019750036010099100.
[322] D.A. Yablonskiy, E.M. Haacke, Theory of NMR signal behavior in magnetically inhomogeneous tissues: The static dephasing regime, Magn. Reson. Med. 32 (1994) 749–763.

doi:10.1002/mrm.1910320610.
[323] A. Roch, Y. Gossuin, R.N. Muller, P. Gillis, Superparamagnetic colloid suspensions: Water magnetic relaxation and clustering, J. Magn. Magn. Mater. 293 (2005) 532–539. doi:10.1016/j.jmmm.2005.01.070.
[324] R.J. S Brown, Distribution of fields from randomly placed dipoles: Free-precession signal decay as result of magnetic grains, Phys. Rev. 121 (1961) 1379–1382. doi:10.1103/PhysRev.121.1379.
[325] Q.L. Vuong, J.F. Berret, J. Fresnais, Y. Gossuin, O. Sandre, A universal scaling law to predict the efficiency of magnetic nanoparticles as MRI T_2-contrast agents, Adv. Healthc. Mater. 1 (2012) 502–512. doi:10.1002/adhm.201200078.
[326] R.J. Speedy, C.A. Angell, Isothermal compressibility of supercooled water and evidence for a thermodynamic singularity at -45°C, J. Chem. Phys. 65 (1976) 851–858. doi:10.1063/1.433153.
[327] R.A. Brooks, T_2-shortening by strongly magnetized spheres: A chemical exchange model, Magn. Reson. Med. 47 (2002) 388–391. doi:10.1002/mrm.10064.
[328] H.W. De Haan, Mechanisms of proton spin dephasing in a system of magnetic particles, Magn. Reson. Med. 66 (2011) 1748–1758. doi:10.1002/mrm.22966.
[329] M. Lévy, F. Gazeau, C. Wilhelm, S. Neveu, M. Devaud, P. Levitz, Revisiting MRI contrast properties of nanoparticles: Beyond the superparamagnetic regime, J. Phys. Chem. C. 117 (2013) 15369–15374. doi:10.1021/jp404199f.
[330] A.-L. Rollet, S. Neveu, P. Porion, V. Dupuis, N. Cherrak, P. Levitz, New approach for understanding experimental NMR relaxivity properties of magnetic nanoparticles: focus on cobalt ferrite, Phys. Chem. Chem. Phys. 18 (2016) 32981–32991. doi:10.1039/C6CP06012A.
[331] Q.L. Vuong, P. Gillis, Y. Gossuin, Monte Carlo simulation and theory of proton NMR transverse relaxation induced by aggregation of magnetic particles used as MRI contrast agents, J. Magn. Reson. 212 (2011) 139–148. doi:10.1016/j.jmr.2011.06.024.
[332] Y. Matsumoto, A. Jasanoff, T_2 relaxation induced by clusters of superparamagnetic nanoparticles: Monte Carlo simulations, Magn. Reson. Imaging. 26 (2008) 994–998. doi:10.1016/j.mri.2008.01.039.
[333] M.G. Shapiro, T. Atanasijevic, H. Faas, G.G. Westmeyer, A. Jasanoff, Dynamic imaging with MRI contrast agents: quantitative considerations, Magn. Reson. Imaging. 24 (2006) 449–462. doi:10.1016/j.mri.2005.12.033.
[334] K.A. Brown, C.C. Vassiliou, D. Issadore, J. Berezovsky, M.J. Cima, R.M. Westervelt, Scaling of transverse nuclear magnetic relaxation due to magnetic nanoparticle aggregation, J. Magn. Magn. Mater. 322 (2010) 3122–3126. doi:10.1016/j.jmmm.2010.05.044.
[335] Z. Zhou, R. Tian, Z. Wang, Z. Yang, Y. Liu, G. Liu, R. Wang, J. Gao, J. Song, L. Nie, X. Chen, Artificial local magnetic field inhomogeneity enhances T_2 relaxivity, Nat. Commun. 8 (2017) 15468. doi:10.1038/ncomms15468.
[336] L.E.W. LaConte, N. Nitin, O. Zurkiya, D. Caruntu, C.J. O'Connor, X. Hu, G. Bao, Coating thickness of magnetic iron oxide nanoparticles affects R_2 relaxivity, J. Magn. Reson. Imaging. 26 (2007) 1634–1641. doi:10.1002/jmri.21194.
[337] J. Huang, L. Wang, R. Lin, A.Y. Wang, L. Yang, M. Kuang, W. Qian, H. Mao, Casein-coated iron oxide nanoparticles for high MRI contrast enhancement and efficient cell targeting, ACS Appl. Mater. Interfaces. 5 (2013) 4632–4639. doi:10.1021/am400713j.
[338] T. Dědourková, O. Kaman, P. Veverka, J. Koktan, M. Veverka, J. Kuličková, Z. Jirák, V. Herynek, Clusters of magnetic nanoparticles as contrast agents for MRI: Effect of aggregation on transverse relaxivity, IEEE Trans. Magn. 51 (2015) 5300804. doi:10.1109/TMAG.2015.2438112.
[339] S. Laurent, D. Forge, M. Port, A. Roch, C. Robic, L. Vander Elst, R.N. Muller, Magnetic iron oxide nanoparticles: Synthesis, stabilization, vectorization, physicochemical characterizations, and biological applications, Chem. Rev. 108 (2008) 2064–2110. doi:10.1021/cr068445e.
[340] M. Holz, S.R. Heil, A. Sacco, Temperature-dependent self-diffusion coefficients of water

and six selected molecular liquids for calibration in accurate ^{1}H NMR PFG measurements, Phys. Chem. Chem. Phys. 2 (2000) 4740–4742. doi:10.1039/b005319h.

[341] L.B. Kiss, J. Söderlund, G.A. Niklasson, C.G. Granqvist, New approach to the origin of lognormal size distributions of nanoparticles, Nanotechnology. 25 (1999) 25–28. doi:10.1088/0957-4484/10/1/006.

[342] O.B. Miguel, Y. Gossuin, M.P. Morales, P. Gillis, R.N. Muller, S. Veintemillas-Verdaguer, Comparative analysis of the ^{1}H NMR relaxation enhancement produced by iron oxide and core-shell iron-iron oxide nanoparticles, Magn. Reson. Imaging. 25 (2007) 1437–1441. doi:10.1016/j.mri.2007.04.006.

[343] F. Brero, M. Basini, M. Avolio, F. Orsini, P. Arosio, C. Sangregorio, C. Innocenti, A. Guerrini, J. Boucard, E. Ishow, M. Lecouvey, J. Fresnais, L. Lartigue, A. Lascialfari, Coating effect on the ^{1}H-NMR relaxation properties of iron oxide magnetic nanoparticles, Nanomaterials. 10 (2020) 1660. doi:10.3390/nano10091660.

[344] I.C. Bourg, C.I. Steefel, Molecular dynamics simulations of water structure and diffusion in silica nanopores, J. Phys. Chem. C. 116 (2012) 11556–11564. doi:10.1021/jp301299a.

[345] P. Reimer, N. Jähnke, M. Fiebich, W. Schima, F. Deckers, C. Marx, N. Holzknecht, S. Saini, Hepatic lesion detection and characterization: Value of nonenhanced MR imaging, superparamagnetic iron oxide-enhanced MR imaging, and spiral CT - ROC analysis, Radiology. 217 (2000) 152–158. doi:10.1148/radiology.217.1.r00oc31152.

[346] H.E. Daldrup-Link, Ten things you might not know about iron oxide nanoparticles, Radiology. 284 (2017) 616–629. doi:10.1148/radiol.2017162759.

[347] D.D. Stark, R. Weissleder, G. Elizondo, P.F. Hahn, S. Saini, L.E. Todd, J. Wittenberg, J.T. Ferrucci, Superparamagnetic iron oxide: Clinical application as a contrast agent for MR imaging of the liver, Radiology. 168 (1988) 297–301. doi:10.1148/radiology.168.2.3393649.

[348] P. Reimer, T. Balzer, Ferucarbotran (Resovist): A new clinically approved RES-specific contrast agent for contrast-enhanced MRI of the liver: Properties, clinical development, and applications, Eur. Radiol. 13 (2003) 1266–1276. doi:10.1007/s00330-002-1721-7.

[349] Y.-X. Wang, Superparamagnetic iron oxide based MRI contrast agents: Current status of clinical application, Quant. Imaging Med. Surg. 1 (2011) 35–40. doi:10.3978/j.issn.2223-4292.2011.08.03.

[350] M.G. Harisinghani, J. Barentsz, P.F. Hahn, W.M. Deserno, S. Tabatabaei, C.H. van de Kaa, J. de la Rosette, R. Weissleder, Noninvasive detection of clinically occult lymph-node metastases in prostate cancer, N. Engl. J. Med. 348 (2003) 2491–2499. doi:10.1056/nejmoa022749.

[351] M.G. Harisinghani, R. Weissleder, Sensitive, noninvasive detection of lymph node metastases, PLoS Med. 1 (2004) 202–209. doi:10.1371/journal.pmed.0010066.

[352] W. Li, S. Tutton, A.T. Vu, L. Pierchala, B.S.Y. Li, J.M. Lewis, P. V. Prasad, R.R. Edelman, First-pass contrast-enhanced magnetic resonance angiography in humans using ferumoxytol, a novel ultrasmall superparamagnetic iron oxide (USPIO)-based blood pool agent, J. Magn. Reson. Imaging. 21 (2005) 46–52. doi:10.1002/jmri.20235.

[353] M.M. Vellinga, H. Vrenken, H.E. Hulst, C.H. Polman, B.M.J. Uitdehaag, P.J.W. Pouwels, F. Barkhof, J.J.G. Geurts, Use of ultrasmall superparamagnetic particles of iron oxide (USPIO)-enhanced MRI to demonstrate diffuse inflammation in the normal-appearing white matter (NAWM) of multiple sclerosis (MS) patients: An exploratory study, J. Magn. Reson. Imaging. 29 (2009) 774–779. doi:10.1002/jmri.21678.

[354] E.A. Neuwelt, C.G. Várallyay, S. Manninger, D. Solymosi, M. Haluska, M.A. Hunt, G. Nesbit, A. Stevens, M. Jerosch-Herold, P.M. Jacobs, J.M. Hoffman, The potential of ferumoxytol nanoparticle magnetic resonance imaging, perfusion, and angiography in central nervous system malignancy: A pilot study, Neurosurgery. 60 (2007) 601–611. doi:10.1227/01.NEU.0000255350.71700.37.

[355] W.S. Enochs, G. Harsh, F. Hochberg, R. Weissleder, Improved delineation of human brain tumors on MR images using a long-circulating, superparamagnetic iron oxide agent, J. Magn. Reson. Imaging. 9 (1999) 228–232. doi:10.1002/(SICI)1522-

2586(199902)9:2<228::AID-JMRI12>3.0.CO;2-K.
[356] Y.X.J. Wang, Current status of superparamagnetic iron oxide contrast agents for liver magnetic resonance imaging, World J. Gastroenterol. 21 (2015) 13400–13402. doi:10.3748/wjg.v21.i47.13400.
[357] A.S. Thakor, J. V Jokerst, P. Ghanouni, J.L. Campbell, E. Mittra, S.S. Gambhir, Clinically approved nanoparticle imaging agents, J. Nucl. Med. 57 (2016) 1833–1837. doi:10.2967/jnumed.116.181362.
[358] R.A.M. Heesakkers, G.J. Jager, A.M. Hövels, B. De Hoop, H.C.M. Van Den Bosch, F. Raat, J.A. Witjes, P.F.A. Mulders, C.H. Van Der Kaa, J.O. Barentsz, Prostate cancer: Detection of lymph node metastases outside the routine surgical area with ferumoxtran-10-enhanced MR imaging, Radiology. 251 (2009) 408–414. doi:10.1148/radiol.2512071018.
[359] I.J.M. De Vries, W.J. Lesterhuis, J.O. Barentsz, P. Verdijk, J.H. Van Krieken, O.C. Boerman, W.J.G. Oyen, J.J. Bonenkamp, J.B. Boezeman, G.J. Adema, J.W.M. Bulte, T.W.J. Scheenen, C.J.A. Punt, A. Heerschap, C.G. Figdor, Magnetic resonance tracking of dendritic cells in melanoma patients for monitoring of cellular therapy, Nat. Biotechnol. 23 (2005) 1407–1413. doi:10.1038/nbt1154.
[360] M.R. Bernsen, J. Guenoun, S.T. Van Tiel, G.P. Krestin, Nanoparticles and clinically applicable cell tracking, Br. J. Radiol. 88 (2015) 20150375. doi:10.1259/bjr.20150375.
[361] J.C. Glover, M. Aswendt, J.L. Boulland, J. Lojk, S. Stamenković, P. Andjus, F. Fiori, M. Hoehn, D. Mitrecic, M. Pavlin, S. Cavalli, C. Frati, F. Quaini, In vivo cell tracking using non-invasive imaging of iron oxide-based particles with particular relevance for stem cell-based treatments of neurological and cardiac disease, Mol. Imaging Biol. 22 (2020) 1469–1488. doi:10.1007/s11307-019-01440-4.
[362] E.T. Ahrens, J.W.M. Bulte, Tracking immune cells in vivo using magnetic resonance imaging, Nat. Rev. Immunol. 13 (2013) 755–63. doi:10.1038/nri3531.
[363] S.M. Cromer Berman, P. Walczak, J.W.M. Bulte, Tracking stem cells using magnetic nanoparticles, Wiley Interdiscip. Rev. Nanomedicine Nanobiotechnology. 3 (2011) 343–355. doi:10.1002/wnan.140.
[364] P. Walczak, J. Ruiz-Cabello, D.A. Kedziorek, A.A. Gilad, S. Lin, B. Barnett, L. Qin, H. Levitsky, J.W.M. Bulte, Magnetoelectroporation: improved labeling of neural stem cells and leukocytes for cellular magnetic resonance imaging using a single FDA-approved agent, Nanomedicine. 2 (2006) 89–94. doi:10.1016/j.nano.2006.01.003.
[365] B. Qiu, D. Xie, P. Walczak, X. Li, J. Ruiz-Cabello, S. Minoshima, J.W.M. Bulte, X. Yang, Magnetosonoporation: Instant magnetic labeling of stem cells, Magn. Reson. Med. 63 (2010) 1437–1441. doi:10.1002/mrm.22348.
[366] C.M. Long, H.W.M. Van Laarhoven, J.W.M. Bulte, H.I. Levitsky, Magnetovaccination as a novel method to assess and quantify dendritic cell tumor antigen capture and delivery to lymph nodes, Cancer Res. 69 (2009) 3180–3187. doi:10.1158/0008-5472.CAN-08-3691.
[367] E.M. Shapiro, K. Sharer, S. Skrtic, A.P. Koretsky, In vivo detection of single cells by MRI, Magn. Reson. Med. 55 (2006) 242–249. doi:10.1002/mrm.20718.
[368] R. Guzman, N. Uchida, T.M. Bliss, D. He, K.K. Christopherson, D. Stellwagen, A. Capela, J. Greve, R.C. Malenka, M.E. Moseley, T.D. Palmer, G.K. Steinberg, Long-term monitoring of transplanted human neural stem cells in developmental and pathological contexts with MRI, Proc. Natl. Acad. Sci. U. S. A. 104 (2007) 10211–10216. doi:10.1073/pnas.0608519104.
[369] P. Walczak, D.A. Kedziorek, A.A. Gilad, B.P. Barnett, J.W.M. Bulte, Applicability and limitations of MR tracking of neural stem cells with asymmetric cell division and rapid turnover: The case of the shiverer dysmyelinated mouse brain, Magn. Reson. Med. 58 (2007) 261–269. doi:10.1002/mrm.21280.
[370] E. Duguet, S. Vasseur, S. Mornet, J.-M. Devoisselle, Magnetic nanoparticles and their applications in medicine, Nanomedicine (Lond). 1 (2006) 157–168. doi:10.2217/17435889.1.2.157.
[371] M. Mahmoudi, I. Lynch, M.R. Ejtehadi, M.P. Monopoli, F.B. Bombelli, S. Laurent, Protein-nanoparticle interactions: Opportunities and challenges, Chem. Rev. 111 (2011) 5610–5637.

doi:10.1021/cr100440g.
[372] F. Joris, B.B. Manshian, K. Peynshaert, S.C. De Smedt, K. Braeckmans, S.J. Soenen, Assessing nanoparticle toxicity in cell-based assays: Influence of cell culture parameters and optimized models for bridging the in vitro-in vivo gap, Chem. Soc. Rev. 42 (2013) 8339–8359. doi:10.1039/c3cs60145e.
[373] S.J. Soenen, P. Rivera-Gil, J.M. Montenegro, W.J. Parak, S.C. De Smedt, K. Braeckmans, Cellular toxicity of inorganic nanoparticles: Common aspects and guidelines for improved nanotoxicity evaluation, Nano Today. 6 (2011) 446–465. doi:10.1016/j.nantod.2011.08.001.
[374] S.J. Soenen, W.J. Parak, J. Rejman, B. Manshian, (Intra)cellular stability of inorganic nanoparticles: Effects on cytotoxicity, particle functionality, and biomedical applications, Chem. Rev. 115 (2015) 2109–2135. doi:10.1021/cr400714j.
[375] W. Strober, Trypan blue exclusion test of cell viability, Curr. Protoc. Immunol. 111 (2015) A3.B.1-A3.B.3. doi:10.1002/0471142735.ima03bs111.
[376] J. Dapprich, R. Gilbert, K.P. Dresdner, C. Johnson, Superparamagnetic particle scaffold for regenerating damaged neural tissue, US20180064951A1, 2017. http://www.derwentinnovation.com/tip-innovation/recordView.do?datasource=T3&category=PAT&selRecord=1&totalRecords=1&databaseIds=PATENT&recordKeys=US20180064951A120180308 (accessed June 20, 2021).
[377] H. Hamidi, J. Lilja, J. Ivaska, Using xCELLigence RTCA instrument to measure cell adhesion, Bio-Protocol. 7 (2017) 2646. doi:10.21769/bioprotoc.2646.
[378] G.M. Cooper, The Eukaryotic Cell Cycle, in: Cell A Mol. Approach, 2nd ed., Sinauer Associates, 2000. https://www.ncbi.nlm.nih.gov/books/NBK9876/ (accessed June 18, 2021).
[379] J. He, M. Huang, D. Wang, Z. Zhang, G. Li, Magnetic separation techniques in sample preparation for biological analysis: A review, J. Pharm. Biomed. Anal. 101 (2014) 84–101. doi:10.1016/j.jpba.2014.04.017.
[380] Q.A. Pankhurst, J. Connolly, S.K. Jones, J. Dobson, Applications of magnetic nanoparticles in biomedicine, J. Phys. D. Appl. Phys. 36 (2003) 167–181. doi:10.1088/0022-3727/36/13/201.
[381] M.J.B. Matos, A.S. Pina, A.C.A. Roque, Rational design of affinity ligands for bioseparation, J. Chromatogr. A. 1619 (2020) 460871. doi:10.1016/j.chroma.2020.460871.
[382] H.Y. Xie, C. Zuo, Y. Liu, Z.L. Zhang, D.W. Pang, X.L. Li, J.P. Gong, C. Dickinson, W. Zhou, Cell-targeting multifunctional nanospheres with both fluorescence and magnetism, Small. 1 (2005) 506–509. doi:10.1002/smll.200400136.
[383] E.Q. Song, J. Hu, C.Y. Wen, Z.Q. Tian, X. Yu, Z.L. Zhang, Y.B. Shi, D.W. Pang, Fluorescent-magnetic-biotargeting multifunctional nanobioprobes for detecting and isolating multiple types of tumor cells, ACS Nano. 5 (2011) 761–770. doi:10.1021/nn1011336.
[384] A.J. Kell, G. Stewart, S. Ryan, R. Peytavi, M. Boissinot, A. Huletsky, M.G. Bergeron, B. Simard, Vancomycin-modified nanoparticles for efficient targeting and preconcentration of gram-positive and gram-negative bacteria, ACS Nano. 2 (2008) 1777–1788. doi:10.1021/nn700183g.
[385] V.C. Ozalp, G. Bayramoglu, M.Y. Arica, H.A. Oktem, Design of a core-shell type immuno-magnetic separation system and multiplex PCR for rapid detection of pathogens from food samples, Appl. Microbiol. Biotechnol. 97 (2013) 9541–9551. doi:10.1007/s00253-013-5231-0.
[386] J. Wang, X. Guo, Adsorption isotherm models: Classification, physical meaning, application and solving method, Chemosphere. 258 (2020) 127279. doi:10.1016/j.chemosphere.2020.127279.
[387] M. Silva Da Rocha, K. Iha, A.C. Faleiros, E.J. Corat, M.E.V. Suárez-Iha, Henry's law as a limit for an isotherm model based on a statistical mechanics approach, J. Colloid Interface Sci. 208 (1998) 211–215. doi:10.1006/jcis.1998.5779.
[388] H. Freundlich, Über die Adsorption in Lösungen, Zeitschrift Für Phys. Chemie. 57U (1907) 385–470. doi:10.1515/zpch-1907-5723.
[389] G. Halsey, H.S. Taylor, The adsorption of hydrogen on tungsten powders, J. Chem. Phys. 15

(1947) 624–630. doi:10.1063/1.1746618.
[390] G. Limousin, J.P. Gaudet, L. Charlet, S. Szenknect, V. Barthès, M. Krimissa, Sorption isotherms: A review on physical bases, modeling and measurement, Appl. Geochemistry. 22 (2007) 249–275. doi:10.1016/j.apgeochem.2006.09.010.
[391] I. Langmuir, The constitution and fundamental properties of solids and liquids. Part I. Solids, J. Am. Chem. Soc. 38 (1916) 2221–2295. doi:10.1021/ja02268a002.
[392] I. Langmuir, The adsorption of gases on plane surfaces of glass, mica and platinum, J. Am. Chem. Soc. 40 (1918) 1361–1403. doi:10.1021/ja02242a004.
[393] R.A. Latour, The Langmuir isotherm: A commonly applied but misleading approach for the analysis of protein adsorption behavior, J. Biomed. Mater. Res. - Part A. 103 (2015) 949–958. doi:10.1002/jbm.a.35235.
[394] J. Toth, State equations of the solid-gas interface layers, Acta Chim. Acad. Sci. Hungaricae. 69 (1971) 311–317.
[395] M.I. Temkin, V. Pyzhev, Kinetics of ammonia synthesis on promoted iron catalysts, Acta Physicochim. U.R.S.S. 12 (1940) 327–356.
[396] O. Redlich, D.L. Peterson, A useful adsorption isotherm, J. Phys. Chem. 63 (1959) 1024. doi:10.1021/j150576a611.
[397] R. Sips, On the structure of a catalyst surface, J. Chem. Phys. 16 (1948) 490–495. doi:10.1063/1.1746922.
[398] S. Brunauer, P.H. Emmett, E. Teller, Adsorption of gases in multimolecular layers, J. Am. Chem. Soc. 60 (1938) 309–319. doi:10.1021/ja01269a023.
[399] M. Ahmadi, H. Elmongy, T. Madrakian, M. Abdel-Rehim, Nanomaterials as sorbents for sample preparation in bioanalysis: A review, Anal. Chim. Acta. 958 (2017) 1–21. doi:10.1016/j.aca.2016.11.062.
[400] R. Koch, Methylene Blue, in: Some Drugs Herb. Prod., IARC monog, International Agency for Research on Cancer, Lyon, 2016: pp. 155–183.
[401] P. Guttmann, P. Ehrlich, Über die Wirkung des Methylenblau bei Malaria, Berliner Klin. Wochenschrift. 28 (1891) 953–956. https://www.scienceopen.com/document?vid=051547e1-2c6c-48ef-944f-50cbe55d3b46 (accessed May 22, 2021).
[402] M. Rafatullah, O. Sulaiman, R. Hashim, A. Ahmad, Adsorption of methylene blue on low-cost adsorbents: A review, J. Hazard. Mater. 177 (2010) 70–80. doi:10.1016/j.jhazmat.2009.12.047.
[403] V.K. Gupta, Suhas, Application of low-cost adsorbents for dye removal - A review, J. Environ. Manage. 90 (2009) 2313–2342. doi:10.1016/j.jenvman.2008.11.017.
[404] L. Barreiros, J.F. Queiroz, L.M. Magalhães, A.M.T. Silva, M.A. Segundo, Analysis of 17-β-estradiol and 17-α-ethinylestradiol in biological and environmental matrices - A review, Microchem. J. 126 (2016) 243–262. doi:10.1016/j.microc.2015.12.003.
[405] Y. Dai, C.C. Liu, Detection of 17 β-estradiol in environmental samples and for health care using a single-use, cost effective biosensor based on differential pulse voltammetry (DPV), Biosensors. 7 (2017) 15. doi:10.3390/bios7020015.
[406] T. Mori, Novel principles and nanostructuring methods for enhanced thermoelectrics, Small. 13 (2017) 1702013. doi:10.1002/smll.201702013.
[407] J. He, T.M. Tritt, Advances in thermoelectric materials research: Looking back and moving forward, Science. 357 (2017) eaak9997. doi:10.1126/science.aak9997.
[408] G.J. Snyder, T.S. Ursell, Thermoelectric efficiency and compatibility, Phys. Rev. Lett. 91 (2003) 148301. doi:10.1103/PhysRevLett.91.148301.
[409] D.M. Rowe, Thermoelectrics Handbook: Macro to Nano, CRC Press, Boca Raton, 2006. doi:10.1201/9781420038903.
[410] T.M. Tritt, ed., Thermal Conductivity: Theory, Properties, and Applications, Kluwer Academic/Plenum Publishers, New York, 2004. doi:10.1007/b136496.
[411] K. Biswas, J. He, I.D. Blum, C.I. Wu, T.P. Hogan, D.N. Seidman, V.P. Dravid, M.G. Kanatzidis, High-performance bulk thermoelectrics with all-scale hierarchical

architectures, Nature. 489 (2012) 414–418. doi:10.1038/nature11439.
[412] G.J. Snyder, E.S. Toberer, Complex thermoelectric materials, Nat. Mater. 7 (2008) 105–114. doi:10.1038/nmat2090.
[413] C.-W. Nan, R. Birringer, Determining the Kapitza resistance and the thermal conductivity of polycrystals: A simple model, Phys. Rev. B. 57 (1998) 8264–8268. doi:10.1103/PhysRevB.57.8264.
[414] D.T. Morelli, V. Jovovic, J.P. Heremans, Intrinsically minimal thermal conductivity in cubic I-V-VI_2 semiconductors, Phys. Rev. Lett. 101 (2008) 035901. doi:10.1103/PhysRevLett.101.035901.
[415] D.M. Rowe, ed., CRC Handbook of Thermoelectrics, CRC Press, Boca Raton, 1995. doi:10.1201/9781420049718.
[416] M. Beekman, D.T. Morelli, G.S. Nolas, Better thermoelectrics through glass-like crystals, Nat. Mater. 14 (2015) 1182–1185. doi:10.1038/nmat4461.
[417] G.S. Nolas, D.T. Morelli, T.M. Tritt, Skutterudites: a phonon-glass-electron crystal approach to advanced thermoelectric energy conversion applications, Annu. Rev. Mater. Sci. 29 (1999) 89–116. doi:10.1146/annurev.matsci.29.1.89.
[418] M. Ohtaki, S. Miyaishi, Extremely low thermal conductivity in oxides with cage-like crystal structure, J. Electron. Mater. 42 (2013) 1299–1302. doi:10.1007/s11664-012-2382-1.
[419] N.-L.H. Liu, D. Emin, Thermoelectric power of small polarons in magnetic semiconductors, Phys. Rev. B. 30 (1984) 3250–3256. doi:10.1103/PhysRevB.30.3250.
[420] M. Bailyn, Maximum variational principle for conduction problems in a magnetic field, and the theory of magnon drag, Phys. Rev. 126 (1962) 2040–2054. doi:10.1103/PhysRev.126.2040.
[421] R. Ang, A.U. Khan, N. Tsujii, K. Takai, R. Nakamura, T. Mori, Thermoelectricity generation and electron-magnon scattering in a natural chalcopyrite mineral from a deep-sea hydrothermal vent, Angew. Chemie - Int. Ed. 54 (2015) 12909–12913. doi:10.1002/anie.201505517.
[422] C.C. Zhao, C. Xiao, When thermoelectric materials come across with magnetism, Rare Met. 40 (2021) 752–766. doi:10.1007/s12598-020-01652-6.
[423] E. Dutková, Z. Bujňáková, J. Kováč, I. Škorvánek, M.J. Sayagués, A. Zorkovská, J. Kováč, P. Baláž, Mechanochemical synthesis, structural, magnetic, optical and electrooptical properties of $CuFeS_2$ nanoparticles, Adv. Powder Technol. 29 (2018) 1820–1826. doi:10.1016/J.APT.2018.04.018.
[424] J. Callaway, Model for lattice thermal conductivity at low temperatures, Phys. Rev. 113 (1959) 1046–1051. doi:10.1103/PhysRev.113.1046.
[425] J. Callaway, H.C. von Baeyer, Effect of point imperfections on lattice thermal conductivity, Phys. Rev. 120 (1960) 1149–1154. doi:10.1103/PhysRev.120.1149.

List of figures

List of tables

List of abbreviations

A549	specific human lung adenocarcinoma cell line
bcc	body-centered cubic
CA	contrast agent
CFSE	crystal field stabilization energy
CI	cell index
CP	Carr-Purcell
CPMG	Carr-Purcell-Meiboom-Gill
CTAB	cetyltrimethylammonium bromide
DAPI	2-(4-amidinophenyl)-1*H*-indole-6-carboxamidine, a fluorescent stain
DOTA	dodecane tetraacetic acid, i.e., 2,2',2'',2'''-(1,4,7,10-tetraazacyclododecane-1,4,7,10-tetrayl)tetraacetic acid, serving as a chelating ligand
DTBA-BMA	2-[bis[2-(carboxylatomethyl-(methylcarbamoylmethyl)amino)ethyl]amino]acetate, serving as a chelating ligand
EFG	electric field gradient
EMA	European Medicines Agency
FC	field-cooling
fcc	face-centered cubic
FID	free induction decay
GKA	Goodenough-Kanamori-Anderson
HRTEM	high-resolution transmission electron microscopy
MAR	motional averaging regime
MCF-7	specific human breast adenocarcinoma cell line
MSPE	magnetic solid-phase extraction
MPI	magnetic particle imaging
MRI	nuclear magnetic resonance imaging
NMR	nuclear magnetic resonance, nuclear magnetic resonance spectroscopy
NMRD	nuclear magnetic relaxation dispersion
OSPE	octahedral site preference energy
PCR	polymerase chain reaction
PEO	poly(ethylene oxide)
PET	positron emission tomography
PGEC	phonon-glass-electron-crystal

PPO	poly(propylene oxide)
PRM	partial refocusing model
RES	reticuloendothelial system
rf	radiofrequency
RKKY	Ruderman-Kittel-Kasuya-Yosida
RTG	radioisotope thermoelectric generator
SBA	“Santa-Barbara-Amorphous”-type of mesoporous silica
SD	single-domain
SERS	surface-enhanced Raman spectroscopy
SPION	superparamagnetic iron oxide nanoparticle
SPM	superparamagnetic, superparamagnetism
SDR	static dephasing regime
TEM	transmission electron microscopy
TEOS	tetraethoxysilane
THE	thermoelectric
TMOS	tetramethoxysilane
USPION	ultra-small superparamagnetic iron oxide nanoparticle
XANES	X-ray absorption near-edge structure
XPS	X-ray photoelectron spectroscopy
ZFC	zero-field-cooling

List of symbols

Vectors are shown in **bold**, the same symbol in a normal font marks the magnitude of the vector quantity, if not stated otherwise.

[*hkl*]	crystallographic direction or axis, alternatively a set of parallel directions/axes
⟨*hkl*⟩	set of crystallographic directions or axes that are equivalent to the [*hkl*] direction under the symmetry group of the crystal, alternatively a direction/axis in the set
(*hkl*)	crystallographic plane, alternatively a set of parallel planes
{*hkl*}	set of crystallographic planes that are equivalent to the (*hkl*) plane under the symmetry group of the crystal, alternatively a plane in the set
[…]	in a structural formula: ions in the octahedral sites
(…)	in a structural formula: ions in the tetrahedral sites
▢	cation vacancy
∇	nabla (del) operator, i.e., vector differential operator

A	area fraction of a component in the Mössbauer spectrum
A',B',C'	adjustable parameters in the formula (6.14)
A_{ex}	exchange stiffness
a	distance between magnetic atoms
a, b, c	lattice constants
$\boldsymbol{B}$	magnetic flux density
$\mathcal{B}$	thermoelectric quality factor
$\boldsymbol{B}_0$	magnetic flux density characterizing the applied static magnetic field in nuclear magnetic resonance spectroscopy/imaging
$\boldsymbol{B}_{\mathrm{dip}}$	magnetic flux density characterizing the dipolar magnetic field of a magnetic nanoparticle
$\bar{B}_{\mathrm{dip},z}$	average z-component of $\boldsymbol{B}_{\mathrm{dip}}$
$\boldsymbol{B}_{\mathrm{eff}}$	magnetic flux density characterizing the effective hyperfine magnetic field
$\boldsymbol{B}_{\mathrm{ext}}$	magnetic flux density characterizing the external (applied) magnetic field
$\boldsymbol{B}_{\mathrm{hf}}$	magnetic flux density characterizing the hyperfine magnetic field
$\langle B_{\mathrm{hf}} \rangle$	mean magnetic flux density characterizing the hyperfine magnetic field
C	constant of proportionality
C_V	isochoric heat capacity
CI	cell index
c_{CA}	concentration of a contrast agent in a suspension/solution
c_{e}	equilibrium concentration of an analyte in a solution
D	self-diffusion coefficient of water
D_0	constant in the Speedy-Angell power-law for the self-diffusion coefficient of water, $D_0 = 1.635(2) \cdot 10^{-8}$ m^2 s^{-1}
$\boldsymbol{D}_{ij}$	Dzyaloshinskii-Moriya vector for a given pair of spins $\boldsymbol{S}_i$ and $\boldsymbol{S}_j$
D_{DM}	magnitude of the overall Dzyaloshinskii-Moriya vector from summed $\boldsymbol{D}_{ij}$
d	size of a particle
d_{c}	size of the magnetic core (a single crystallite or their cluster) of a nanoparticle, excluding nonmagnetic coating
d_{ij}	distance between particles i and j
d_{PRM}	critical size of a spherical particle which marks the transition from the static dephasing regime to the partial refocusing model.
d_{p}	size of a coated particle (including nonmagnetic coating)
d_{SDR}	critical size of a spherical particle which marks the transition from the motional averaging to the static dephasing regime
E	energy functional of a uniaxial magnet
E^{sh}	magnetostatic energy of a uniformly magnetized ellipsoid

$E_{\mathrm{an}}^{\mathrm{uni}}$ anisotropy energy of a particle with uniaxial anisotropy

E_{B} anisotropy energy barrier between easy axes of magnetization of a particle

E_{dd} energy of the magnetic dipole-dipole interaction

e thickness of silica coating

F_{d} hydrodynamic drag force

$\boldsymbol{F}_{\mathrm{m}}$ magnetic force

f volume fraction that particles occupy in a suspension

$f_{\mathrm{mc}}^{\mathrm{cub}}$ density of magnetocrystalline anisotropy energy in the case of a cubic anisotropy

$f_{\mathrm{mc}}^{\mathrm{uni}}$ density of magnetocrystalline anisotropy energy in the simplest case of a uniaxial anisotropy

$f_{\mathrm{mc}}^{\mathrm{uni}\prime}$ density of magnetocrystalline anisotropy energy in the uniaxial case expanded with higher-order powers of directional cosines

$\boldsymbol{H}$ magnetic field strength

H_{c} strength of the coercive field

$H_{\mathrm{c}}(\|)$ strength of the coercive field if the applied field is oriented along the particle easy axis

$\boldsymbol{H}_{\mathrm{d}}$ strength of the magnetostatic self-interaction field, alternatively the demagnetizing field in homogeneously magnetized ellipsoids of revolution

H_{int} strength of the mean interaction field

H_{sw} strength of the coercive field of a particle at zero temperature

$\mathcal{H}_{ij}$ exchange interaction Hamiltonian

$\mathcal{H}_{ij}^{\mathrm{DM}}$ exchange interaction Hamiltonian of the Dzyaloshinskii-Moriya interaction

$\mathcal{H}_{ij}^{\mathrm{tet}}$ exchange interaction Hamiltonian with symmetrical part of $\hat{J}$ in a tetragonal structure

h_{c} reduced coercive field, the ratio of H_{c} and $H_{\mathrm{c}}(\|)$

ħ reduced Planck constant, ħ = 1.054 571 817... · 10^{-34} J s

$\boldsymbol{I}$ spin angular momentum of a nucleus

I nuclear spin quantum number

I_{sd} coupling constant between the conduction s and localized d-electrons or between itinerant and localized d-electrons

i, j indices denoting individual species (atoms, electrons, etc.)

i inversion parameter of a spinel-type compound

$\hat{J}$ exchange interaction tensor

J exchange interaction constant in the isotropic Heisenberg exchange

$J_{\|}$ exchange interaction constant along the z-axis, e.g., in a tetragonal structure

$J_\perp$ exchange interaction constant in the xy-plane, e.g., in a tetragonal structure

J_i exchange interaction constant of the interaction of an ion with its ith nearest neighbor

J_{RKKY} exchange interaction constant in the Ruderman-Kittel-Kasuya-Yosida interaction

$J_{\alpha\beta}$ component of the exchange interaction tensor

K effective anisotropy constant

K_1 first magnetocrystalline anisotropy constant

K_2 second magnetocrystalline anisotropy constant

K_{cf} surface anisotropy constant

K'_i magnetocrystalline anisotropy constant including the magnetostrictive contribution

K_{w} ionization product of water

k instrumental proportionality factor modifying the magnitude of detected MRI signal

k_{a} kinetic rate constant of adsorption

k_{B} Boltzmann constant, $k_{\mathrm{B}} = 1.380\,649 \cdot 10^{-23}$ J K^{-1}

k_{d} kinetic rate constant of desorption

k_{F} radius of the Fermi sphere

$\boldsymbol{L}$ angular momentum of an atom

$L(x)$ Langevin function

l_{ex} exchange length

l_{p} phonon mean free path

$\boldsymbol{M}$ magnetization

$M_\perp$ transverse component of magnetization (perpendicular to the static magnetic field in NMR/MRI)

M_0 initial magnetization, e.g., magnetization of an ensemble before relaxation

M_{AFM} magnetization of antiferromagnetic nanoparticles

M_{core} magnetization of the magnetic phase in the magnetic core of a nanoparticle

M_{r} remanent magnetization

$M_{\mathrm{r}}(\parallel)$ remanent magnetization if the applied field was oriented along the particle easy axis

M_{s} magnitude of the spontaneous magnetization

M_{sat} saturation magnetization

M_{unc} magnetization from uncompensated spins in an antiferromagnetic material

M_w	molar mass of a magnetic phase
M_α	component of the magnetization vector $\boldsymbol{M}$ along the Cartesian axis $\alpha = x, y, z$
$\boldsymbol{m}$	magnetic moment
m^*	effective mass of a charge carrier
$\boldsymbol{m_0}$	magnetic moment of an atom in an octahedral site
m_r	reduced remanent magnetization, ratio of M_r and $M_\mathrm{r}(\|\|)$
$\langle m \rangle$	average magnetic moment
N_ag	number of particles in an aggregate
N_α	demagnetizing factor along the Cartesian axis $\alpha = x, y, z$
$\boldsymbol{n}$	unit vector of the easy axis of magnetization
PF	power factor
Q_e	adsorbed amount of an analyte on a solid sorbent
Q_s	maximum adsorption capacity of a sorbent
q	transferred charge
R	radial distance (radial coordinate) in the spherical coordinates
R_1	longitudinal (spin-lattice) relaxation rate
R_2	transverse (spin-spin) relaxation rate
$R_\mathrm{2,MAR}$	transverse relaxation rate in the motional averaging regime
$R^*_\mathrm{2,MAR}$	transverse relaxation rate of the free induction decay in the motional averaging regime
$R^*_\mathrm{2,SDR}$	transverse relaxation rate of the free induction decay in the static dephasing regime
$R_{i,0}$	longitudinal (i = 1) or transverse (i = 2) relaxation rate of medium without a contrast agent
R_K	Kapitza resistance
$\boldsymbol{r}$	position vector
r	distance from the selected origin or between selected points in space
r'	radius of an inner region around a magnetic particle in a suspension at whose border $\Delta\omega'\tau_\mathrm{D} = 1$, in the partial refocusing model
r_c	radius of the magnetic core (a single crystallite or their cluster) of a nanoparticle, excluding nonmagnetic coating
r_1	longitudinal (spin-lattice) relaxivity
r_2	transverse (spin-spin) relaxivity
$r_\mathrm{2,MAR}$	transverse relaxivity in the motional averaging regime
$r_\mathrm{2,PRM}$	transverse relaxivity described by the partial refocusing model
$r^*_\mathrm{2,PRM}$	transverse relaxivity of the free induction decay described by the partial refocusing model

$r_{2,\mathrm{SDR}}$ transverse relaxivity in the static dephasing regime

$r^*_{2,\mathrm{SDR}}$ transverse relaxivity of the free induction decay in the static dephasing regime

r_{coh} critical radius of a particle below which all atomic spins rotate coherently in an applied field

r_{p} radius of a spherical particle

r_{SD} critical radius of a spherical particle below which the particle is in the single-domain state

$\boldsymbol{S}$ spin angular momentum of an atom

S spin quantum number

$S_{i\alpha}$ α component of the spin angular momentum of an atom i

S_{THE} thermoelectric compatibility factor

S_{ξ} component of spin normal to the surface of a particle

$\langle S \rangle$ average sublattice magnetization related to the atomic spins

s, s' refinable parameters scaling fit of temperature dependence of relaxivity by theoretical models to experimental values in expressions (5.15) and (5.16)

T temperature in kelvins

T_0 phenomenological temperature characterizing the interaction in an ensemble of magnetic particles

T_1 longitudinal (spin-lattice) relaxation time

T_2 transverse (spin-spin) relaxation time

T_2^* accelerated transverse relaxation time of the free induction decay

T_{B} blocking temperature

T_{C} Curie temperature

T_{cold} temperature of the cold side of a thermoelectric device

T_{f} freezing temperature, below which spins are in a magnetically frozen state

T_{hot} temperature of the hot side of a thermoelectric device

T_{irr} temperature of irreversibility – bifurcation point of ZFC and FC curves

T_{M} Morin temperature

T_{max} maximum temperature or temperature of a maximum, e.g., the temperature at which maximum of the ZFC curve is achieved

T_{N} Néel temperature

T_{o} ordering temperature

T_{S} spin-reorientation temperature

T_{s} characteristic temperature in the Speedy-Angell power-law for the self-diffusion coefficient of water, $T_{\mathrm{s}} = 215.1(12)$ K

T_{V} Verwey transition temperature

TE echo-time in MRI, TE = $2t_{\mathrm{e}}$

TR	repetition time in MRI
t	time; in unambiguous cases might denote also temperature provided in degrees Celsius
t_e	time interval between the π/2-pulse and the π-pulse in the spin-echo NMR pulse sequence, the spin echo occurs at time $2t_\mathrm{e}$ = TE after the π/2-pulse
u	fractional coordinate of anion in the spinel structure
V	volume
V_hd	hydrodynamic volume of a particle
v	velocity
v_s	mean speed of sound
w_MAR	weight of the motional averaging regime in transverse relaxivity of an ensemble of particles
w_SDR	weight of the static dephasing regime in transverse relaxivity of an ensemble of particles
x_i	the ith coordination axis
ZT	figure of merit
ZT_m	figure of merit at the average temperature between T_cold and T_hot
α, β	indices denoting Cartesian axes x, y, z when describing components of a vector/tensor
α	Seebeck coefficient (thermopower)
α_0	Seebeck coefficient at T = 0 K
α_ph	phenomenological exponent in the expression (2.13) for $E_\mathrm{B}(H)$
α_β	directional cosines characterizing the angle between magnetization and main crystal axes, $\beta = x, y, z$
β	angle between vectors of the dipolar magnetic field of a nanoparticle and a static magnetic field in NMR/MRI
γ	domain-wall energy
γ_N	nuclear gyromagnetic ratio, γ_N (^{1}H) = 267 522 187.44(11) rad s^{-1} T^{-1} or $\gamma_\mathrm{N}(^1\mathrm{H})/2\pi$ = 42.577 478 518(18) MHz T^{-1}
γ_SA	exponent in the Speedy-Angell power-law for the self-diffusion coefficient of water, $\gamma_\mathrm{SA} = 2.06(5)$
Δ_oct	crystal field splitting between $t_{2\mathrm{g}}$ and e_g d-orbital levels of a transition metal ion in an octahedral site
Δ_t	crystal field splitting between e_g and $t_{2\mathrm{g}}$ d-orbital levels of a transition metal ion in a tetrahedral site
Δ_Q	quadrupole splitting

$\langle \Delta_Q \rangle$	mean quadrupole splitting
δ	isomer shift
δ_0	domain-wall width parameter
δT_f	difference of freezing temperatures in an applied magnetic field and at zero fields
ε	quadrupole shift
$\langle \varepsilon \rangle$	mean quadrupole shift
ε_F	Fermi energy
η	dynamic viscosity of a medium
η_{Car}	Carnot efficiency
η_{max}	maximum power-generation efficiency of a thermoelectric device
θ	polar angle in the spherical coordinates, e.g., between the *z*-axis and magnetization
θ_{cone}	angle between the *z*-axis and magnetization in the case of an easy-cone anisotropy
θ_D	Debye temperature
ϑ	angle between the local symmetry axis and the local hyperfine magnetic field
κ	thermal conductivity
κ_0	thermal conductivity of bulk
κ_e	charge-carrier thermal conductivity
κ_F	constant prefactor in the Freundlich isotherm
κ_L	adsorption equilibrium constant for the Langmuir adsorption process
κ_l	lattice thermal conductivity
λ	spin-orbit coupling constant
$\boldsymbol{\mu}$	magnetic moment of a nucleus
μ_0	permeability of vacuum; $\mu_0 = 4\pi \cdot 10^{-7}$ H m^{-1}
μ_B	Bohr magneton; μ_B = 9.274 010 078 3(28) · 10^{-24} J T^{-1}
μ_c	charge carrier mobility
μ_{eff}	effective magnetic moment of an atom
ξ	canting angle between neighboring spins due to the Dzyaloshinskii-Moriya interaction
ξ_m	magnetophoretic mobility of a particle in a solvent
ρ	volumetric mass density
Σ	spin-echo induction voltage providing the signal in MRI
σ	electrical conductivity
σ_B	standard deviation of a distribution of hyperfine magnetic flux density
σ_{QS}	standard deviation of a distribution of quadrupole shift/splitting

ς	temperature-independent prefactor in the magnon law for the temperature dependence of magnetization of antiferromagnets
τ	relaxation time
τ_0	preexponential factor in the Néel relaxation time, the time between jump attempts of a particle moment between opposite directions of the easy axis
τ_0'	modified preexponential factor in the Vogel-Fulcher relaxation time τ_{VF}
τ_{B}	Brownian relaxation time
τ_{D}	diffusion correlation time
τ_{eff}	effective relaxation time
τ_{m}	characteristic time of a probing method
τ_{N}	Néel relaxation time
τ_{VF}	Vogel-Fulcher law for the relaxation time in an ensemble of weakly interacting magnetic nanoparticles
Φ_0	magnetic flux quantum, $\Phi_0 = 2.067\ 833\ 848\ldots \cdot 10^{-15}$ T m^2
φ	azimuthal angle in the spherical coordinates
χ	magnetic susceptibility
χ_{AFM}	antiferromagnetic susceptibility
χ_{FC}	magnetic susceptibility of a sample measured during heating after cooling in an external magnetic field
χ_{M}	molar magnetic susceptibility
χ_{p}	magnetic susceptibility of a particle
χ_{s}	magnetic susceptibility of a solvent
χ_{ZFC}	magnetic susceptibility of a sample measured during heating after cooling in zero magnetic fields
$\Delta\chi$	difference in susceptibility
ψ	angle between the applied magnetic field and anisotropy axis (easy axis) of a particle
ω	angular frequency
ω_0	Larmor frequency of a nucleus in a magnetic field
ω_{tot}	Larmor frequency of a ^{1}H nucleus in a static external magnetic field and the dipolar magnetic field of a nanoparticle
$\Delta\omega$	dispersion of ^{1}H Larmor frequency shifts
$\Delta\omega'$	dispersion of ^{1}H Larmor frequency shifts at the boundary of an inner region near a magnetic nanoparticle in a suspension, where $\Delta\omega' = 1/\tau_{\mathrm{D}}$, in the partial refocusing model

Author's articles included in the thesis – in attachment

[D1] O. Kaman, V. Herynek, P. Veverka, L. Kubíčková, M. Pashchenko, J. Kuličková, Z. Jirák, Transverse relaxivity of nanoparticle contrast agents for MRI: Different magnetic cores and coatings, IEEE Trans. Magn. 54 (2018) 5300405. doi:10.1109/TMAG.2018.2844253.

[D2] J. Stergar, Z. Jirák, P. Veverka, L. Kubíčková, T. Vrba, J. Kuličková, K. Knížek, F. Porcher, J. Kohout, O. Kaman, Mn-Zn ferrite nanoparticles coated with mesoporous silica as core material for heat-triggered release of therapeutic agents, J. Magn. Magn. Mater. 475 (2019) 429–435. doi:10.1016/j.jmmm.2018.11.020.

[D3] L. Kubíčková, P. Brázda, M. Veverka, O. Kaman, V. Herynek, M. Vosmanská, P. Dvořák, K. Bernášek, J. Kohout, Nanomagnets for ultra-high field MRI: Magnetic properties and transverse relaxivity of silica-coated ε-Fe_2O_3, J. Magn. Magn. Mater. 480 (2019) 154–163. doi:10.1016/j.jmmm.2019.02.067.

[D4] P. Veverka, M. Pashchenko, L. Kubíčková, J. Kuličková, Z. Jirák, R. Havelek, K. Královec, J. Kohout, O. Kaman, Rod-like particles of silica-coated maghemite: Synthesis via akaganeite, characterization and biological properties, J. Magn. Magn. Mater. 476 (2019) 149–156. doi:10.1016/j.jmmm.2018.12.037.

[D5] L. Kubíčková, O. Kaman, P. Veverka, V. Herynek, P. Brázda, M. Vosmanská, T. Kmječ, P. Dvořák, D. Kubániová, J. Kohout, The ε-$Al_xFe_{2-x}O_3$ nanomagnets as MRI contrast agents: Factors influencing transverse relaxivity, Colloids Surfaces A Physicochem. Eng. Asp. 589 (2020) 124423. doi:10.1016/j.colsurfa.2020.124423.

[D6] P. Baláž, E. Dutková, P. Levinský, N. Daneu, L. Kubíčková, K. Knížek, M. Baláž, J. Navrátil, J. Kašparová, V. Ksenofontov, A. Möller, J. Hejtmánek, Enhanced thermoelectric performance of chalcopyrite nanocomposite via co-milling of synthetic and natural minerals, Mater. Lett. 275 (2020) 128107. doi:10.1016/j.matlet.2020.128107.

[D7] K. Královec, R. Havelek, D. Koutová, P. Veverka, L. Kubíčková, P. Brázda, J. Kohout, V. Herynek, M. Vosmanská, O. Kaman, Magnetic nanoparticles of Ga-substituted ε-Fe_2O_3 for biomedical applications: Magnetic properties, transverse relaxivity, and effects of silica-coated particles on cytoskeletal

networks, J. Biomed. Mater. Res. - Part A. 108 (2020) 1563–1578. doi:10.1002/jbm.a.36926.

[D8] L. Kubíčková, J. Koktan, T. Kořínková, M. Klementová, T. Kmječ, J. Kohout, A. Weidenkaff, O. Kaman, Zn-substituted iron oxide nanoparticles from thermal decomposition and their thermally treated derivatives for magnetic solid-phase extraction, J. Magn. Magn. Mater. 498 (2020) 166083. doi:10.1016/j.jmmm.2019.166083.

[D9] P. Baláž, M. Achimovičová, M. Baláž, K. Chen, O. Dobrozhan, E. Guilmeau, J. Hejtmánek, K. Knížek, L. Kubíčková, P. Levinský, V. Puchý, M.J. Reece, P. Varga, R. Zhang, Thermoelectric Cu–S-based materials synthesized via a scalable mechanochemical process, ACS Sustain. Chem. Eng. 9 (2021) 2003–2016. doi:10.1021/acssuschemeng.0c05555.

[D10] P. Veverka, L. Kubíčková, Z. Jirák, V. Herynek, M. Veverka, O. Kaman, Temperature and field dependences of transverse relaxivity of Co–Zn ferrite nanoparticles coated with silica: The role of magnetic properties and different regimes, Mater. Chem. Phys. 260 (2021) 124178. doi:10.1016/j.matchemphys.2020.124178.

[D11] L. Kubíčková, O. Kaman, P. Veverka, V. Herynek, P. Brázda, K. Bernášek, M. Veverka, J. Kohout, Magnetic properties, ^{57}Fe Mössbauer spectroscopy and ^{1}H NMR relaxometry of ε-$Fe_{2-x}Ga_xO_3$ nanoparticles: The effect of gallium doping on magnetic and MRI performance, J. Alloys Compd. 856 (2021) 158187. doi:10.1016/j.jallcom.2020.158187.

[D12] M. Pashchenko, P. Veverka, T. Kmječ, O. Kaman, L. Kubíčková, J. Kohout, M. Klementová, O. Kravchuk, A. Vakula, S. Tarapov, J. Hejtmánek, K. Knížek, Magnetic, FMR and mössbauer studies of nanocrystalline greigite, J. Alloys Compd. 857 (2021) 157569. doi:10.1016/j.jallcom.2020.157569.

Author's other articles

[O1] J. Kohout, P. Brázda, K. Závěta, D. Kubániová, T. Kmječ, L. Kubíčková, M. Klementová, E. Šantavá, A. Lančok, The magnetic transition in ε-Fe_2O_3 nanoparticles: Magnetic properties and hyperfine interactions from Mössbauer spectroscopy, J. Appl. Phys. 117 (2015) 17D505. doi:10.1063/1.4907610.

[O2] L. Kubíčková, J. Kohout, P. Brázda, M. Veverka, T. Kmječ, D. Kubániová, P. Bezdička, M. Klementová, E. Šantavá, K. Závěta, Impact of silica environment on hyperfine interactions in ε-Fe_2O_3 nanoparticles, Hyperfine Interact. 237 (2016) 159. doi:10.1007/s10751-016-1356-8.

[O3] D. Kubániová, L. Kubíčková, T. Kmječ, K. Závěta, D. Nižňanský, P. Brázda, M. Klementová, J. Kohout, Hematite: Morin temperature of nanoparticles with different size, J. Magn. Magn. Mater. 475 (2019) 611–619. doi:10.1016/j.jmmm.2018.11.126.

[O4] J. Navrátil, P. Levinský, J. Hejtmánek, M. Pashchenko, K. Knížek, L. Kubíčková, T. Kmječ, Č. Drašar, Peculiar magnetic and transport properties of $CuFeS_2$: Defects play a key role, J. Phys. Chem. C. 124 (2020) 20773–20783. doi:10.1021/acs.jpcc.0c06490.

[O5] M. Sorolla, X. Wang, L. Kubíčková, V. Ksenofontov, A. Möller, A.J. Jacobson, A mixed-valent iron(II/III) diamond chain with single-ion anisotropy, Inorg. Chem. 59 (2020) 1068–1074. doi:10.1021/acs.inorgchem.9b02616.

[O6] O. Kaman, D. Kubániová, K. Knížek, L. Kubíčková, J. Kohout, Z. Jirák, Structure and magnetic state of hydrothermally prepared Mn-Zn ferrite nanoparticles, J. Alloys Compd. (2021) under review.

[O7] I. Smytschkow, W. Gidt, Y. Sun, J. Langer, T. Böttcher, L. Kubíčková, O. Kaman, H. Sitzmann, Chromium(II) alkylcyclopentadienyl complexes with carbon or hydride donor ligands, Organometallics. (2021) under review.